PhD in

INDUSTRIAL ENGINEERING

Energy and Innovative Industrial and Environmental Technologies

CYCLE XXXV

COORDINATOR Prof. Giovanni Ferrara

Multi-physics and multi-fidelity simulation techniques for turbochargers

Academic Discipline (SSD) ING-IND/08

Doctoral Candidate	**Supervisor**
Dr. Catalani Iacopo	Prof. Ferrara Giovanni

Coordinator
Prof. Ferrara Giovanni

Years 2019/2023

Università degli Studi di Firenze, Dipartimento di Ingegneria Industriale (DIEF).

Acknowledgements

There are so many people that I wish to thank for making this work possible, so I'll just start with the highest in rank: many thanks to Prof. Giovanni Ferrara for guiding my research work through interesting and engaging suggestions, the trust he gave me always nourished my sense of responsibility. My gratitude also goes to my technical supervisor, Dr. Francesco Balduzzi, withouth whom most of the fluid dynamic mysteries I encountered would've been left unsolved: what else can I say, he's the person that makes you feel smarter the moment he agrees with you. Many thanks also to my co-supervisors: Dr. Alessandro Bianchini, an unstoppable engine of productivity, and Dr. Luca Romani, a never-ending source of wit. Eventually, I extend my thanks to all the people I shared my working environment with: there's no one that I don't consider a friend. So, thank you Alberto, Claretta, Claudio, Francesco P., Francesco S., Leonardo, Lorenzo, Marco C., Marco D., Niccolò, Omar, Pier, Riccardo, Sandro, Simone, Stefano, you all eased my burden.

At last, my deepest gratitude goes to my family and friends, and to Chiara, who always managed to draw out the adult in me.

Abstract

In the field of internal combustion engines (ICEs), forced induction by means of turbocharging is an industrial standard in many applications, from the automotive to the power generation sector. Turbocharging enhances an ICE's performance with respect to a naturally-aspirated engine of the same displacement, and is currently a key technology in the development of increasingly more efficient and environmentally sound ICEs. Currently, manufacturers heavily rely on computational methods during development, devoting experimental tests, while still indispensable, to more advanced development stages. Numerical modelling techniques are indeed a robust and cost-effective tool for the development of turbochargers. The present work focuses on the main drivers for turbochargers research and development, namely, the characterization through performance maps, thermal and structural analyses, and design optimizaton strategies. In the framework of industrial cooperation with leading companies in the ICEs field, such as Ferrari S.p.A. and Yanmar Co. Ltd., different test cases and simulation techniques were investigated. The commercial software suite ANSYS® was employed for the calculations. Initially, the prediction capability of steady-state 3D CFD (Computational Fluid Dynamics) approaches was assessed on a double-entry turbine, a particular design for which the available literature findings are remarkably scarce, especially under asymmetric, partial admission operation. The study was then extended to 3D CHT (Conjugate Heat Transfer) approaches with the aim of performing transient thermo-structural analyses on a turbine wheel: specifically, a computationally efficient model was developed in order to avoid expensive, often unfeasible, transient CHT calculations. Eventually, a multi-fidelity mixed 1D-3D approach for the aerodynamic optimization of a compressor's stationary parts (i.e. diffuser and volute) was developed with the aim of avoiding a lengthy iterative procedure for the matching with the ICE. In the development of the above-mentioned numerical models, several collateral aspects were investigated through sensitivity analyses, enhancing the scientific value of the work, moreover, the availability of experimental data for validation improves the robustness of the study.

Keywords: Turbocharger, ICE, Computational Fluid Dynamics, Multi-Physics, Multi-Fidelity, Double-Entry, Thermal, Structural, Optimization

Contents

List of Figures

List of Tables

Nomenclature

Acronyms

BC	Boundary Condition
BSL	Baseline
CFD	Computational Fluid Dynamics
CHT	Conjugate Heat Transfer
DNS	Direct Numerical Simulation
DOE	Design Of Experiments
EGR	Exhaust Gas Recirculation
FEM	Finite Element Method
FR	Frozen Rotor
FVM	Finite Volume Method
HTC	Heat Transfer Coefficient	$[J\ kg^{-1} K^{-1}]$
ICE	Internal Combustion Engine
LES	Large Eddy Simulation
MFP	Mass Flow Parameter	$[kg\ s^{-1}\ K^{0.5}\ Pa^{-1}]$
MP	Mixing Plane
NSE	Navier-Stokes Equations
OPT	Optimized
RANS	Reynolds-Averaged Navier-Stokes
SST	Shear Stress Transport
TC	Turbocharger
TRN	Transient
VGT	Variable Geometry Turbocharger
VM	Von Mises

Greek symbols

ζ	Loss coefficient	
Λ	Unsteadiness criterion	
Π	Pulse amplitude weighing factor	
β	Pressure ratio	
ε	Turbulence kinetic energy dissipation	$[m^2 s^{-3}]$
η	Efficiency	
λ	Thermal conductivity	$[W\ m^{-1}\ K^{-1}]$
μ	Dynamic viscosity	$[kg\ m^{-1}\ s^{-1}]$
ρ	Density	$[kg\ m^{-3}]$
υ	Kinematic viscosity	$[m^2\ s^{-1}]$

Latin symbols

c_p	Specific heat at constant pressure	$[J\ kg^{-1}\ K^{-1}]$
h	Specific enthalpy	$[J\ kg^{-1}]$
P	Pressure	$[Pa]$
Re	Reynolds number	
St	Strouhal number	
T	Temperature	$[K]$
k	Turbulence kinetic energy	$[m^2\ s^{-2}]$
t	Time	$[s]$

Subscripts and superscripts

*	Non-dimensionalized/Normalized quantity
0	Total quantity
in	Evaluated at domain's inlet
out	Evaluated at domain's outlet
ts	Total-to-static
tt	Total-to-total

Summary

In the field of internal combustion engines (ICEs), forced induction by means of turbocharging is an industrial standard in many applications, from the automotive to the power generation sector. Turbocharging enhances an ICE's performance with respect to a naturally-aspirated engine of the same displacement, and is currently a key technology in the development of increasingly more efficient and environmentally sound ICEs: innovative combustion processes, dual-fuel applications, NO_x containment by heavy use of exhaust gas recirculation (EGR), not to mention specific requirements of the automotive sector such as improved driveability, all require high-pressure, high-efficiency boosting and advanced turbocharging architectures. The development of turbochargers revolves around two main aspects. Firstly, the improvement of the turbocharger's performance capabilities by means of aerodynamic and mechanical design optimization: this reflects on the development of improved stator vanes and rotor geometries, better variable geometry turbochargers (VGT) actuators and advanced materials and coatings able to withstand increasingly higher turbine inlet temperature. Secondly, one must also strive for the optimal matching between engine and turbocharger, therefore it is paramount to accurately characterize turbocharger performance. To this end, experimental testing sets the benchmark, but the use of numerical techniques is nowadays fundamental and indispensable both in the R&D field and in the optimization of existing products.

The present work focuses on the main drivers for turbochargers research and development, namely, the characterization through performance maps, thermal and structural analyses, and design optimizaton strategies. In the framework of industrial cooperation with leading companies in the ICEs field, such as Ferrari S.p.A. and Yanmar Co. Ltd., different test cases and simulation techniques were investigated. The commercial software suite ANSYS® was employed for the calculations.

The first part of the study focused on assessing whether steady-state techniques represent a viable option to model a turbocharger's turbine in case of steady-state operation. Indeed, even under the engine's steady-state operation, a turbine coupled to an internal combustion engines is inherently supplied with a pulsating flow: this may hinder the prediction capabilities of a steady-state approach. The case study selected for this analysis is a double-entry turbine, a particular design for which the available literature findings are remarkably scarce. Depending on the engine's load demand, this type of turbine can operate under equal and unequal admission. In case of equal (or full) admission, both inlets supply the turbine with similar flow conditions; in case of unequal admission, the inlets are supplying the turbine at different flow conditions. Furthermore, the partial (or single) admission condition represents an extreme case of unequal admission, where only one inlet supplies the turbine. This latter operating condition is particulary worthy of investigation, since the unsteady phenomena that occur in the rotor due to the asymmetric supply may undermine the effectiveness of steady-state modelling approaches. Initially, an introductory

literature review on the modelling of pulsating flow was carried out, then, the performance prediction capabilities of steady-state approaches, such as the Mixing Plane (MP) and Frozen Rotor (FR) stator-rotor interface models, were assessed under full and partial admission operation.

Moving from the results of this analysis, effort was put in the development of a computationally efficient method for the transient thermo-structural analysis of a turbine wheel. The developed transient thermal model allows to carry out analyses that only feature the solid domain, taking advantage of adequate boundary conditions that model the effects of the fluid domain without simultaneously solving it. Eventually, transient thermo-structural analyses of different engine maneuvers were carried out. In the development of the thermo-structural numerical setup, several modelling aspects were investigated, ranging from the effects of environmental heat transfer of the turbine's housing to the cooling effects of the oil lubricates the turbine's shaft.

Lastly, a multi-fidelity methodology for the aerodynamic optimization of a compressor's diffuser and volute was developed. Throughout the optimization activity, a 1D engine model was coupled to the developed 3D CFD model with the aim of always granting the optimal matching between engine and turbocharger. This translates into optimizing the turbocharger's performance for the very conditions at which the optimized configuration is expected to operate, therefore avoiding incorrect matching and lengthy iterative procedures that would loop over the 1D and 3D models. Indeed, the optimization strategy that was developed starts by hypothesizing the efficiency increase that is expected from the forthcoming optimization, so the operating conditions of the "guessed" optimized configuration can be obtained through the 1D model. The subsequent design optimization is DOE-based: several diffuser configurations were generated and tested, and flow structures were thoroughly investigated to better understand the resulting performance parameters. Additionally, different volute cross-sectional shape and area distribution laws were analyzed: for each configuration, contour plots of total pressure and entropy generation rate were employed to investigate the flow behavior within the volute.

In the development of the above-mentioned numerical models, several collateral aspects were investigated through sensitivity analyses, enhancing the scientific value of the work, moreover, the availability of experimental data for validation greatly improves the robustness of the study.

Thesis outline

The thesis is structured as follows:

- *Chapter 1* provides a brief introduction to turbocharging technology, its applications and the numerical modelling techniques that are typically employed in turbochargers development;

- *Chapter 2* provides an overview of the governing equations and key concepts of 3D CFD modelling, with special focus on the modelling of moving reference frames;

- *Chapter 3* represents an outline of the research work and provides an extended introduction to each analysis that is presented in the following chapters;

- *Chapter 4* presents the assessment of steady-state techniques for the performance characterization of a double-entry turbine, under full and partial admission conditions;

- *Chapter 5* presents the model that was developed for carrying out cost-efficient transient thermo-structural analyses on a turbine wheel. The results of the analyses, in terms of temperature and stress distributions are also presented;

- *Chapter 6* presents the multi-fidelity optimization strategy for the aerodynamic optimization of a compressor's diffuser and volute.

1. Introduction

The health issues derived from pollutant emissions and the effects of pollutants in the wider biosphere, as well as the high economic and social impact of climate change [1,2], are rising concerns in the society that are translated into increasingly stricter environmental regulations that put strong limits in CO_2, NO_x and particulate emissions. On this matter, the European Union (EU) is leading by example in setting ambitious targets for reducing net emissions by at least 55%, compared to 1990, by 2030, and for being the first climate neutral continent by 2050.

Internal combustion engines (ICEs) play a relevant role in the emission of pollutant and climate-altering species. EU policies report that light-duty vehicles are responsible for 15% of the European Union's emissions of CO_2. Moreover, emissions from heavy-duty vehicles have risen by over 30% between 1990 and 2007, mainly due to increasing road traffic. Nowadays, emissions have been measured to be around 19% above 1990 levels. This certainly is one of the reasons that have led the EU to strike an agreement on legislation to phase out new CO_2-emitting vehicles by 2035. Indeed, the period from 2025-2035 could bring the most fundamental transformation in the 100-plus year history of the automotive sector: battery electric vehicle costs might fall and reach parity with internal combustion engine vehicles, new generations of fuel cell vehicles may be produced, connected and automated vehicle technologies could become more common, including likely deployment of some fully automated vehicles. These new categories of vehicles might for the first time assume a major portion of new vehicle sales, while internal combustion engines with improved design will continue to be an important part of new powertrain mix.

Currently, however, although the usage of electric and hybrid engines is increasing, the internal combustion engine is still the most widespread propulsion system installed on vehicles [3]. The relative scarcity of fossil fuels, however, together with the political and social convulsions of the main producers, are accompanied by the astounding economic rise of some Asian giants such as India or China. As the times of cheap fuel are far in the past and only price surges are expected, the market is pushing towards increasingly efficient vehicles.

1.1 - Turbocharged ICEs

Forced induction by means of turbocharging currently represent a well-established technical solution that allows to increase an ICE's power output with respect to a naturally-aspirated engine of the same displacement. In an ICE, the energy of the exhaust gases is about 30-40% of the chemical energy released by the combustion [4], as depicted in Figure 1.1: P_b is the brake power, $\dot{Q}_{cool}$ is the heat transfer rate to the cooling medium, $\dot{Q}_{misc}$ represents heat rejected to any separate oil coolant, added to the convection and radiation heat transfer rates from the exterior

surfaces of the engine, $\dot{H}_{ic}$ is the exhaust enthalpy lost because of incomplete combustion, and $\dot{m}h_{ex}$ is the exhaust enthalpy flux to the atmosphere.

CI   **SI**

30%   40%

38%   28%

2%   4%   4%   7%   22%

27%

P_b $\dot{Q}_{cool}$ $\dot{Q}_{misc}$ $\dot{H}_{ic}$ $\dot{m}h_{ex}$
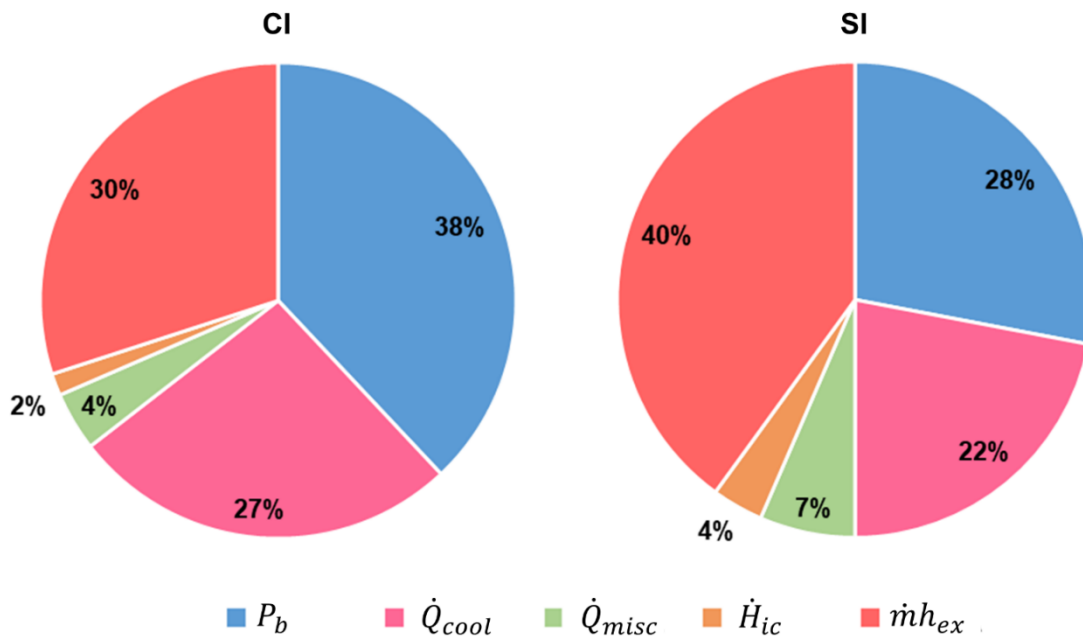
Figure 1.1   Energy balance for automotive engines at maximum power [4].

Turbocharging technologies take advantage of the exhaust gas flow by expanding it in a turbine that drives a compressor upstream of the cylinder's intake: the compressor increases the density of the air admitted to the cylinder. Very high pressure ratio can be achieved by means of turbocharging, especially in Diesel engines where knocking limit is typically not an issue: this grants high volumetric efficiency. Moreover, when forced induction is employed, the high turbulence level of the intake flow enhances fuel mixing and combustion. Consequently, turbocharging allows to obtain a given power output with smaller displacement ICEs, according to the technique known as downsizing. By reducing the cylinders' volume and weight with respect to naturally-aspirated engines delivering the same power, smaller volumes are swept by the piston: friction losses are therefore decreased and, as a consequence, engine efficiency is improved. It has been estimated that a 40% downsizing achieved through turbocharging can lead to about 20% reduction in fuel consumption [5,6]. Regarding automotive engines, it has been proved that turbocharging strategies can increase fuel economy by 30% to 50% [7]. Since Diesel engines allow higher compression ratios than gasoline engines, the implementation of turbochargers had been typically associated with Diesel engines, but small displacement turbocharged gasoline engines are currently very common in the automotive sector.

Turbocharging also reduces emissions of PM since the resulting increase in charge density allows the engine to operate with a leaner mixture. The rate of NO_x formation, however, increases with the temperature inside the combustion chamber: this issue can be addressed via cooling of the charge and by adding exhaust gas recirculation (EGR) to lower both combustion temperatures

and N_2 concentration. Heavy use of EGR is key NO_x reduction technique, though increased EGR flow requires an additional boost from the turbocharger. Therefore, high-pressure turbocharging is essential for improving engine fuel consumption and lowering emissions through downsizing and lean-boost [8]. Additionally, improvements in the combustion process and innovative combustion processes, including dual-fuel strategies, are typically enabled by very high boosting pressures [9].

Besides the target design parameters that make ICEs compliant with the increasingly stricter regulations on CO_2 and pollutant emissions, a peculiar goal of automotive manufacturers is to improve vehicle driveability, by granting sufficient low-end torque and fast turbocharger response. This means that high charging pressures must be available at low engine speeds, when there is relatively little energy in the exhaust flow, while maintaining turbine efficiency at higher speeds. One method to achieve this is with variable geometry turbochargers (VGTs). While conventional turbochargers are limited at low engine speeds by the obligation to provide a flow rate above the surge limit of the compressor, VGTs achieve optimal turbine inlet flow conditions in a wide operating range, thanks to variable geometry turbine nozzles. A different method of achieving fast transient response while maintaining high boost pressures and eliminating compressor surge is by series turbocharging: typically, a smaller, lighter turbocharger is used to provide high pressures at low engine speeds before a larger turbocharger is engaged.

Another technical solution that allows for low-end high charging pressure is strictly related to hybrid powertrain architectures. Indeed, the energy stored in the battery of a HEV (Hybrid Electric Vehicle) can be made available to the turbocharger even at low engine speed: the shaft of a conventional turbocharger can be fitted with an electrical machine that can work as a motor and a generator, depending on the engine's load demand [10]. With this architecture, the compressor has additional support for a faster acceleration, and the turbine can be designed for higher flow capacity [11].

The requirements for turbochargers used in passenger vehicles are very demanding and it is clear that this technology plays a key role in the future development of ICEs. Turbochargers development revolves around two main aspects [12]. Firstly, the improvement of the turbocharger's performance capabilities by means of aerodynamic and mechanical design optimization: this reflects on the development of improved stator vanes and rotor geometries, better VGT actuators and advanced materials and coatings able to withstand increasingly higher turbine inlet temperature. Secondly, one must also strive for the optimal matching between engine and turbocharger, therefore it is paramount to accurately characterize turbocharger performance. To this end, experimental testing sets the benchmark [13,14], but the use of numerical techniques is nowadays fundamental and indispensable both in the R&D field and in the optimization of existing products. The beneficial effects of this type of approach become apparent whenever there is a need to perform predictions and analyses on a large number of cases, given the considerable reduction in time and cost with respect to experimental testing; the use of

experimental tests, while indispensable, can therefore be minimized and dedicated to more advanced stages of development.

1.2 - Turbocharged engines modelling

Engine manufacturers rely on computational methods during engine development. The methods employed in the industry vary in their grade of complexity, with a clear trade-off between potential accuracy and computational cost. The main modelling approaches are hereby presented:

- Current turbocharger simulation codes are mostly based on zero-dimensional models that rely on maps entered as **look-up tables**. The maps, typically of air mass flow and efficiency, are given by the turbocharger's manufacturers. This raises two points. Firstly, the characteristics are known only in the same conditions as manufacturers' tests. Secondly, the isentropic efficiency of the turbine is assessed starting from the measured thermo-mechanical efficiency and evaluating the mechanical efficiency through models developed by turbocharger manufacturers. Also, the turbine efficiency given by turbochargers manufacturers might have been calculated as the product of the isentropic efficiency and the turbocharger mechanical efficiency [15]. This global efficiency is suitable for the calculation of the power transferred to the compressor, but the isentropic efficiency has to be determined. Moreover, during a simulation, it is not uncommon for the operating engine or the turbocharger component to operate beyond the points defined in these maps. This will numerically destabilize the solution and lead to calculation errors [16]. To prevent this, the maps have to be extended to include the range of operations that are beyond those in the data. Furthermore, in case of a variable-geometry turbocharger, the vane position introduces a third dimension into these maps, and their implementation requires three-dimensional interpolations with increased complexity [17]. Look-up tables-based methods have limited accuracy but demand minimum computational resources, and are suitable for preliminary design purposes.

- **Mean value engine models** are models which dynamically describe the time development of an engine's physical variables over time periods which are long compared to an engine cycle but short compared to the dominant time constants of the engine [18]. Such models do not include explicitly a description of the intake, exhaust or combustion processes, but simply represent the overall result of the processes as described by the crank shaft speed, the mean scavenge (or manifold) pressure, the air mass flow or a small number of other measureable engine variables. As such, these simple models predict the time development of the time averaged mean values of the engine states, rather than their instantaneous values.The time scale for mean value engine models is typically on the

order of 3 to 5 revolutions. They are therefore fast enough to give an accurate prediction of overall dynamic engine operation, but cannot react to sub-cycle events, such as variation of cylinder pressure throughout the engine cycle. The relationships used in the models are usually derived from basic physical and thermodynamic principles. In the cases where empirical relationships must be used, fundamental physical and thermodynamic principles are used to establish the correct independent and dependent variables in the empirical relationships [19]. Such approach usually results in simpler and more general relationships throughout the model. Figure 1.2 shows a comparison between data from a mean value engine model and a higher-fidelity 1D model developed in GT-POWER® framework.
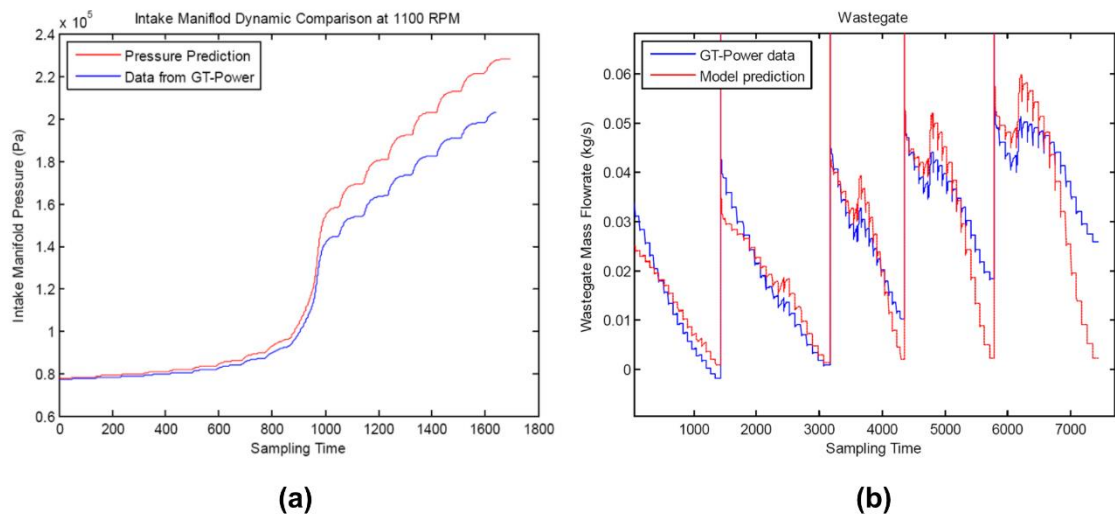
Figure 1.2   Comparison between (red) mean value and (blue) 1D engine model results, in terms of (a) intake manifold pressure and (b) wastegate mass flow [20].

However, when the complexity of the engine increases, heavy use of empirical formulas and steady-state maps must be made, which leads to a great dependence on experimental data for the sake of calculation accuracy [21]. Still, with their low computational cost, mean value engine models represent the basis of control design for advanced internal combustion engines [20].

- **Filling and emptying models** have higher time resolutions with respect to mean value engine models. The simplified approach of quasi-steady filling and emptying concept considers a multi-cylinder engine as a series of control volumes (e.g. airbox, cylinders and exhaust manifolds). These are interconnected via variable geometry orifices (representing valves or ports), in conjunction with the compressor and turbine of the turbocharger as boundary conditions [22]. The problem of determining the time-varying conditions of the gas in each control volume is treated over the whole cycle as that of simultaneous charging and discharging. Such an analysis generates the pressure pulses known to occur in the exhaust manifolds of pulse-turbocharged engines. Filling and emptying models'

computational cost is largely dependent on the number of control volumes that discretize the engine, since energy and mass conservation equations are applied to every volume. Success in predicting the performance of a single-entry, nozzleless turbine can be achieved by filling and emptying models, as shown in Figure 1.3.
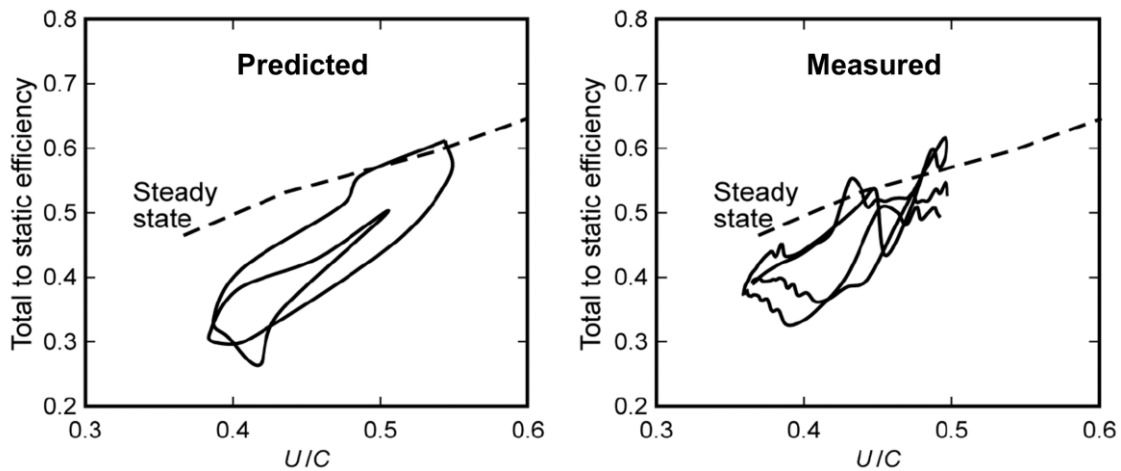
Figure 1.3 Filling and emptying model prediction capability for a single-entry turbine [23].

However, due to the assumption of uniform state of the gas and the zero-dimensional calculation space, it's impossible to model complex acoustic phenomena [24]. Filling and emptying 0D modelling approach has now been surpassed by solutions of the 1D gas dynamic equations, which are able to predict the spatial and time variations in the fluid state and velocity in pipes and manifolds more successfully than 0D methods [25].

- For a turbine working under unsteady conditions, some of the most important unsteady behaviors originate from the wave dynamics within the turbine, which renders zero-dimensional models such as filling-and-emptying models insufficient to predict the turbine performance due to the lack of a spatial dimension [26]. **One-dimensional models** have better time resolution and nonlinear acoustic performance than filling and emptying models, as the momentum conservation equation is also taken into account. Engine manufacturers routinely use one-dimensional gas dynamics software to simulate turbocharged engines. Indeed, good agreement with experimental data even under pulsating flow conditions can be achieved with 1D models, as apparent from Figure 1.4.
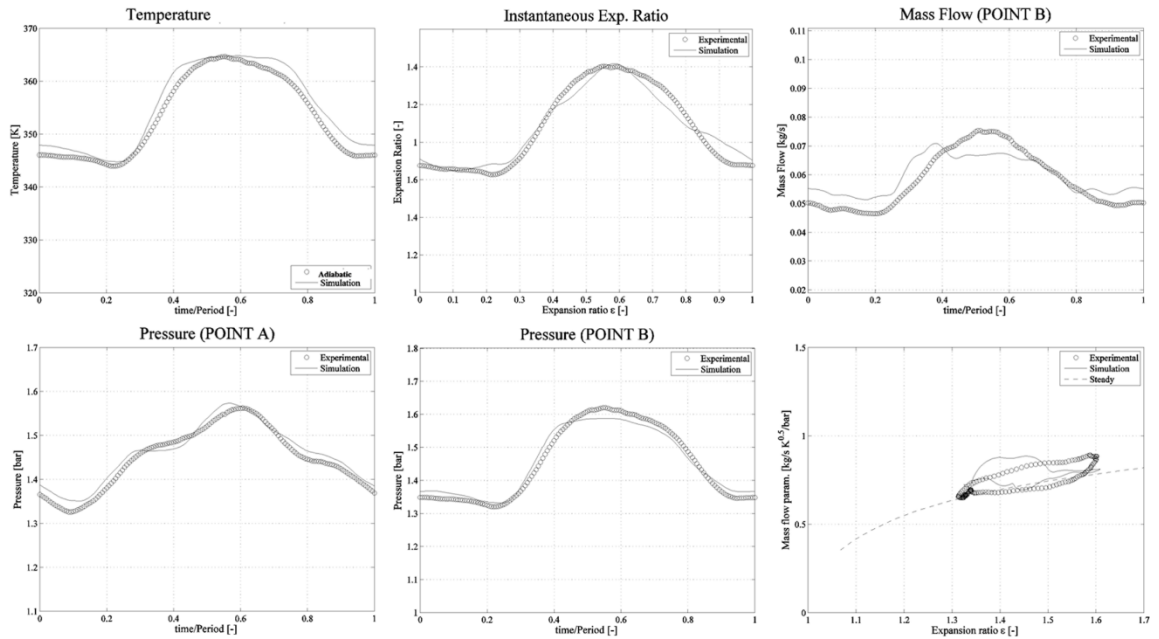
Figure 1.4   Comparison of 1D simulation and experiments for different flow quantities of a nozzleless turbine [27].

Since Wallace and Adgey proposed a fully unsteady model which treated the turbine volute and nozzles as 1D convergent straight pipes and the rotor as a single two-dimensional duct [28], one-dimensional models have reached a high degree of sophistication in many respects [29], including acoustic design of intake and exhaust systems, combustion and emissions analysis [30–32].

- **Three-dimensional simulation techniques** represent the state-of-the-art for high-fidelity modelling of fluid flows, and are often referred to as CFD (Computational Fluid Dynamics) techniques, although 0D/1D/2D modelling should also be considered CFD. 3D CFD codes are based on conservation laws: by considering a given quantity of matter or control volume and its extensive properties, mass, momentum in the 3 spatial dimensions and energy conservation laws can be formulated. The resulting set of equations is usually solved through numerical approach, allowing to obtain the thermodynamic quantities of interest for each control volume. Three-dimensional simulation techniques usually involve high computational costs, but allow for a detailed modelling of fluid flows inside turbochargers. Indeed, aerodynamic losses inside radial turbines can be accurately evaluated [33–35] and small scale phenomena like compressor tip clearance flows [36] can be investigated. Detailed 3D modelling also allows for deep optimization through geometry parametrization [37,38]. The available tools for the numerical modelling of turbochargers are numerous and well established, from CFD solvers for purely aerodynamic aspects to CHT (Conjugate Heat Transfer) and structural solvers for thermo-mechanical analyses. In the case of a turbocharged engine, the strong fluid-dynamic coupling between engine and turbocharger may require the concurrent analysis of both

systems, but the direct 3D modelling of the engine would require an extremely high computational cost due to the inherently transient operation of the machine and the complexity of the combustion process. In this case, it is possible to resort to multi-fidelity or multi-dimensional [39] numerical techniques, employing, for example, a one-dimensional numerical model for the engine and a more accurate (and computationally onerous) 3D model for the turbocharger.

The present work focuses on three-dimensional numerical techniques and their application to both steady and unsteady phenomena, multi-physics analyses and multi-fidelity optimization strategies. For this reason, the next chapter presents the key aspects of 3D CFD techniques, with special focus on the modelling of a moving reference frame.

2 - 3D CFD for turbochargers

Computational Fluid Dynamic codes are based on conservation laws formulation. Conservation laws can be obtained by considering a given quantity of matter or control mass and its extensive properties, such as mass, momentum and energy. This approach is used to study solid bodies' dynamics, where the control mass is easily identified. In fluid flows, however, it is difficult to follow a parcel of matter. It is more convenient to deal with the flow within a certain spatial region called control volume, rather than in a parcel of matter that quickly passes through the region of interest. This analysis method is called control volume approach. The conservation equations are:

- Continuity equation (conservation of mass)
- Momentum equation (conservation of momentum)
- Energy equation (conservation of energy)

In 3D this is a 5 equations system, as momentum equation is a vectorial quantity. To determine the state of the fluid, additional information is required: equation of state is used for this purpose. Under the assumption of thermodynamic equilibrium (acceptable if strong shockwaves do not occur), this equation provides the link between the thermodynamic variables (p, T, e, ρ). This set of equations, when applied to viscous flow is known as Navier-Stokes equations, while when applied to an inviscid flow it is known as Euler equations.

2.1 - Governing equations

A fundamental concept in the formulation of conservation laws is the flux: the variation of the total amount of a quantity inside a given domain is equal to the balance between the amount of that quantity entering and leaving the considered domain, plus the contribution from any sources generating that quantity. A conservation equation for a generic scalar quantity ϕ:

$$\frac{\partial}{\partial t} \int_\Omega \phi d\Omega = - \oint_S \vec{F} \cdot d\vec{S} + \int_\Omega Q_v d\Omega + \oint_S \overrightarrow{Q_s} \cdot d\vec{S} \qquad (2.1)$$

Where:

- Ω is the control volume domain;
- S is the surface defining the volume domain;
- $\vec{F}$ is the flux;
- Q_v and Q_s are volume and surface source terms, respectively.

Conservation equation written like Eq. (2.1) is the integral form for a generic scalar quantity. Applying Gauss' theorem to surface integrals, it is possible to write the conservation equation in differential form:

$$\oint_S \vec{F} \cdot d\vec{S} = \int_\Omega \vec{\nabla} \cdot \vec{F} d\Omega \tag{2.2a}$$

$$\frac{\partial}{\partial t} \int_\Omega \phi d\Omega + \int_\Omega \vec{\nabla} \cdot \vec{F} d\Omega = \int_\Omega Q_v \cdot d\Omega + \int_\Omega \vec{\nabla} \cdot \overrightarrow{Q_s} d\Omega \tag{2.2b}$$

$$\frac{\partial \phi}{\partial t} + \vec{\nabla} \cdot \vec{F} = Q_v + \vec{\nabla} \cdot \overrightarrow{Q_s} \tag{2.2c}$$

Since Eq. (2.2b) is valid for an arbitrary volume it must be valid for any point of the flow and it is possible to write them in a differential form like Eq. (2.2c). From Eq. (2.2c) it is possible to see that fluxes appear only under divergence operator, and they could be generated from two contributions:

- **Convective** contribution: it represents the amount of ϕ that is carried out away or transported by the fluid flow, $\overrightarrow{F_C} = \phi \vec{u}$. The convective flux is proportional to the flow velocity and has directional properties. It appears as a first order partial derivative term and represents a non-linear term as the velocity field depends on the transported variables.

- **Diffusive** contribution: It represents the amount of ϕ that is carried away or transported by the presence of its gradient, $\overrightarrow{F_D} = -k\rho\vec{\nabla}\phi$. The diffusive flux appears as a second order partial derivative term, i.e. under the Laplace operator.

The differential conservation equation written considering the two types of fluxes then becomes:

$$\frac{\partial \phi}{\partial t} + \vec{\nabla} \cdot \phi \vec{u} = \vec{\nabla} \cdot \left(k\rho\vec{\nabla}\phi\right) + Q_v + \vec{\nabla} \cdot \overrightarrow{Q_s} \tag{2.3}$$

If the conserved property is a vector, the flux becomes a tensor as well as the surface source term (stress tensor), whereas the volume source terms become a vector. The conservation equation for a vector property is represent by Eq. (2.4a).

$$\frac{\partial}{\partial t} \int_\Omega \vec{\phi} d\Omega = -\oint_S \bar{\bar{F}} \cdot d\vec{S} + \int_\Omega \overrightarrow{Q_v} \cdot d\Omega + \oint_S \overline{\overline{Q_s}} \cdot d\vec{S} \tag{2.4a}$$

$$\frac{\partial}{\partial t} \int_\Omega \vec{\phi} d\Omega + \int_\Omega \vec{\nabla} \cdot \bar{\bar{F}} d\Omega = \int_\Omega \overrightarrow{Q_v} \cdot d\Omega + \int_\Omega \vec{\nabla} \cdot \overline{\overline{Q_s}} d\Omega \tag{2.4b}$$

As for scalar quantity, since the integral formulation is valid for any arbitrary control volume, the differential form is derived:

$$\frac{\partial}{\partial t}\vec{\phi} + \vec{\nabla} \cdot (\bar{\bar{F}} - \overline{\overline{Q_S}}) = \overrightarrow{Q_V} \tag{2.5}$$

From these general formulations, the conservation equations of fluid dynamics can be derived [40].

Continuity equation: this conservation equation is referred to a scalar property $\phi = \rho$.

$$\frac{\partial}{\partial t}\int_\Omega \rho d\Omega + \oint_S \rho\vec{u} \cdot d\vec{S} = 0 \tag{2.6a}$$

$$\frac{\partial \rho}{\partial t} + \vec{\nabla} \cdot (\rho\vec{u}) = 0 \tag{2.6b}$$

Eq. (2.6b) is the differential form of continuity equation. Diffusion term is not included in continuity equation because mass does not diffuse.

Momentum equation: this conservation equation is referred to a vectorial property $\phi = \rho\vec{u}$. In the momentum equation the source terms account for internal force (stress) and external volume forces (gravity, applied forces). Internal forces are the expression of fluid's deformability and since it depends on the position and orientation of the surface it acts on, it must be represented by a tensor. Assuming Newtonian fluid, the stress tensor is:

$$\bar{\bar{\sigma}} = -p\bar{\bar{\delta}} + \bar{\bar{\tau}} \tag{2.7}$$

Where $-p\bar{\bar{\delta}}$ is the isotropic pressure component and $\bar{\bar{\tau}}$ is the viscous shear stress, representing the internal friction force of fluid layers against each other. Newton's constitutive law suggests the following model for the shear stress:

$$\overline{\overline{\tau_{ij}}} = \mu\left[\left(\frac{\partial u_j}{\partial x_i} + \frac{\partial u_i}{\partial x_j}\right) - \frac{2}{3}(\vec{\nabla} \cdot \vec{u})\delta_{ij}\right] \tag{2.8}$$

Inside the control volume the internal forces cancel out, whereas they do not have any counterpart on the volume surface. The integral form of the momentum conservation equation will be:

$$\frac{\partial}{\partial t}\int_\Omega \rho\vec{u}d\Omega + \oint_S (\rho\vec{u}\vec{u}) \cdot d\vec{S} = \int_\Omega \rho\overrightarrow{f_e}d\Omega + \oint_S \bar{\bar{\sigma}} \cdot d\vec{S} \tag{2.9}$$

Applying Gauss' theorem:

$$\frac{\partial}{\partial t}\int_\Omega \rho\vec{u}d\Omega + \int_\Omega \vec{\nabla}(\rho\vec{u}\vec{u})d\Omega = \int_\Omega \rho\overrightarrow{f_e}d\Omega + \int_\Omega \overrightarrow{\nabla \cdot}\bar{\bar{\sigma}}d\Omega \tag{2.10}$$

Finally, as for the continuity equation, the differential form is derived:

$$\frac{\partial(\rho\vec{u})}{\partial t} + \vec{\nabla}\cdot\left(\rho\vec{u}\vec{u} + p\bar{\bar{\delta}} - \bar{\bar{\tau}}\right) = \rho\vec{f_e} \tag{2.11}$$

Note that momentum diffuses into the fluid via viscous shear stresses, in Eq. (2.11) the Laplace operator is not explicitly written but it is expressed in the shear stress definition (Eq. (2.8)).

Energy equation: the conserved quantity is the total energy E, defined as the sum of fluid internal energy plus its kinetic energy per unit mass $\phi = \rho E$, where $E = e + \frac{1}{2}u^2$. According to previous considerations on the terms constituting a conservation equation, each term is described:

- For the energy equation two types of fluxes are considered, convective and diffusive (thermal conductivity of the fluid) fluxes:

  - Convective term $\vec{F_C}$ is $\vec{F_C} = \rho E\vec{u}$.
  - Diffusive term $\vec{F_D}$ is $\vec{F_D} = -\lambda\vec{\nabla}T$, where λ is the thermal conductivity of the fluid.

- Volume source terms are represented by the work of the volume forces f_e and heat sources:

$$Q_V = \rho\vec{f_e}\cdot\vec{u} + q_H \tag{2.12}$$

- Surface sources $\vec{Q_S}$ result from the work done on the fluid by pressure and internal shear stress acting on control volume surface:

$$\vec{Q_S} = \bar{\bar{\sigma}}\cdot\vec{u} = -p\vec{u} + \bar{\bar{\tau}}\cdot\vec{u} \tag{2.13}$$

Considering all these terms, the energy equation can be written in its integral form:

$$\frac{\partial}{\partial t}\int_\Omega \rho E d\Omega + \oint_S (\rho E\vec{u})\cdot d\vec{S} = \oint_S \lambda\vec{\nabla}T\cdot d\vec{S} + \int_\Omega (\rho\vec{f_e}\cdot\vec{u} + q_H)d\Omega + \oint_S (\bar{\bar{\sigma}}\cdot\vec{u})\cdot d\vec{S} \tag{2.14}$$

In differential form the energy equation will be:

$$\frac{\partial(\rho E)}{\partial t} + \vec{\nabla}\cdot(\rho E\vec{u}) = \vec{\nabla}\cdot\left(\lambda\vec{\nabla}T\right) + \vec{\nabla}\cdot(\bar{\bar{\sigma}}\cdot\vec{u}) + \rho\vec{f_e}\cdot\vec{u} + q_H \tag{2.15}$$

Then, if the stress tensor is written in its isotropic and viscous shear stress form, and introducing enthalpy, the energy conservation equation becomes:

$$\frac{\partial(\rho H)}{\partial t} + \vec{\nabla}\cdot\left(\rho H\vec{u} - \lambda\vec{\nabla}T - \bar{\bar{\tau}}\right) = \frac{\partial p}{\partial t} + \rho\vec{f_e}\cdot\vec{u} + q_H \tag{2.16}$$

These three conservation equations are sufficient to study a non-reacting case. Nonetheless, in order to take into account the turbulent motion of the nonreacting flow, turbulence must be modelled.

2.2 - Turbulence: an overview

There are many opportunities to observe turbulent flows in everyday surroundings, whether it could be smoke from a chimney, water in a river or waterfall, or a strong wind buffeting. Observing a waterfall, it is possible to understand that the flow is unsteady, irregular, seemingly random and chaotic, and surely the motion of every eddy or droplet is unpredictable [41]. Turbulence modelling is one of the three key elements in CFD, and due to its unpredictability, a considerable modelling effort is required. Turbulence is characterized by [42]:

1. **Fluctuations**: turbulent flows contain fluctuations in the dependent-field quantities (velocity, pressure, temperature, etc.) even when the flow's boundary conditions are steady. Turbulent fluctuations appear to be irregular, chaotic, and unpredictable.

2. **Nonlinearity**: turbulence is found to occur when the relevant nonlinearity parameter, i.e. the Reynolds number Re, exceeds a critical value. The turbulence nonlinearity is evident since it is the final state of a nonlinear transition process. Once the critical parametric value is exceeded, small perturbations can grow spontaneously and may equilibrate as finite amplitude disturbances. However, the new equilibrium state can become unstable to more complicated disturbances, and so on, until the flow eventually reaches a non-repeating unpredictable state (turbulence).

3. **Vorticity**: turbulence is characterised by fluctuating vorticity. A cross-section view of a turbulent flow typically appears as a diverse collection of streaks, strain regions, and swirls of various sizes that deform, coalesce, divide, and spin. Turbulence always involves a range of eddy sizes and the size range increases as Reynolds number increases.

4. **Dissipation**: on average, the vortex stretching mechanism transfers fluctuation energy and vorticity to smaller and smaller scales via nonlinear interactions, until velocity gradients become so large that the energy is converted into heat (i.e., dissipated) by the action of viscosity and the motion of the smallest eddies. Persistent turbulence, therefore, requires a continuous supply of energy to make up for this energy loss.

5. **Diffusivity**: due to the prevalence of agitation and overturning motions (macroscopic mixing), turbulent flows are characterized by a rapid rate of mixing and diffusion of species, momentum, and heat compared to equivalent laminar flows that lack fluctuations.

Many techniques have been used with the aim to investigate and try to solve the turbulence problem, which is still one of the most challenging phenomena of applied science. In the past the experimental approach was the only method to understand this problem and empirical correlations were exploited for analytical studies. More recently, with the rapid growth of computer power several numerical models have been developed in order to aid experimental results.

2.2.1 - The physics of turbulence

Turbulence is the natural state of a fluid flow and occurs when the Reynolds number $Re = \frac{\rho L}{\nu}$ exceeds a critical value which depends on the studied problem. In this case inertia of the flow (convection contribution) is higher than viscous forces (diffusion contribution) and the flow becomes irregular and chaotic. The main consequence of such behavior is that transport phenomena, such as diffusion of species, heat and momentum arise a strong increment. In such conditions measurements of flow velocity reveal the appearance of stochastic velocity fluctuations $u_i'(t)$. Statistical analysis of these results shows that, below a certain distance, called integral length scale l_0, velocity fluctuations in two points are correlated. In fact, from a microscopic point of view, turbulent flows are characterized by small coherent vortices, called eddies, which generate in random positions and are responsible for $u_i'(t)$. These turbulent structures are superimposed in space, the larger ones containing the smaller ones. As shown in Figure 2.1, the characteristic size of the smallest vortices strongly depends on Reynolds number and, since eddies evolve in all directions, the phenomenon is intrinsically three-dimensional.
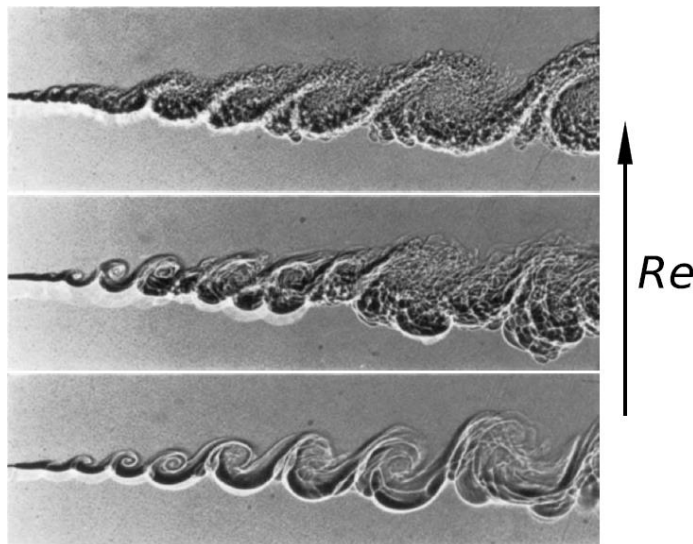
Figure 2.1   Effects of Reynolds number on turbulent structures in a mixing layer.

As stated in [41], the random nature of turbulent flows is consistent with the deterministic nature of the governing equations, due to unavoidable perturbations in material properties, initial conditions and boundary conditions and flow sensitivity to such perturbations.

Turbulence can be represented with the so-called Reynolds decomposition:

$$u_i(x,t) = \bar{u}_i(x) + u_i'(x,t) \tag{2.17}$$

where $\bar{u}_i$ is the mean value, while the fluctuating component can be seen as a statistical population with a related statistical distribution. Hence, both physical and statistical considerations are required to study and predict these kinds of flow. For example, from measurements of $u_i(t)$, its standard deviation $u_{i,rms}$, called turbulence strength, can be computed. This quantity is related to some important characteristic turbulent quantities, such as turbulence intensity I:

$$I = \frac{u_{rms}}{\bar{u}} = \frac{\sqrt{u_{x,rms}^2 + u_{y,rms}^2 + u_{z,rms}^2}}{\sqrt{\bar{u}_x + \bar{u}_y + \bar{u}_z}} \tag{2.18}$$

and turbulent kinetic energy (TKE) k, expressed as:

$$k = \frac{1}{2}\left(u_{x,rms}^2 + u_{y,rms}^2 + u_{z,rms}^2\right) = \frac{3}{2}u_{rms}^2 = \frac{3}{2}(I\bar{u})^2 \tag{2.19}$$

which reflects the level of unsteadiness.

In a turbulent flow, eddies can be found in a wide range of spatial, temporal and velocity scales. Each one has a specific role in the so-called Energy Cascade process, which explains how the flow dissipates the turbulent kinetic energy: biggest anisotropic scales (*energy containing range*), that have a characteristic length similar to the domain dimension, introduce this energy in the cascade process whereas the smallest isotropic ones work to dissipate it (*dissipation range*). Between these scales there is the *inertial sub-range* that transports k towards smaller scales. This transfer process occurs because eddies break down and become ever smaller and more isotropic. In some cases, backscattering phenomena can also occur, where the energy flux between the scales is inverse with respect to the cascade process. The energy distribution between eddies of different scales is represented by the energy spectrum $E(\kappa)$ (Figure 2.2), so that:

$$E(\kappa)d\kappa = dk \tag{2.20}$$

Where $\kappa = \frac{2\pi}{l}$ is the wave number related to eddies of size l.
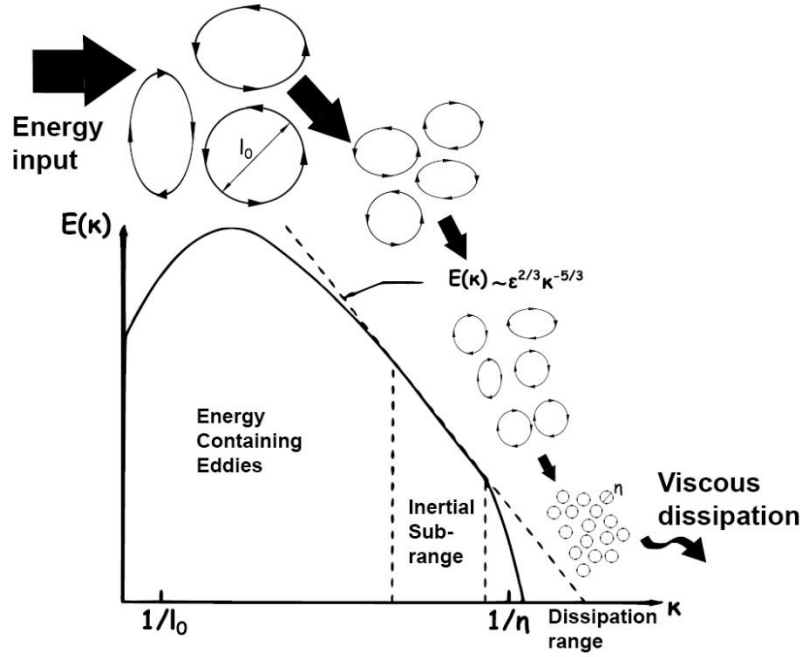
Figure 2.2   Energy distribution between eddies of different scales.

From the shape of $E(\kappa)$ in the inertial subrange shown in Figure 2.2, a more general expression of the energy spectrum may be determined as:

$$E(\kappa) = C\varepsilon^{\frac{2}{3}}\kappa^{-\frac{5}{3}}f_L f_\eta \qquad (2.21)$$

where f_L and f_η are empirical functions that must be introduced to model respectively the energy containing range and the dissipation range. As already reported, the largest eddies have scales, called integral scales (l_0, u_0, τ_0). The dimension of these scales has the same order of the characteristic scales of the flow $(l_0 = o(L),\ u_0 = o(u_{rms}) = o(\bar{u}))$, therefore they are influenced by boundary conditions. As a result, these turbulent structures do not show universal features and represent the main source of energy and anisotropy of the flow. On the other hand, the smallest scales, called Kolmogorov scales, are responsible for the dissipation process and present viscous forces comparable to the inertial ones $(Re_\eta = \frac{u_\eta \eta}{\upsilon} \approx 1)$. Since in equilibrium condition the energy transfer equals the energy dissipation, this last term depends only on the integral scales. Through dimensional analysis it is possible to define a parameter called turbulent dissipation rate ε:

$$\varepsilon \approx \frac{u_0^3}{l_0} \approx \frac{u_0^2}{\tau_0} \qquad (2.22)$$

It is worth noting that this quantity is independent from cinematic viscosity υ and that the equilibrium hypothesis is especially valid for the small eddies, which promptly adapt themselves

on large scales dynamics. Combining Eq. (2.22) with $k \approx u_0^2$, the integral turbulent length scale can be rewritten as:

$$l_0 \propto \frac{k^{1.5}}{\varepsilon} \tag{2.23}$$

The remaining scales may be calculated for high Re flows using the well-known three Kolmogorov hypothesis [41]:

1. In turbulent flows exist a length scale $l_{E1} \ll l_0$ below which the turbulent scales are statistically isotropic. These are the Kolmogorov scales.

2. These isotropic scales and their statistics have a universal shape only determined by ν and ε. Thus, by means of dimensional analysis, those quantities can be estimated as:

$$\eta = \left(\frac{\nu^3}{\varepsilon}\right)^{0.25} , \quad u_\eta = (\varepsilon\nu)^{0.25} , \quad \tau_\eta = \left(\frac{\nu}{\varepsilon}\right)^{0.5} \tag{2.24}$$

3. Statistics quantities of intermediate scales l, so that $\eta \ll l \ll l_0$, have a universal shape which depends only on ε. In this range, for a given length scale l, velocity and time scales are estimated as:

$$u(l) \approx (\varepsilon l)^{\frac{1}{3}} \approx u_0 \left(\frac{l}{l_0}\right)^{\frac{1}{3}} , \quad \tau(l) \approx \left(\frac{l^2}{\varepsilon}\right)^{\frac{1}{3}} \approx \tau_0 \left(\frac{l}{l_0}\right)^{\frac{2}{3}} \tag{2.25}$$

It is clear that, in this range, smaller eddies also have a smaller characteristic velocity ($\approx u(l)$) and "lifetime" ($\approx \tau(l)$).

2.3 - Turbulence modelling

During the last decades, computational fluid dynamics has become an important numerical tool for engineers and researchers. In the context of computational fluid dynamics, Navier-Stokes Equations (NSE) are a suitable model for flow simulations and intrinsically include all possible turbulent phenomena. However, the strong non-linearity of these equations leads to interactions between different scales. Therefore, in their original formulation, NSE have an analytical solution only for laminar flows, while, from a numerical point of view, DNS (Direct Numerical Simulation) techniques should be adopted, but only using a computational grid fine enough to resolve all flow scales. In this context, the resolution of the smallest scales is responsible for the high computational cost, which can be related to flow Reynolds number as $o(Re^{11/4})$. Otherwise, NSE must be integrated through proper models in order to take account of the turbulence effects on the flow field. As stated in [43], an ideal model should introduce the minimum amount of

complexity while capturing the essence of relevant physics, rather than solving all the eddies dynamics. Three different level of approximation for the turbulence are available:

- Direct Numerical Simulation (**DNS**): simulates the whole range of the turbulent statistical fluctuations at all relevant physical scales. The size of the smallest turbulent eddies is inversely proportional to $Re^{3/4}$. This technique requires a notable computational effort, assuming a resolution of n points per direction per unit length, the number of operations to be computed is proportional to $n^3 \cdot Re^{9/4}$. To solve even the smallest turbulent velocity fluctuations, the spatial grid needs to be extremely fine and time steps small enough to resolve the fastest fluctuations.

- Large Eddy Simulation (**LES**): it is similar to DNS approach because it computes directly the turbulent fluctuations in space and time but above a certain length scale. Below that scale, turbulence is modelled by semiempirical laws.

- Reynolds-averaged Navier-Stokes (**RANS**) equations: this method involves time averaging of Navier-Stokes equations. From the averaging procedure some extra terms appear, which are the mean of the product between the fluctuations component. This approach will be explained in detail in the following paragraphs.

2.3.1 - RANS approach

In RANS approach, a time average operation is applied to NSE. Therefore, a generic quantity $\phi(x,t)$ is decomposed to a mean value $\bar{\phi}(x)$ and a fluctuating component $\phi'(x,t)$, so that $\phi = \bar{\phi} + \phi'$. By performing this mathematical operation, a new tensor $\tau'_{ij} = \rho\overline{u'_i u'_j}$, called Reynolds Stress Tensor, appears in the non-linear convective term of the momentum equations. This tensor represents the turbulence fluctuations effects on the mean flow, and similarly affects the energy equation. This tensor must be modelled with the so-called turbulence closure problem, normally based on simplified considerations, such as Boussinesq hypothesis, where model constants are tuned on experimental results. Several RANS models are available in literature and can be summarized in the following four main classes [43]:

- Algebraic models (*Van Driest, Cebeci and Smith, Baldwin and Lomax*).
- One-equation models (*Baldwin and Barth, Goldberg, Spalart-Allmaras*).
- Two-equation models (k-ε, k-ω and their variants).
- Second-order Closure models (*Reynolds stress models*)

Based on Boussinesque hypothesis, the objective of the first three classes is computing an artificial viscosity μ_t, called turbulent viscosity, that should be added to molecular viscosity in the diffusion term of the NSE, in order to model Reynolds stress tensor effects. Algebraic models are unused nowadays. One-equation models solve a transport equation for a scalar quantity, such as k or μ_t. However, these last models are not accurate enough for CFD applications, because an algebraic expression should be used to evaluate the so-called mixing length, which is a characteristic length of the turbulence.

In RANS techniques two-equation models are the state of art, being a good tradeoff between computational efforts and accuracy. Dissipation of turbulence is introduced to properly simulate energy cascade process. Turbulent viscosity can be calculated as function of two scalars, that are k and either ε or the specific turbulence dissipation rate $\omega = \frac{\varepsilon}{k}$. Then, in order to evaluate these scalars, two transport equations are solved.

On the other hand, Reynolds stress models (RSM) solve a transport equation for each component of the Reynolds stress tensor, bearing in mind its symmetry property. As a result, anisotropy of turbulence can be naturally modelled even though longer simulation time is expected.

Among all turbulence models, RANS are the less time consuming, because mesh requirements are not related to turbulence scales. This is the main reason why RANS models are widely used in industrial applications.

2.3.2 - The *k-ω SST model*

The k-ω SST (Shear Stress Transport) model is a modified version of Wilcox's k-ω model, developed by Menter [44]. Both k-ε and k-ω are two-equation models where turbulent viscosity μ_t is estimated by means of closure equations, starting from the turbulence kinetic energy k and a parameter that represents its rate of dissipation. In the k-ε model, the turbulence kinetic energy dissipation term causes a singularity in the near-wall region of the flow: for this reason, this model is not suggested for phenomena that are directly related to boundary layer modelling. On the other hand, the k-ω model (Wilcox, 1988) avoids near-wall singularity by employing the specific turbulent kinetic energy dissipation rate ω: boundary layer can then be solved even under adverse pressure gradients and layer separation phenomena. The modelling of the freestream region is however, less accurate with respect to the k-ε model. The k-ω SST model aims to take advantage of both k-ε and k-ω models by introducing a so-called "blending function" F_1, which allows to switch between the two models depending on the wall distance. Being a RANS model, the momentum equation includes the Reynolds stress tensor. This second order tensor, according to Boussinesq, is proportional to mean deformation rates:

$$\overline{\overline{\tau'}} = \rho \overrightarrow{u'} \otimes \overrightarrow{u'} \tag{2.26}$$

Where $\vec{u'}$ is the velocity fluctuation. Writing Eq. (2.26) for the *i-j* component of the fluctuation:

$$\tau'_{ij} = \rho\overline{u'_i u'_j} = \mu_t \left(\frac{\partial u_i}{\partial x_j} + \frac{\partial u_j}{\partial x_i}\right) - 2\rho k \delta_{ij} \tag{2.27}$$

Where μ_t is the turbulent viscosity. The purpose of the turbulence model is to estimate the value of μ_t, and closure equations are required. The k-ω SST model uses the following as a closure equation:

$$\mu_t = \rho \frac{k}{\omega} \tag{2.28}$$

Transport equations for k and ω are:

$$\frac{\partial(\rho k)}{\partial t} + \frac{\partial}{\partial x_j}\left(\rho U_j k\right) = \frac{\partial}{\partial x_j}\left[\left(\mu + \frac{\mu_t}{\sigma_{k3}}\right)\frac{\partial k}{\partial x_j}\right] + P - C_\mu \rho k\omega + P_{kb} \tag{2.29}$$

$$\frac{\partial(\rho\omega)}{\partial t} + \frac{\partial}{\partial x_j}\left(\rho U_j k\right) = \frac{\partial}{\partial x_j}\left[\left(\mu + \frac{\mu_t}{\sigma_{\omega3}}\right)\frac{\partial\omega}{\partial x_j}\right] + \alpha_3\frac{\omega}{k}P + 2(1-F_1)\frac{1}{\omega\sigma_{\omega2}}\frac{\partial k}{\partial x_j}\frac{\partial\omega}{\partial x_j} - \beta_3\rho\omega^2 + P_{\omega b} \tag{2.30}$$

Equations (2.29) and (2.30) contain several adjustable constant parameters. Table 2.1 shows the typical values of the model constant parameters, valid for a wide range of turbulent flows:

Parameter	Value
C_μ	0.09
α_1	0.555
α_2	0.44
β_1	0.075
β_2	0.0828
σ_{k1}	2
σ_{k2}	1
$\sigma_{\omega1}$	2
$\sigma_{\omega2}$	1.168

Table 2.1 Typical k-ω SST model constant parameters.

2.4 - Moving reference frame modelling

The above-described equations for fluid flow modelling are intended for a stationary (or inertial) reference frame. However, there are many problems where it is advantageous to solve the equations in a moving (or non-inertial) reference frame. These problems typically involve moving parts, such as rotating blades, impellers, and moving walls, and it is the flow around the moving parts that is of interest. That is certainly the case for turbocharger applications, being the compressor and turbine stages composed of both rotating and stationary components (Figure 2.3).
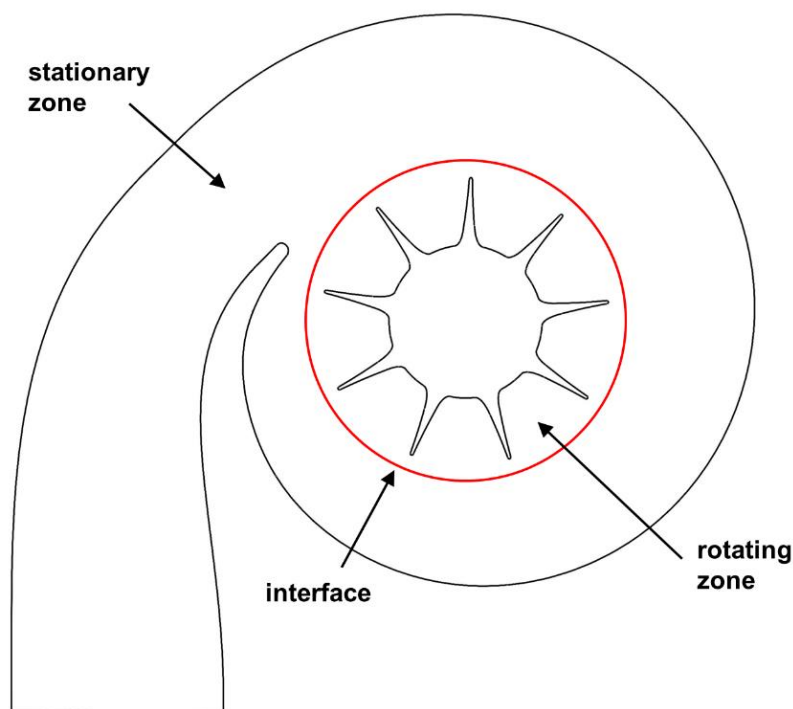
Figure 2.3   Multiple reference frames of a turbine stage.

In most cases, the moving parts render the problem unsteady when viewed from a stationary frame. With a moving reference frame, however, the flow around the moving part can (with certain restrictions) be modeled as a steady-state problem with respect to the moving frame. Indeed, for a steadily moving frame (e.g. a frame with constant rotational speed), it is possible to transform the equations of fluid motion to the moving frame such that steady-state solutions are possible: the equations of motion are modified by the solver to incorporate the additional acceleration terms that occur due to the transformation from the stationary to the moving reference frame.

Figure 2.4 illustrates a coordinate system that is translating with a linear velocity $\vec{v}_t$ and rotating with angular velocity $\vec{\omega}$ relative to a stationary (inertial) reference frame. The origin of the moving system is located by a position vector $\vec{r}_0$.
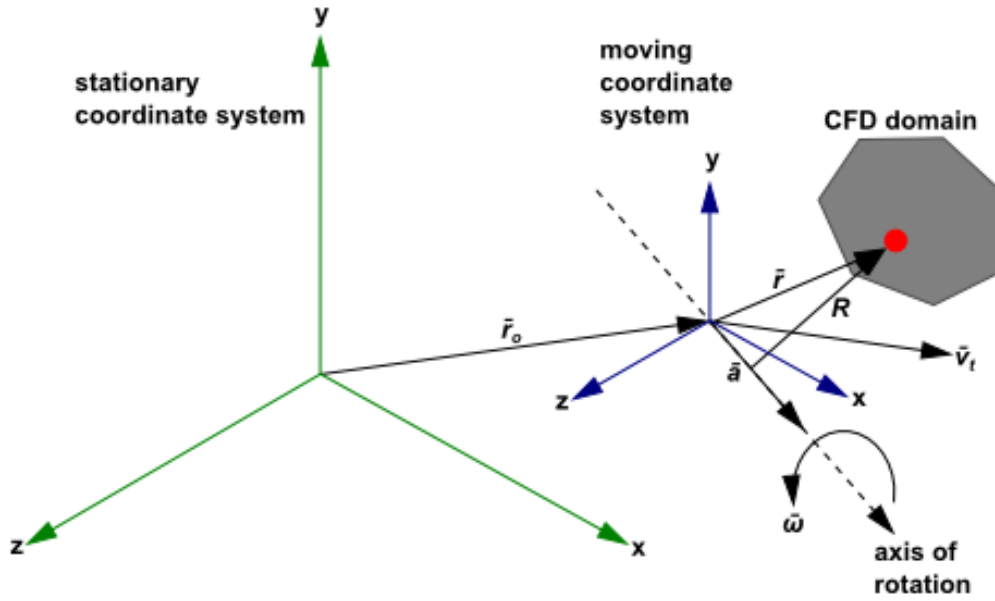
Figure 2.4   Stationary and moving reference frames.

The axis of rotation is defined by a unit direction vector $\hat{a}$ such that

$$\vec{\omega} = \omega \hat{a} \tag{2.40}$$

The computational domain for the CFD problem is defined with respect to the moving frame such that an arbitrary point in the CFD domain is located by a position vector $\vec{r}$ from the origin of the moving frame. The fluid velocities can be transformed from the stationary frame to the moving frame using the following relation:

$$\vec{v}_r = \vec{v} - \vec{u}_r \tag{2.41}$$

where

$$\vec{u}_r = \vec{v}_t + \vec{\omega} \times \vec{r} \tag{2.42}$$

In the above equations, $\vec{v}_r$ is the relative velocity (the velocity viewed from the moving frame), $\vec{v}$ is the absolute velocity (the velocity viewed from the stationary frame), $\vec{u}_r$ is the velocity of the moving frame relative to the inertial reference frame, $\vec{v}_t$ is the translational frame velocity, and $\vec{\omega}$ is the angular velocity. When the equations of motion are solved in the moving reference frame, the acceleration of the fluid is augmented by additional terms that appear in the momentum equations. Moreover, the equations can be formulated in two different ways:

- Expressing the momentum equations using the relative velocities as dependent variables (known as the relative velocity formulation).
- Expressing the momentum equations using the absolute velocities as dependent variables in the momentum equations (known as the absolute velocity formulation).

For the relative velocity formulation, the governing equations of fluid flow in a moving reference frame can be written as follows.

Conservation of mass:

$$\frac{\partial \rho}{\partial t} + \nabla \cdot \rho \vec{v}_r = 0 \tag{2.43}$$

Conservation of momentum:

$$\frac{\partial}{\partial t}(\rho \vec{v}_r) + \nabla \cdot (\rho \vec{v}_r \vec{v}_r) + \rho(2\vec{\omega} \times \vec{v}_r + \vec{\omega} \times \vec{\omega} \times \vec{r} + \vec{\alpha} \times \vec{r} + \vec{a}) = -\nabla p + \nabla \cdot \bar{\bar{\tau}}_r + \vec{F} \tag{2.43}$$

where $\vec{\alpha} = \frac{d\vec{\omega}}{dt}$ and $\vec{a} = \frac{d\vec{v}_t}{dt}$

Conservation of energy:

$$\frac{\partial}{\partial t}(\rho E_r) + \nabla \cdot (\rho \vec{v}_r H_r) = \nabla \cdot (k\nabla T + \bar{\bar{\tau}}_r \cdot \vec{v}_r) + S_h \tag{2.44}$$

The momentum equation contains four additional acceleration terms. The first two terms are the Coriolis acceleration ($2\vec{\omega} \times \vec{v}_r$) and the centripetal acceleration ($\vec{\omega} \times \vec{\omega} \times \vec{r}$), respectively. These terms appear for both steadily moving reference frames and accelerating reference frames. The third and fourth terms are due to the unsteady change of the rotational speed and linear velocity, respectively. These terms are null for constant translation and/or rotational speeds. The energy equation is written in terms of the relative internal energy (E_r) and the relative total enthalpy (H_r), also known as the rothalpy. These variables are defined as:

$$E_r = h - \frac{p}{\rho} + \frac{1}{2}(v_r^2 - u_r^2) \tag{2.45}$$

$$H_r = E_r + \frac{p}{\rho} \tag{2.46}$$

For the absolute velocity formulation, the governing equations of fluid flow for a steadily moving frame can be written as follows.

Conservation of mass:

$$\frac{\partial \rho}{\partial t} + \nabla \cdot \rho \vec{v}_r = 0 \tag{2.47}$$

Conservation of momentum:

$$\frac{\partial}{\partial t}(\rho \vec{v}) + \nabla \cdot (\rho \vec{v}_r \vec{v}) + \rho[\vec{\omega} \times (\vec{v} - \vec{v}_t)] = -\nabla p + \nabla \cdot \bar{\bar{\tau}} + \vec{F} \tag{2.48}$$

Conservation of energy:

$$\frac{\partial}{\partial t}(\rho E) + \nabla \cdot (\rho \vec{v}_r H + \rho \vec{u}_r) = \nabla \cdot (k\nabla T + \bar{\bar{\tau}} \cdot \vec{v}) + S_h \tag{2.49}$$

In this formulation, the Coriolis and centripetal accelerations can be simplified into a single term ($[\vec{\omega} \times (\vec{v} - \vec{v}_t)]$). Notice that the momentum equation for the absolute velocity formulation contains no explicit terms involving $\vec{\alpha}$ or $\vec{a}$.

For the modelling of moving reference frames, three approaches are typically employed:

- The Frozen Rotor, or MRF model;
- The Mixing Plane model;
- The sliding mesh approach.

Both the Frozen Rotor and Mixing Plane approaches are steady-state approximations, and differ primarily in the manner in which conditions at the interfaces are treated. These approaches will be discussed in the following sections. The sliding mesh model approach is, on the other hand, inherently unsteady due to the motion of the mesh with time.

2.4.1 - Frozen Rotor model

The Frozen Rotor, or MRF (Multiple Reference Frame), model is, perhaps, the simplest of the approaches for multiple zones. It is a steady-state approximation in which individual domain zones can be assigned different rotational speeds. The flow in each moving zone is solved using the moving reference frame equations. If the zone is stationary ($\omega = 0$), the equations reduce to their stationary forms. At the interfaces between cell zones, a local reference frame transformation is performed to enable flow variables in one zone to be used to calculate fluxes at the boundary of the adjacent zone. It should be noted that the Frozen Rotor approach does not account for the relative motion of a moving zone with respect to adjacent zones (which may be moving or stationary); indeed, the mesh remains fixed for the computation. This is analogous to freezing the motion of the moving part in a specific position and observing the instantaneous flow field with the rotor in that position, hence, the name "frozen rotor".

While this approach clearly represents an approximation, it can provide a reasonable model of the flow for many applications. For example, the model can be used for turbomachinery applications in which rotor-stator interaction is relatively weak, and the flow is relatively uncomplicated at the interface between the moving and stationary zones. Another potential use of the MRF model is to compute a flow field that can be used as an initial condition for a transient sliding mesh calculation. This eliminates the need for a startup calculation. The multiple reference frame model should not be used, however, if it is necessary to actually simulate the transients that may occur in strong rotor-stator interactions, as the sliding mesh model alone should be used. It should be noted that the interface treatment applies to the velocity and velocity gradients, since these vector quantities change with a change in reference frame. Scalar quantities, such as temperature, pressure, density, turbulent kinetic energy, and so on, do not require any special treatment, and therefore are passed locally without any change.

The governing equations in each zone (or subdomain) are written with respect to its reference frame. At the boundary between two subdomains, the diffusion and other terms in the governing

equations in one subdomain require values for the velocities in the adjacent subdomain, as shown in Figure 2.5.
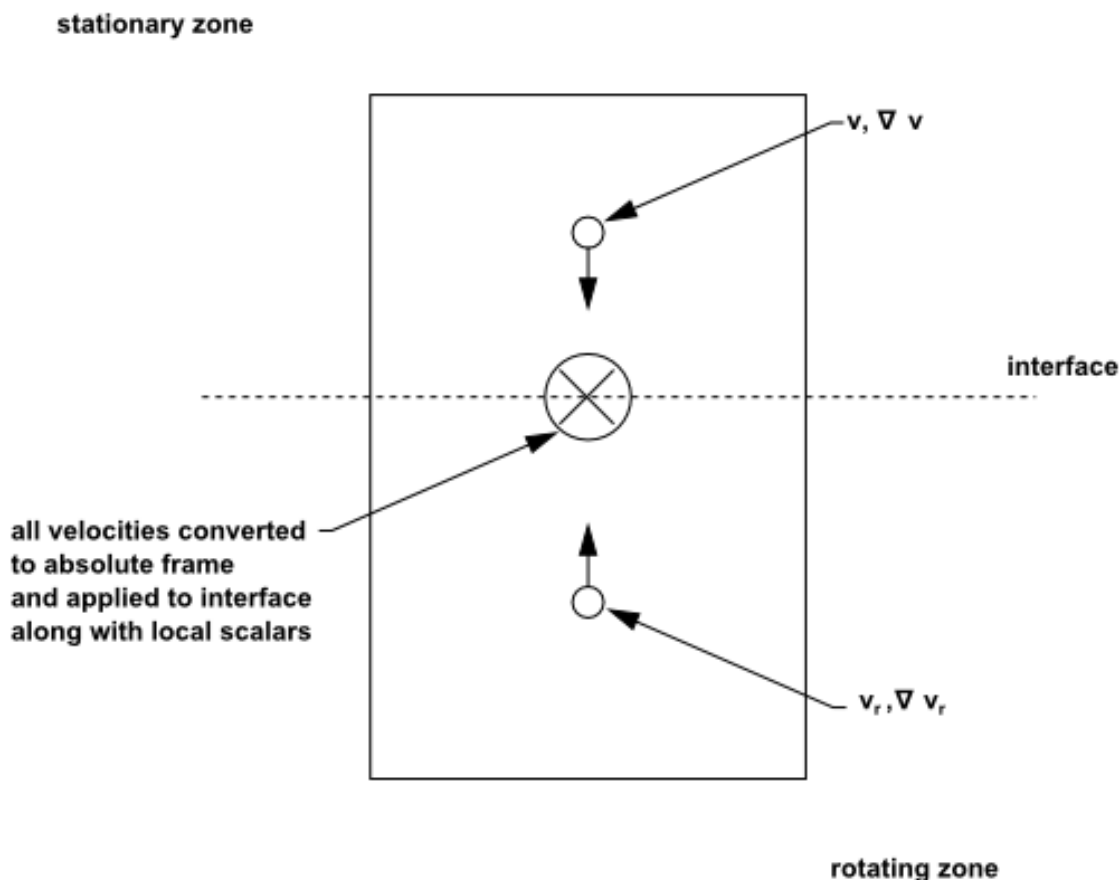
Figure 2.5   Interface treatment for the Frozen Rotor model.

The solver enforces the continuity of the absolute velocity, $\vec{v}$, to provide the correct neighbor values of velocity for the subdomain under consideration. When the relative velocity formulation is used, velocities in each subdomain are computed relative to the motion of the subdomain. Velocities and velocity gradients are converted from a moving reference frame to the absolute inertial frame using Equation 2.50.

$$\vec{v} = \vec{v}_r + (\vec{\omega} \times \vec{r}) + \vec{v}_t \tag{2.50}$$

The gradient of the absolute velocity vector is

$$\nabla\vec{v} = \nabla\vec{v}_r + \nabla(\vec{\omega} \times \vec{r}) \tag{2.51}$$

When the absolute velocity formulation is used, the governing equations in each subdomain are written with respect to that subdomain's reference frame, but the velocities are stored in the absolute frame. Therefore, no special transformation is required at the interface between two subdomains. Scalar quantities such as density, static pressure, static temperature, species mass fractions, and so on, are simply obtained locally from adjacent cells.

2.4.2 - Mixing Plane model

The Frozen Rotor model is applicable when the flow at the interface between adjacent moving/stationary zones is nearly uniform. If the flow at this interface is not uniform, the Frozen Rotor model may not provide a physically meaningful solution. The sliding mesh approach may be appropriate for such cases, but sliding mesh calculations are necessarily unsteady, and therefore require significantly more computation to achieve a final solution. For situations where using the sliding mesh model is not feasible, the Mixing Plane model can be a cost-effective alternative. In the Mixing Plane approach, each fluid zone is treated as a steady-state problem. Flow-field data from adjacent zones are passed as boundary conditions that are spatially averaged (or "mixed") at the Mixing Plane interface. This mixing removes any unsteadiness that would arise due to circumferential variations in the passage-to-passage flow field (for example, wakes, shock waves, separated flow), therefore yielding a steady-state result.

Figure 2.6 shows a meridional plane within a mixed-flow device such as a centrifugal compressor. The stage consists of two flow domains: the rotor domain, which is rotating at a prescribed angular velocity, followed by the stator domain, which is stationary. The order of the rotor and stator is arbitrary, meaning that a situation where the rotor is downstream of the stator, like in a radial turbine, is equally valid.
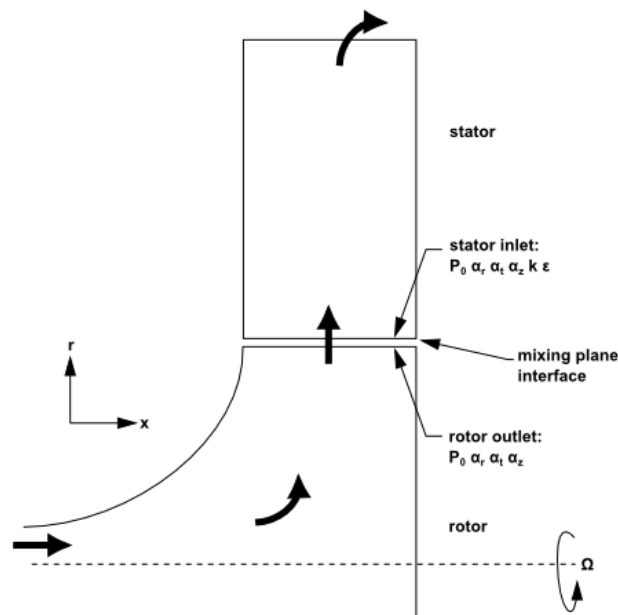
Figure 2.6   Radial rotor-stator interaction in the Mixing Plane approach.

The essential idea behind the mixing plane concept is that each fluid zone is solved as a steady-state problem. At some prescribed iteration interval, the flow data at the mixing plane interface are averaged in the circumferential direction on both the stator outlet and the rotor inlet boundaries. Typically, area-weighted averaging is performed, although commercial solvers make mass averaging also available. By performing circumferential averages at specified radial or axial

stations, profiles of boundary condition flow variables can be defined. These profiles, which will be functions of either the axial or the radial coordinate, depending on the orientation of the mixing plane, are then used to update boundary conditions along the two zones of the mixing plane interface. In the examples shown in Figure 2.6, profiles of averaged total pressure (p_0), direction cosines of the local flow angles in the radial, tangential, and axial directions ($\alpha_r, \alpha_t, \alpha_z$), total temperature ($T_0$), turbulence kinetic energy (k), and turbulence dissipation rate (ε) are computed at the rotor exit and used to update boundary conditions at the stator inlet. Likewise, a profile of static pressure (p), direction cosines of the local flow angles in the radial, tangential, and axial directions ($\alpha_r, \alpha_t, \alpha_z$), are computed at the stator inlet and used as a boundary condition on the rotor exit. Mixing Plane algorithm can be described as follows:

1. Updates the flow field solutions in the stator and rotor domains.
2. Averages the flow properties at the stator exit and rotor inlet boundaries, obtaining profiles for use in updating boundary conditions.
3. Passes the profiles to the boundary condition inputs required for the stator exit and rotor inlet.
4. Repeats steps 1–3 until convergence.

Despite the simplifications inherent in the mixing plane model, the resulting solutions can provide reasonable approximations of the time-averaged flow field.

2.4.3 - Sliding mesh approach

Contrary to Frozen Rotor and Mixing Plane models, the sliding mesh approach is inherently unsteady due to the motion of the mesh with time. Indeed, the sliding mesh model is a special case of general dynamic mesh motion wherein the nodes move rigidly in a given dynamic mesh zone. Additionally, multiple cells zones are connected with each other through non-conformal interfaces. As the mesh motion is updated in time, the non-conformal interfaces are likewise updated to reflect the new positions each zone. It is important to note that the mesh motion must be prescribed such that zones linked through non-conformal interfaces remain in contact with each other (that is, "slide" along the interface boundary).

With respect to sliding meshes, the integral form of the conservation equation for a general scalar, ϕ, on an arbitrary control volume, V, whose boundary is moving can be written as:

$$\frac{d}{dt}\int_V \rho\phi dV + \int_{\partial V} \rho\phi(\vec{u} - \vec{u}_g)\cdot d\vec{A} = \int_{\partial V} \Gamma\nabla\phi\cdot d\vec{A} + \int_V S_\phi dV \qquad (2.52)$$

Where ρ is the fluid density, $\vec{u}$ is the flow velocity vector, $\vec{u}_g$ is the mesh velocity of the moving mesh, Γ is the diffusion coefficient and S_ϕ is the source term of ϕ.

By using a first-order backward difference formula, the time derivative term in Equation 2.52 can be written as:

$$\frac{d}{dt} \int_V \rho\phi dV = \frac{(\rho\phi V)^{n+1} - (\rho\phi V)^n}{\Delta t}$$

(2.53)

Where n and $n+1$ denote the respective quantity at the current and next time step, respectively. Because the mesh motion in the sliding mesh formulation is rigid, all cells retain their original shape and volume. As a result, the time rate of change of the cell volume is zero, and Equation 2.53 simplifies to:

$$\frac{d}{dt} \int_V \rho\phi dV = \frac{[(\rho\phi)^{n+1} - (\rho\phi)^n]V}{\Delta t}$$

(2.54)

The flow in the moving mesh zones is therefore updated at every time step, provided that an appropriate specification of the rigid mesh motion is defined for each zone. Note that due to the fact that the mesh is moving, the solutions to Equation 2.52 for sliding mesh applications will be inherently unsteady.

3 - Research outline

As anticipated, the present work aims to investigate the key aspects that represent the main drivers of turbochargers research and development, namely, the characterization through performance maps, thermal and structural analyses, and design optimizaton strategies. Figure 3.1 schematically depicts an overview of the studies that were carried out and the corresponding numerical techniques that were employed.
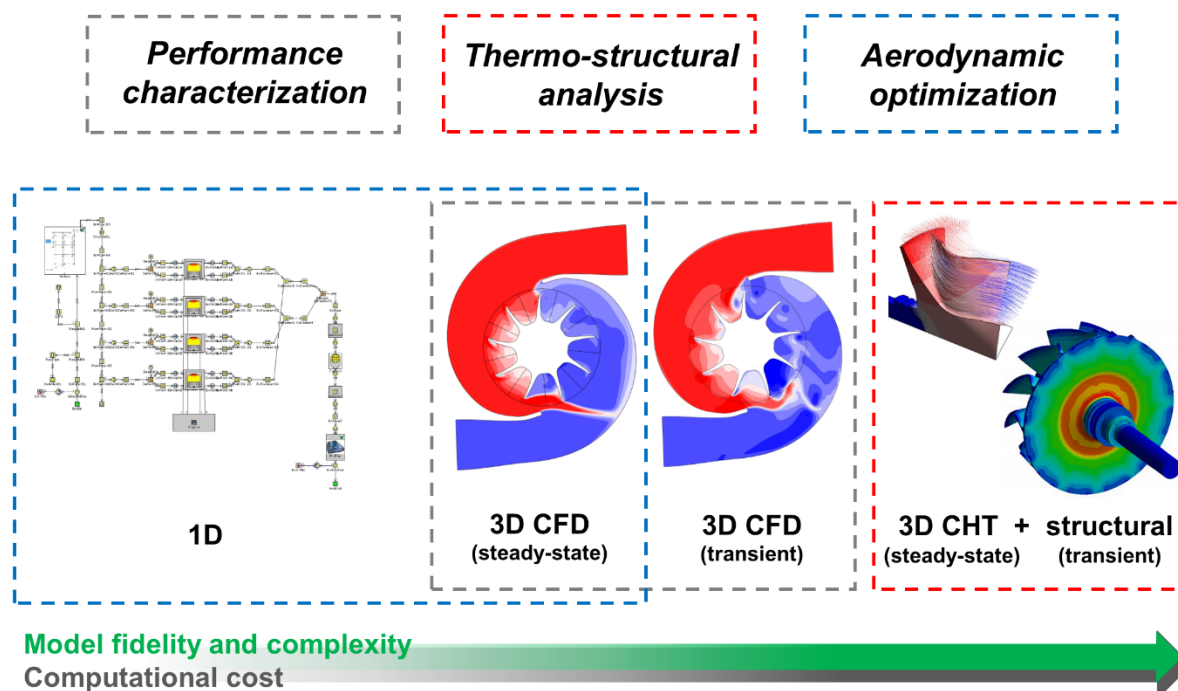
Figure 3.1   Overview of the different studies and the applied numerical techniques.

This research work takes advantage of different modelling approaches, from 1D techniques that are coupled to 3D CFD models for the design optimization of existing components, to the thermo-structural analysis of a turbine wheel subjected to engine load transient. Indeed, effort was put on gaining insight on the main challenges of turbochargers development, while at the same time developing effective and computationally efficient numerical modelling approaches.

One of the main challenges with the turbocharger technology consists in correctly matching the turbocharger to the internal combustion engine. This problem is inherent when trying to connect a rotor dynamic device which is designed to accept a steady flow of working fluid to a positive displacement internal combustion engine that produces a pulsating exhaust flow used to drive the turbine [14]. To this end, an accurate characterization of the turbocharger's performance is paramount. Indeed, the first part of the study, presented in *Chapter 4*, focuses on assessing whether steady-state techniques represent a viable option to model a turbocharger's turbine in case of steady-state operation. Even under the engine's steady-state operation, a turbine coupled

to an internal combustion engines is inherently supplied with a pulsating flow: this may hinder the prediction capabilities of a steady-state approach. The case study selected for this analysis is a double-entry turbine, a particular design for which the available literature findings are remarkably scarce. This study serves both as an assessment of different 3D CFD approaches for the performance characterization of turbochargers and as a numerical validation of the developed models, which sets the basis for the following numerical analyses on different key aspects of turbochargers development. Specifically, still focusing on the turbine stage, the strong tendency towards increasingly higher turbine inlet temperature [45] makes the evaluation of thermally-induced stress of particular importance for the turbine's life cycle prediction. To this end, a computationally efficient method for the transient thermo-structural analysis of a turbine wheel was developed. The approach that was developed and adopted for transient thermal calculations is presented in *Chapter 5*: by taking advantage of adequate boundary conditions that model the effects of the fluid domain without actually solving it, the developed model allows for cost-effective thermo-structural simulations. The performance of a turbine strongly depends on the available energy of the exhaust gases: this is the reason why turbocharger's turbines development is typically oriented towards their capability to withstand extremely high inlet temperature [46–48]. The performance of a turbocharger's compressor, on the other hand, mainly depends on its aerodynamic design. Indeed, the research activity presented in *Chapter 6* allows to come full circle on the analysis of a turbocharger's components, by carrying out a DOE-based optimization of a compressor's diffuser and volute by means of a multi-fidelity methodology approach. Throughout the optimization activity, a 1D engine model was coupled to the developed 3D CFD model with the aim of modelling the fluid dynamic interactions between engine and turbocharger. Several diffuser configurations were generated and tested, and flow structures were thoroughly investigated to better understand the resulting performance parameters. Additionally, different volute cross-sectional shape and area distribution laws were analyzed: for each configuration, contour plots of total pressure and entropy generation rate [49] were employed to investigate the flow behavior within the volute.

The following paragraphs provide an extended introduction to the topics that will be thoroughly presented in the following chapters.

3.1 - Performance characterization

Moving from the contents of section 2.4, the modelling of turbochargers by means of 3D CFD techniques can be categorized in two approaches:

- steady-state modelling, by employing Frozen Rotor (FR) or Mixing Plane (MP) interface models at the volute-rotor interface;
- transient modelling, by employing a sliding mesh approach.

Besides sliding mesh modelling techniques, several methods have been developed to reduce the computational cost of transient calculations. For example, Fourier transformation-based techniques use a Fourier series to approximate the flow variables at the circumferentially periodic boundaries of a blade passage: then, a phase shift is applied to the temporally summed Fourier coefficients to retrieve the equivalent flow [50]. Additionally, compared to a time-marching simulation, a significant reduction in computational time can be achieved by performing the calculations using an harmonic analysis solution method, where the temporal derivatives are discretized using a spectral operator, instead of a 2nd order backwards Euler approximation [51]. While these alternative methods grant a reduced calculation time, they can be quite restrictive concerning the model's geometry and boundary conditions. The sliding mesh approach, however, while computationally expensive, represents the most straightforward transient modelling technique and, as such, the most versatile in handling complex geometries and unsteady phenomena. For this reason, the sliding mesh model will be considered as the reference transient approach in the present study.

The modelling of an unsteady phenomenon such as a ramp-up phase due to engine acceleration requires transient calculations: indeed, mass flow rate, pressure and temperature are expected to increase over time in the above example case. Generally speaking, transient calculations are unavoidable in presence of time-dependent boundary conditions.

However, as discussed in the previous chapter, when boundary conditions are time-invariant and the machine operates at steady-state conditions, the rotating motion can be modelled through steady-state calculations by employing special numerical treatment at the rotor-volute interface (i.e. a FR or MP approach). This allows major savings of computational resources with respect to transient simulations, which often require extremely small timesteps (of the order of 10^{-5} s) and therefore longer calculation time.

However, the first approximation introduced by such steady-state approaches is related to the very definition of steady-state operation: indeed, it is often unclear how valid this assumption under the range of pulsating conditions that a turbocharger turbine is subjected to. Early researchers into the unsteady performance of turbochargers such as Benson et. al [52,53], Wallace et. al. [54–56], Kosuge, et al [57] and later Capobianco et. al [58–60] all sought to quantify the degree to which the turbocharger could be assumed steady, or, more precisely, quasi-steady [61–63] when exposed to a pulsating flow. Several researchers [64–66] have used the Strouhal number as a parameter to define the onset of unsteady effects in a flow. The Strouhal number, however, only takes into account the frequency of the pulsations. Other authors [53,57,58,60] proposed that the differences between quasi-steady and unsteady mean values were not only dependent on the frequency of pulsation, but also on the amplitude and pulse shape. Capobianco and Gambarotta [60] also did considerable work on the influence of pulse amplitude and published results, which suggested that the amplitude of the unsteady pulse had a greater impact on the departure from quasi-steady behavior than the frequency. More recently, Copeland et. al [67]

formulated an unsteadiness criterion (Λ) that accounts for both frequency and amplitude of the pulsations, as shown in Eq (3.1):

$$\Pi \cdot St = \Lambda \qquad (3.1)$$

Where St is the Strouhal number and Π is a pressure amplitude weighting factor. In conclusion, while a small Strouhal number does give a clear indication of a quasi-steady flow, once the Strouhal number approaches unity the amplitude of the flow pulsations must also be considered. The choice between a steady-state and a transient modelling approach should be made according to the order of unsteadiness of the turbocharger's operation. If a steady-state approach is viable, then the choice between the available volute-rotor interface models (i.e. Frozen Rotor or Mixing Plane) should be made according to the turbocharger's design and operating conditions. Typically, a Frozen Rotor interface model is best used when the rotor-stator interaction is weak, while a Mixing Plane approach gains accuracy when the flow is homogeneous throughout the interface: however, such conditions are hardly met in turbocharger applications. With the aim of investigating 3D CFD quasi-steady modelling techniques, a turbine stage with a double-entry volute was selected for this study. As apparent from Figure 3.2, a double-entry turbine contains two circumferentially-divided inlets, each of which supplies a separate 180° sector of the turbine.
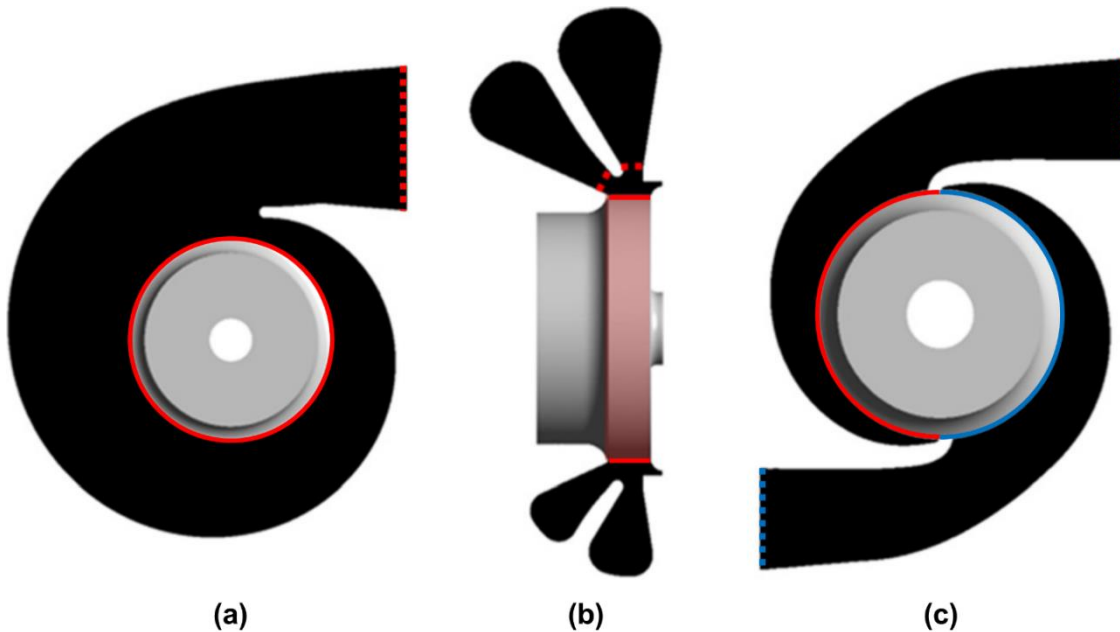
Figure 3.2 Different turbine architectures: (a) single scroll (b) twin-entry and (c) double-entry.

Each inlet is typically connected to an engine bank and the turbine can operate under different conditions depending on the engine's load demand, specifically:

- equal admission: both inlets are supplying the turbine with similar flow conditions;
- unequal admission: the inlets are supplying the turbine at different flow conditions; in the extreme case of partial admission, only one inlet is supplying the turbine.

For its diverse operating conditions, this turbine architecture represents an interesting case study to model by means of 3D CFD techniques, moreover, literature findings on double-entry turbines are remarkably few, especially under unequal admission conditions [68]. Most of the available numerical analyses of multiple-entry turbines (i.e. twin and double-entry turbines) are transient [33,69], requiring either major computational effort [70] or very low mesh density [71]. Indeed, multiple-entry turbines are specifically designed to isolate overlapping exhaust pulses from different cylinders and, unsurprisingly, unsteady analyses of the pulsating flow are of particular interest. Nervertheless, there are some examples of steady-state 3D CFD analyses, but they are either limited to the definition of the turbine's performance maps [72,73] or coupled to lower-fidelity transient modelling techniques [74]. Most notably, it appears that every steady-state 3D CFD analysis on twin and double-entry turbines adopts the Frozen Rotor approach. The aim of this study is to investigate steady-state 3D CFD modelling techniques on a double-entry turbine test case, with special focus on the criticalities of the Frozen Rotor and Mixing Plane approaches under full and partial admission operation. The computational models for the study were developed within ANSYS® framework. For the evaluation of the different modelling approaches, calculation results were compared to experimental data from a hot gas test bench.

3.2 - Thermo-structural analysis

Increasingly stricter regulations on emissions have pushed the development of Internal Combustion Engines (ICEs) towards high standards of performance and efficiency. Turbocharged engines are common in the automotive sector [5] and technologies such as multi-stage turbochargers and variable turbine geometry systems are often employed to meet the growing demand for turbocharger performance. Overall, regardless of the turbocharger's architecture, there is a strong tendency towards higher turbine inlet temperature, as this clearly represents the most straightforward solution to increase the turbocharger's available power [45]. High turbine inlet temperature, however, together with the highly unsteady operation that typically characterizes automotive turbochargers, leads to significant thermal stress: indeed, thermo-mechanical load has become a critical aspect in the design of a turbine wheel.

The accurate evaluation of thermally-induced stresses is of particular importance for life cycle predictions, and knowing the temperature distribution inside the turbine wheel is essential to a thermo-structural analysis. To this end, experimental testing is feasible, but expensive: the temperature of the turbine wheel can be measured at different locations by means of wireless thermocouple transmitters, but special machining is required to house the measuring equipment. Additionally, modifications to the wheel's geometry demand a dynamic balancing to grant failure-free operation [75].

In this framework, numerical techniques are a valuable and cost-effective tool. 3D Conjugate Heat Transfer (CHT) calculations (Figure 3.3) represent the state-of-the-art for steady-state thermal

analyses, coupling fluid and solid domains to obtain the temperature distribution of the latter, among a large number of other thermodynamic quantities.
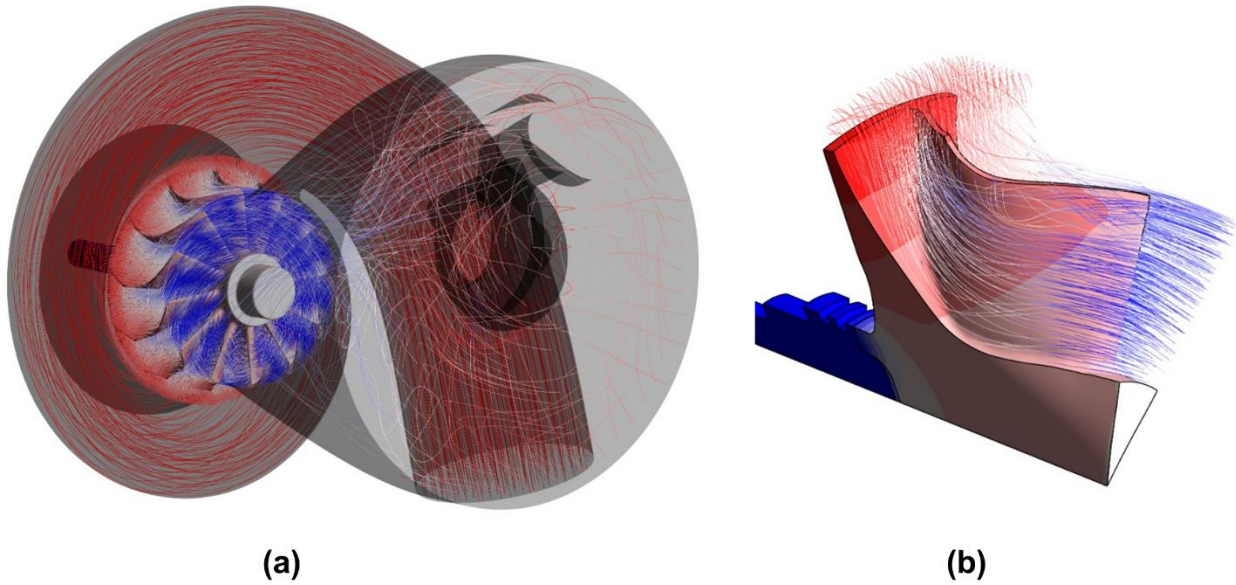
Figure 3.3   Example of the temperature field resulting from a CHT analysis on (a) the whole turbine stage and (b) the blade passage solid and fluid domain, here represented by flow streamlines.

According to Heuer et al. (2005) [76], however, thermal stresses are especially high in transient operation, where temperature gradients combine with local mechanical strain. Therefore, transient thermal analyses are usually required. Due to the different timescales of convective and conductive heat transfer mechanisms, transient CHT simulations are burdened by extremely high computational costs. As shown in Table 3.1, in the specific case of turbocharged engines, the timescales of engine load transients and turbocharger response may differ by a factor of up to 10^6, as unsteady turbine flow calculations would imply the use of a solver timestep in the order of 10^{-5} s [33].

	Timescale [s]	Relative timescale [orders of magnitude]
Engine load transient	10^1	0
Solid domain timestep	10^{-1}	2
Fluid domain timestep	10^{-5}	6

Table 3.1   Timescale comparison for different phenomena.

Unsurprisingly, literature reports several methods to conduct transient thermo-mechanical numerical analyses without resorting to transient CHT calculations. Heuer et al. (2005) first proposed a new approach to simulate the heating and cooling processes of a turbine housing by employing steady state CHT calculations [76]. An alternative approach was presented by Ahdad et al. (2010), who developed a semi-empirical model to calculate thermal stresses in the turbine housing [77]. Being based on empirical correlations, this model had to be calibrated for each case study. Oberste-Brandenburg et al. (2012) presented a simplified approach by replacing 3D

simulations with a simpler 1D model and by reducing their structural FEA geometry model to its essential components [78]. This approach delivers a good agreement with 3D calculations, but more recent work by Diefenthal et al. (2015) shows that 1D approaches are not sufficient to describe the transient temperature fields with regards to thermal or thermo-mechanical fatigue [46]. Heuer et al. [75] extended their previous work on a turbine wheel: the investigation proved that thermal stresses are critical in the fillets on the back of the turbine wheel. Similar results were presented by Makarenko et al. [79]. Diefenthal et al. [46,47] extended the modelling approach that was initially proposed by Heuer et al. [76]. More recently [48], Diefenthal's Equalized Timescale Method [47] was employed to evaluate the stress distribution on both turbine wheel and housing, proving how transient operation is critical in the evaluation of the thermo-mechanical load.

The present study proposes an approach for carrying out transient thermo-structural analyses of the solid domain only, characterized by a physical time in the order of 10^1 s, without the need for unsteady fluid flow calculations. In the proposed methodology, the effects of the fluid flow in the heat transfer process are modelled by imposing adequate boundary conditions to the solid domain's wet surfaces. By performing two steady-state CHT calculations and one steady-state Computational Fluid Dynamics (CFD) calculation, time-dependent boundary conditions can be derived in terms of convective heat transfer coefficient spatial distribution and near-wall fluid temperature.

The case study of the present activity is a high-performance turbocharger turbine for automotive applications, responding to engine load transients of tenths of seconds. Initially, steady-state CFD and CHT models of the turbine stage are validated against experimental data. Then, transient analyses on the turbine wheel are carried out following the developed computationally-efficient approach. Eventually, the results of these transient calculations are imported as thermal loads into an unsteady structural solver, in order to evaluate the stress distribution on the turbine wheel over time. The commercial suite ANSYS® was employed for fluid dynamics, thermal and structural analyses.

3.3 - Aerodynamic optimization

Turbocharged engines are an industrial standard in many applications, from automotive [5] to energy production [80]. Depending on the application, however, the technical requirements for the turbocharging unit are quite different. More specifically, while in automotive applications the operating range needs to be sufficiently wide to cover all the off-design functioning conditions of the engine and high efficiency has to be ensured also in transitory phases [81], in stationary power production the matching between the turbocharger and the engine can be optimized at a specific operating point. This represents the rated power of the engine, in which it is expected to work during most of the time, assuming that off-design conditions are limited. Focusing on the

aerodynamic implications, one may argue that this opens room for a more refined optimization of the turbocharger design. In fact, turbomachines can be effectively optimized on condition that attended working conditions are constant in time [82].

In industrial applications, while some manufactures usually buy from an external supplier a turbocharging unit that fits the requirements of their engine, some others do have the know-how and the technical facilities to produce both components. In this case, a joint design and optimization of the turbocharger can be particularly beneficial. Focusing more specifically on the methods for designing a new turbocharger, the preliminary definition of its main features is typically based on empirical correlations and 1D simulation tools [83]. These methods usually provide a guess of the overall dimensions and operating speed, as well as of an estimation of the inlet and outlet flow angles or the area ratio of the blade passages. Starting from this, further refinement is usually carried out by means of methods with higher fidelity. For examples, there are examples of steady state optimization works on radial machinery that were conducted employing mean-line models [84]. Despite an interesting ratio between accuracy and computational cost, these models require experimentally validated correction factors in order to be predictive; this makes them very sensitive to calibration factors, possibly leading also to bad design choices [85]. On this basis, it is apparent that Computational Fluid Dynamics (CFD) currently represents the real standard for the analysis and aerodynamic optimization of turbochargers, allowing for the modelling of 3D phenomena and a thorough analysis of the flow field. As an example, Figure 3.4 shows contour plots of dimensionless total pressure and radial velocity on a cross-section of different compressor volutes and diffusers, respectively: it is apparent that 3D CFD analyses allow to achieve deep insight on flow phenomena and their underlying mechanisms.
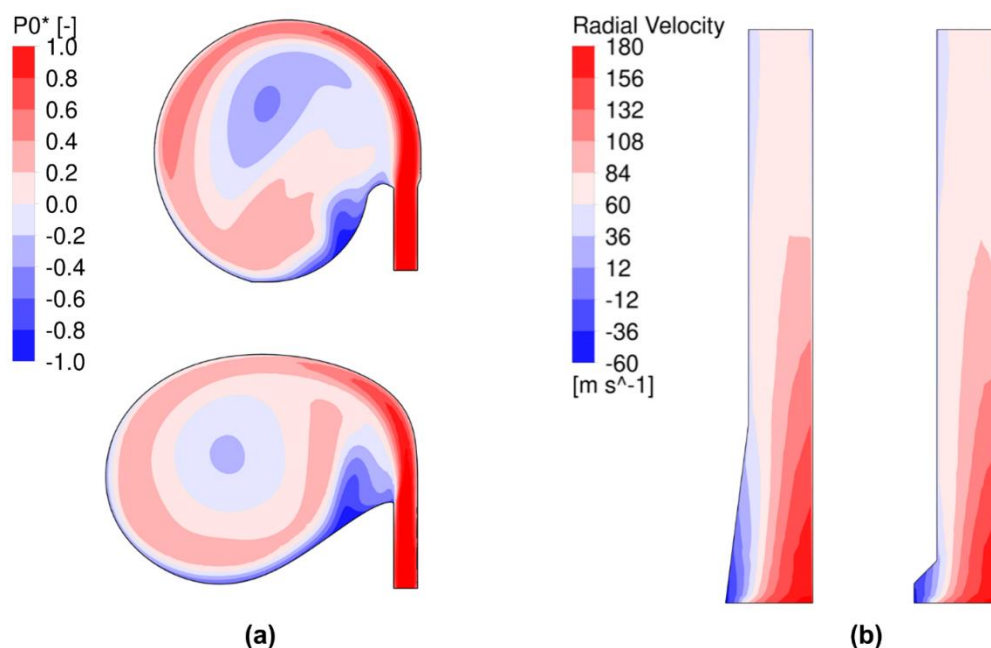
Figure 3.4   Dimensionless total pressure and radial velocity contour plots over the cross-sectional views of two different (a) compressor volutes and (b) diffusers.

More specifically, while time dependent CFD analyses are becoming more and more feasible for detailed analyses thanks to the increasing calculation resources, they are still impractical for an optimization activity, where multiple configurations need to be tested before the target is reached. To this end, steady state analyses represent the best trade off between accuracy of the performance prediction and calculation costs [86].

While many examples can be found in the literature regarding the optimization of the compressor as a standalone system [87], one should also bear in mind that the turbocharger is not indeed an isolated turbomachine, but it is in strong fluid dynamic connection with the engine itself. As a result, modifying its performance implies a change of the engine operating conditions and, in turn, of the boundary conditions the turbocharger itself must work with [88]. Figure 3.5 shows the coupling between the engine and turbocharger, as implemented in the present study.
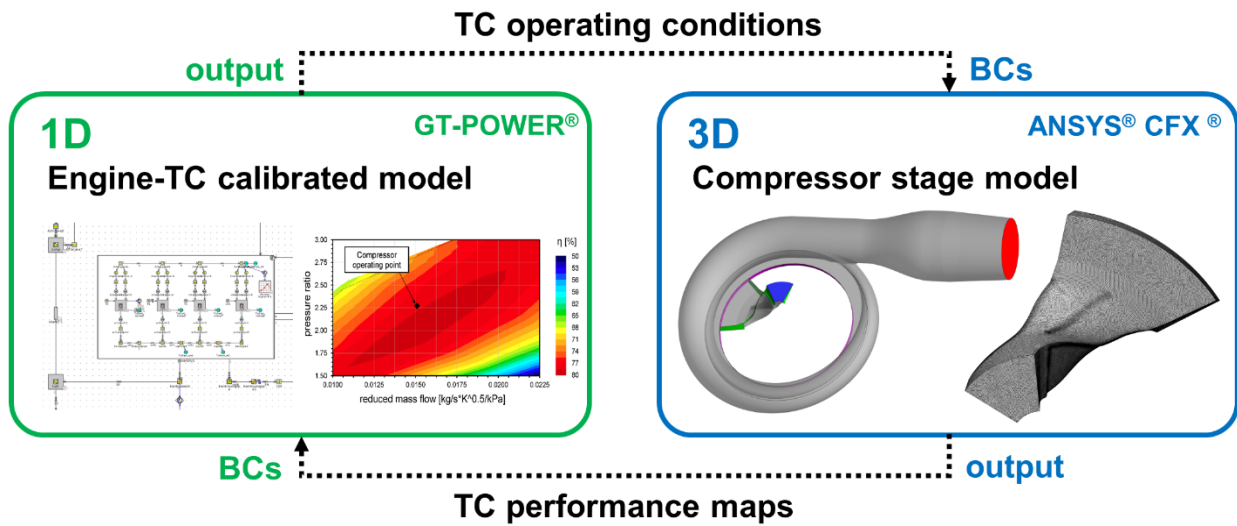
Figure 3.5 **The coupling layout between the 1D engine model and the 3D compressor stage model of the present study.**

Moving from this background, the present work reports the results of a joint research activity between academia and industry to evaluate how much a dedicated optimization of the turbocharger's compressor stage static parts can improve the overall performance of an engine for stationary power production. The optimization has been applied to an existing turbocharged engine, in which a state-of-the-art turbocharger was bought from an external supplier as that providing the best matching with the engine. In doing so, the study shows how an integrated approach can provide efficiency advantages even in comparison to commercial products that were thought to be already optimized. To this end, a variety of techniques has been used, ranging from 1D modelling of the powertrain to higher-fidelity 3D Computational Fluid Dynamics (CFD) for the optimization of the static parts of the compressor stage. Experimental test rig data were also used to calibrate the numerical models.

4 - Performance characterization

4.1 - Case study

As anticipated, the case study for the present activity is a double-entry turbine for a high-performance automotive engine. This design offers a twofold benefit in terms of turbocharger performance: firstly, with the engine cylinders split into two banks, each feeding a separate volute entry, it is easier to avoid exhaust pulse overlap, which could otherwise have a detrimental effect on the engine performance [14]. Secondly, with less chance for mixing, more of the pulsating exhaust flow energy will be preserved so that this is available at the turbine wheel [81]. When both volute entries are feeding the turbine equally (i.e. full admission operation) the turbine will act in the same manner as a single entry device [14]. In reality, the exhaust pulses feeding each limb of the turbine will be timed so that they are out of phase with each other; as a result the turbocharger turbine will rarely act in full admission and will spend the majority of time with unequal flows driving each 180° sector of the turbine wheel; in the most extreme case, one limb may be flowing while the other has no flow, a condition known as partial admission. The present case study was tested at a hot gas test bench at steady-state conditions: therefore, pulsating flow operation is neither an issue nor the focus of this study. Instead, steady-state 3D CFD modelling was investigated focusing on the extreme cases of equal admission and partial admission operation. Figure 4.1 depicts the double-entry turbine and the test bench measurement stations: experimental data represents the benchmark for the assessment of the developed 3D CFD models.
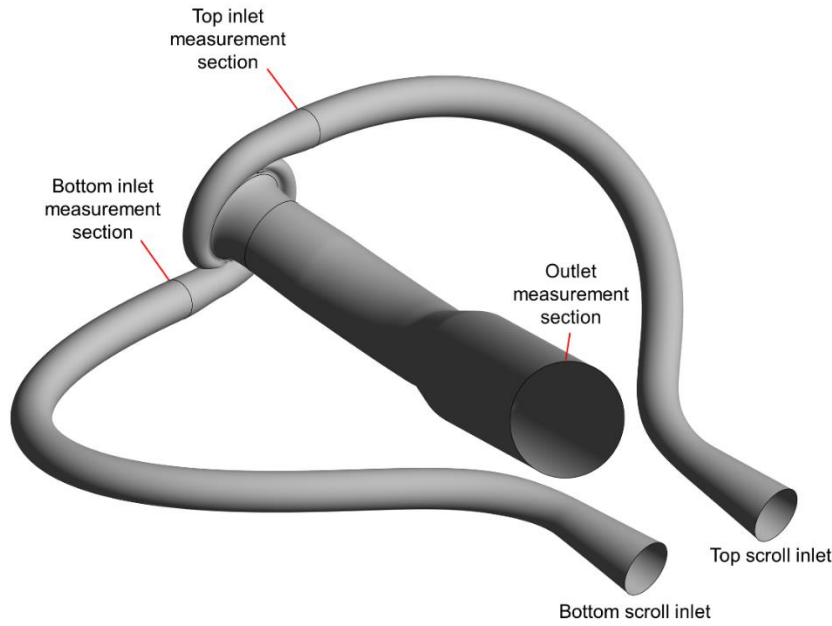
Figure 4.1   Case study and test-rig measurement stations.

Specifically, mass flow parameter (MFP) and total-to-static isentropic efficiency maps were available from the test bench, for equal and partial admission operation. In case of partial admission operation, gas supply was cut off at the bottom inlet. The turbine sectors are symmetrical and the same swallowing capacity (i.e. the same MFP) is expected for the bottom scroll. For confidentiality purposes, the turbine's performance parameters (i.e MFP and isentropic efficiency) were normalized against their corresponding maximum experimental value. Figure 4.3 shows the turbine's MFP maps from experimental measurements: in case of equal admission, inlet values of total pressure and temperature were calculated as an average between the two entries, since the use of a hot gas test bench allowed to steadily provide similar flow conditions at both inlets. Figure 4.4 shows the turbine's maps of total-to-static isentropic efficiency, defined in Eq. (4.1).

$$\eta_{ts} = \frac{T_{0,in} - T_{0,out}}{T_{0,in} - T_{out,is}} = \frac{T_{0,in} - T_{0,out}}{T_{0,in}\left(1 - \beta_{ts}^{\frac{1-\gamma}{\gamma}}\right)} \tag{4.1}$$

It is worth pointing out that the experimental evaluation of isentropic efficiency is a challenging task. Indeed, due to the strong non-uniformity of the turbine outlet temperature field [89,90], it is difficult to accurately measure outlet temperature and, by extension, isentropic efficiency. Figure 4.2 shows, as a preview, some results of the present numerical study (transient calculation, partial admission): it is apparent that, especially in partial admission operation, the outlet temperature field (here normalized against the inlet temperature, for confidentiality reasons) is significantly non-uniform close to the wheel.
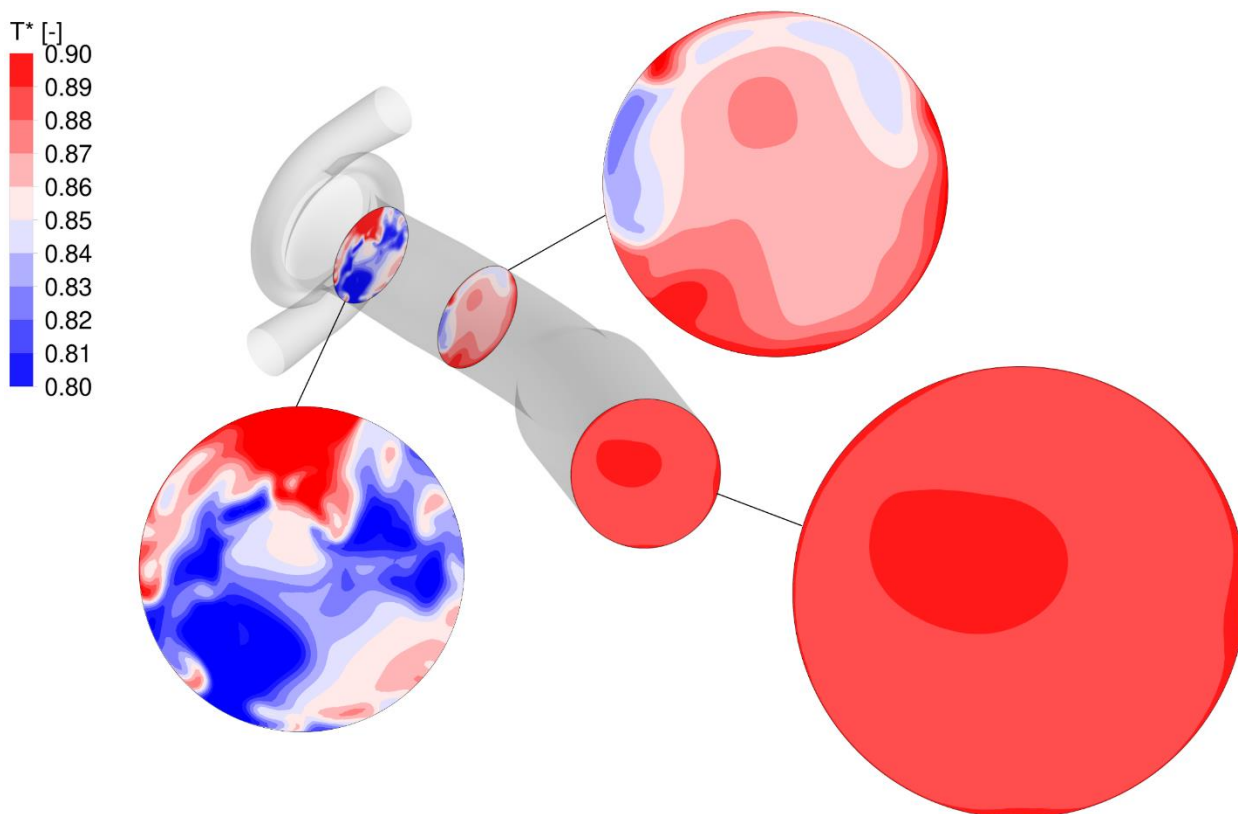
Figure 4.2   Normalized temperature field on different outlet sections.

The fact that the outlet measurement station is located far from the rotor exit (Figure 4.1) might partially address this issue, since diffusion and mixing along the outlet duct promote flow uniformity. However, with the aim of performing accurate measurements, more effective solutions should be adopted, such as a flow conditioner downstream of the turbine [91]. Still, the available experimental maps represent valuable reference data for the assessment of the numerical models that were developed in the present study.
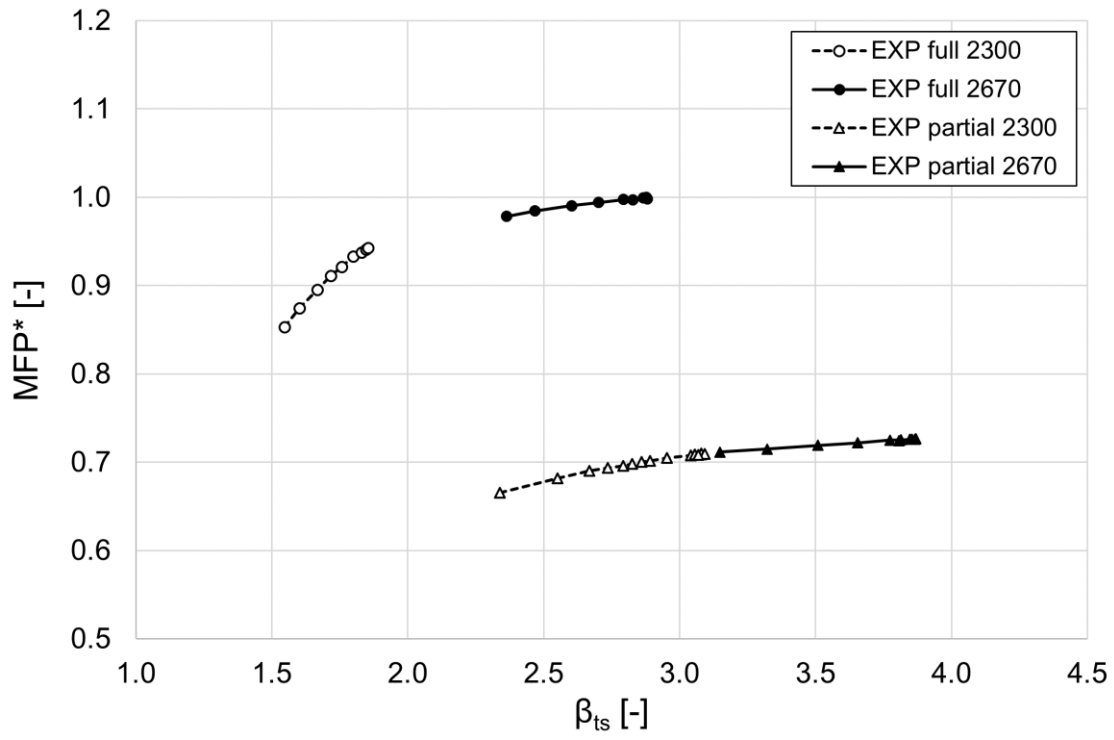
Figure 4.3   Experimental normalized MFP map.
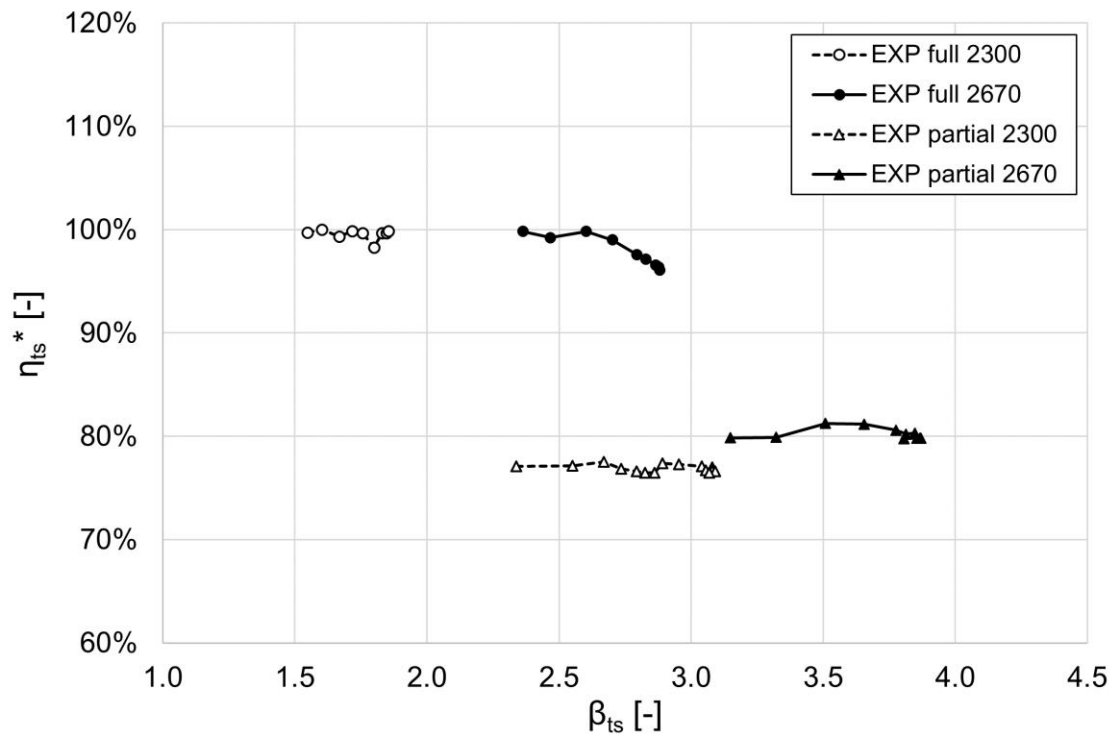
Figure 4.4   Experimental normalized total-to-static isentropic efficiency map.

4.2 - Methods

4.2.1 - Test plan

The aim of this study is to investigate steady-state 3D CFD modelling techniques on the above-presented double-entry turbine, with special focus on the criticalities of the Frozen Rotor and Mixing Plane approaches under full and partial admission operation. To this end, four different steady state 3D CFD models were developed in ANSYS® framework: one with a Frozen Rotor (FR) volute-rotor interface and one with a Mixing Plane (MP) interface, each one for full and partial admission operation. Additionally, one transient analysis was carried out at the highest rotating speed in order to assess the capability of the developed steady-state models for partial admission operation. Due to its extremely high computational cost, however, the transient analysis was carried out for a single operating point. Table 4.1 summarizes the test plan of the present study, showing the analyzed speedlines (identified by their reduced speed N_{red}) or operating points.

Simulation	Steady-state (FR)	Steady-state (MP)	Transient (TRN)
Full admission	N$_{red}$2300 (speedline) N$_{red}$2670 (speedline)	N$_{red}$2300 (speedline) N$_{red}$2670 (speedline)	-
Partial admission	N$_{red}$2300 (speedline) N$_{red}$2670 (speedline)	N$_{red}$2300 (speedline) N$_{red}$2670 (speedline)	N$_{red}$2670 ($\beta_{ts} = 2.6$)

Table 4.1   Test-plan of the double-entry turbine analysis.

4.2.2 - 3D CFD turbine model

The commercial code ANSYS® CFX® was used for the analysis of the compressor stage and for the optimization of its static parts. The selection of this software, very common for these applications, is due to the great flexibility in handling complex geometries. A steady-state RANS approach, using a pressure-based formulation of the solver, was adopted. ANSYS® CFX® features a pressure-based, coupled solver: mass, momentum and energy equations are solved as a single system using a fully implicit discretization of the equations at any given time step. For steady-state problems, the time-step behaves like an acceleration parameter, to guide the approximate solutions in a physically based manner to a steady-state solution. The shear stress transport (SST) turbulence model [44] was used, together with an automatic near-wall treatment that allows the solver to overcome mesh resolution requirements by gradually switching between wall functions treatment and low-Re formulations [92]. A high resolution, second order upwind scheme was used for the spatial discretization of the RANS and turbulence equations.

The computational domain for the steady-state FR model consists in five fluid sub-domains: one for each inlet duct, the volute domain, the rotor domain and the outlet duct domain. As the FR

modelling approach requires, the whole rotor geometry is employed. The flow inside the rotor wheel is solved in the relative frame of reference: two FR interfaces were employed, one placed between the volute and the rotor domain, and the other between the rotor the outlet domain. Figure 4.5 shows the setup of the steady-state FR model.
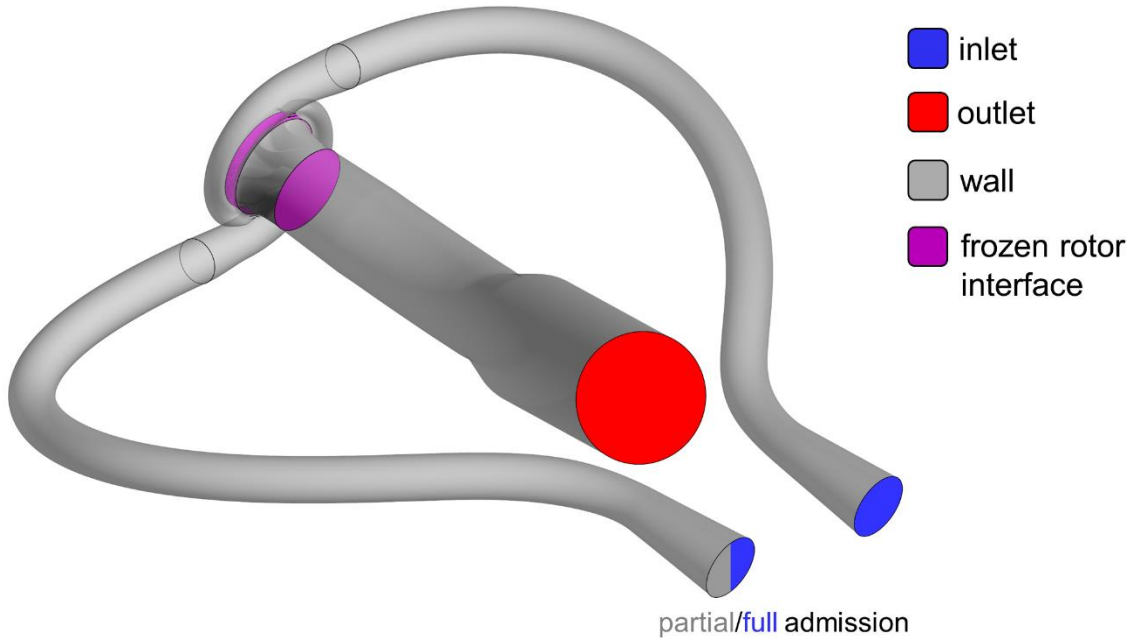
Figure 4.5   3D CFD turbine model: FR approach.

Total pressure and total temperature were imposed at the inlet boundary, while static pressure was set at the outlet boundary. The walls, both stationary and rotating, were set as adiabatic. In case of partial admission, a wall is set at the bottom inlet boundary, instead of a total pressure inlet. The fluid for the simulations was set starting from the default "air (ideal gas)" material, imposing temperature-dependent specific heat capacity at constant pressure, as shown in Eq. (4.2). Table 4.2 shows the coefficients of Eq. (4.2).

$$c_p(T) = [A_0 + A_1 \cdot T + A_2 \cdot T^2 + A_3 \cdot T^3 + A_4 \cdot T^4] \cdot R_{gas} \tag{4.2}$$

Coefficient	A_0	A_1	A_2	A_3	A_4	R_{gas}
Unit	-	K^{-1}	K^{-2}	K^{-3}	K^{-4}	$J\,kg^{-1}K^{-1}$
Value	3.692	$-1.675 \cdot 10^{-3}$	$4.299 \cdot 10^{-6}$	$-3.107 \cdot 10^{-9}$	$7.650 \cdot 10^{-13}$	289.90

Table 4.2   Cp correlation coefficients.

Concerning transport properties, both dynamic viscosity (μ) and thermal conductivity (k) were calculated as a function of temperature through Sutherland's law (Eq. (4.3) and Eq. (4.4)). Table 4.3 shows Sutherland's law coefficients for the fluid's transport properties.

$$\mu(T) = \mu_0 \frac{T_{ref}+S}{T+S}\left(\frac{T}{T_{ref}}\right)^n \qquad (4.3)$$

$$k(T) = k_0 \frac{T_{ref}+S}{T+S}\left(\frac{T}{T_{ref}}\right)^n \qquad (4.4)$$

Quantity	μ				k			
Coefficient	μ_0	T_{ref}	S	n	k_0	T_{ref}	S	n
Unit	$\text{kg}\,m^{-1}s^{-1}$	K	K	-	$\text{W}\,m^{-1}K^{-1}$	K	K	-
Value	$1.716\cdot10^{-5}$	273.15	110.4	1.5	$2.436\cdot10^{-2}$	273.15	110.4	1.5

Table 4.3 Sutherland's law coefficients for transport properties.

The steady-state model for the investigation of the MP approach is fundamentally similar to the FR one. The main difference, besides obviously the rotor-stator interface type, is the fact that the rotor fluid domain is modelled by a single blade passage with cyclic boundaries, as shown in Figure 4.6 .
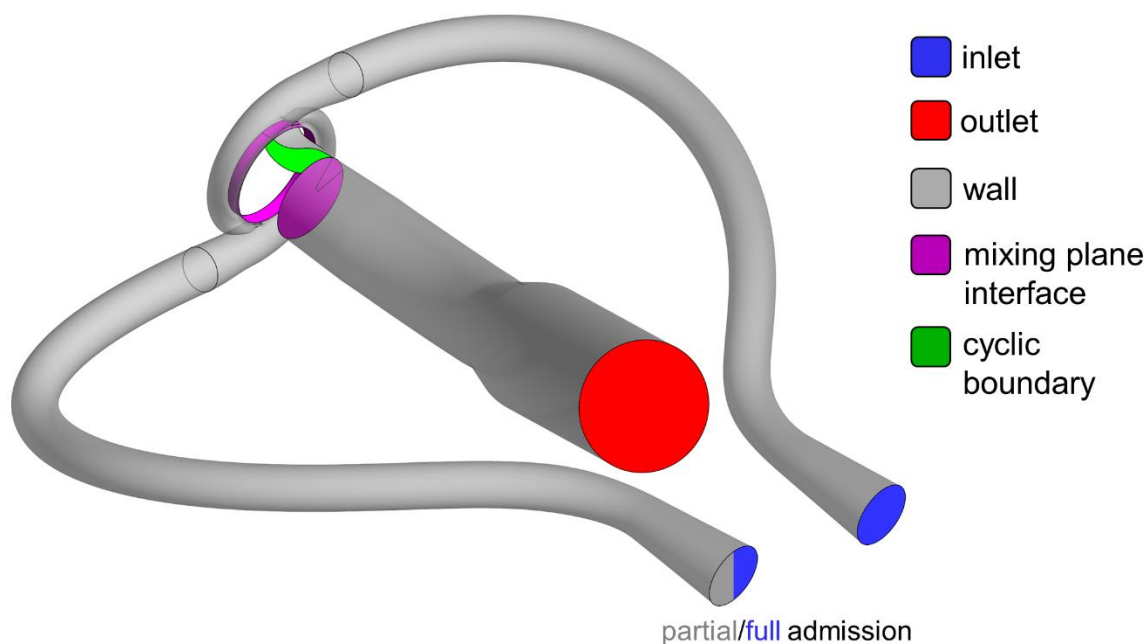
Figure 4.6 3D CFD turbine model: MP approach.

Indeed, the circumferential averaging operation of the MP interface model allows to take advantage of cyclic boundaries in order to reduce the mesh size and therefore the computational cost of the simulation.

The computational grid, of unstructured and hybrid type, was generated with ANSYS® Meshing®. A tetrahedral-based grid was adopted in the core flow region, with the addition of prismatic elements in the boundary layer zones. The first element height was chosen to guarantee that the

dimensionless wall distance at the grid nodes of the first prismatic layer from the walls did not exceed the limit of $y^+=1$. In order to assess, and, eventually, achieve mesh-independence, a mesh sensitivity analysis was carried out and three different meshes were tested. Table 4.4 summarizes the properties of the tested meshes, while Figure 4.7 shows the mesh sensitivity analysis results. It is worth pointing out that, in order to contain calculation time, the steady-state MP model was employed for the mesh sensitivity analysis.

Mesh	A	B	C
# elements (M)	17	29	38
Volute global sizing [mm]	0.70	0.45	0.35
Rotor global sizing [mm]	0.50	0.35	0.20
First layer height [mm]	$1.0 \cdot 10^{-3}$	$1.0 \cdot 10^{-3}$	$1.0 \cdot 10^{-3}$
# layers	20	20	20
Growth rate	1.15	1.15	1.15

Table 4.4   Main properties of the tested meshes.
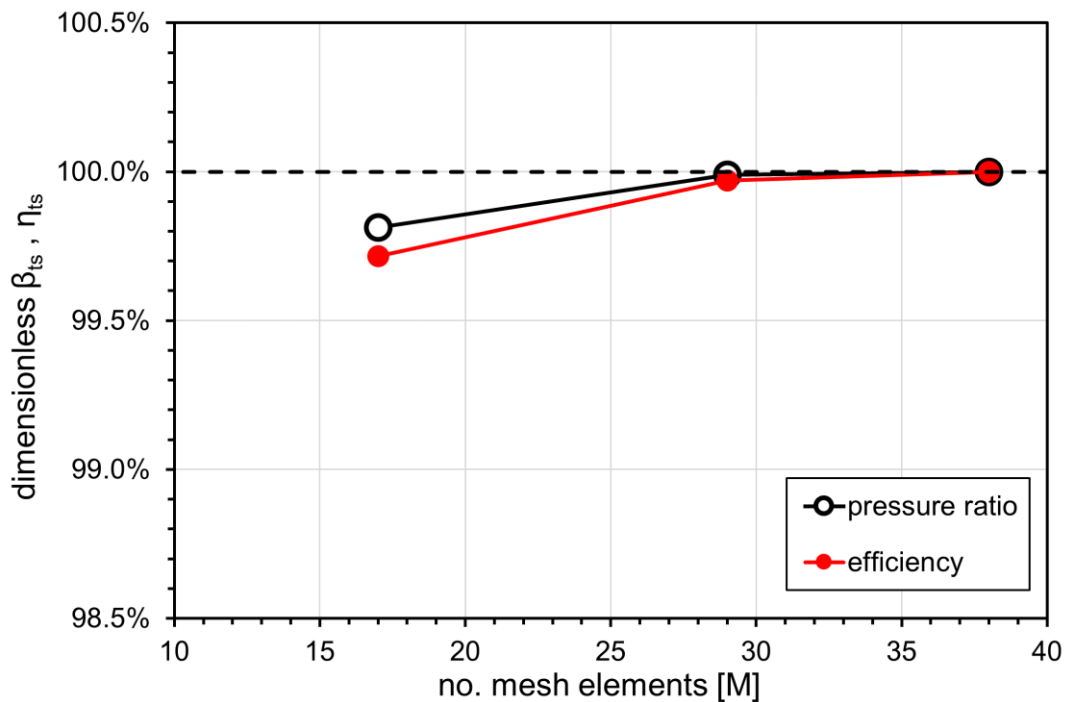
Figure 4.7   Mesh sensitivity analysis results.

The values obtained with the finest refinement level were used to non-dimensionalize the total-to-static pressure ratio and efficiency, and a convergence threshold of 0.1% on both quantities was set. As apparent from Figure 4.7, mesh B was able to respect the threshold and it was therefore selected as the best tradeoff between calculation accuracy and computational effort.

Figure 4.8 shows the selected mesh of the volute and rotor fluid domains. It is worth pointing out that the rotor fluid domain mesh for the FR model has the same properties of the MP one, but it's repeated along the rotation axis in order to form the full rotor geometry.
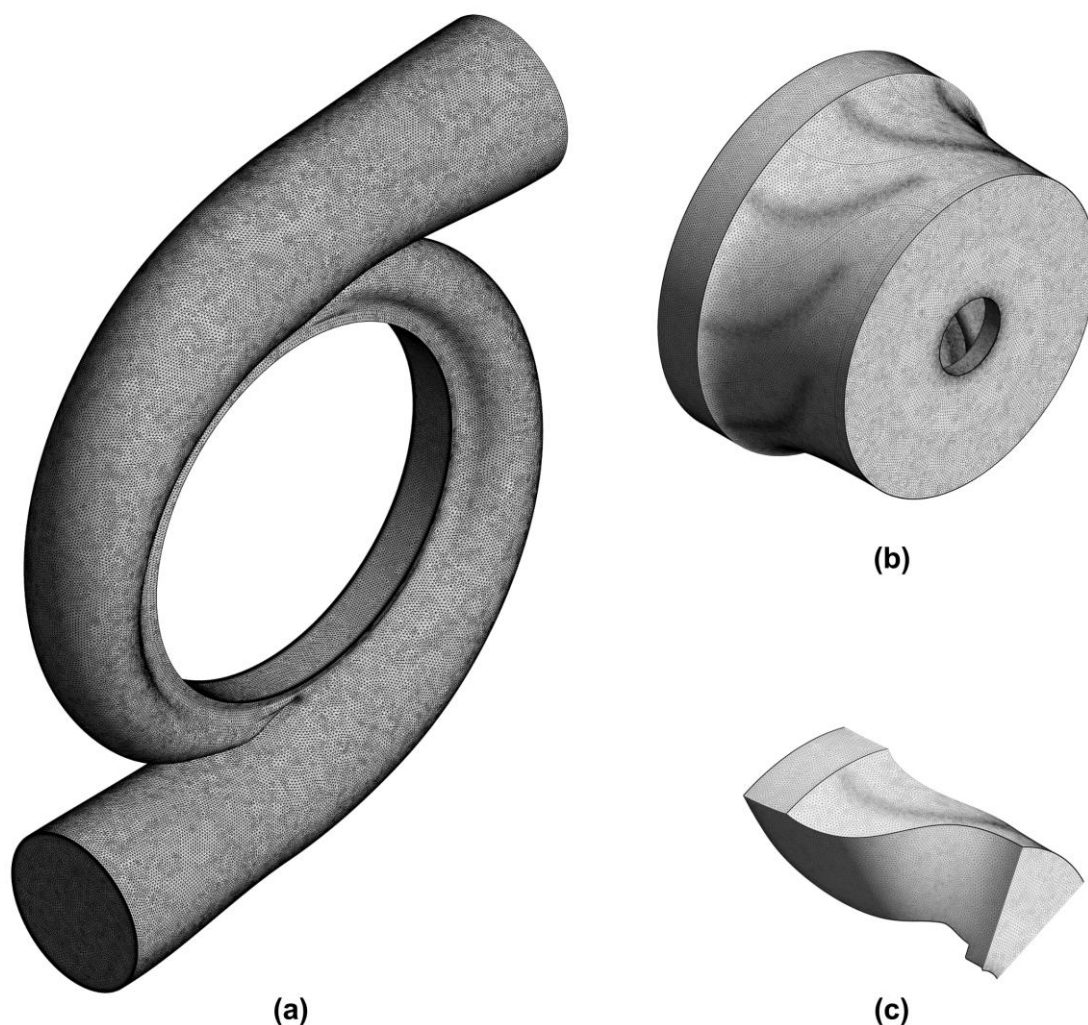
Figure 4.8   Selected (a) volute and rotor meshes for the (b) FR and (c) MP calculations.

Although mesh convergence was achieved, it is worth pointing out that only a tetrahedral mesh was tested. This type of mesh allows for extreme flexibility when discretizing very complex geometries, however, non-orthogonality is inherently an issue: ideally, its value should be as close as possible to zero, since the diffusion term is evaluated along the line connecting the cells' centers and any non-orthogonality between two adjacent cells would deteriorate accuracy. Indeed, diffusion is dependent on the type of mesh and a second order of accuracy is achieved on uniform and orthogonal meshes. In case of a non-orthogonal mesh, a correction term is added to grant a second order of accuracy. Therefore, it is worth pointing out that, in the present case, the use of a flow-oriented mesh of hexahedral elements might lead to a similar (or greater) level of accuracy with a reduced computational cost, and represents an interesting future development of the present research work.

As anticipated in the previous section, a transient (TRN) model was also developed for the study of partial admission operation. The TRN model's boundaries are exactly the same as the steady-state, partial admission, FR model (Figure 4.5), with the exception that the coupling between the volute and the rotor domains is handled by a sliding mesh approach. A 2° angular timestep was selected for the TRN calculations, resulting in a timestep of the order of 10^{-5} s, moreover, at least 10 rotor revolutions were necessary for cyclic convergence. Figure 4.9 depicts the sliding mesh approach that was adopted at the volute-rotor interface of the TRN model: specifically, one node of the rotor side mesh is highlighted (in green) to better appreciate mesh rotation.
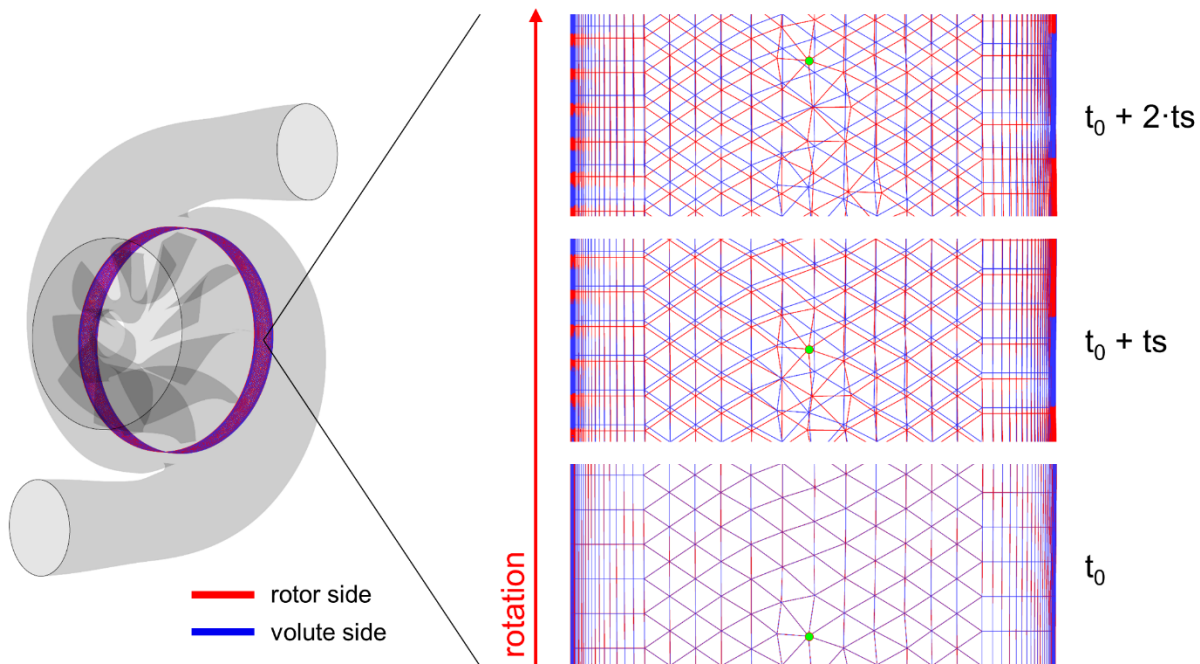
Figure 4.9   Mesh of the volute-rotor interface of the TRN model, over 3 consecutive timesteps.

When the mesh nodes of the two sides of the interface are not matching, the solver employs a General Grid Interface (GGI) connection. In the case of a transient rotor-stator interface, the current relative position of each side of the sliding interface is first computed at the start of each timestep. Then, the frame change model proceeds by discretizing the surface fluxes along each side of the interface, in terms of nodal dependent variables and in terms of control surface equations and control surface variables. Each interface surface flow is discretized using the standard flux discretization approach, however, both the nodal dependent variables on the local side of the interface and the control surface variables on the interface region are employed. Balance equations within the interface region are generated for the interface variables from the flux contributions from both sides of the interface. These equations are called "control surface equations" because they enforce balance over a given surface area: strict conservation is maintained across the interface, for all fluxes of all equations.

In order to directly compare the transient results against the ones of the steady-state FR and MP models, the same mesh of the FR model was used in the TRN calculations, although literature

findings show that the meshes that are typically employed in transient analyses for similar applications are 1/10[70] to 1/50[71] the size of the selected one. Unsurprisingly, the computational cost of a TRN calculation is extremely high and, as anticipated, this analysis was limited to a single operating point.

4.3 - Results

4.3.1 - Sensitivity analysis on the turbine wheel's position

In the development of the steady-state Frozen Rotor model, the turbine wheel is implemented as a fluid domain which is locked in a certain angular position. Unlike the sliding mesh modelling approach, the FR approach keeps the rotating domain in a fixed ("frozen") position: it is important to assess the influence of the wheel's angular position on the calculated performance parameters. In case of relevant variations with respect to the wheel's position, calculation results may be averaged over the different positions. Alternatively, one may establish which position is the most suitable for steady-state simulations by running a preliminary sensitivity analysis: for example, Walkingshaw et al. (2016) performed a preliminary transient simulation to find correlation between certain performance parameters and the wheel's angular position [73]. In the present study, a sensitivity analysis on the wheel's angular position was carried out by means of steady-state analyses. Figure 4.10 shows two of the angular positions that were tested.

(a)   **(b)**
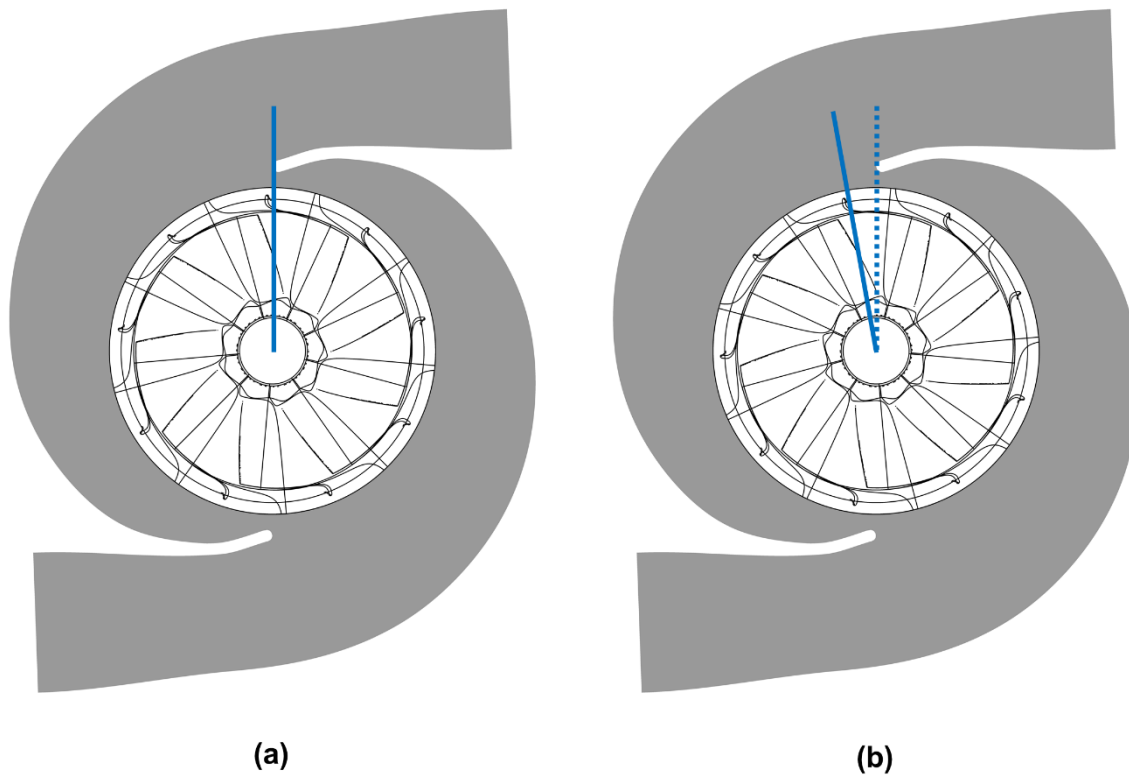
Figure 4.10   Wheel's geometry configurations, namely (a) FR-A and (b) FR-B.

The two configurations named FR-A and FR-B differ by 10 degrees rotation. In the full admission case, this angular span is enough to assess the clocking effects due to the blade position with respect to the volute's tongue. In the partial admission case, however, it was necessary to test additional configurations, due to the "asymmetrical" operating conditions. Specifically, FR-C and FR-D refer to a 20° and 30° rotation, respectively. Figure 4.11 shows the results of this sensitivity analysis in terms of normalized MFP, while Figure 4.12 shows the same comparison for the normalized total-to-static isentropic efficiency.
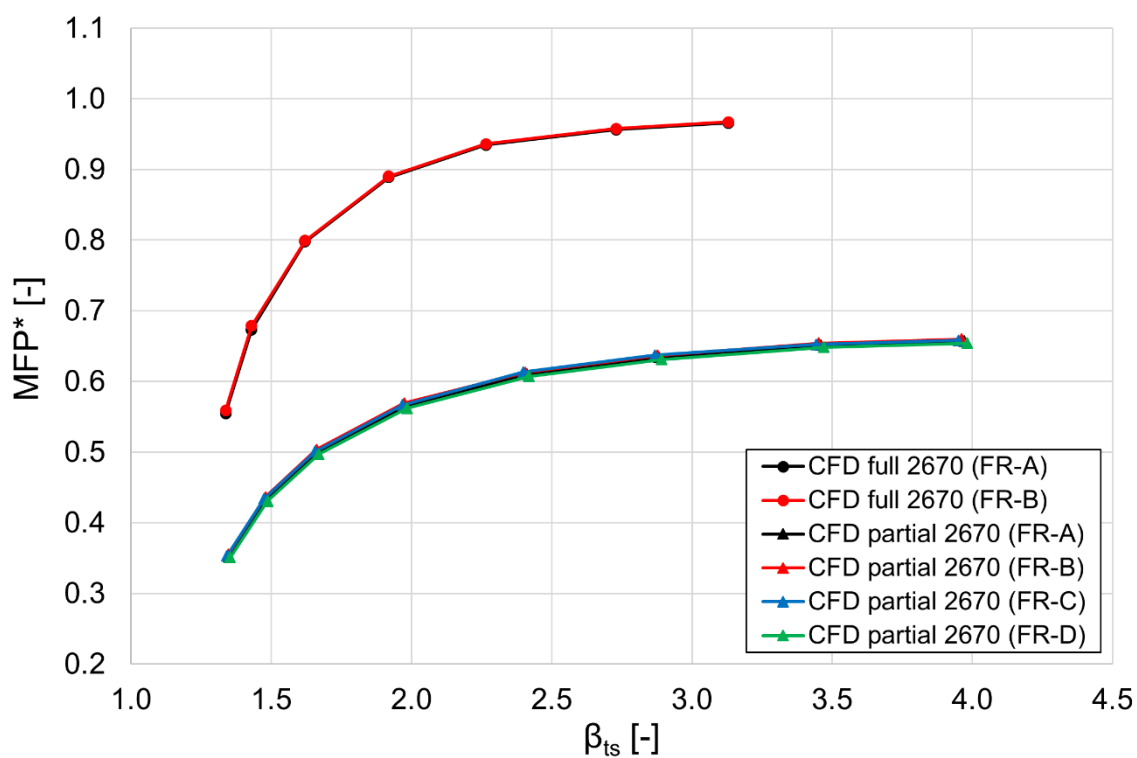
Figure 4.11 Wheel's position sensitivity analysis results for the FR approach: mass flow parameter.
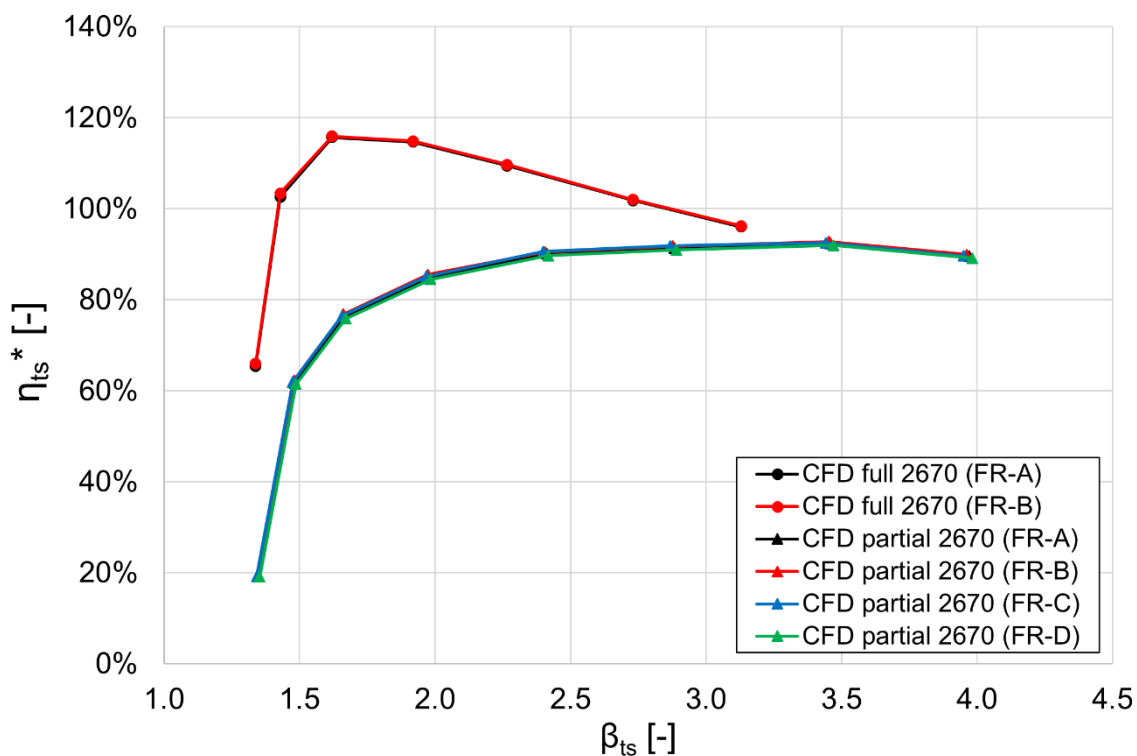
Figure 4.12 Wheel's position sensitivity analysis results for the FR approach: isentropic efficiency.

It is apparent that, for each speedline, there is overlap between the curves that represent the different configurations, suggesting that the mass flow parameter is not significantly sensitive to

the wheel's angular position. A similar behavior can be observed for the isentropic efficiency. One may notice that the discrepancy between the configurations is slightly higher at lower-to-mid expansion ratios: the relative difference in MFP, however, ranges from 0.2% at the highest expansion ratio to 0.8% at the lowest expansion ratio, at least in the full admission case. Regarding partial admission, discrepancy between the curves is, as expected, higher than the full admission case: the maximum discrepancy, considering the highest and the lowest calculated MFP, is about 1.3%. Given the negligible discrepancy in the full admission case and the fact that the FR-A configuration stands in the middle ground among the other partial admission curves, the FR-A configuration was used for the rest of the activity, and simply referred to as "FR" in the following plots.

4.3.2 - Full admission operation

Initially, the assessment of the steady-state models capabilities was carried out under full admission operation. As anticipated, both the Frozen Rotor (FR) and Mixing Plane (MP) simulations were compared against experimental data from the hot gas test bench. Figure 4.13 and Figure 4.14 shows the calculated performance maps.
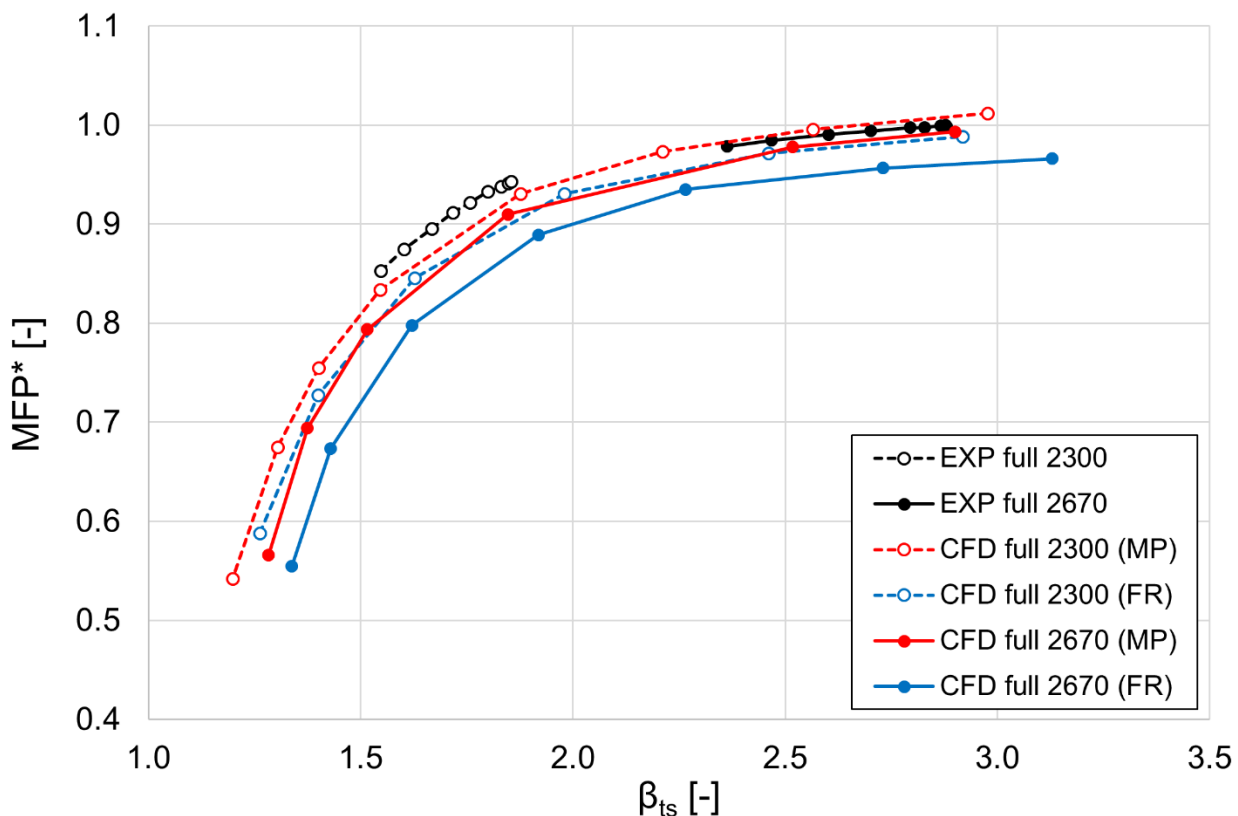
Figure 4.13   Full admission analysis results: MFP.
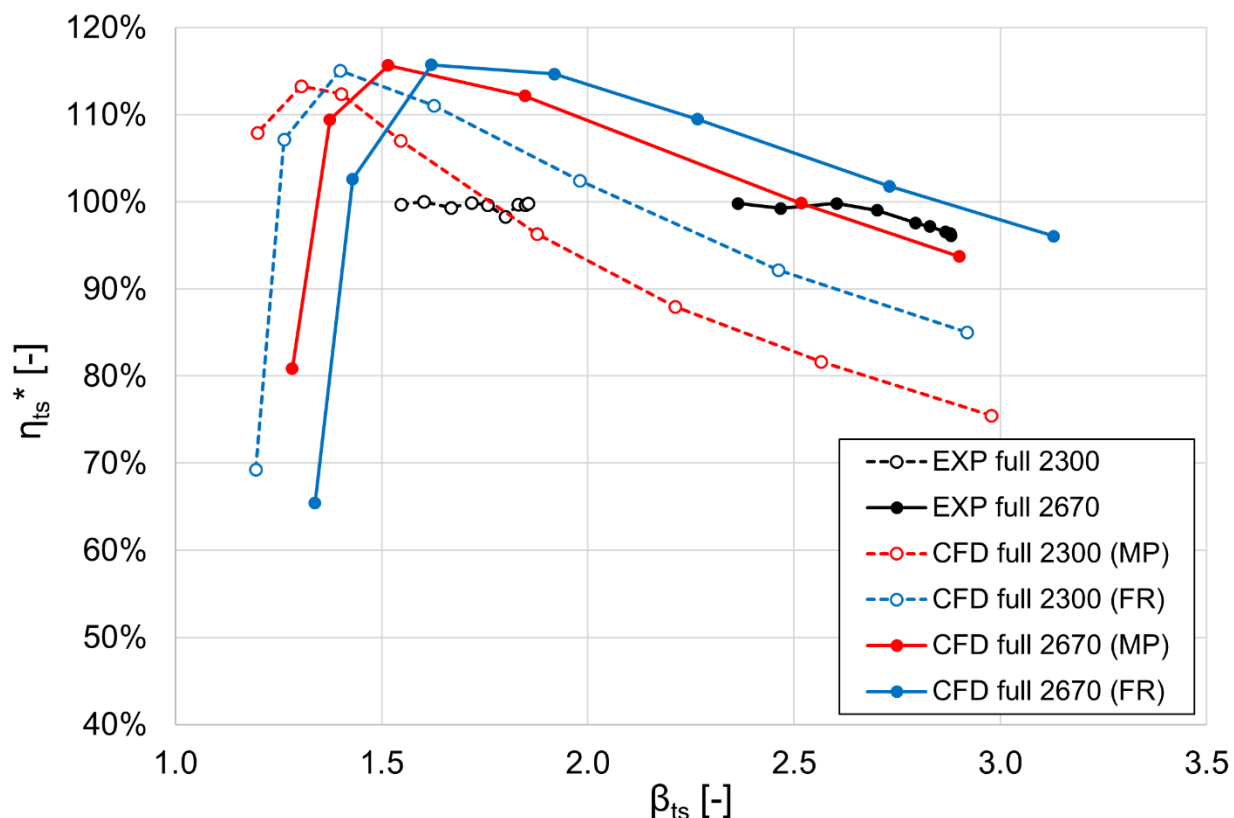
Figure 4.14   Full admission analysis results: isentropic efficiency.

It is worth reminding that, in the 3D CFD calculations, the total-to-static expansion ratio is set by the boundary conditions, while mass flow is a result of the calculations. By looking at the curves in Figure 4.13, it is apparent that calculated MFP is overall lower than the measured one. Still, the speedlines obtained with the Mixing Plane approach show maximum relative errors of roughly 2% with respect to experimental data, indicating that the steady-state MP approach correctly predicts MFP trends in full admission operation. On the other hand, the Frozen Rotor approach shows higher discrepancy with experimental data: relative error ranges from 3% to 4%, indicating reduced prediction capability with respect to the MP approach. As apparent from Figure 4.14, discrepancies are higher for the isentropic efficiency curves, still, the superior prediction capability of the MP approach seems confirmed. Indeed, although neither model achieves a high level of accuracy in comparison with the available experimental data, the FR approach tends to calculate higher efficiency values at medium and high expansion ratios with respect to the MP model. Based upon these results, a steady-state model that employs a Mixing Plane approach represents the best solution. However, if the scope of the analysis is to investigate the flow structures inside the turbine, issues arise. Figure 4.15 shows contour plots of normalized total pressure (P_0^n) on a radial plane that cuts the wheel at the leading edge's midspan: total pressure was normalized against the top inlet total pressure.

P0n [-]
1.00
0.97
0.93
0.89
0.86
0.82
0.79
0.75
0.72
0.69
0.65

MP

FR
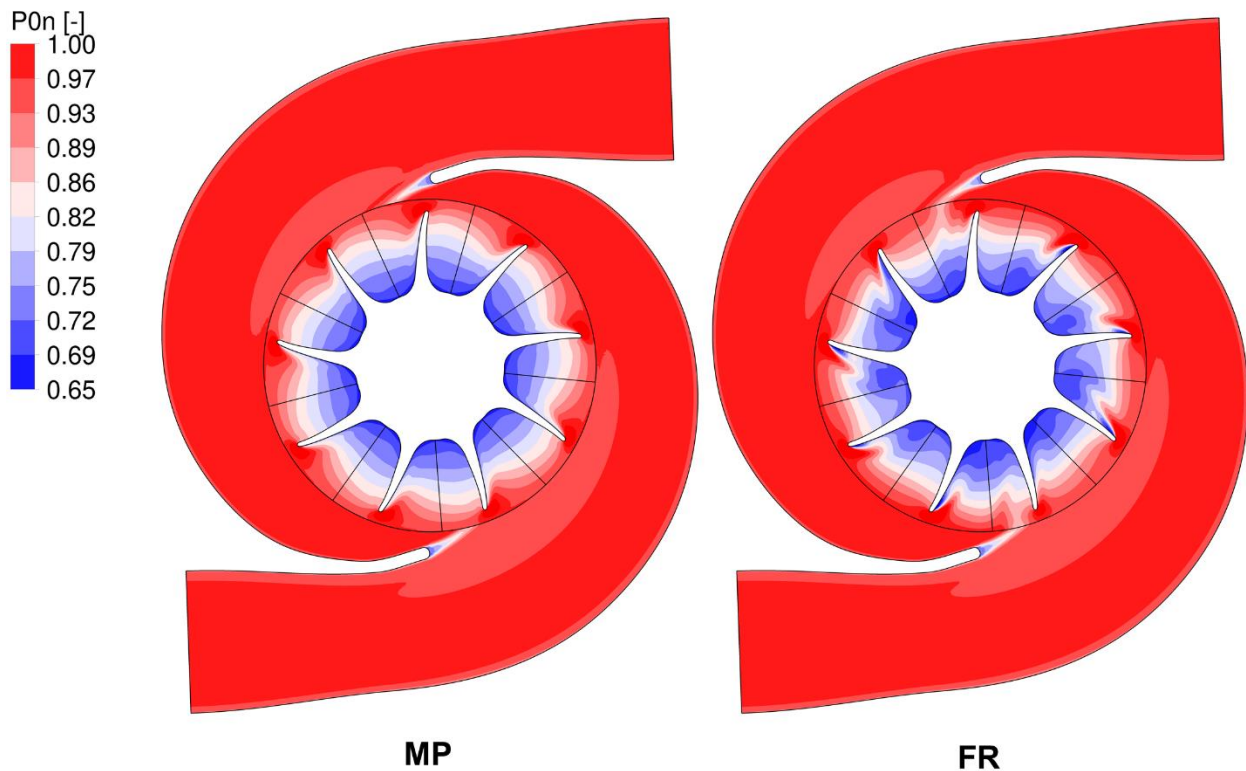
Figure 4.15   Normalized total pressure contour plots for MP and FR models (full admission).

First of all, it is worth pointing out that the results from the MP calculation are actually limited to a single blade passage, but, for the sake of a clearer comparison against the FR calculation, MP data has been circumferentially repeated during post-processing to show the full wheel's flow field. The underlying mechanisms that define the MP and FR approaches are apparent from the flow field visualizations of Figure 4.15. In the case of a MP interface local flow structures like the wakes at the volute's tongues do not directly propagate beyond the volute-rotor interface, instead, their effect is averaged along the interface and passed through the rotor domain. Indeed, the flow within the blade passage is periodic. On the contrary, with a FR interface, the flow visualization clearly shows how the wakes at the volute's tongues enter the rotor domain and interfere with the local flow structures inside the blade passages. Additionally, wakes are clearly visible at the blades' leading edge. The MP model is meant to model the effects of the wheel's rotation by performing a circumferential average of the quantities at the interface: while this operation may enhance calculation accuracy, the resulting flow field is physically inconsistent. The flow field resulting from a FR approach may seem realistic, as it represents a sort of instantaneous visualization of the actual flow field; however, it is worth pointing out that FR modelling does not account for flow inertia, leading to, again, a physically inconsistent flow field.

The computational efficiency of the FR approach is higher than the one of the MP approach thanks to the lack of the circumferential averaging iteration loops. Notwithstanding this, the MP approach allows to employ cyclic boundaries to model only one blade passage instead of the full wheel. As a consequence, mesh size is reduced and so is the overall computational time: the

calculation time of the performed steady-state MP simulations is 27% lower than the one of FR calculations.

4.3.3 - Partial admission operation

The prediction capability of the developed steady-state MP and FR models was also assessed for partial admission operation, although a steady-state approach may not be adequate to model this condition. When the turbine is fed by two steady but unequal flows, a given blade passage will be subject to a change in pressure and velocity as it rotates from one 180° sector to the next. This change becomes increasingly abrupt as the pressure difference between the two entries increases, up to the extreme case of partial admission. In this case, the time for the fluid to travel through the rotor passage gains importance [71]. If the fluid travels very quickly relative to the wheel's rotation, the flow will be rapidly established and hold little "memory" of the fluid conditions in the previous sector. However, if the fluid requires a significant amount of the 180° rotation to travel through the rotor wheel, the flow in each blade passage may never have the opportunity to establish itself to an optimal condition. In the former case, the flow in the passage can be assumed to be quasi-steady, and fully unsteady in the latter. It is therefore significant how quickly the flow will be convected through the rotor passage: this can be quantified by the ratio of the rotor crossing time to the time the time taken for the turbine wheel to rotate half of a revolution. Indeed, this fraction is actually a measure of the Strouhal number (St) associated with the pulses that are produced as the rotor is periodically fed with two different flows. Figure 4.16 shows the calculated Strouhal number for different full admission operating points.
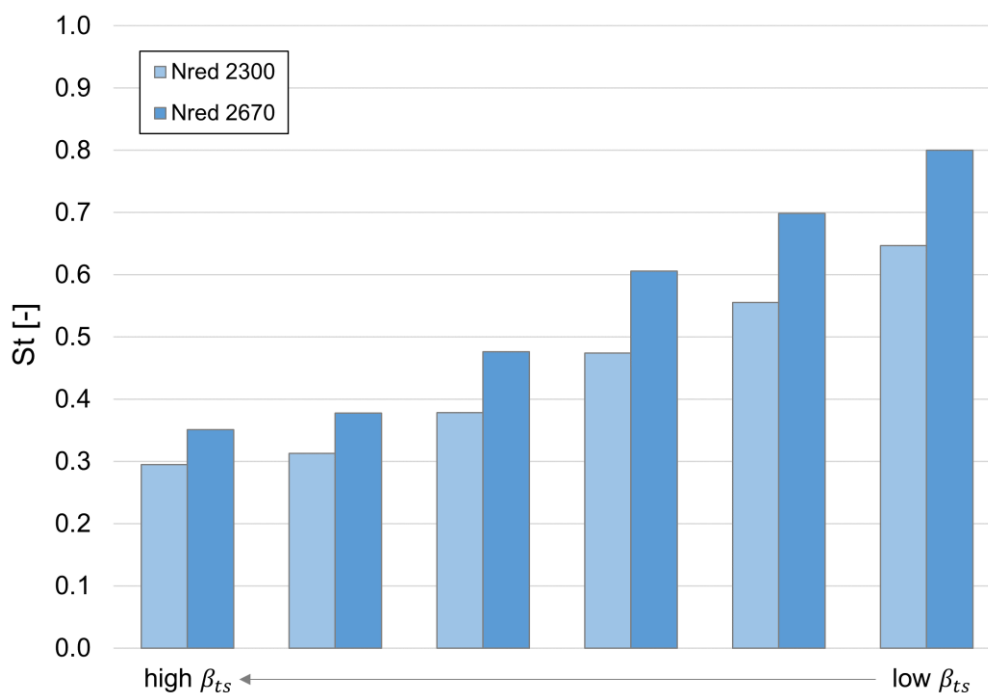
Figure 4.16   Strouhal number for full admission operating points.

Two trends can be highlighted. Firstly, the higher the rotation speed, the higher the Strouhal number, as defined above. Secondly, the Strouhal number decreases at higher expansion ratio, because higher flow velocities reduce the time taken for the flow to convect through the blade passage. In the present case study, St never surpasses unity, yet, the level of unsteadiness becomes significant under some operating conditions. The results of the steady-state FR and MP calculations were compared against experimental data, together with the results of the transient (TRN) calculation that was carried out for one operating point. Cyclic convergence was obtained after 10 wheel's revolutions, however, TRN calculation results refer to 15 wheel's revolutions: they are presented with an error bar that describes oscillations around the quantitiy's mean value over the last 5 revolutions. Figure 4.17 and Figure 4.18 show the comparison with experimental data for partial admission operation.
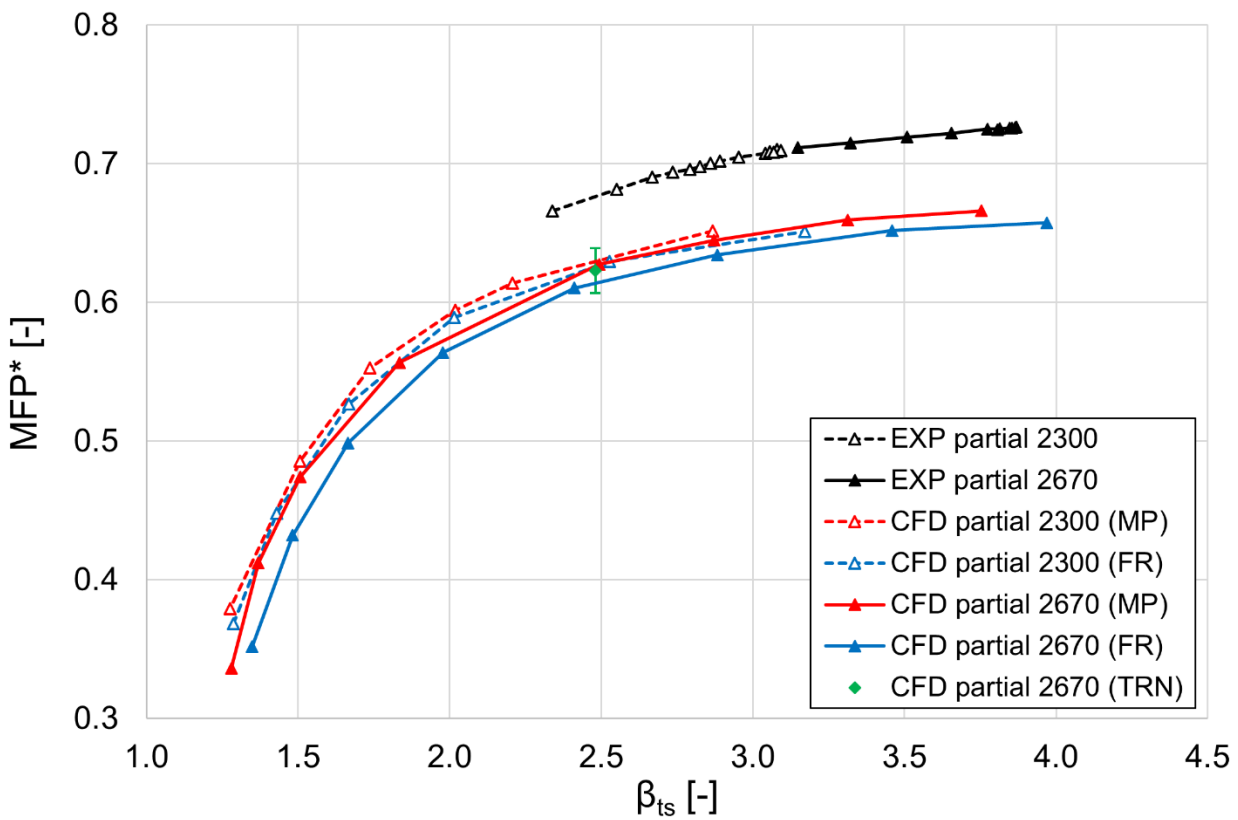
Figure 4.17   Partial admission analysis results: MFP.
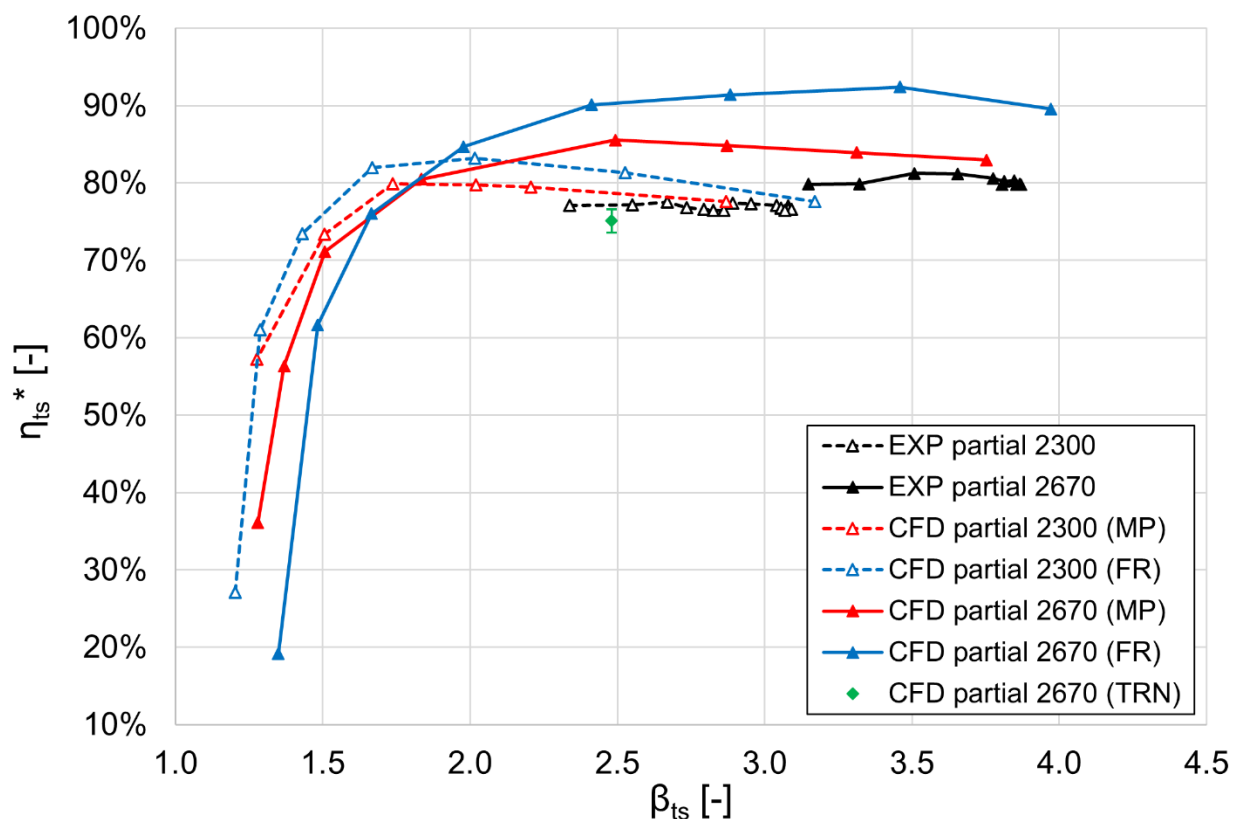
Figure 4.18   Partial admission analysis results: isentropic efficiency.

By looking at the normalized MFP speedlines, it is apparent that agreement with experimental data in partial admission operation is not as good as the one in full admission. The MP model still represents the most accurate steady-state approach, although discrepancy with experimental MFP data ranges from 6% to 7%. The mass flow calculated by the FR approach is generally lower than the one obtained with the MP model, therefore discrepancy with experimental data increases for the FR approach, reaching almost 10%. While the lower prediction capability of the steady-state calculations might be attributable to adopting the quasi-steady assumption to model a significantly unsteady phenomenon, it is worth pointing out that the TRN analysis returns similar results as the ones of the steady-state approaches. Indeed, the TRN point shows good matching with the corresponding MP speedline, moreover, mass flow oscillations cover the variability range of every steady-state curve. Moving from these results, it can be hypothesized that discrepancy with MFP experimental data is not attributable to the unsteadiness of the partial admission operation. However, one must also consider that the agreement between TRN and the steady-state models might be caused by the significant non-orthogonality of the tetrahedra-based mesh that was used: indeed, pressure and velocity gradients might be smoothed out and calculation accuracy might be inferior with respect to the one achievable with a hexahedra-based mesh. Still, some discrepancy between the TRN and the steady-state models can be observed in Figure 4.18. The values of isentropic efficiency obtained through the steady-state MP and FR approaches are roughly 10 and 15 percentage points higher, respectively, than the one calculated by the TRN

model. The reason for such relevant discrepancy can be found by investigating the temperature field resulting from the simulations, shown in Figure 4.19 and Figure 4.20 . Again, for confidentiality issues, temperature was normalized against the turbine inlet value.
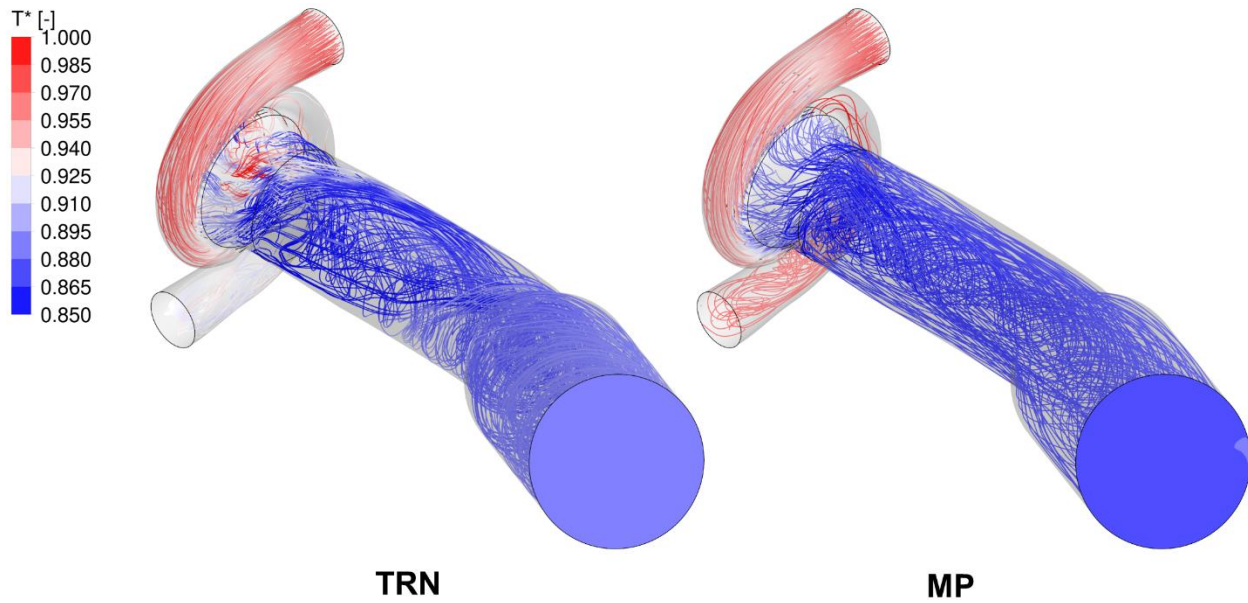
Figure 4.19   Normalized temperature field: TRN vs MP.
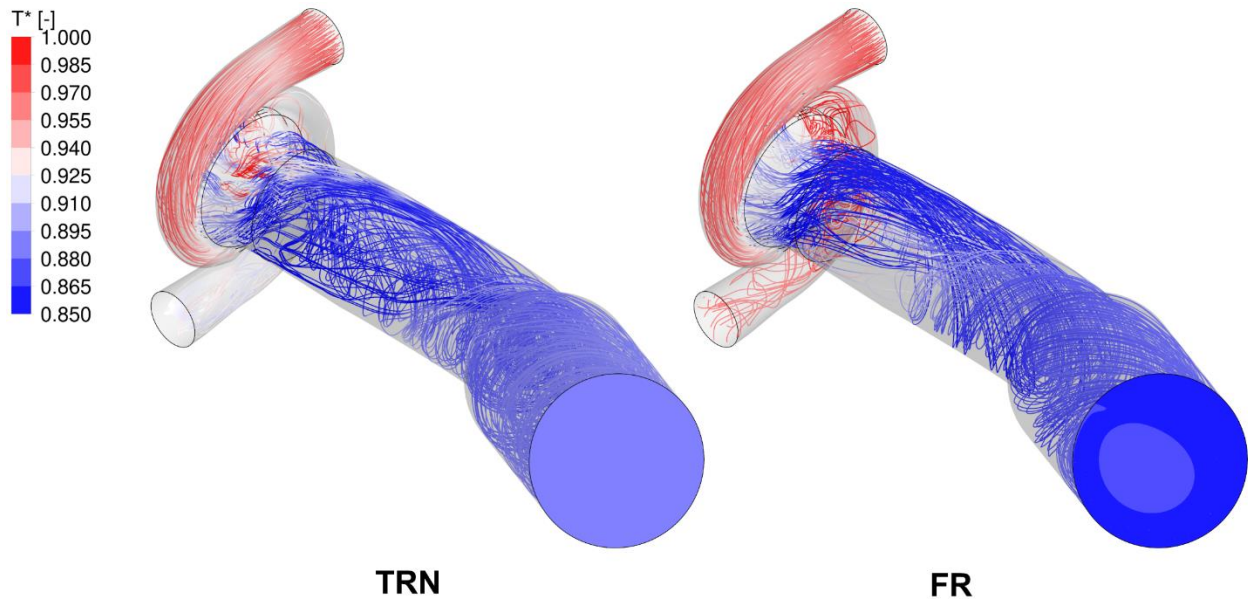
Figure 4.20   Normalized temperature field: TRN vs FR.

By looking at the figures above, it is clear that the TRN model returns the highest outlet temperature of all the analyzed approaches: this directly relates to the discrepancies of isentropic efficiency. The above-discussed trends are confirmed by the fact that the FR model returns lower outlet temperature with respect to the MP model. Furthermore, it is unsurprising that, by looking at Figure 4.19 and Figure 4.20, the only physically consistent flow field appears to be the one

calculated with the TRN approach. Indeed, in the MP simulation, the flow exiting the rotor does not seem affected by the unequal admission condition, showing a rather orderly swirling motion that originates from the circumferential averaging at the rotor-outlet interface upstream. On the contrary, the flow of the FR model is quite similar to the one of the TRN calculation, but the expansion of the flow within the rotor is not accurately calculated, as suggested by the significantly lower flow temperature at the rotor exit.

As already discussed regarding the full admission case, the inaccuracies of the calculated flow field indeed represent the most critical aspect of the two steady-state approaches. Figure 4.21 shows contour plots of normalized total pressure (P_0^n) on a radial plane that cuts the wheel at the leading edge's midspan, for FR and MP calculations.
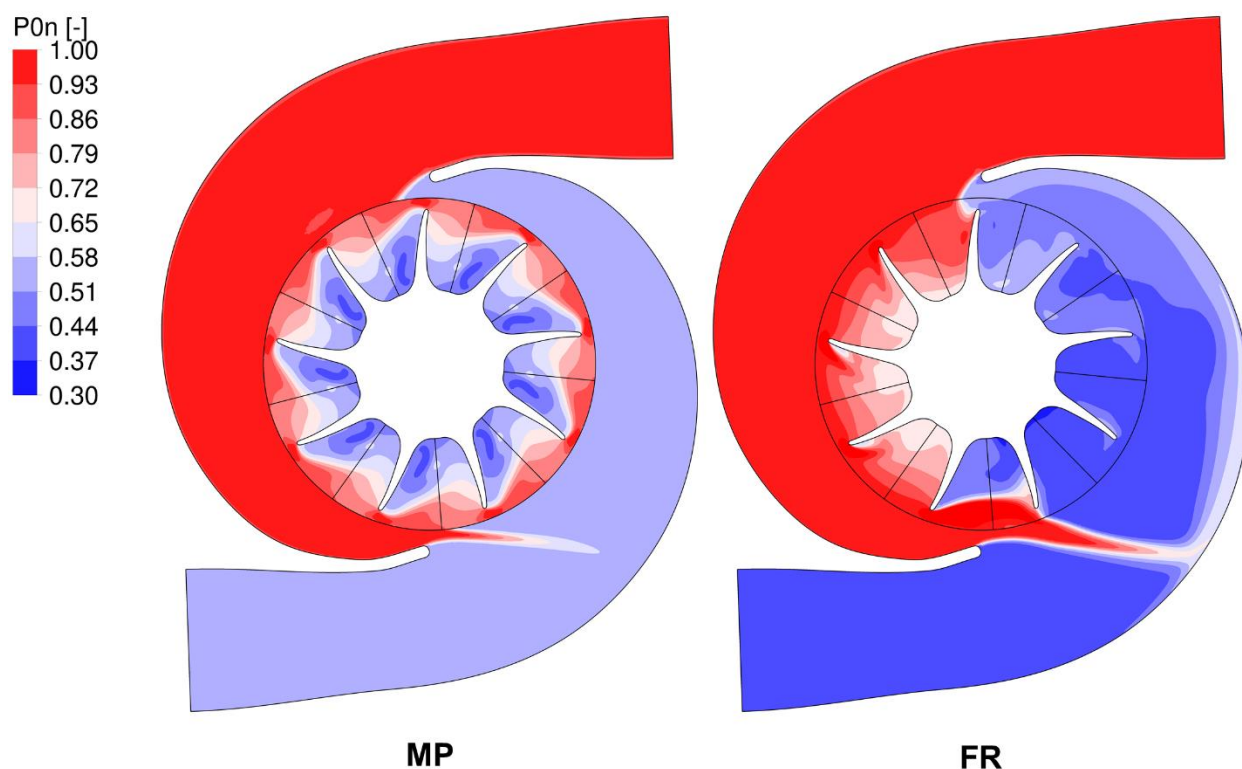
Figure 4.21   Normalized total pressure contour plots for MP and FR models (partial admission).

By looking at the MP model results, it is apparent that the flow within the rotor domain is periodic. Considering the partial admission condition, the flow field obtained with the Mixing Plane approach is, again, physically inconsistent. While some similarities withe the FR flow field could be observed under full admission operation (Figure 4.15), major discrepancies are apparent in case of partial admission, where the FR approach returns a more realistic flow field. Figure 4.22 shows the same contour plots for the transient (TRN) approach, over one wheel's revolution, while Figure 4.23 shows a direct comparison against the FR approach.
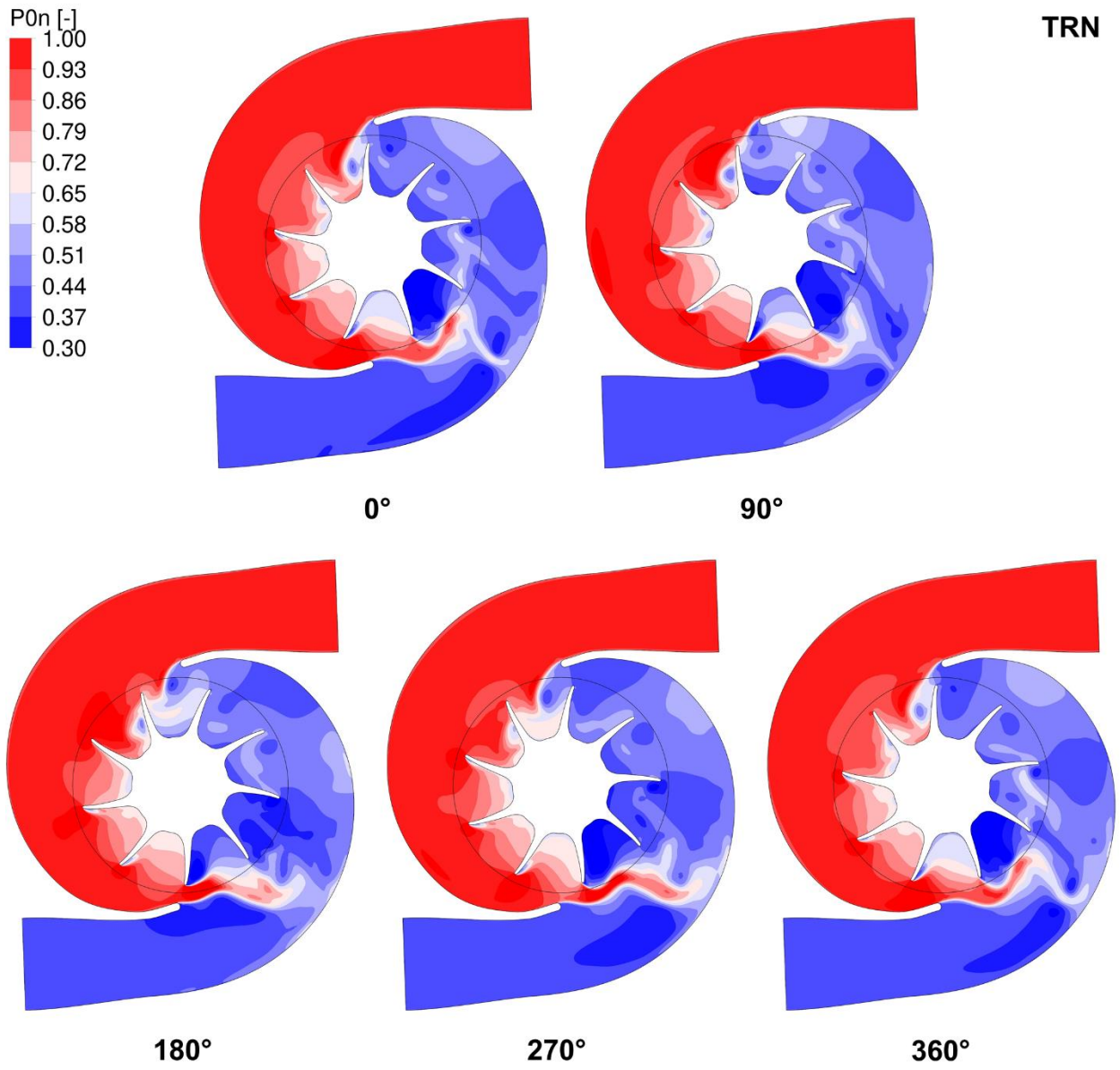
Figure 4.22   Normalized total pressure contour plots at different timesteps of the TRN calculation.
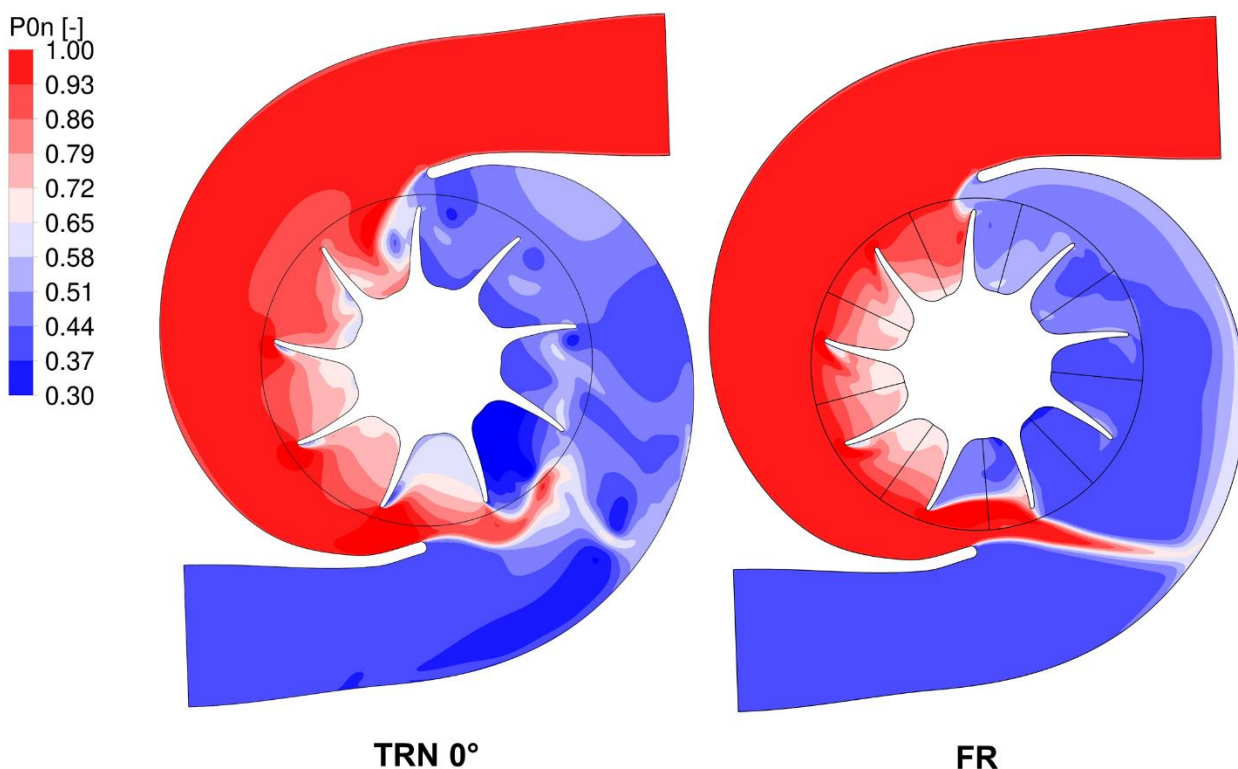
Figure 4.23   Normalized total pressure contour plots for TRN and FR models (partial admission).

It is apparent that the flow field resembles the one of the FR calculation: this was expected and it's not surprising that FR results are typically employed to initialize transient calculations. However, the main criticality of the FR rotor approach is that flow inertia is not taken into account, on the contrary, a TRN calculation timestep always carries the effects of the flow field from the previous timestep. This is apparent in Figure 4.22, where the evolving flow field can be appreciated thanks to the time-marching solution, and in Figure 4.23, with special focus on the bottom tongue area. In case of unequal admission, flow interaction in the interspace between the scroll and the rotor is not negligible, especially if there is a large pressure difference between the inlets: in the present case, such interaction appears as a jet coming from the supplied 180° sector. According to the TRN model, this jet is continuosly distorted by the interactions with the flow inside the moving blade passages. On the contrary, the FR model shows a high-penetration jet that impinges on the unsupplied scroll and, from there, reaches the top tongue. This confirms that the flow field obtained by means of a FR approach is physically inconsistent. Unlike the MP approach, however, it is apparent that a FR model can give some insight on the flow structures inside the machine. As shown in Figure 4.21, the MP model is also able to capture the jet at the bottom scroll, but the jet structure itself depends on the volute-rotor interface location, which is arbitrarily set during pre-processing.

As a final remark, the results of the study show that the Mixing Plane (MP) approach has the greatest MFP prediction capability of the two steady-state models that were tested. Even under partial admission operation, the MP approach is preferrable to the FR one when evaluating the

turbine's performance, but one must always bear in mind that the flow field resulting from a MP calculation is not representative of the real one. On the other hand, the FR approach is able to calculate a flow field that, although still physically inconsistent due to the quasi-steady modelling assumption, resembles more the actual one. If the main objective of the analysis is to investigate the turbine's flow field under unequal admission conditions, then a transient analysis is definitely recommended, although it has been shown that the mass flow calculated with a transient approach is similar to the one obtained by steady-state calculations. Ultimately, the choice between the modelling approach, when steady-state modelling is a viable option, should be made based on the current goals and available computational resources. Table 4.5 summarizes the calculation time of the developed models, normalized against the FR time.

Modelling approach	Steady-state (FR)	Steady-state (MP)	Transient (TRN)
Normalized calculation time	100%	73%	2000%

Table 4.5   Normalized calculation time of the analyzed modelling approaches.

The computational effort required by the TRN calculation is significant, but it is worth pointing out that, in the present study, the same mesh of the steady-state calculations was employed. This was done with the aim of performing a direct comparison with steady-state calculations. Typically, however, transient calculations involve a low mesh density precisely to contain their computational cost, which is inherently high.

5 - Thermo-structural analysis

5.1 - Case study

The test case of the present study consists in the turbine wheel of a high-performance turbocharger for automotive application. Figure 5.1 shows the whole turbine stage: the turbine volute is of single-entry type and the bypass flow is controlled by a wastegate valve.

Figure 5.1   3D model of the analyzed test case.

The present test case undergoes high temperature exhaust gas flow and mostly operates in unsteady conditions, therefore, it represents an interesting case study for a thermo-mechanical analysis. The available experimental data for the test case consists in the following quantities: the volute inlet total pressure and temperature, the turbine outlet static pressure, the volute inlet mass flow and the wastegate opening angle. As will thoroughly be presented in the following paragraphs, these quantities were employed as boundary conditions for the fluid dynamics numerical analyses. Additionally, the turbine blade's surface temperature near the trailing edge was obtained by means of infrared measurements, as shown in Figure 5.2. Experimental measurements in Point A and Point B were then compared to calculated temperature in order to validate the developed CHT setup.
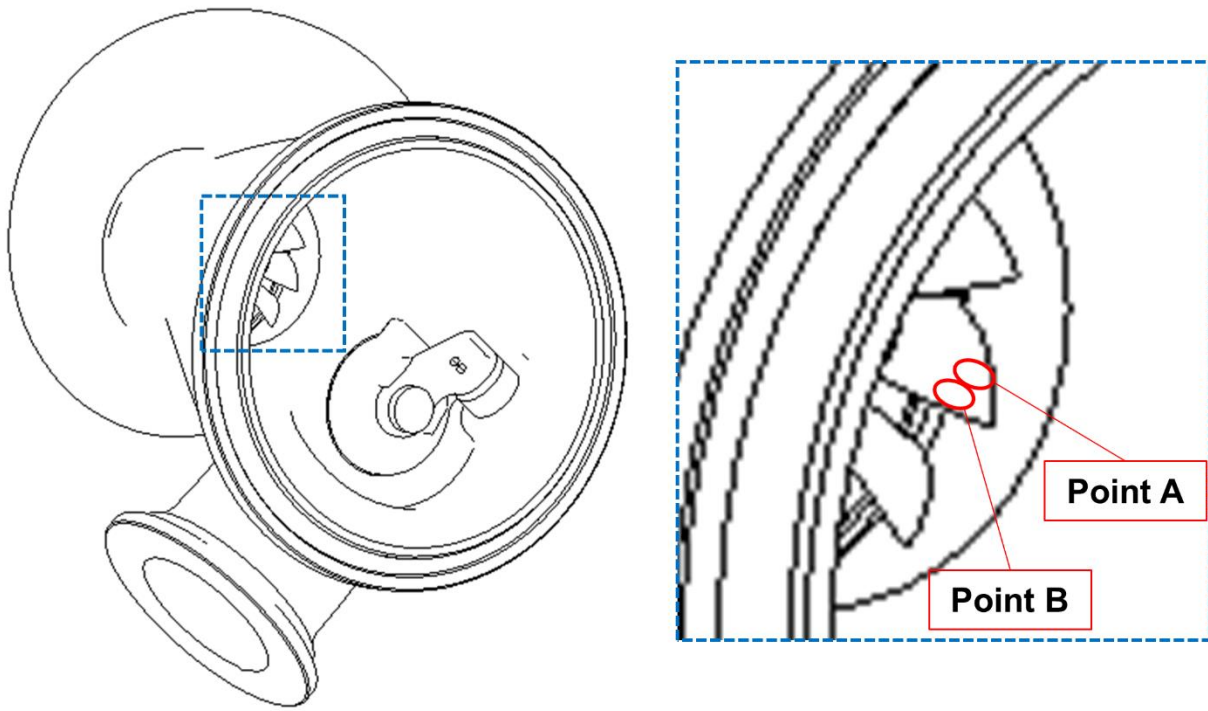
Figure 5.2   Temperature measurement locations, namely Point A and Point B, on the turbine blades' surface near the trailing edge.

5.2 - Methods

5.2.1 - Workflow overview

The goal of the present activity is the definition of a high-fidelity three-dimensional numerical methodology for simulating the transient thermo-structural response of a turbine wheel under an engine transient maneuver. The main assumption at the basis of the proposed approach is that the characteristic timescales of the thermal response of the solid components are several orders of magnitude larger than the fluid-dynamic timescales of the turbocharger itself. Indeed, during a fast change of the engine operating conditions, the response of the fluid-dynamic circuit has a duration in the order of 10^0 s, the subsequent thermal response of the wheel's body has a duration in the order of 10^1 s, while the rotating period of the turbine is in the order of 10^{-3} s. Table 5.1 summarizes the characteristic timescales of the different phenomena.

	Timescale [s]	Relative timescale [orders of magnitude]
Solid thermal response	10^1	0
Fluid-dynamic response	10^0	1
Rotor revolution	10^{-3}	4

Table 5.1   Characteristic timescales of different transient phenomena.

Therefore, the phenomenon of temperature variation of the turbine due to a engine transient maneuver can be seen as a quasi-steady phenomenon from the point of view of the fluid-dynamics of the turbine itself, being roughly four orders of magnitude larger. This allows performing transient thermo-structural analyses on a turbine wheel without relying on transient CHT calculations, which, as previously stated, require major computational effort. To this end, an alternative, cost-effective approach was employed: details on this method will be presented in the following paragraphs, while an overview on the adopted methodology is here provided. Figure 5.3 schematically shows the workflow of the thermo-structural analysis that was carried out.
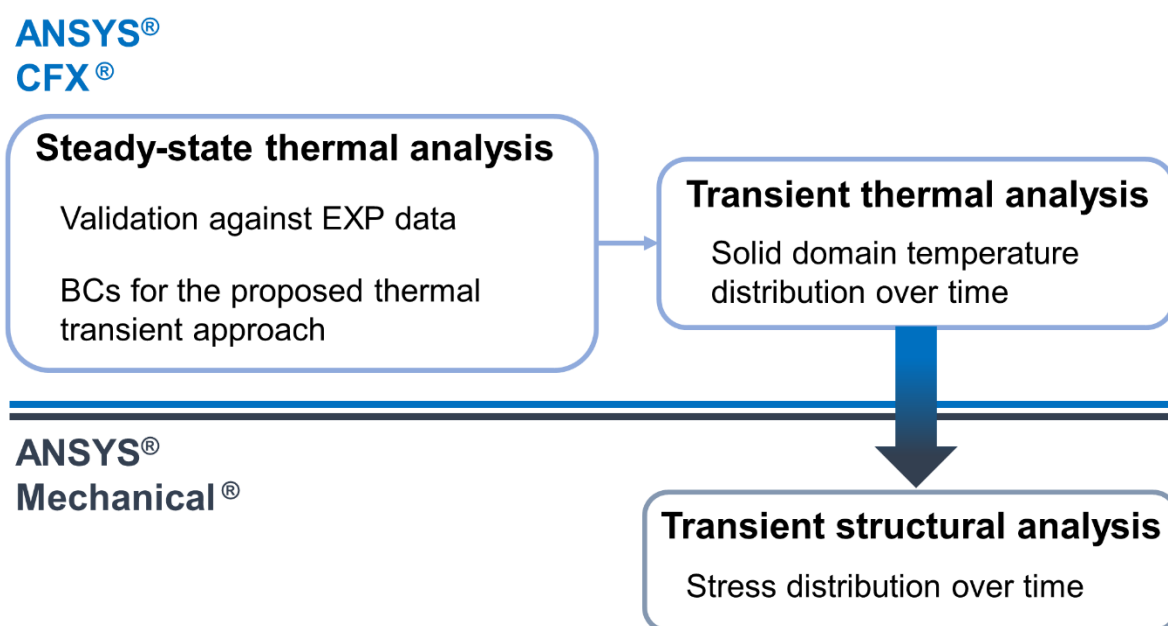
Figure 5.3   Workflow of the thermo-structural analysis that was carried out.

Generally speaking, any decoupled transient thermo-structural analysis involves two steps: first, the time-evolving temperature distribution of the solid part is obtained; lastly, the transient structural solver performs the structural analysis by treating the previously-obtained temperature distribution as a time-varying thermal load. The approach that was used for this activity covers the first step: whereas a transient CHT calculation would represent the most straightforward approach, steady-state calculations are performed in order to set up a thermal transient analysis of the solid domain only. The numerical setup of the steady-state CHT analyses was validated against experimental data, improving the robustness of the whole workflow.

5.2.2 - Steady-state 3D CFD/CHT setup

The commercial code ANSYS® CFX® was used for the numerical analysis of the turbine stage. The selection of this software, very common for these applications, is due to its great flexibility in

handling complex geometries. A steady-state RANS approach, using a pressure-based formulation of the solver, was adopted. The shear stress transport (SST) turbulence model [44] was employed, together with an automatic near-wall treatment that allows the solver to overcome mesh resolution requirements by gradually switching between wall functions treatment and low-Re formulations [92]. A high resolution, second order upwind scheme was used for the spatial discretization of the RANS equations.

Figure 5.4 shows the CFD model's geometry and its boundaries.
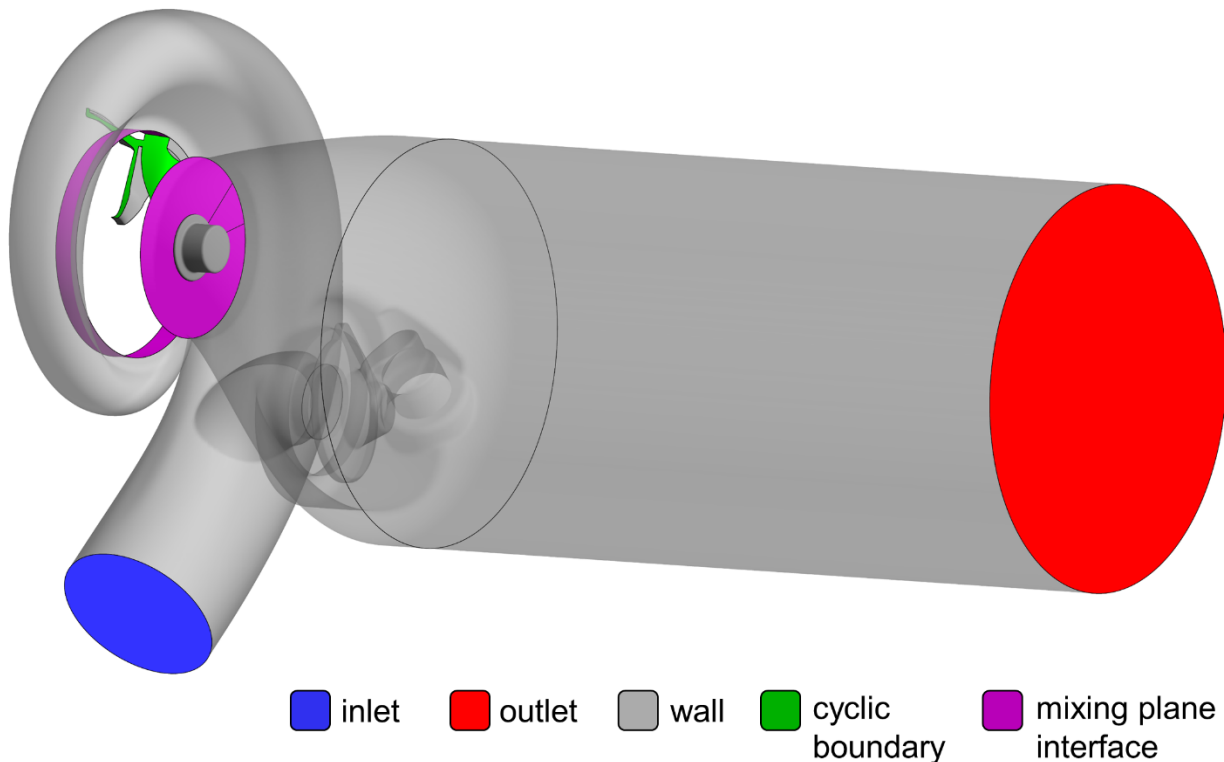
Figure 5.4   Model of the turbine stage for the 3D CFD calculations.

The CFD computational domain consists in three fluid sub-domains: the turbine volute domain, the rotor domain and the outlet domain, which is extended in the axial direction to improve calculation stability. The outlet domain also features the wastegate valve and communicates with the volute domain through an internal interface, for improved modelling accuracy. For the rotor domain, a single blade passage with cyclic boundaries was employed: this allows to limit the number of mesh elements, minimizing the computational effort while keeping an adequate level of accuracy for the steady-state calculations [93]. The flow inside the blade passage of the wheel is solved in the relative frame of reference: two mixing plane rotor-stator interfaces were employed, one placed between the volute and the rotor domain, and the other between the rotor the outlet domain. It is worth pointing out that the rotor sub-domain also features the cavity between the wheel's backdisc and the housing's heat shield, as shown in Figure 5.5. The backdisc cavity includes an additional outlet boundary for the modelling of the blow-by leakage flow.
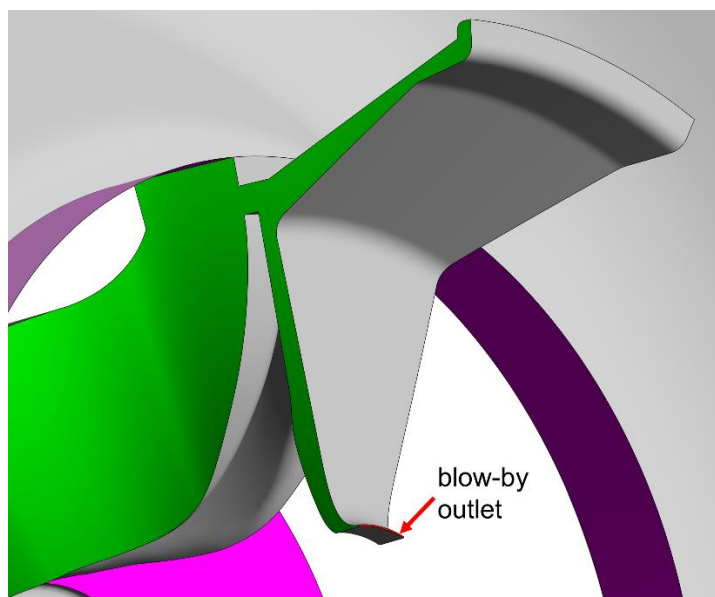
Figure 5.5   Detail view of the rotor fluid domain's backdisc cavity and blow-by outlet.

The developed CHT model shares the same features of the CFD one, with few exceptions: the CHT model also features the rotor's solid domain, therefore, the rotating walls of the CFD domain were replaced by fluid-solid interfaces. Figure 5.6 shows the solid domain of the CHT setup.
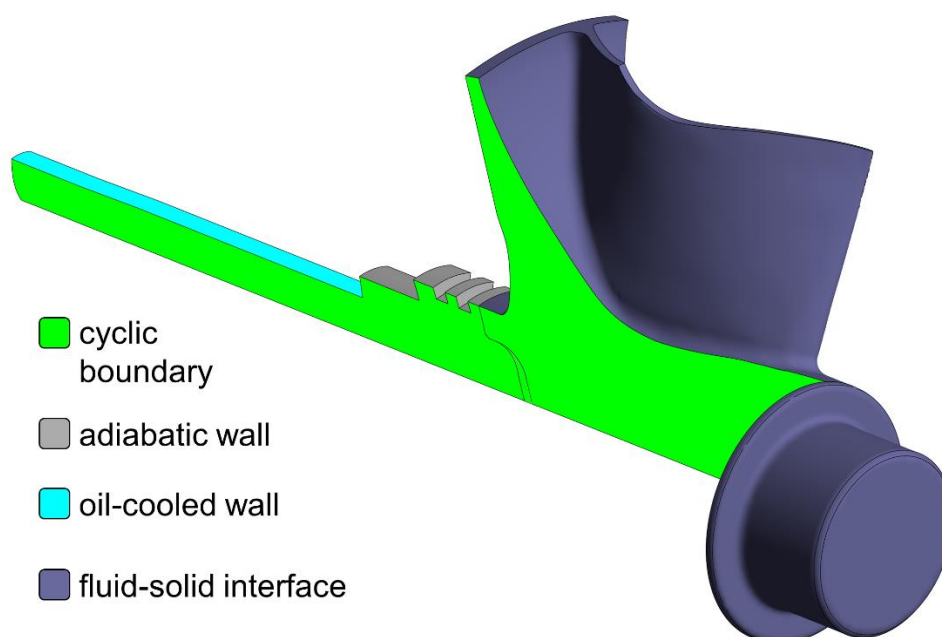
Figure 5.6   Solid domain of the CHT model.

The solid domain consists in four solid sub-domains: the rotor wheel domain, the wheel's nose domain, the shaft domain and the domain of the body that fills the rotor-shaft cavity (Figure 5.7). The wheel domain was separated from its nose to grant mesh conformity between the corresponding fluid domains (i.e. the rotor fluid domain and the outlet fluid domain, respectively); moreover, due to the fact that the outlet domain is not axysimmetric, the interface between the solid wheel domain and the nose domain accounts for the cyclic repetition of the former.
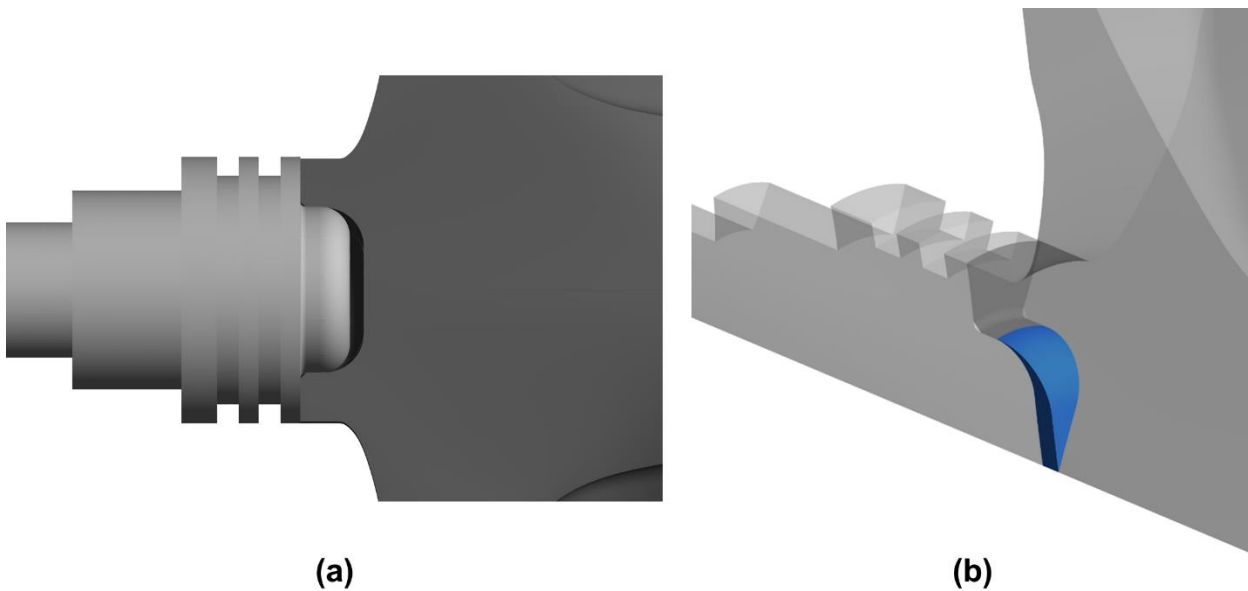
Figure 5.7   Detail view of (a) the shaft-rotor cavity and (b) the filler body within the cavity.

The shaft-rotor cavity is filled with a solid body that has the thermophysical properties of air, in order to account for conduction phenomena. Inside the shaft-rotor cavity, convection phenomena are neglected due to the impossibility to model isolated fluid regions, hence the use of a solid domain as a filler.

Regarding boundary conditions, mass flow rate and total temperature were imposed at the inlet boundary of the volute sub-domain, while static pressure was set at the main outlet boundary. Mass flow rate was set at the blow-by outlet. All the values were set according to available experimental measurements. The walls, both stationary and rotating, were set as adiabatic, except for the "oil-cooled" wall (Figure 5.6), at which a fixed temperature was set for every calculation. In order to limit the computational cost of the simulations, radiation effects were not modelled.

For the simulations, the fluid was set as air (ideal gas), with temperature-dependent specific heat capacity at constant pressure, as shown in Eq. (4.2); the coefficients of the specific heat capacity relation are the same of Table 4.2.

Concerning transport properties, both dynamic viscosity (μ) and thermal conductivity (k) were calculated as a function of temperature through Sutherland's law (Eq. (4.3) and Eq. (4.4)), with the same coefficients of Table 4.3. Based on available material data, temperature-dependent specific heat capacity and thermal conductivity were also assigned to the shaft steel and wheel alloy.

The computational grid, of hybrid type, was generated with ANSYS® Meshing®: a tetrahedral-based grid was adopted in the core flow region, with the addition of prismatic elements in the boundary layer zones of the fluid domains. The first element height was chosen to guarantee that the dimensionless wall distance at the grid nodes of the first prismatic layer from the walls did not exceed the limit of y⁺=1. Mesh sizing was selected based on a mesh sensitivity CHT analysis and

previous experience. Initially, two mesh were tested, one with 28M total elements and one with 50M elements. Results showed that the discrepancy between the two calculations in terms of total-to-static expansion ratio and isentropic efficiency was 0.93% and 1.02%, respectively. The 28M elements mesh was selected, since, based on a previous study [93], a coarser mesh was deemed not suitable. Figure 5.8 shows the selected mesh of the turbine blade passage. Mesh elements global sizing and count is summarized in Table 5.2, for each sub-domain.

Sub-domain	Global sizing [mm]	# elements ($\cdot 10^6$)
Volute	0.4	6
Wheel (fluid)	0.2	7
Outlet	0.8	11
Wheel (solid)	0.2	2.5
Nose	0.4	0.4
Shaft	0.4	1
Cavity body	0.2	0.1

Table 5.2   Mesh elements sizing and count for each sub-domain.
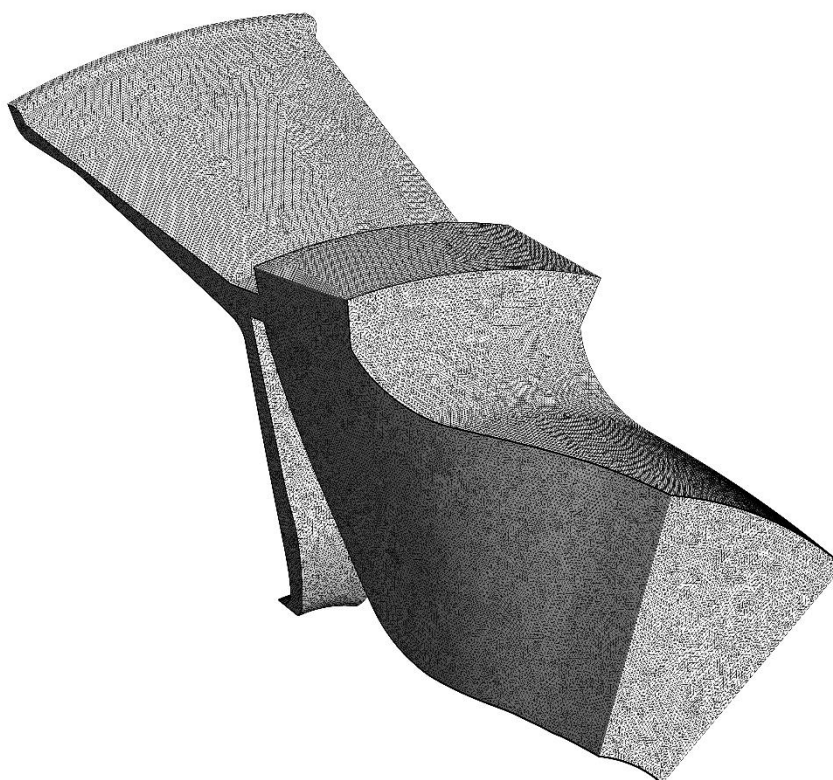
Figure 5.8   Mesh of the rotor fluid domain.

As a convergence criterion for the solution, a tolerance of 10^{-6} was set to all residuals and the solution stability was checked in terms of fluctuation of the outlet mass flow rate and area-averaged static temperature.

5.2.3 - Steady-state 3D CHT setup validation

Validation against experimental measurements was performed on the CHT setup. Specifically, eight operating points corresponding to steady-state engine conditions were analyzed, each one involving the generation of a dedicated outlet sub-domain mesh due to the different wastegate valve position. The operating points are summarized in Table 5.3. For confidentiality reasons, each quantity was normalized against the corresponding quantity of operating point *OP1*, which represents the most severe steady-state condition. Still, in order to provide a better understanding of the wheel's operating conditions, it is worth pointing out that inlet temperatures are above 1000°C for every operating point and rotating speed is generally higher than 100'000 rpm.

Operating point	Inlet mass flow*	Rotating speed*	Inlet P0*	WG angle*	Inlet T0*
OP1	1.00	1.00	1.00	1.00	1.00
OP2	0.81	0.89	0.78	1.30	0.96
OP3	0.63	0.77	0.60	1.54	0.95
OP4	0.42	0.57	0.43	2.48	0.94
OP5	1.06	1.01	1.02	1.10	0.96
OP6	0.94	0.98	0.93	0.98	0.96
OP7	0.80	0.95	0.81	0.81	0.96
OP8	0.65	0.92	0.72	0.52	0.96

Table 5.3   Simulated operating points for the validation of the CHT model

As anticipated in section 5.1, calculated surface temperatures at the turbine blades' trailing edge were compared to infrared temperature measurements. Specifically, two small regions (namely point *A* and point *B*) at the trailing edge were considered for the comparative analysis. Figure 5.9 and Figure 5.10 show the results of the CHT analyses that were carried out for the model validation, in terms of temperature contour plots on the rotor wheel's solid domain. Due to a non-disclosure agreement with the industrial partner, temperature is shown in a non-dimensional form: again, the values were normalized against the *OP1* turbine inlet temperature.
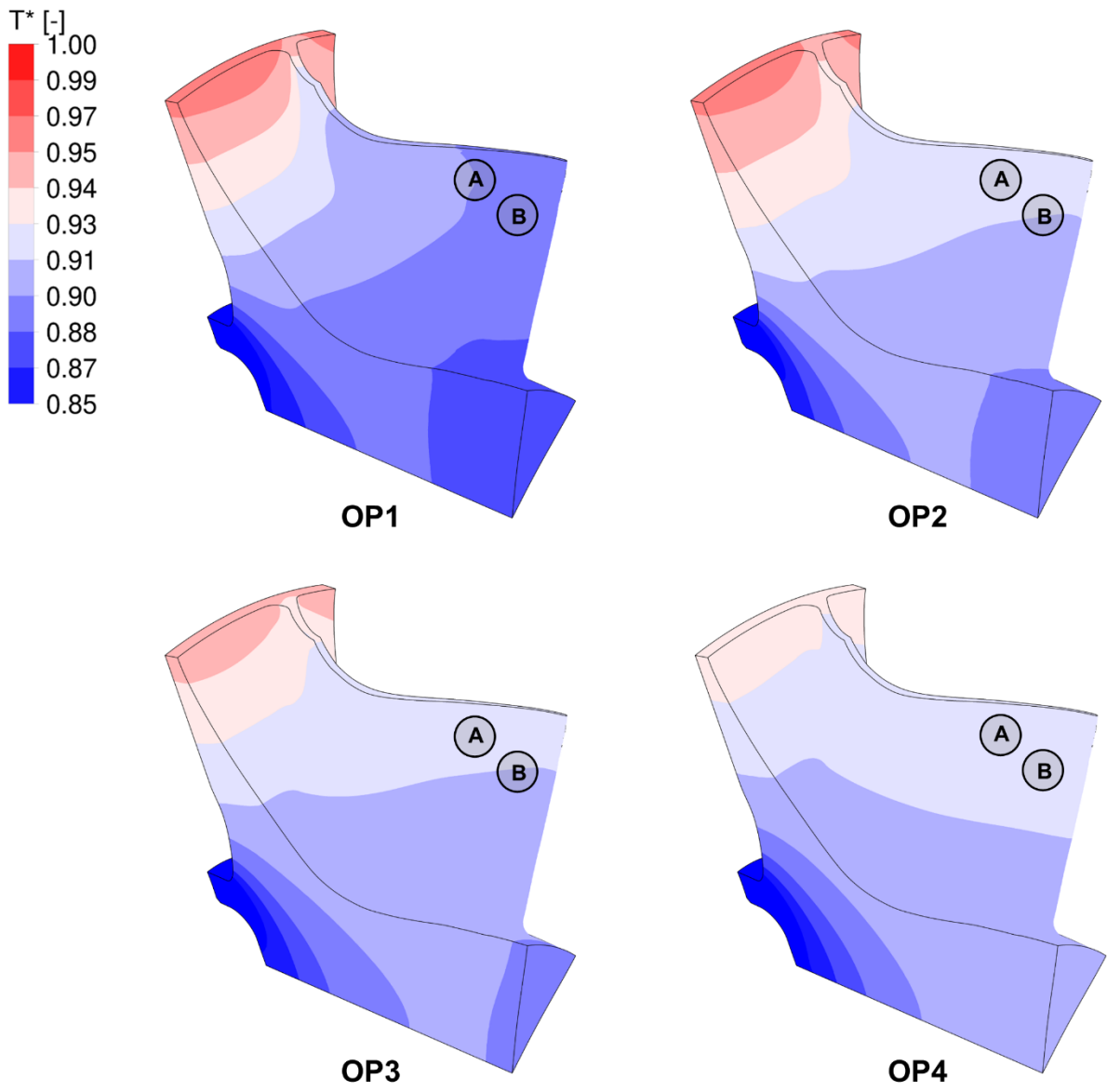
Figure 5.9   Temperature distribution over the wheel's solid domain, for OP1, OP2, OP3 ad OP4.
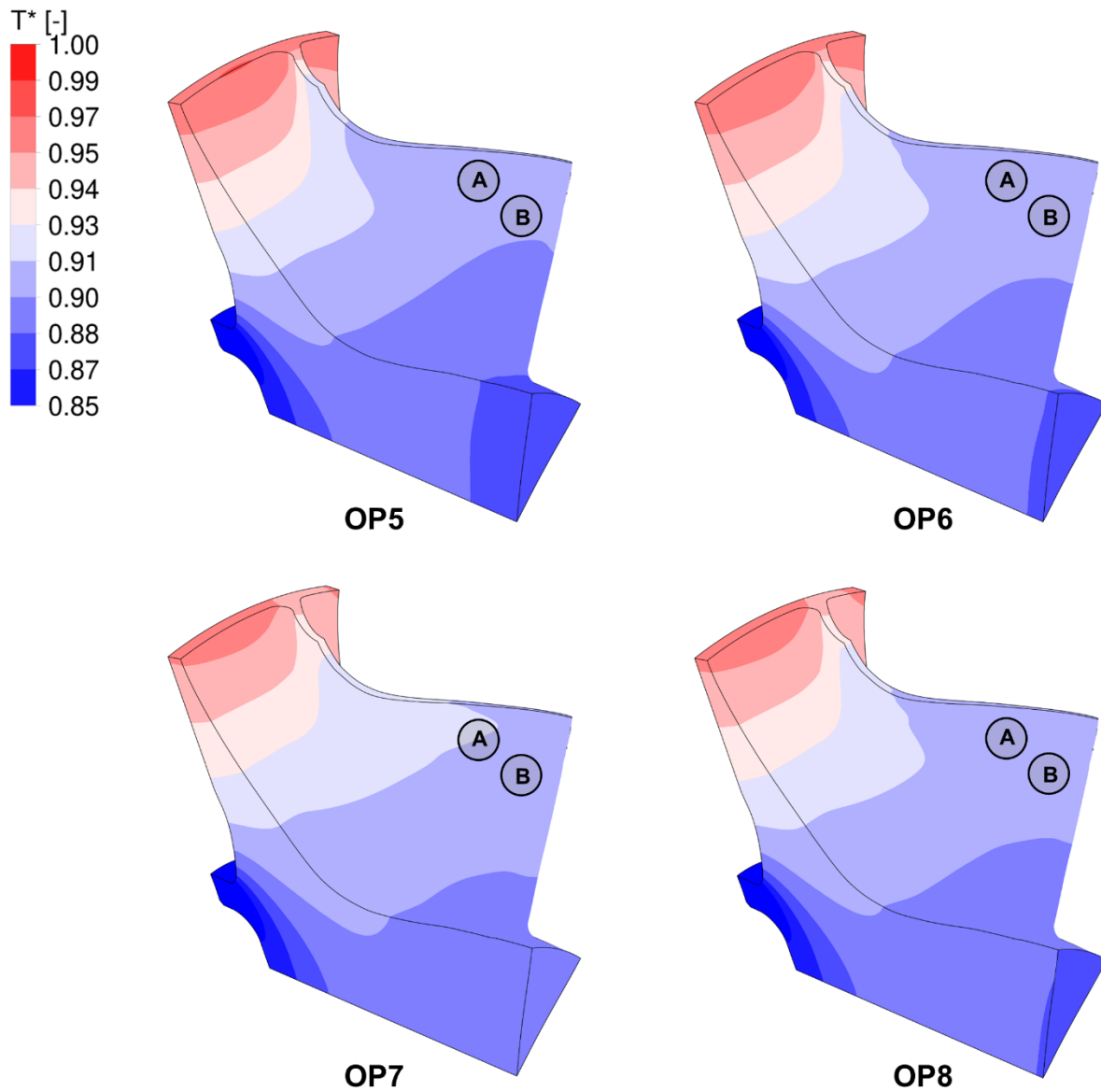
Figure 5.10   Temperature distribution over the wheel's solid domain, for OP5, OP, OP7 ad OP8.

In order to simplify the comparison, given the relatively small difference between the measured temperatures of the two points, the average temperature of *A* and *B* was considered for both the CHT and the experimental data set. Figure 5.11 shows the relative variation between CHT and experimental (EXP) values, defined as Eq. (5.1). The relative variation was calculated using absolute temperature values.

$$\Delta T\% = \frac{\bar{T}_{AB,CHT} - \bar{T}_{AB,EXP}}{\bar{T}_{AB,EXP}}\% \qquad (5.1)$$
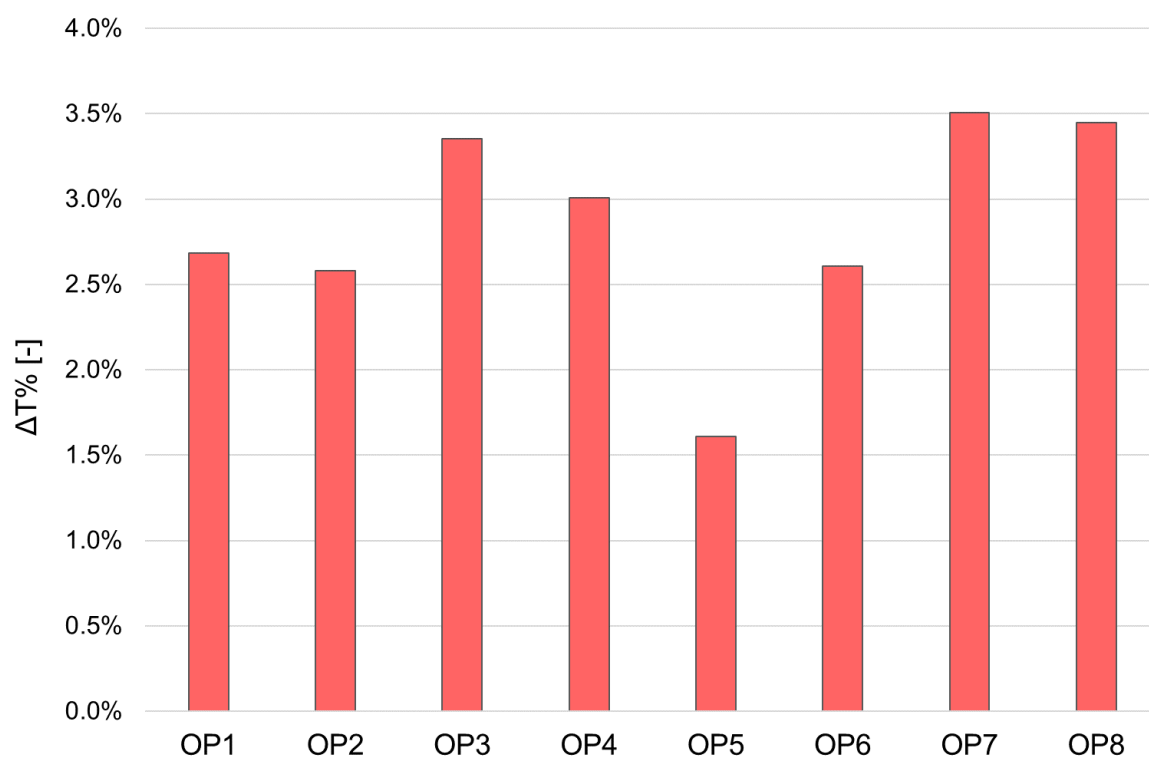
Figure 5.11   Relative error between calculated and measured temperature.

Overall, calculated temperature is always higher than measured one: this is likely due to the fact that the 3D CHT model uses adiabatic walls, therefore environmental heat transfer phenomena are neglected. Nonetheless, it is apparent that a good agreement with experimental data was found, as the relative variation between calculated and measured values is always below 4%.

5.2.4 - Environmental heat transfer sensitivity analysis

One of the main simplifying assumption of the developed 3D CHT model is represented by the fluid domain's adiabatic walls. While heat transfer between the fluid flow and the turbine wheel is thoroughly modelled by means of the fluid-solid interfaces, heat transfer with the environment is not taken into account. With the aim of evaluating the effects of external heat transfer, the turbine housing solid domain was implemented in the developed CHT model: a Heat Transfer Coefficient (HTC) boundary condition, coupled with an ambient temperature of 30°C, was imposed at the housing's external walls, as shown in Figure 5.12.
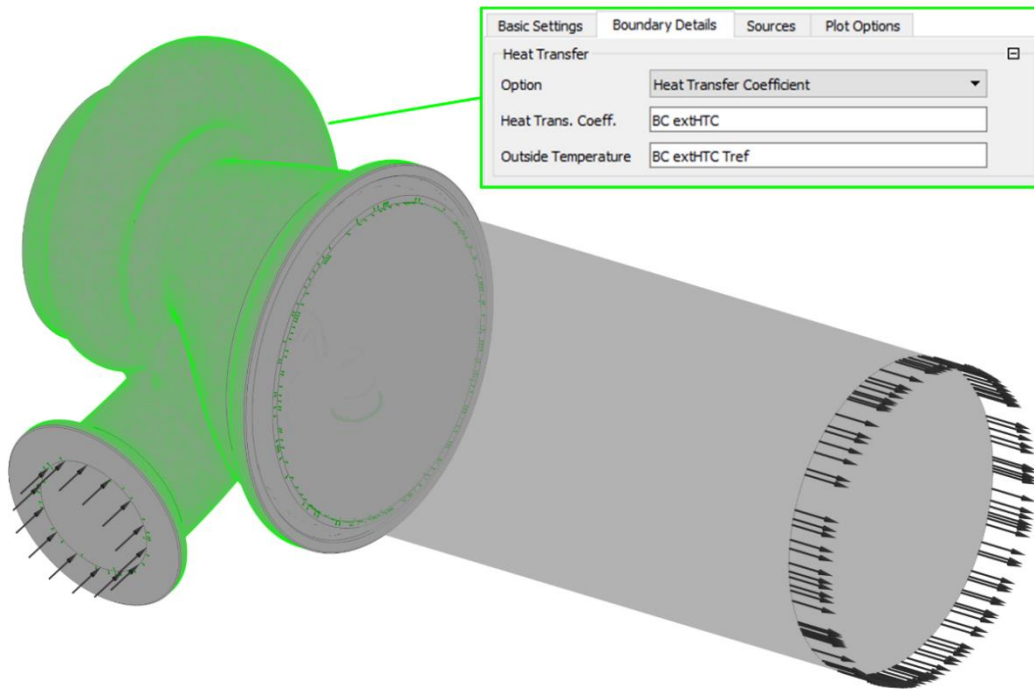
Figure 5.12   3D CHT model with the housing solid domain and its external wall's BCs.

Then, a sensitivity analysis on different HTC values was carried out while maintaining the same ambient temperature. Specifically, HTC values ranging from natural convection (20 W/m^2/K) to intense forced convection (400 W/m^2/K) were tested. An extreme value of 1000 W/m^2/K was also set, in order to exaggerate the effects of external heat transfer and gain a comprehensive understanding of the resulting trends. The test plan for this sensitivity analysis is summarized in Table 5.4.

Case	Operating point	Housing solid domain	HTC BC [W/m^2/K]	Ambient T BC [°C]
adiabatic	OP1	no	-	30
20 W/m^2/K	OP1	yes	20	30
100 W/m^2/K	OP1	yes	100	30
400 W/m^2/K	OP1	yes	400	30
1000 W/m^2/K	OP1	yes	1000	30

Table 5.4   Test plan for the environmental heat transfer sensitivity analysis.

The results of the sensitivity analysis are presented in a similar way to the ones of the CHT model validation: Figure 5.13 shows plot contours of normalized temperature on the rotor wheel's solid domain, while Figure 5.14 shows the average temperature of point *A* and *B* as a function of HTC, compared against the baseline *OP1* case without housing nor external heat transfer (*adiabatic*) and experimental measurements (*EXP*).
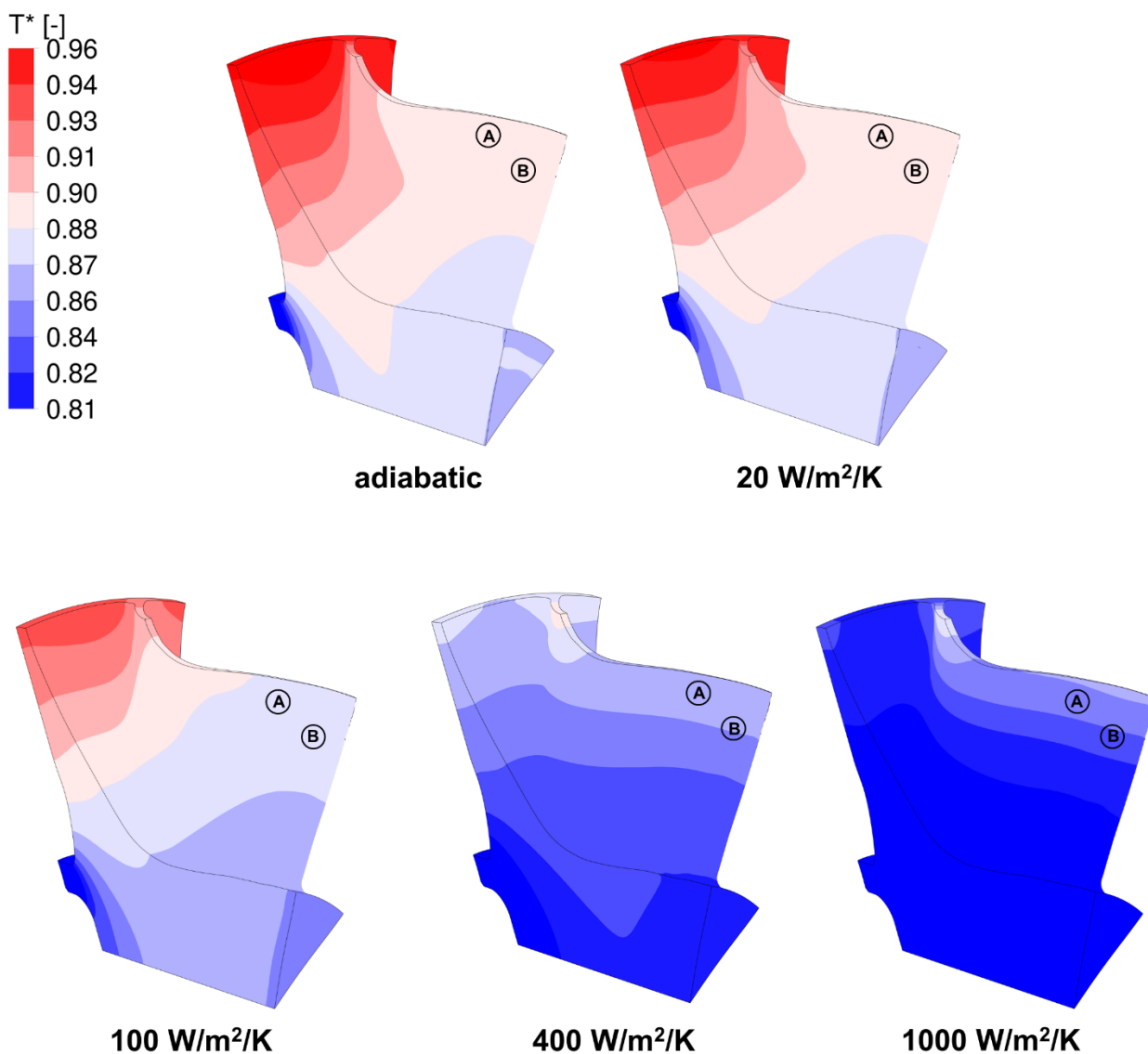
Figure 5.13   Contour plots of normalized temperature for different magnitudes of environmental heat transfer.
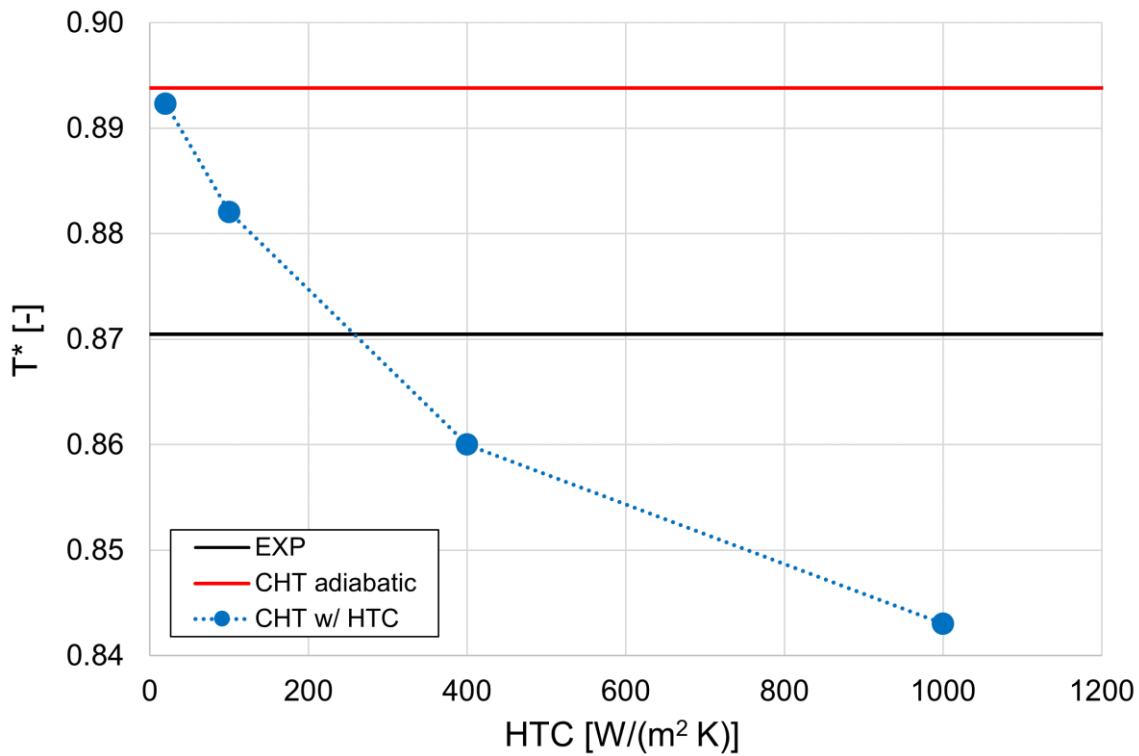
Figure 5.14   Evolution of the blade temperature near the trailing edge for different environmental HTC values.

It is apparent that an HTC value that is typical of natural convection (20 W/m²/K) doesn't show a significant impact on the turbine blades' temperature. In the present application, however, forced convection can be met when, for instance, the instrumented turbine housing is air-cooled by a fan. When moving to the range of forced convection (100 to 400 W/m²/K) external heat transfer lowers the housing's temperature to the point where blade temperature is also affected: at 100 W/m²/K, the average temperature of point *A* and *B* is 1.3% lower than the adiabatic case; at 400 W/m²/K, the same value is roughly 4% lower than the adiabatic case. For a better understanding of how the housing's cooling effects affect the turbine blades' temperature, an in-depth analysis was carried out. Figure 5.15 shows normalized temperature contour plots on a radial plane that cuts the wheel at the leading edge's midspan, for the adiabatic case and the one with strong forced convection.
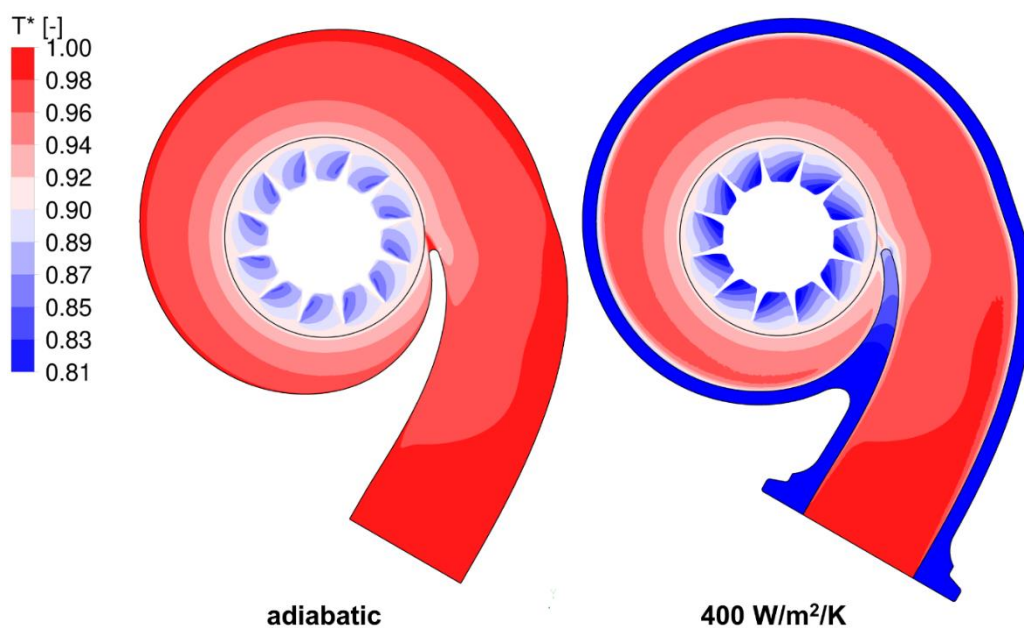
Figure 5.15   Normalized temperature contour plots on a radial plane.

In case of environmental heat transfer, it is apparent that the temperature of the fluid flow near the housing's wall is lower with respect to the adiabatic case. This was expected, and so was the overall lower temperature within the rotor domain, according to the contour plots of Figure 5.13. Nonetheless, the rotor inlet temperature appears to be the same as the adiabatic case, with the only exception of the region near the volute's tongue. Indeed, for a better understanding of the heat transfer phenomena that affect the turbine's wheel, attention must shift towards the backdisc cavity. Figure 5.16 shows normalized temperature contour plots on a meridional plane, highlighting the backdisc cavity region.
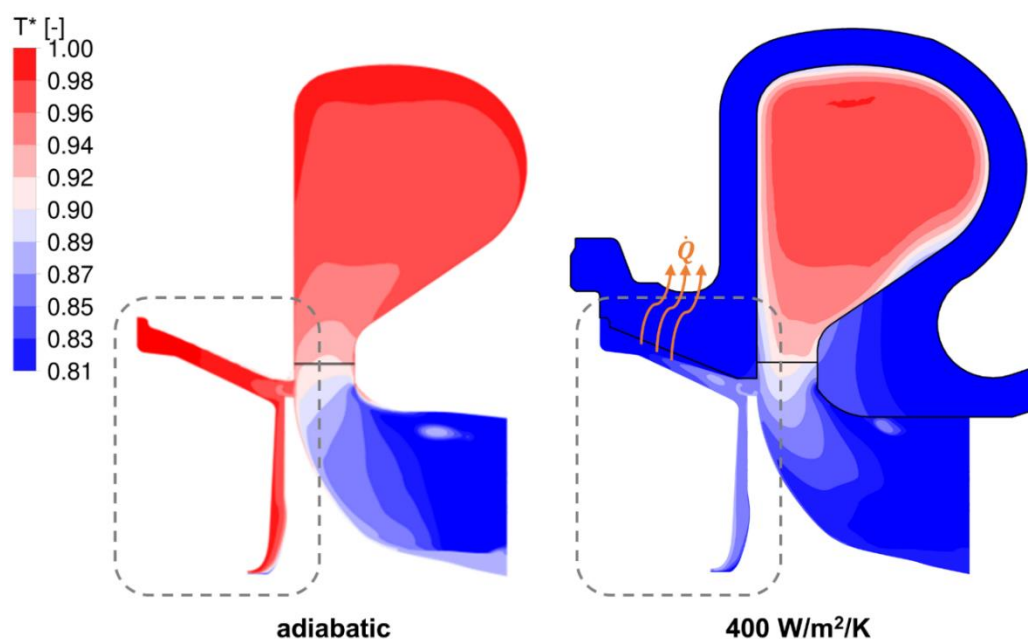
Figure 5.16   Detail view and normalized temperature contour plots of the backdisc cavity.

It is apparent how the rotor inlet flow conditions are similar between the two cases. However, the temperature of the flow within the backdisc cavity is significantly higher in the adiabatic case with respect to the *400 W/m²/K* case. This is due to the heat transfer near the upper part of the cavity, as highlighted in Figure 5.16: in turn, the rotor wheel's backdisc is cooled by the cavity flow. Additional cooling effects can be observed in the blade tip region, as shown in Figure 5.17.
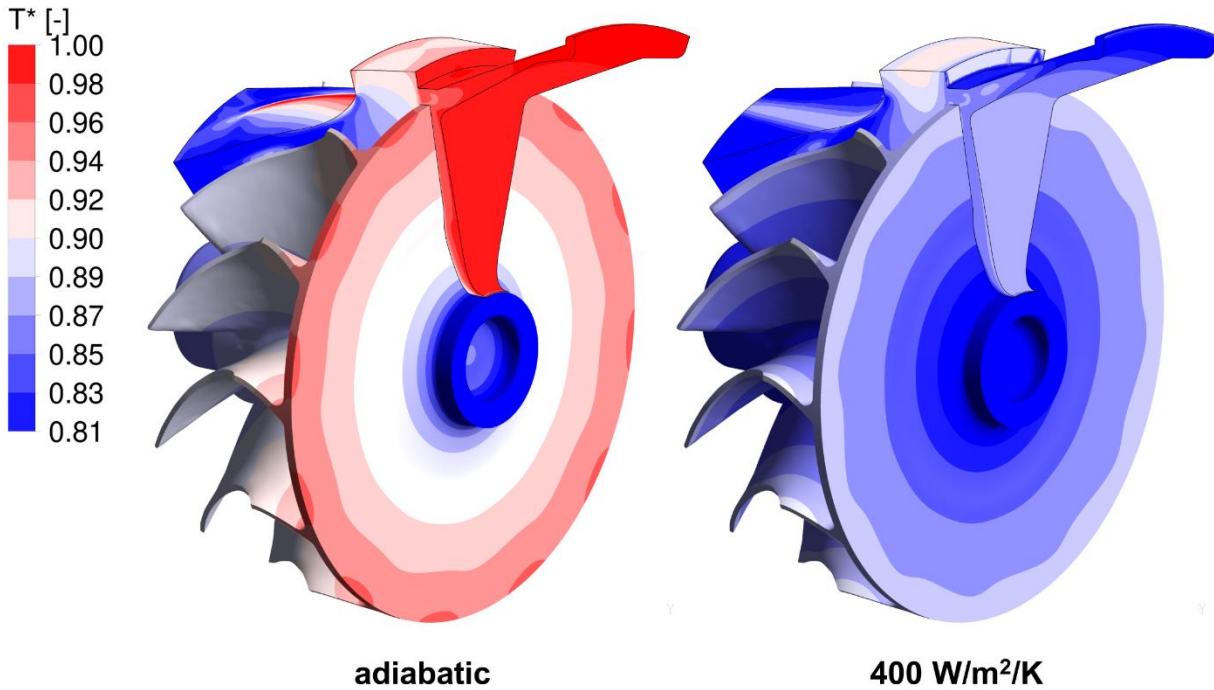
Figure 5.17   View of the solid and fluid domains for the adiabatic and 400 W/m²/K cases.

In conclusion, environmental heat transfer may indeed lower the metal temperature distribution of the wheel. Its effects are, however, localized in certain regions, such as the wheel's backdisc cavity. Therefore, it is worth reminding that a uniform HTC distribution was used in this sensitivity analysis and such condition is most likely not realistic. For this reason, due to the uncertainties on the actual HTC distribution and the good agreement with experimental measurements, the adiabatic 3D CHT model was still employed in the present study.

5.2.5 - Transient thermal model

As briefly anticipated in paragraph 5.2.1, the proposed transient approach, to which the text will from now on refer to as "*Transient-BC-FVM*", aims to perform a thermal transient analysis on the solid domain only, in place of a transient CHT calculation. Therefore, the computational domain for the thermal transient analysis consists in the rotor's solid domain that was already presented in paragraph 5.2.2. The only difference in the model's geometry, as shown in Figure 5.18, is that the full rotor is here modelled: this is due to the inability of the structural solver to perform transient calculations on axisymmetric domains with cyclic boundaries.

■ oil-cooled wall

■ adiabatic wall

■ HTC + T_{ref} wall
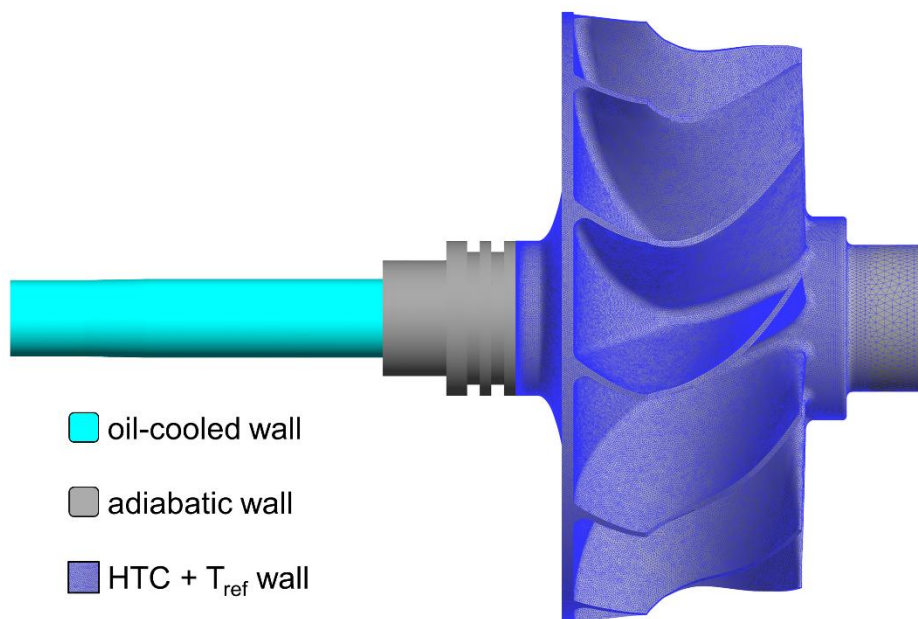
Figure 5.18   Computational domain of the developed thermal transient model.

The setup does not differ from the CHT setup in the numerical treatment of the oil-cooled wall and the adiabatic walls close to the bearing housing. The fluid domain, however, is excluded and no fluid-solid interfaces were set. Instead, a Heat Transfer Coefficient (HTC) distribution, together with a reference ambient temperature, was imposed at the solid's wet surfaces, in order to model the effects of fluid flow without actually resolving the fluid domain. Indeed, the proposed approach revolves on the definition of the HTC boundary condition, as follows. "*Transient-BC-FVM*" approach is based on the assumption that, in a transient CHT problem, the fluid domain reaches steady-state conditions more rapidly than the solid domain. This assumption is pushed further to the point that any variation of the flow conditions is considered instantaneous, allowing to define an initial condition of the transient process where the fluid domain is already at the final steady-state conditions while the solid domain is still at its initial conditions. Figure 5.19 depicts the key aspects of the "*Transient-BC-FVM*" approach, in case of a heating transient process.
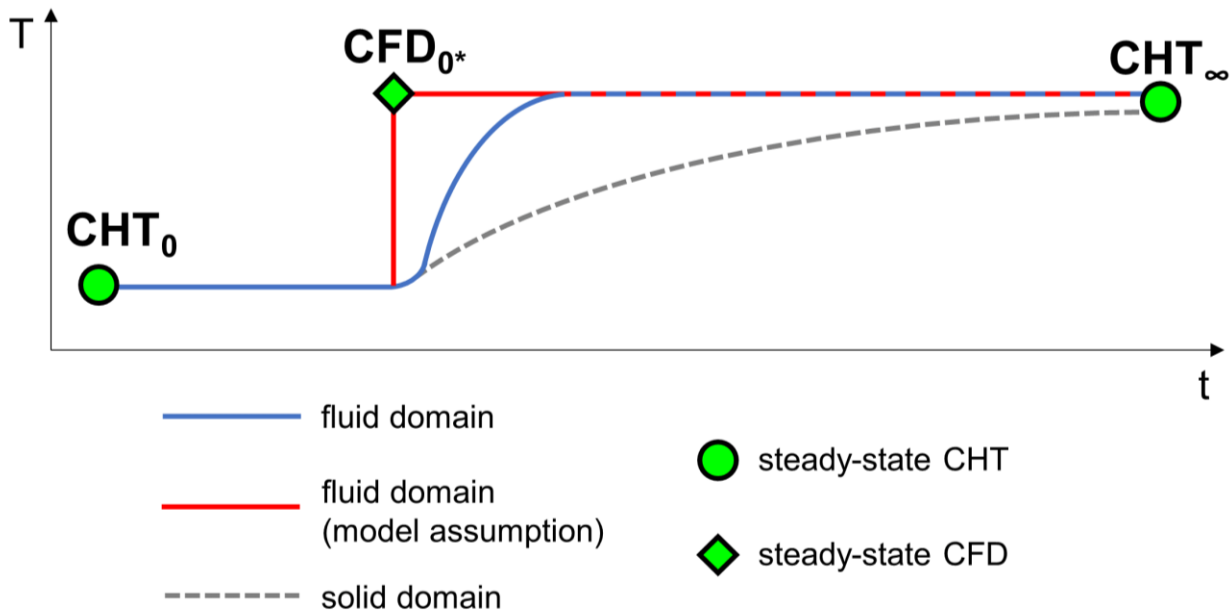
Figure 5.19 Fundamentals of the developed thermal transient model.

The initial condition of the transient process is represented by the *CFD$_{0*}$* step. Indeed, this initial phase can be modelled by a steady-state CFD calculation in which the fluid-dynamic inlet/outlet boundary conditions are the ones of the transient end, while the thermal boundary condition at the walls is the temperature distribution before the transient phase. This pre-transient temperature distribution is obtained through a steady-state CHT calculation (i.e. *CHT$_0$*) with pre-transient flow conditions. The third key point of the transient process is represented by its steady-state condition, which can be modelled by a steady-state CHT calculation with the final steady-state flow conditions (i.e. *CHT$_\infty$*). At this point, two spatial HTC distributions can be defined at the wet surfaces of the solid domain, as shown in Eq. (5.2) and Eq. (5.3).

$$HTC_{0*}(x,y,z) = \frac{\dot{q}_{CFD_{0*}}(x,y,z)}{T_{REF}-T_{CFD_{0*}}(x,y,z)} \tag{5.2}$$

$$HTC_{\infty}(x,y,z) = \frac{\dot{q}_{CHT\infty}(x,y,z)}{T_{REF}-T_{CHT\infty}(x,y,z)} \tag{5.3}$$

Where $\dot{q}$ is the specific heat flux and T_{REF} is an arbitrary reference temperature. The reference temperature should be selected based on the value that best characterizes the transient phase: in the present case, the reference temperature is the volute inlet temperature during the transient phase.

It should be clear that *HTC$_{0*}$* is the HTC distribution at the beginning of the transient phase, and *HTC$_\infty$* is the HTC distribution at steady-state conditions. Moving from this premise, it is possible to define a time-varying HTC distribution that is interpolated between *HTC$_{0*}$* and *HTC$_\infty$* through a function of temperature Eq. (5.4), according to Eq. (5.5).

$$U(x, y, z, t) = \frac{T(x,y,z,t) - T_{CHT_0}(x,y,z)}{T_{CHT_\infty}(x,y,z) - T_{CHT_0}(x,y,z)} \tag{5.4}$$

$$HTC(x, y, z, t) = HTC_{0^*}(x, y, z) + U(x, y, z, t) \cdot [HTC_\infty(x, y, z) - HTC_{0^*}(x, y, z)] \tag{5.5}$$

The time-varying HTC expression of Eq. (5.5) can then be set at the solid domain's wet surfaces of the thermal transient model, together with the reference temperature: this way, the influence of temperature variation on HTC can be modelled, while the effects of mass flow rate and pressure variations are implicitly taken into account in the calculation of HTC_{0^*} and HTC_∞. Figure 5.20 shows, as an example, a HTC distribution boundary condition that was applied to the rotor wheel's solid domain. It is worth pointing out that, since both CFD and CHT steady-state calculations only model one blade passage, HTC_{0^*} and HTC_∞ distributions were exported and then reconstructed over the full wheel's geometry.
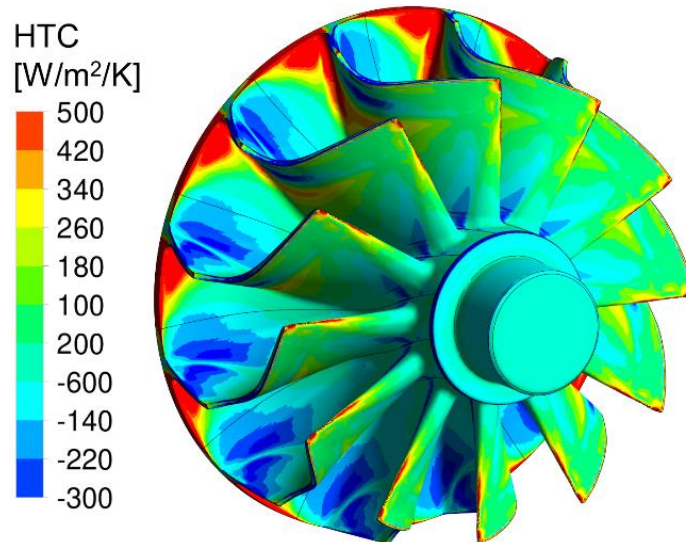
Figure 5.20   Example of a starting HTC distribution to be applied as boundary condition.

The adopted thermal transient approach allows to obtain the evolution of the solid domain's temperature distribution without resorting to transient CHT calculations, which are extremely computationally expensive. Instead, the following calculations are carried out: two steady-state CHT calculations, one steady-state CFD calculation and one thermal transient calculation that only features the solid domain.

5.2.6 - Transient structural setup

The computational domain of the transient structural setup is the same as the one of the thermal transient model, the only exception being the absence of the shaft-rotor cavity filler body (i.e. the "solid" air inside the cavity). Therefore, the solid domain consists in three sub-domains: the wheel domain, the nose domain and the shaft domain. The three bodies that form the solid domains are bound together as a single part, forming a single rigid body that still allows for multiple materials to be assigned (i.e. the shaft's steel and the wheel's material). Details of the structural solver setup are presented as follows: the behavior of the solid bodies is set to be linear elastic, with isotropic thermal expansion. The thermal expansion coefficient, Young's modulus and density are set to be temperature-dependent, based on data provided by the industrial partner.

Constraints are set on the shaft with the aim of modelling the bearing closest to the wheel: specifically, a "cylindrical support" disallows translation in the radial direction, and a "frictionless support" fixes the axial position of the surface on which is applied. Figure 5.21 schematically shows the constraints that were applied to the shaft: please note that the terminology refers to ANSYS® Mechanical® simulation framework.
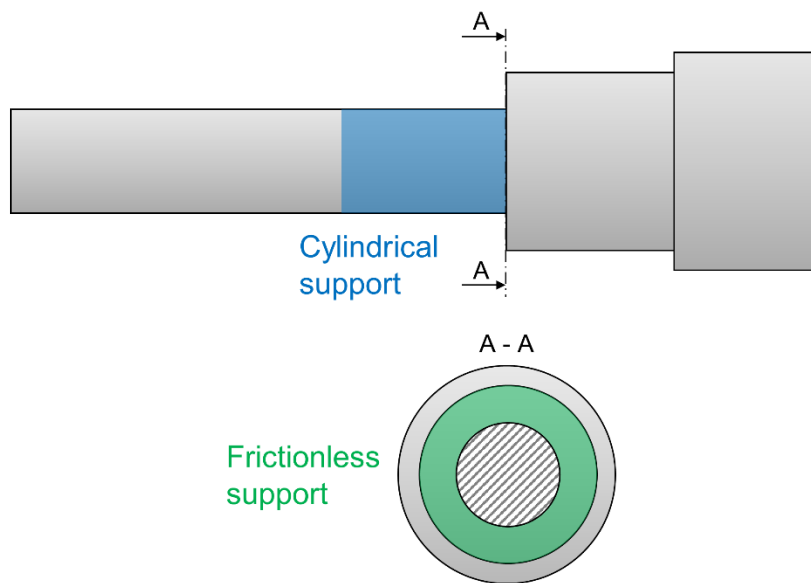
Figure 5.21   Constraints for the structural setup.

The centrifugal load is set by applying a rotating motion to the solid domain. The thermal load is a time-varying load that is derived from the thermal transient analysis: three-dimensional temperature distribution sets are mapped to the structural solver's mesh with a normal interpolation method. Being a transient calculation, the thermal load is mapped at every timestep, depending on the thermal transient results availability, i.e. the output saving frequency of the thermal transient calculation. Figure 5.22 shows, as an example, an initial mapping operation of the thermal loads, for the three bodies that form the solid domain.
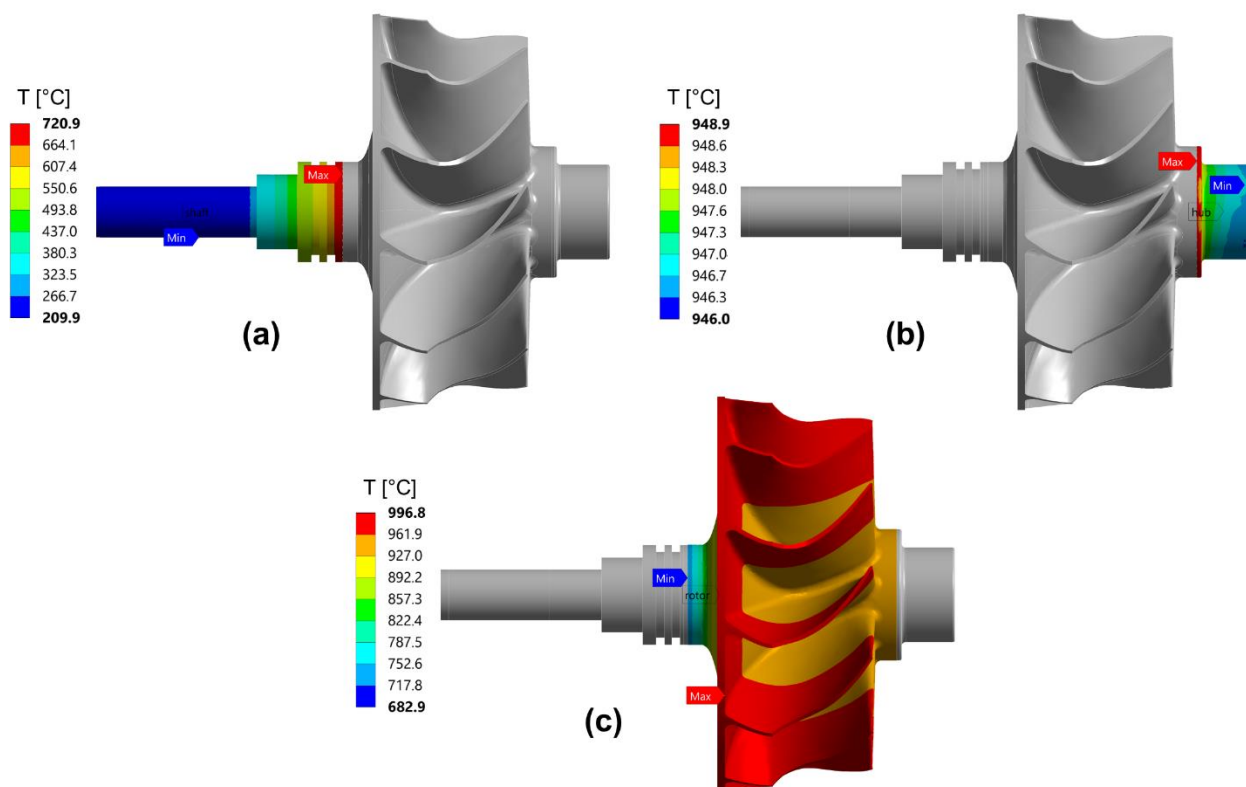
Figure 5.22   Example of thermal load applied to the (a) shaft body, (b) nose body and (c) wheel body.

Before proceeding with the structural analyses, the main issues related to the uncertainties of the numerical setup were addressed. Firstly, a sensitivity analysis on the shaft temperature was carried out. As presented in paragraph 5.2.2, a fixed temperature was set at a surface of the shaft in order to model the cooling effect of the lubrication circuit. This temperature value was not directly measured, but rather estimated based on the oil circuit inlet temperature measurements. Due to the uncertainty on the shaft's wall temperature, different temperature values were simulated and their effects were assessed in terms of temperature gradient at the shaft-rotor connection (Figure 5.23a) and Von Mises stress values (Figure 5.23b) near the backdisc hub fillet. The results of the shaft temperature sensitivity analysis are summarized in Table 5.5, where every quantity is normalized against its baseline value.

(a)   **(b)**
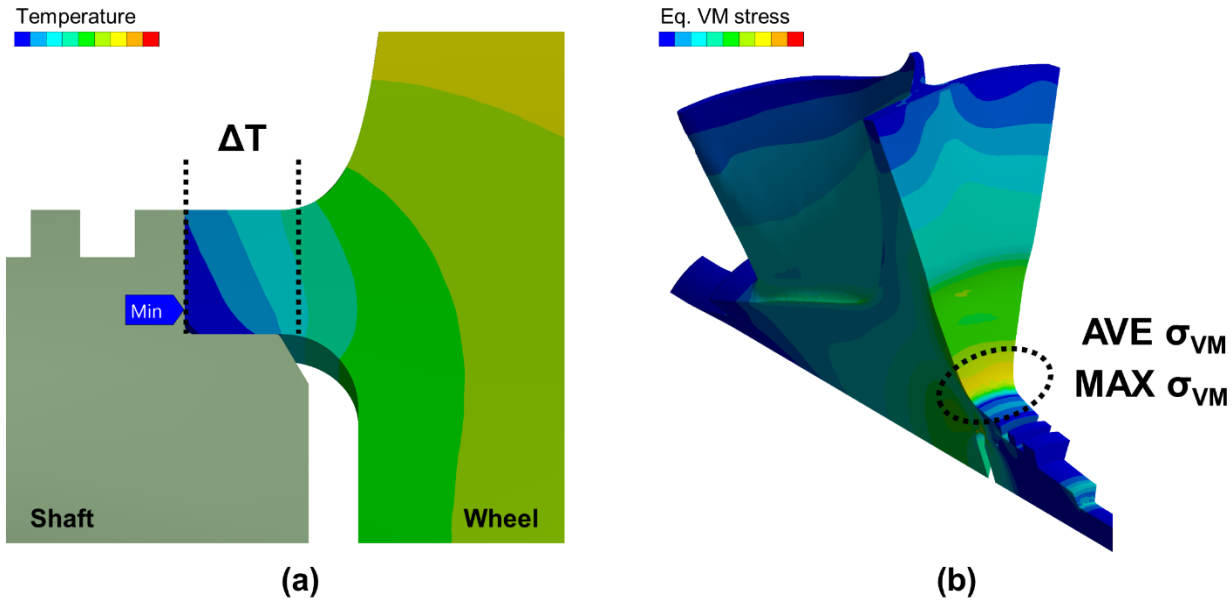
Figure 5.23   **Outputs of the shaft temperature sensitivity analysis: (a) temperature gradient at the shaft-wheel connection and (b) Von Mises stress close to the backdisc hub fillet.**

Case	Operating point	Shaft temperature	ΔT	AVE σ_{VM}	MAX σ_{VM}
C	OP1	0.86	1.05	1.02	1.02
BSL	OP1	1	1	1	1
H	OP1	1.14	0.96	0.99	0.99

Table 5.5   **Shaft temperature sensitivity analysis results.**

It is apparent that significant variations (roughly ±15%) of the shaft's wall fixed temperature lead to minor variations of the calculated Von Mises stress. As expected, the higher the shaft temperature, the lower the temperature gradient at the shaft-rotor connection area and, as a direct consequence, the lower the stress values. Given the small variation (+2% and -1%) of both the average and maximum Von Mises stress, the uncertainty on the shaft temperature was deemed acceptable and the baseline value was maintained for the rest of the study.

A mesh sensitivity analysis was also carried out for the structural model: such analysis was mainly dictated by the observation of a severe stress peak located at the innermost shaft-rotor contact region, as shown in Figure 5.24a. In order to assess whether the stress peak derived from an insufficient discretization of the computational domain, a finer mesh with half the element sizing of the baseline one was tested.

(a)   **(b)**
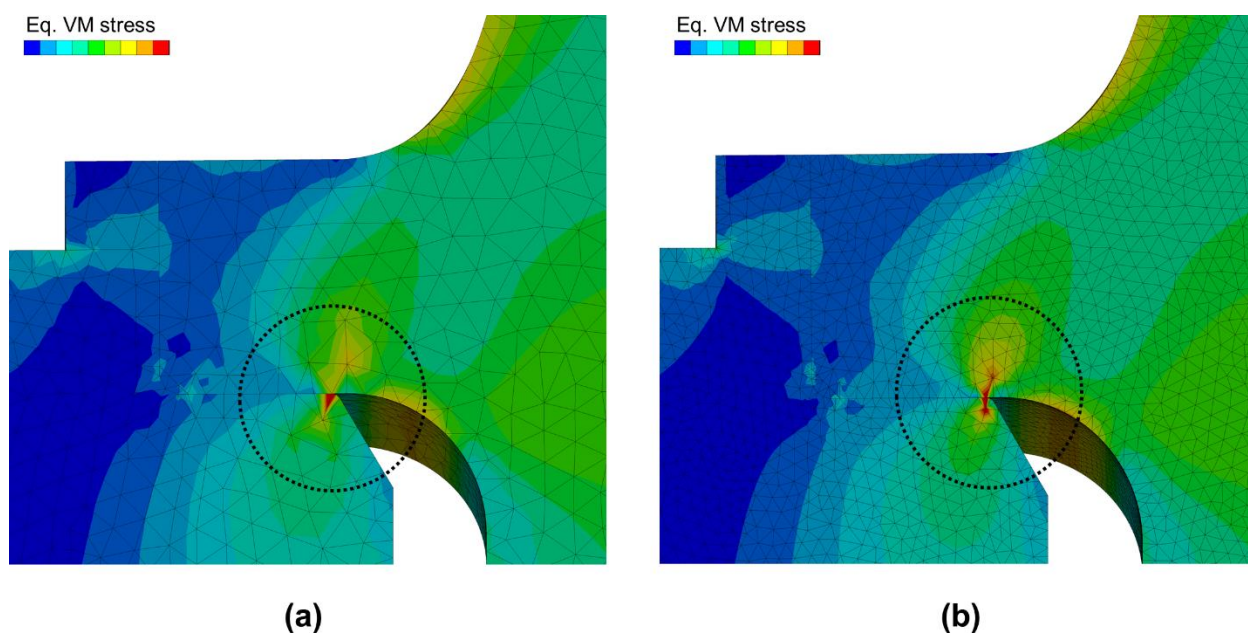
Figure 5.24   Comparison between the Von Mises stress distribution of (a) the baseline mesh and (b) the finer mesh.

Figure 5.24b shows that, even with a finer mesh, the stress peak is calculated in the same area. The stress distribution remains basically unchanged, the only difference being the higher resolution of the contour plots obtained with the finer mesh. Moreover, due to the fact that second order tetrahedral elements were employed, the computational cost of the analysis greatly increases when using the finer mesh. For these reasons, the baseline mesh was selected for the rest of the study.

Although the stress peak is not dependent on the computational domain's discretization, its extreme value still points to a numerical inconsistency: in order to assess the geometrical features that might cause it, a different geometry of the shaft-rotor cavity was analyzed. Figure 5.25 shows the baseline and the alternative geometry.
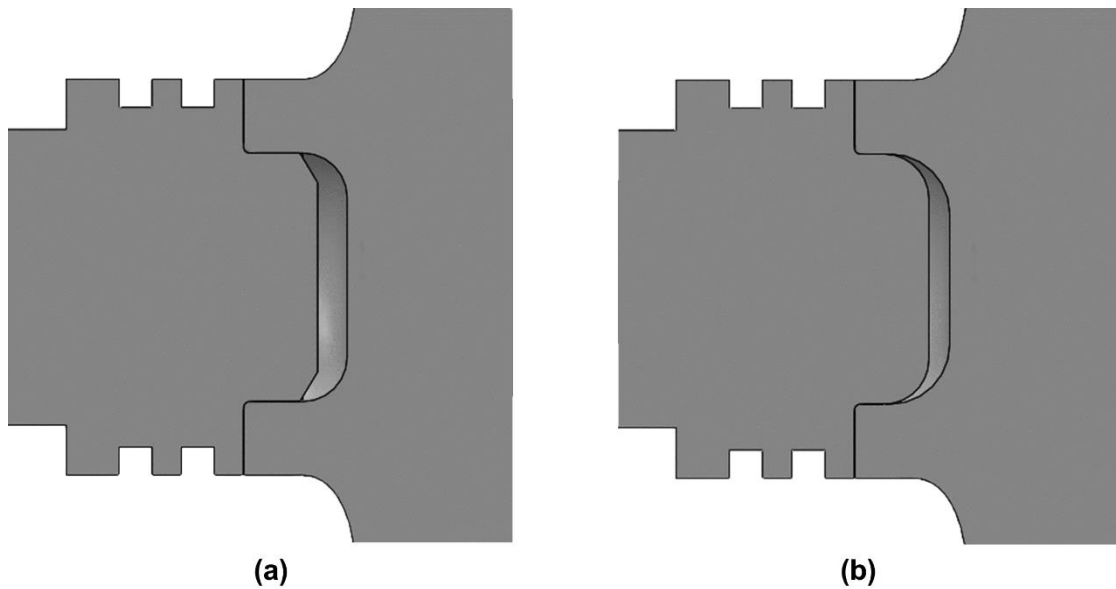
Figure 5.25   Cross sectional view of the (a) baseline and (b) alternative shape of the shaft-rotor cavity.

The shape of the shaft-rotor cavity is another uncertain feature of the numerical setup. While a baseline, original shape can be defined based on the shaft and wheel's design, it is worth pointing out that the two components are typically friction-welded [48]: once welded, the resulting shape of the cavity is hardly similar to the design one. Figure 5.26 shows the resulting stress distribution for both the geometry configurations.
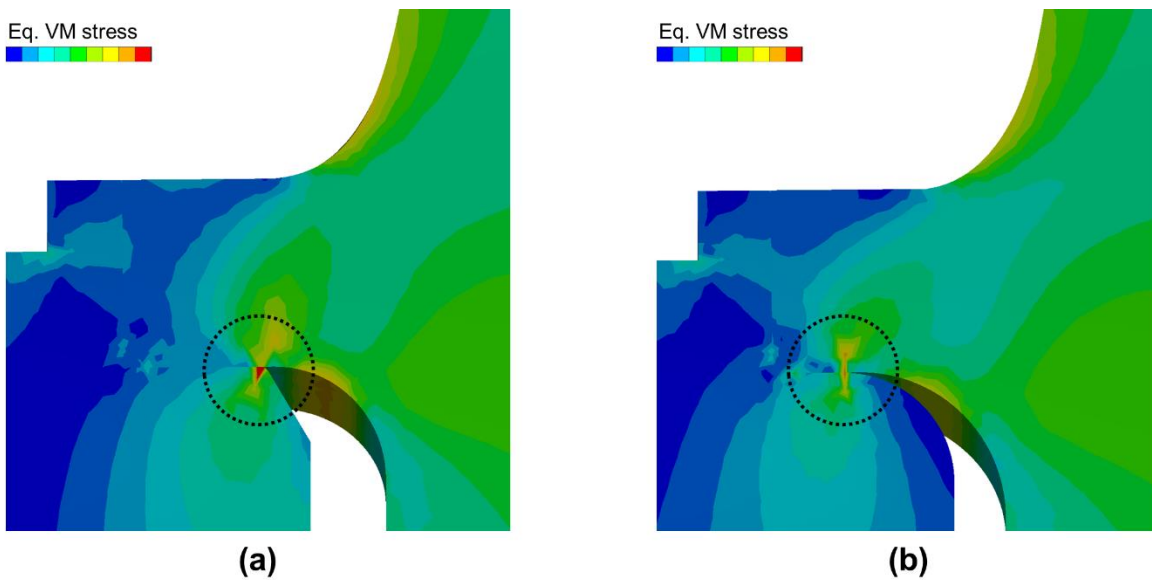
Figure 5.26   Stress distribution over the (a) baseline and (b) alternative shaft-rotor contact region.

A stress peak can be observed in both configurations, but is apparently mitigated by the smooth fillet of the alternative geometry. It is worth pointing out that the stress peak is, in both cases, located at the innermost contact point between the shaft and the rotor: contact in multibody systems is, however, a strongly non-linear phenomenon that would require a dedicated and more

advanced simulation approach, far beyond the scopes of the present study. Since the overall stress distribution remains almost unchanged, no further investigation on the contact point was carried out.

5.2.7 - Thermo-structural analysis test plan

The main goal of the analysis is the assessment of a methodology for simulating the effect of an engine transient maneuver on the transient thermo-structural response of a turbine wheel. In order to assess how a change in the operating condition of the incoming flow affects the heat distribution and instantaneous stress field, a set of study cases was hypothesized. In more detail, different examples of ramp-up (temperature increment due to a fast acceleration) and cut-off (temperature reduction due to a sudden throttle shut) were defined starting from the *OP1* steady-state operating point, as reported in Table 5.6. Here, relative temperature variations are presented with respect to the volute inlet temperature at pre-transient conditions. Transient thermo-structural simulations were carried out considering a total physical time of 20 seconds.

Transient process	*TRN A+*	*TRN B+*	*TRN C+*	*TRN A-*	*TRN B-*	*TRN C-*
Inlet T variation	+2.7%	+5.5%	+11.0%	-2.7%	-5.5%	-11.0%

Table 5.6   Test plan of the thermo-structural transient analysis.

5.3 - Results

5.3.1 - Post-processing methods

The structural solver returns the three-dimensional distribution of Von Mises stress on the solid domain, at each simulation timestep. Contour plots certainly provide extensive information but their use may overburden the presentation of a transient analysis. Aiming for a simpler analytical approach, the structural transient analyses are mainly discussed considering the local maximum stress values and the corresponding temperature within certain solid regions. These solid regions are user-defined according to stress and temperature levels that may identify the regions as critical to the component's durability. Figure 5.27 shows the initial distribution of stress and temperature for *OP1*; for confidentiality issues, stress and temperature values on the backdisc are only displayed qualitatively.
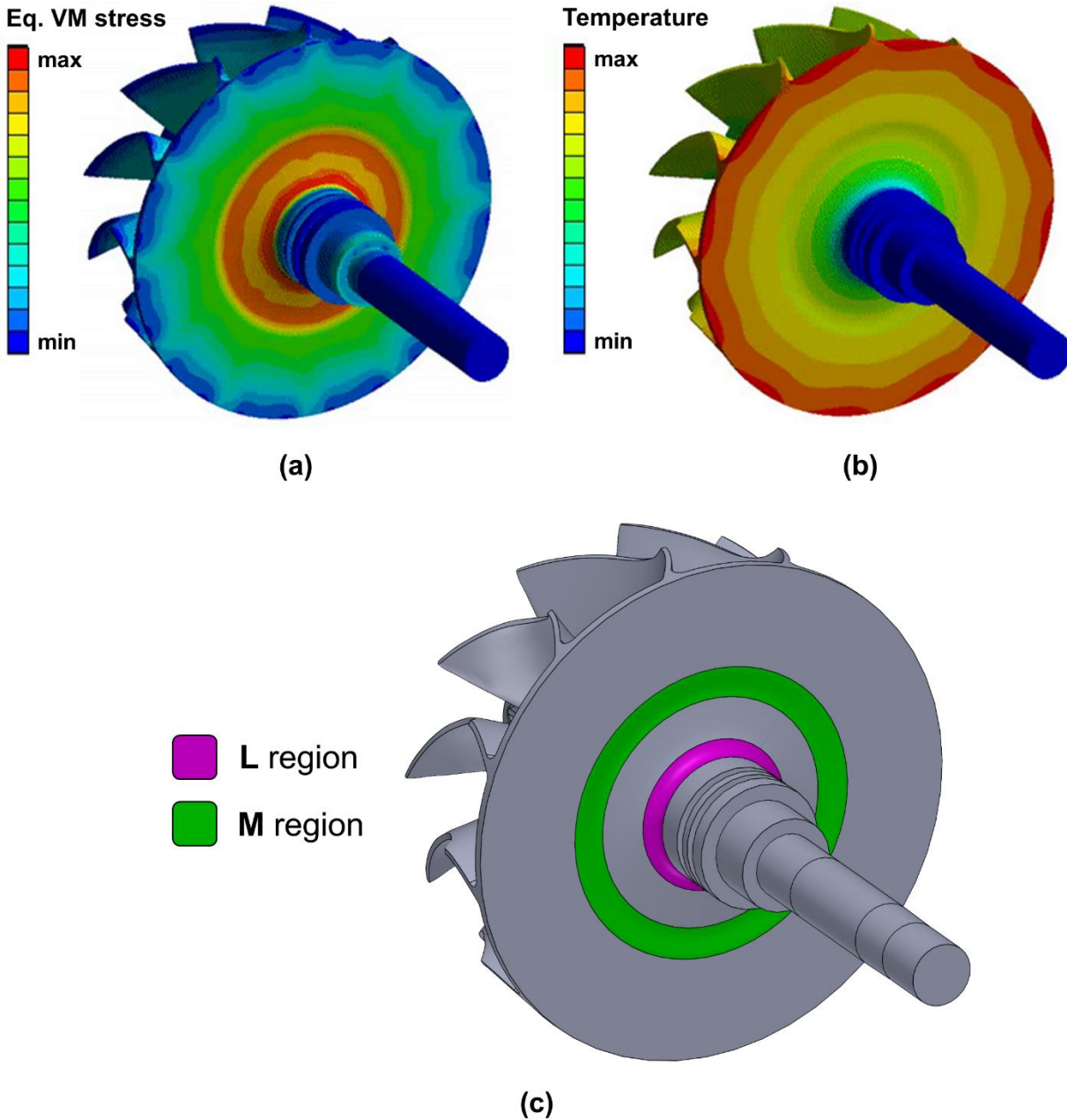
Figure 5.27   Contour plots of (a) Von Mises stress and (b) temperature on the wheel's backdisc, guiding the selection of the (c) regions of interest for the structural analysis.

In this case, two zones on the backdisc were defined, namely the *L* region and the *M* region. The *L* region is located at the low-radius part of the backdisc, close to the shaft: this is the area that shows the highest Von Mises stress values of the whole wheel. The criticality of the backdisc hub fillet zone was expected, being already assessed by literature findings [48,75]. The *M* region is another annular area located in the middle of the wheel's backdisc, at a higher radius with respect to the *L* region. The second highest stress values can be found within the *M* region, moreover, temperature is higher with respect to the hub: this means that tensile strength limits are lower in this region, possibly making it even more critical than the *L* region.

5.3.2 - Thermo-structural analysis results

Figure 5.28 shows the evolution of temperature within the *L* region for volute inlet temperature increments, while Figure 5.29 shows the same contents for decreasing-temperature transients. It is worth pointing out that, for confidentiality issues, the quantities in the following plots were normalized against the corresponding initial value.

Figure 5.28   Temperature evolution within the L region, for ramp-up transient processes.
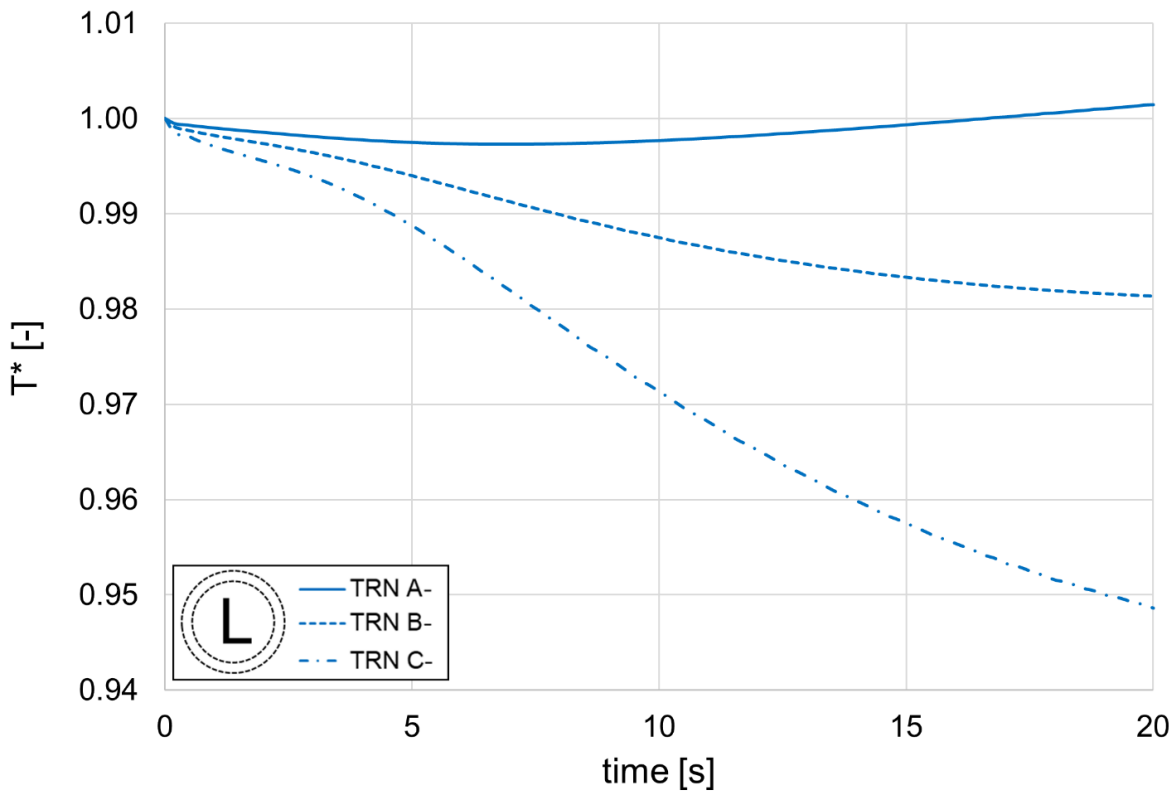
Figure 5.29   Temperature evolution within the L region, for cut-off transient processes.

Unsurprisingly, the greater the inlet temperature increment, the more rapidly temperature rises in the *L* region due to the ingestion of the hot gases inside the backdisc cavity. Analogous behavior can be observed for the cooling transients, although the *TRN A-* case shows a temperature rise towards the end of the process. This is likely due to the fact that the temperature decrement for this case is modest and unable to counter viscous heating phenomena which are particularly intense in the backdisc cavity region.

Figure 5.30 and Figure 5.31 show the evolution of Von Mises (VM) stress within the same region.

Figure 5.30   Stress evolution within the L region, for ramp-up transient processes.

Figure 5.31   Stress evolution within the L region, for cut-off transient processes.

By looking at Figure 5.30, it is apparent that the increasingly higher temperature does not raise the level of thermally-induced stress in the *L* region. On the contrary, the steeper the temperature increment, the more rapidly stresses decrease. This behavior may initially be justified by the fact that the Young's modulus slightly decreases with increasing temperature during the heating processes, thus returning lower stress values. This is reflected in Figure 5.31, where the same behavior can be observed, although in the opposite way. The main underlying phenomenon behind these results, however, is likely related to the temperature distribution in the backdisc fillet area. Indeed, the *L* region stands between the low-temperature shaft area and the high-temperature backdisc: in stationary conditions (i.e. pre-transient conditions), thermal equilibrium is achieved and a high temperature gradient area is located at a certain position (Figure 5.32).
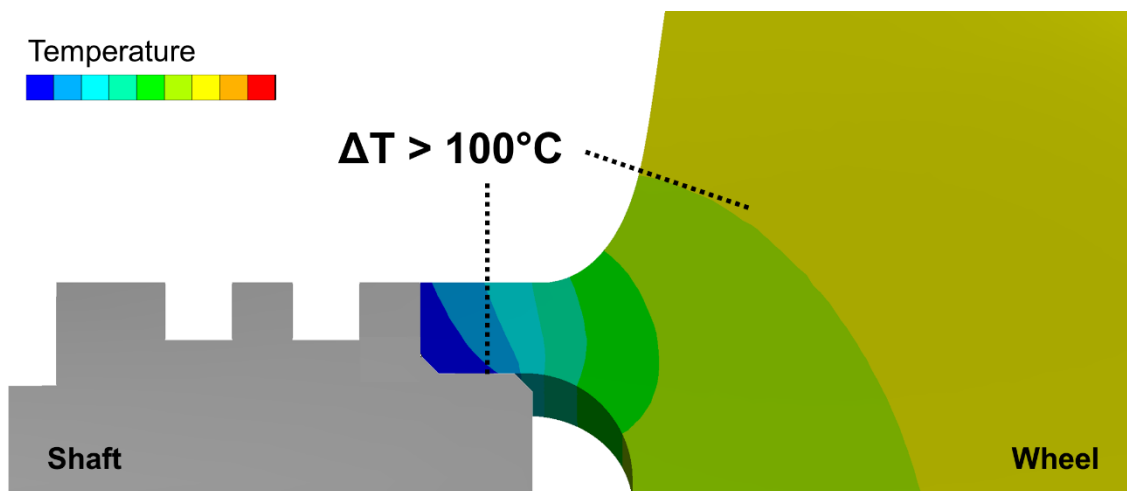
Figure 5.32   Temperature gradient in the backdisc hub fillet area.

In case of a heating transient, the high gradient zone shifts towards the shaft, at a lower radius. Therefore, thermally-induced stresses (which are mainly caused by strong temperature gradients) concentrate in a zone with lower centrifugal stress. On the contrary, in case of cooling transient, the high gradient zone shifts towards a higher radius, therefore combining with stronger centrifugal stress.

 In any case, decreasing stress trend over time can be observed: this is due to the internal conduction phenomena that tend to smoothen temperature gradients within the region. For the same reason, the stress curves of different transient processes tend to converge after a certain amount of time.

Figure 5.33 and Figure 5.34 show the evolution of temperature within the *M* region for the same transient processes.
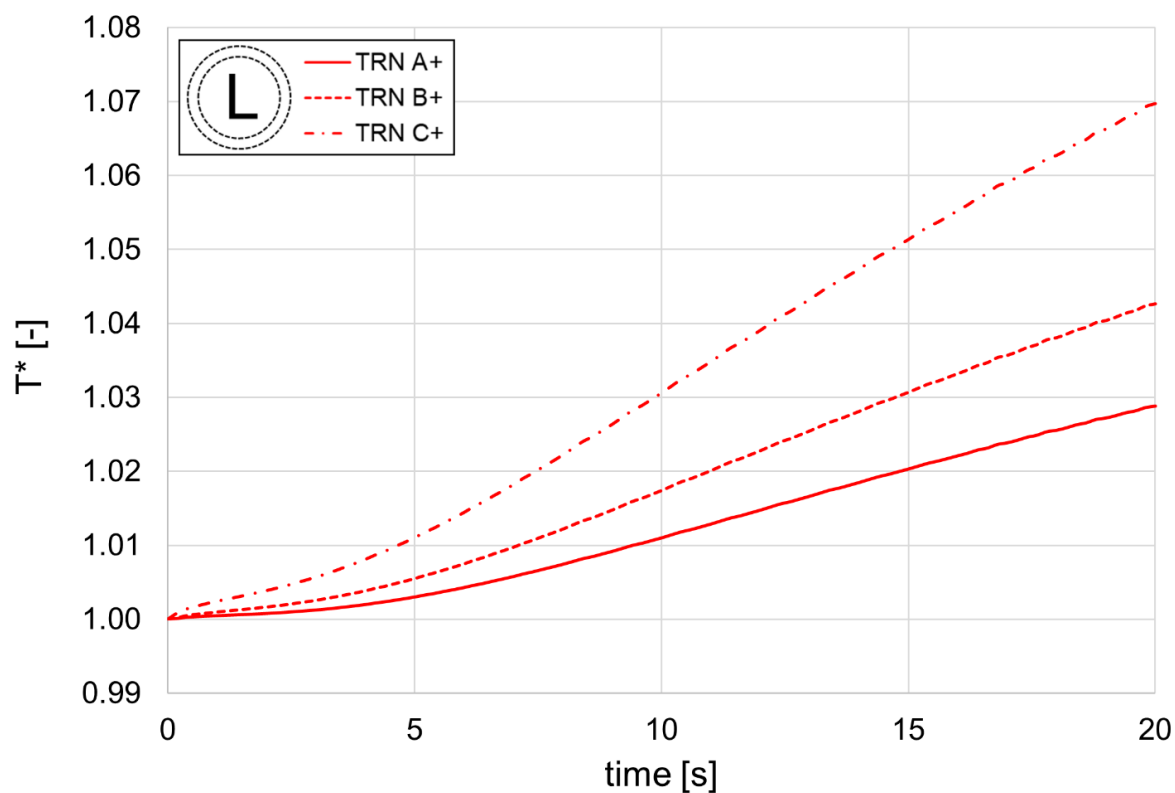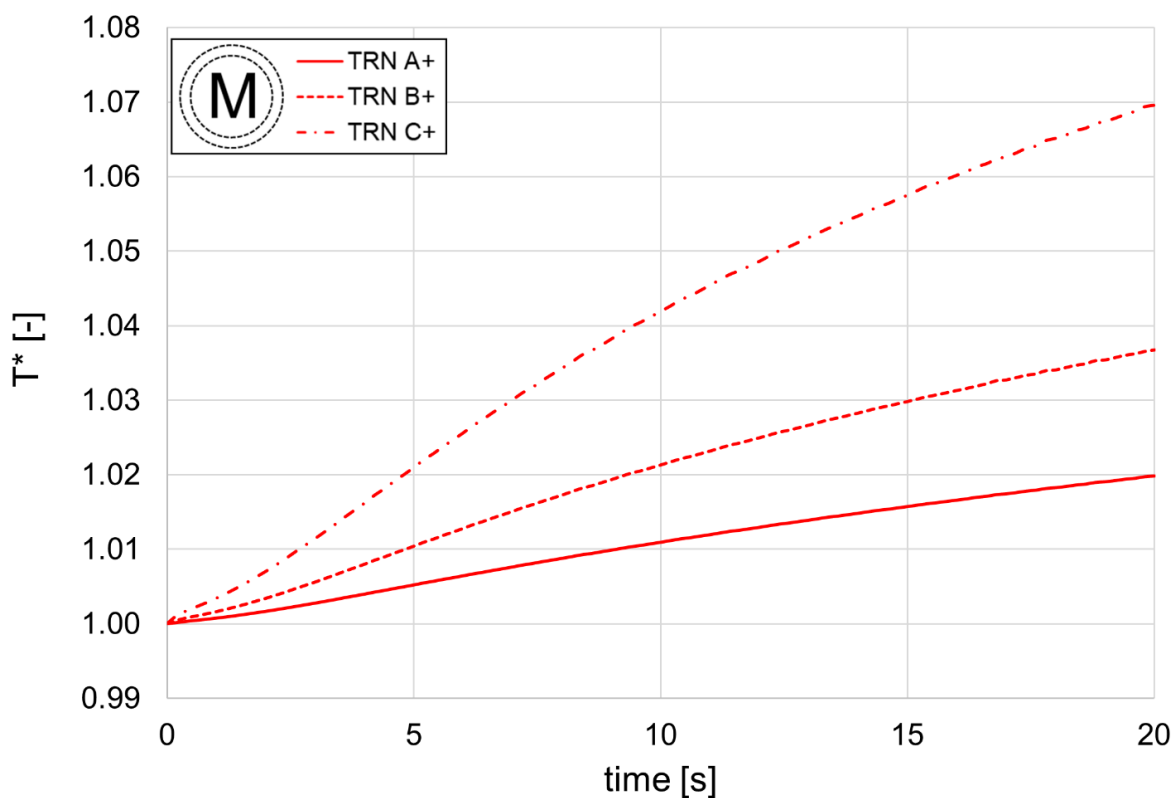
Figure 5.33   Temperature evolution within the M region, for ramp-up transient processes.
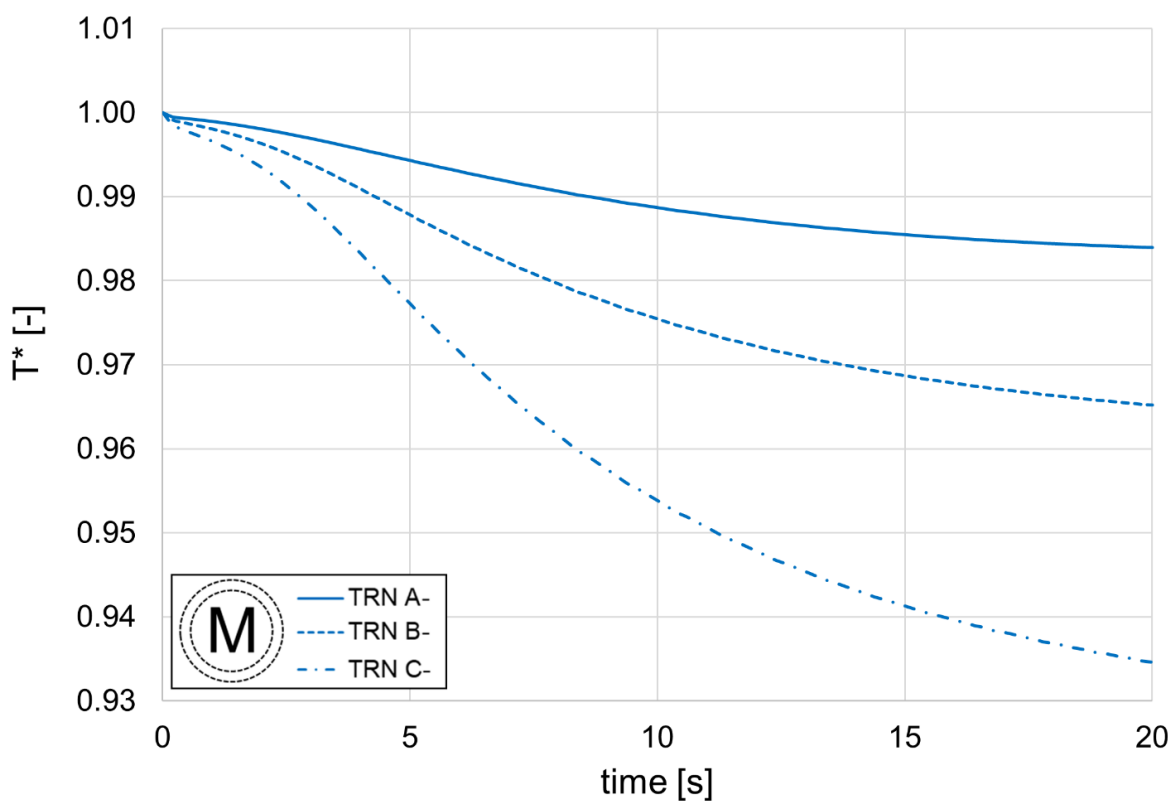
Figure 5.34   Temperature evolution within the M region, for cut-off transient processes.

Such results were, again, expected, but it's still worth pointing out that this region responds to thermal transients more rapidly than the *L* region. Indeed, heat transfer is enhanced in the *M* region because of the higher radius and therefore higher cavity flow velocity.

Figure 5.35 and Figure 5.36 show the evolution of Von Mises stress within the *M* region.
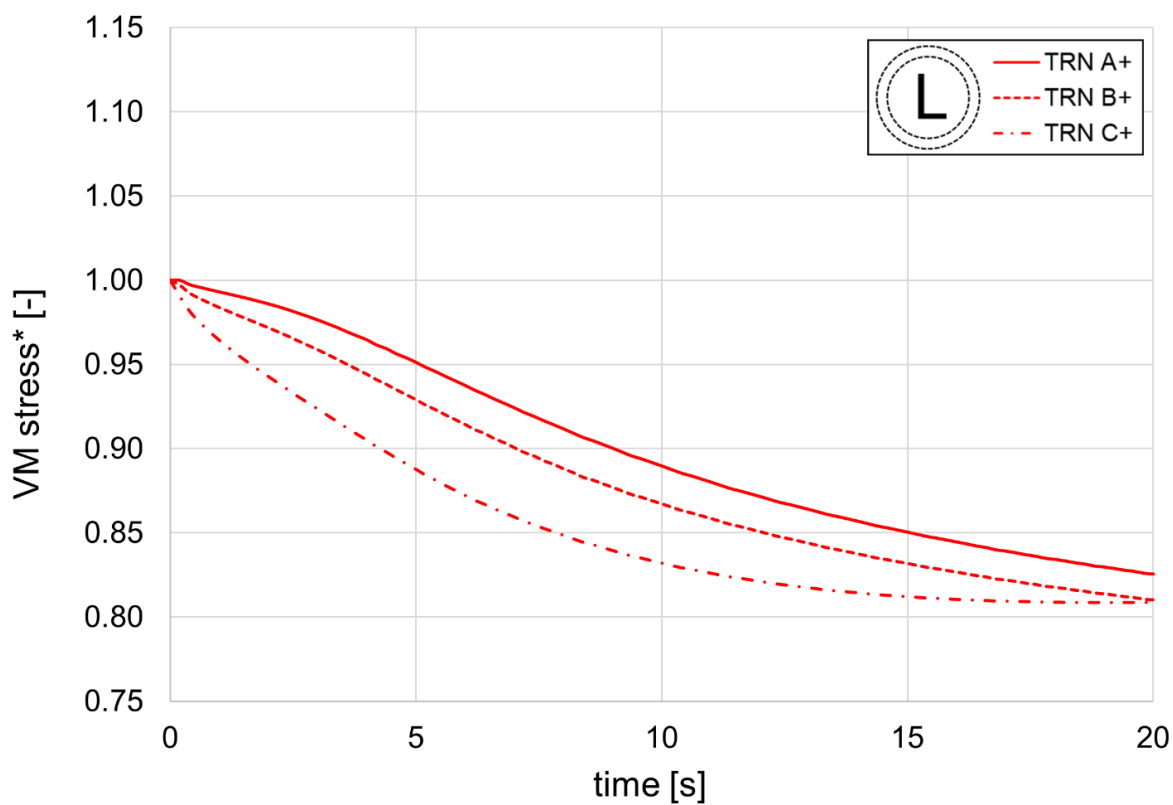

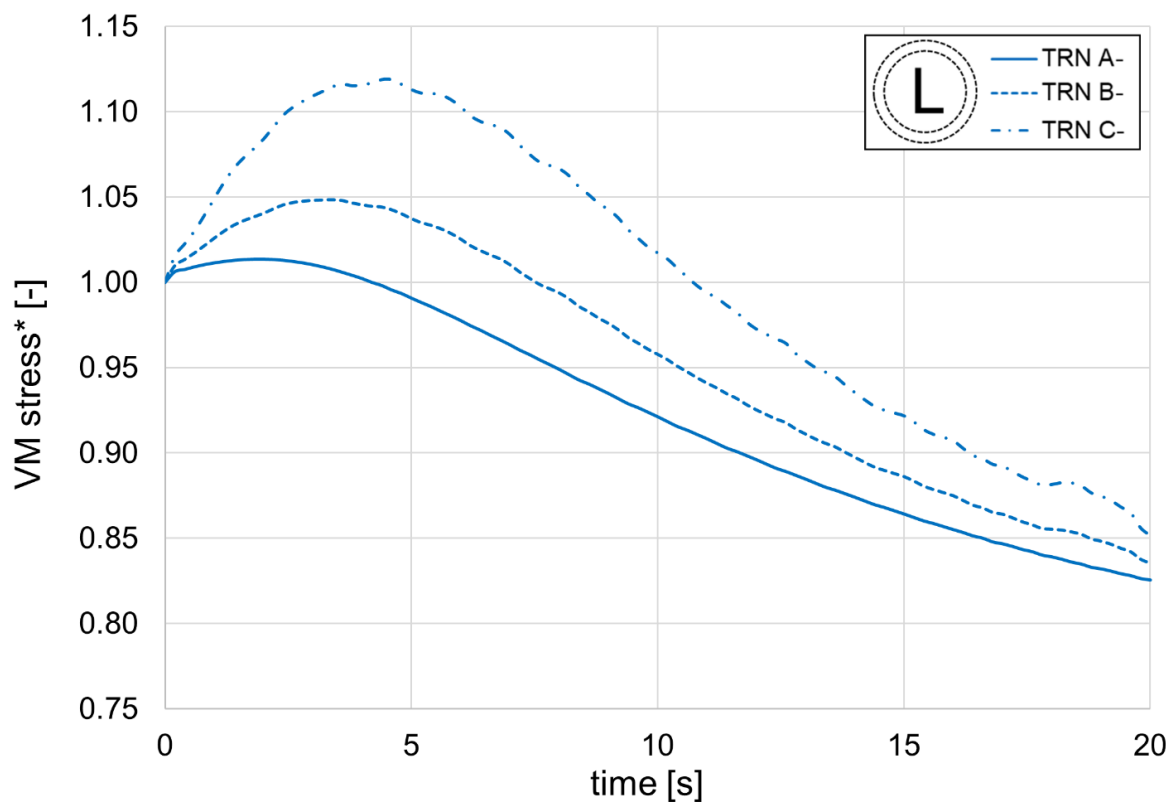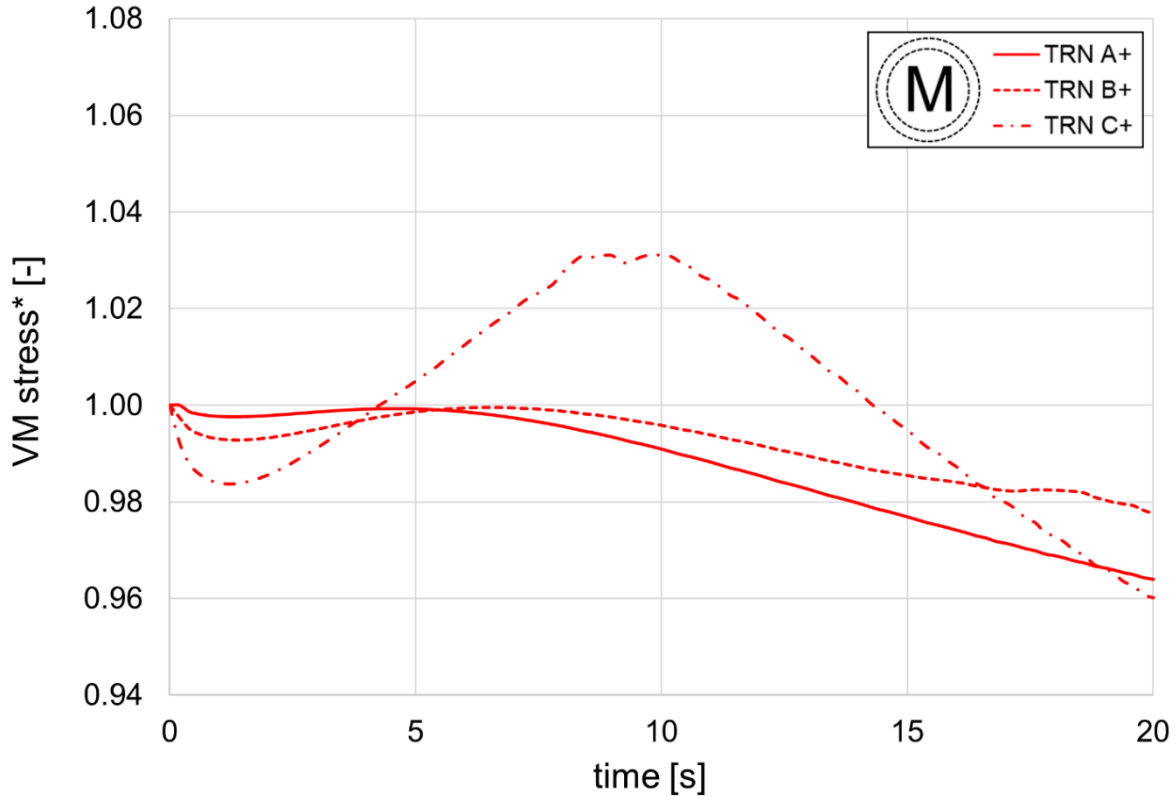**Figure 5.35   Stress evolution within the M region, for ramp-up transient processes.**
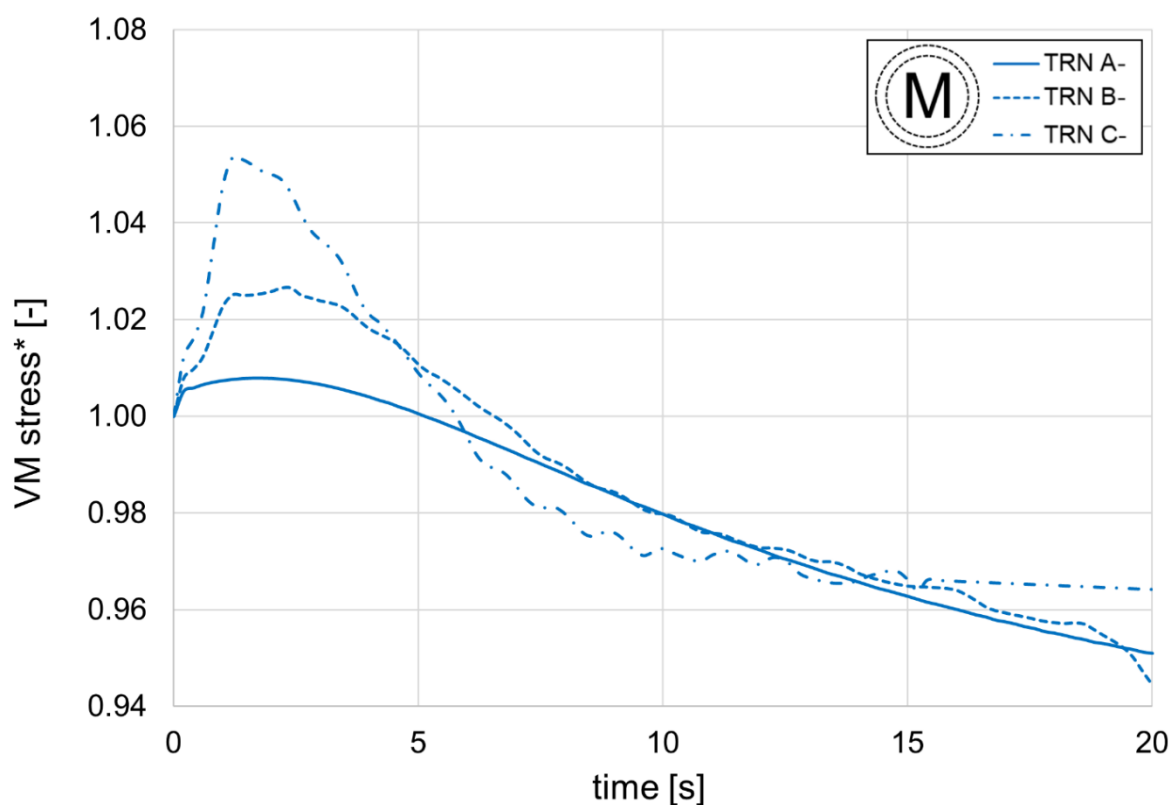
Figure 5.36   Stress evolution within the M region, for cut-off transient processes.

The *M* region, located at a higher radius with respect to the *L* region, shows a structural behavior that is dominated by centrifugal stress. Indeed, overall, thermally-induced stresses have here moderate effects: from transient start to end, VM stress variations of roughly 5%, against the 20% of the *L* region (Figure 5.30 and Figure 5.31), can be appreciated. Nonetheless, heating and cooling effects are by all means non-negligible: especially at the beginning of the transient phase, before the temperature gradients are smoothed by internal conduction, strong heating or cooling may cause high local thermal gradients which result in stress peaks.

In conclusion, the evolution of stress as a function of temperature is presented, for both heating and cooling transient processes within the two regions of interest. Figure 5.37 and Figure 5.38 refer to the *L* region.
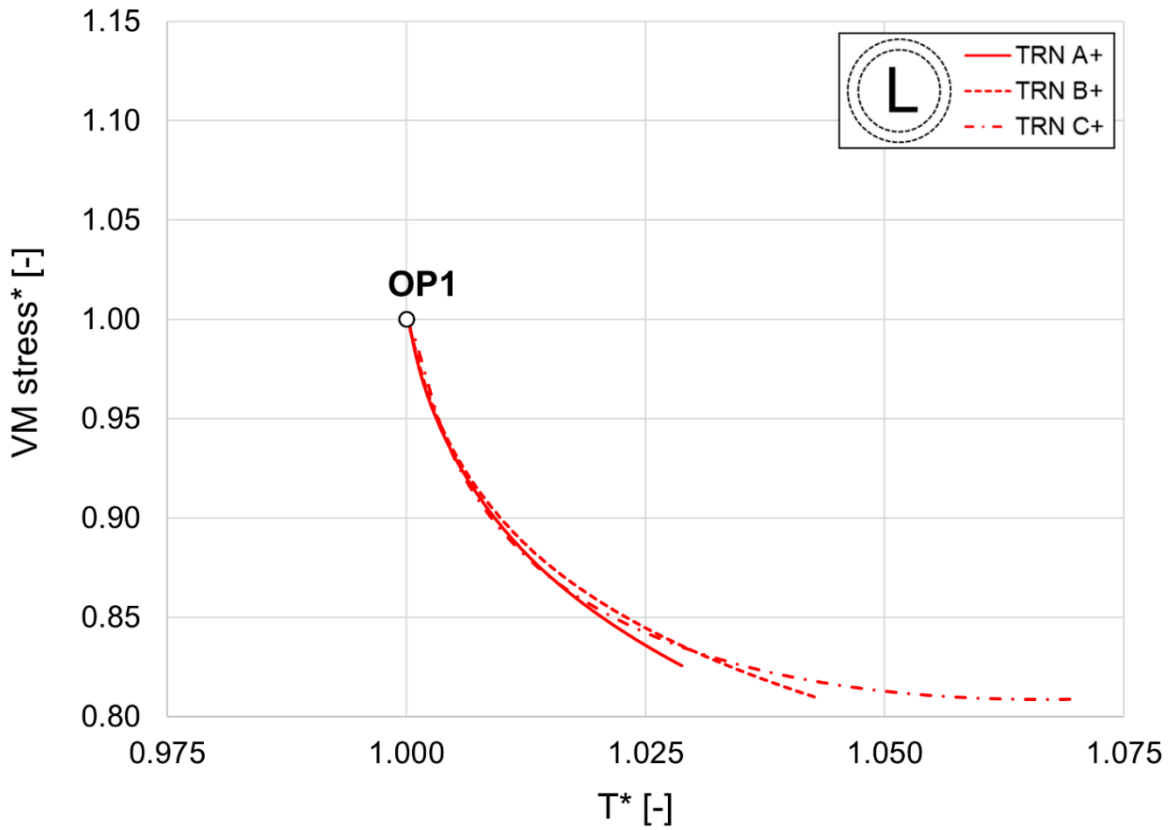
Figure 5.37   Stress as a function of temperature for the L region, for ramp-up transient processes.
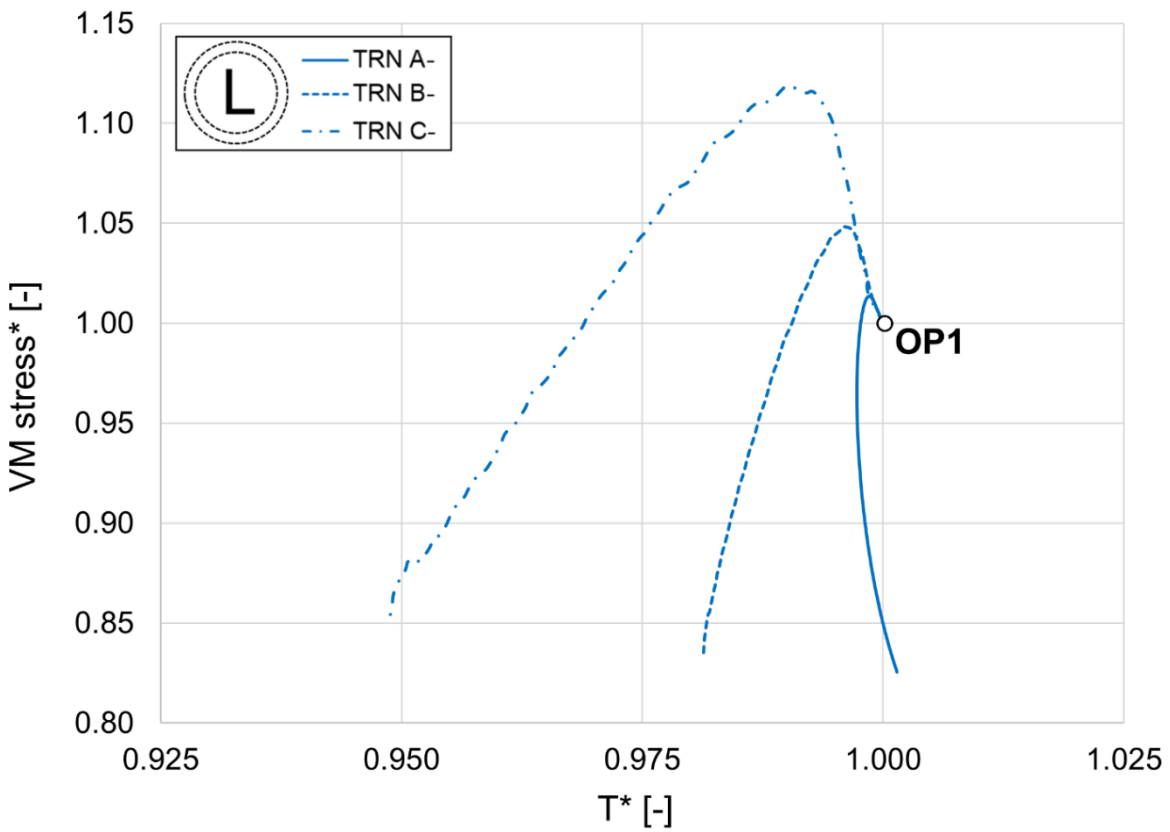
Figure 5.38   Stress as a function of temperature for the L region, for cut-off transient processes.

Within the *L* region, it's interesting to notice how heating transient processes always show roughly the same stress values, regardless of their intensity. Cooling processes eventually reach the same stress conditions, but show different behavior depending on their intensity. Indeed, a strong cooling of the turbine inlet flow may be critical to the backdisc hub region, even more than a sudden temperature rise.

Figure 5.39 and Figure 5.40 show the evolution of stress as a function of temperature for the *M* region.
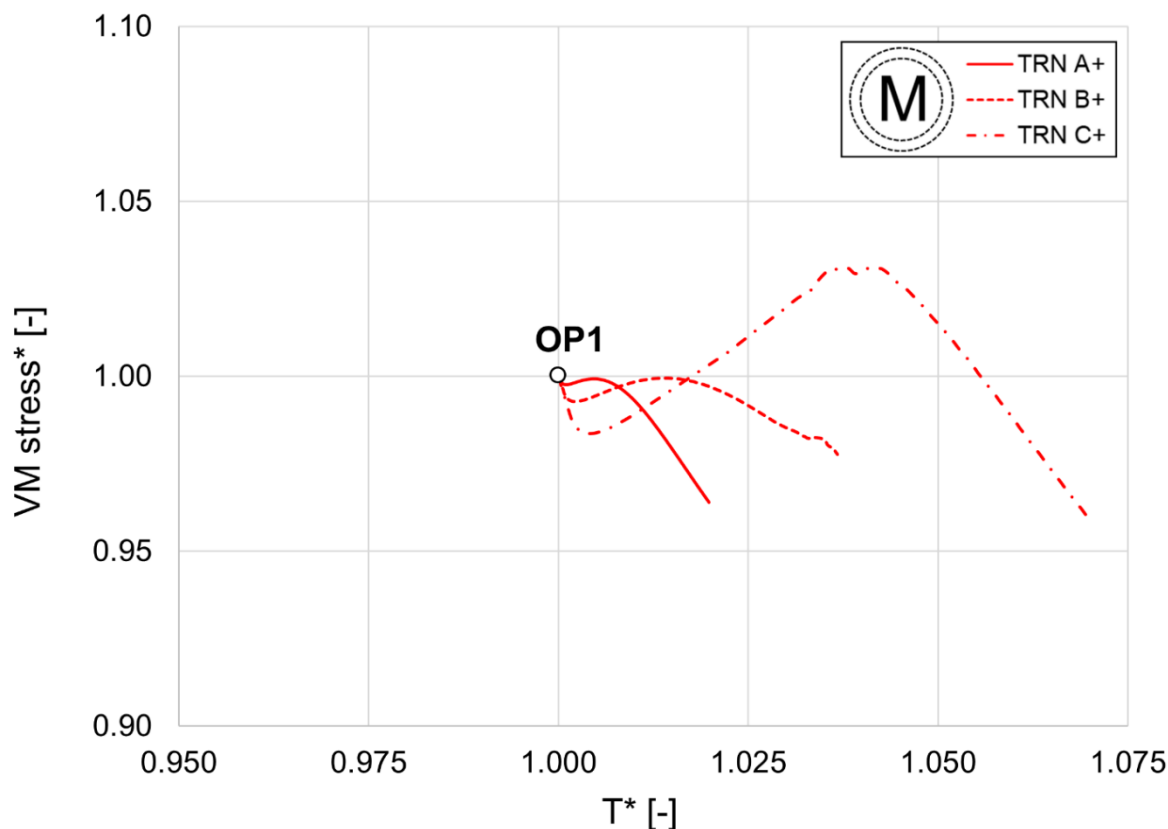
Figure 5.39   Stress as a function of temperature for the M region, for ramp-up transient processes.
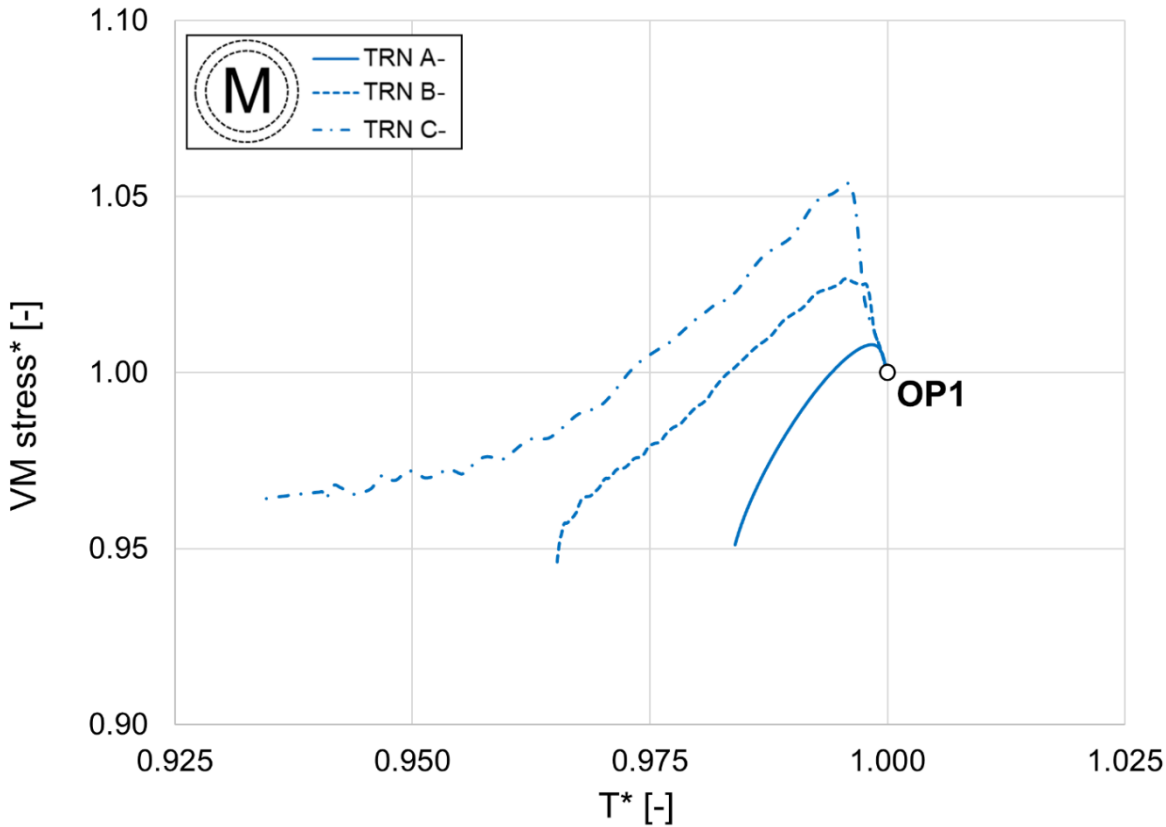
Figure 5.40   Stress as a function of temperature for the M region, for cut-off transient processes.

As previously discussed, stress variations due to thermal transients are moderate within this region. Again, initial stress peaks are an issue in case of strong cooling processes but, unlike in the *L* region, a stress surge can be observed also for the most intense heating process. Overall, given the limited stress variations, heating processes are critical within the *M* region simply because the higher temperature determines lower tensile strength.

Through post-processing within ANSYS® Mechanical® framework, the wheel's deformation due to thermal and centrifugal loads can also be appreciated. Figure 5.41 shows a detail view of the turbine's blade deformations, by overlapping the undeformed (i.e. cold) geometry, depicted in light grey, to the deformed configuration at the end of the most intense ramp-up (red) and cut-off (blue) processes. The deformation of the blade can be observed in the circumferential direction as a small, but sensible, deflection in the direction of rotation. A significant deformation in the radial direction can also be appreciated: indeed, the deformed blades appear elongated. Both deformations are more relevant at higher temperature and the reasons for this are twofold. Firstly, thermal expansion is more severe at higher temperature. Secondly, although the rotational speed (and therefore the centrifugal force) is the same for every analyzed transient process, Young's modulus slightly decreases with increasing temperature: therefore, at higher temperature, the same stress causes a greater deformation.

TRN C+
t=20 s

TRN C-
t=20 s
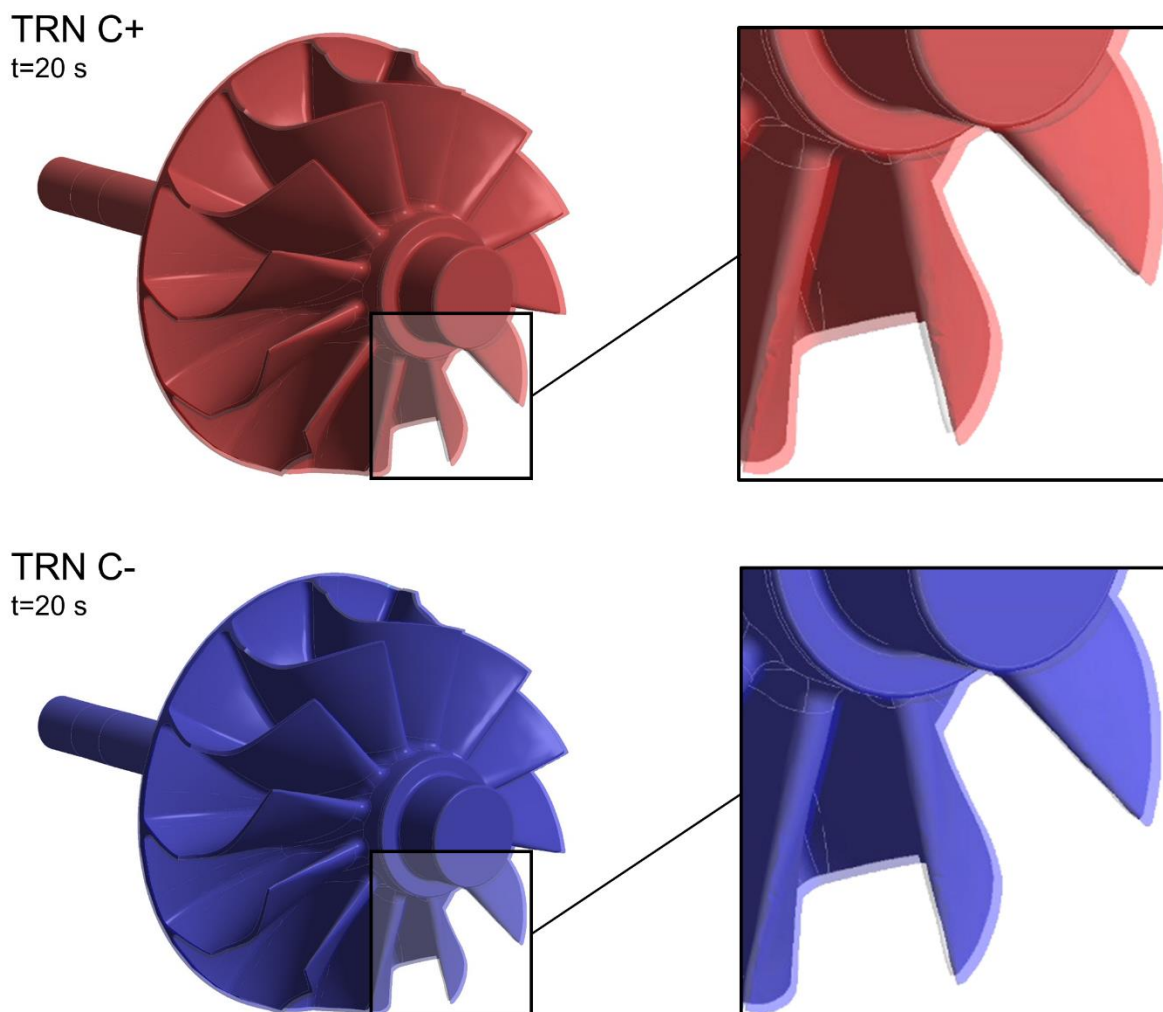
Figure 5.41   Detail view of the blade's deformation for two transient processes.

Moving from the considerations above, the radial elongation of the blades towards the turbine's housing represents a critical issue and the "cold" tip clearance height must be selected accordingly. Figure 5.42 shows the evolution of the tip clearance height for all the analyzed transient processes. For confidentiality reasons, tip clearance is expressed as a percentage of the tip clearance height of the undeformed, cold configuration. The plot shows that, the higher the temperature, the higher the blades' deformation and the lower the tip clearance height. On the contrary, cut-off processes result in an increased tip clearance height with respect to the starting steady-state operating point.
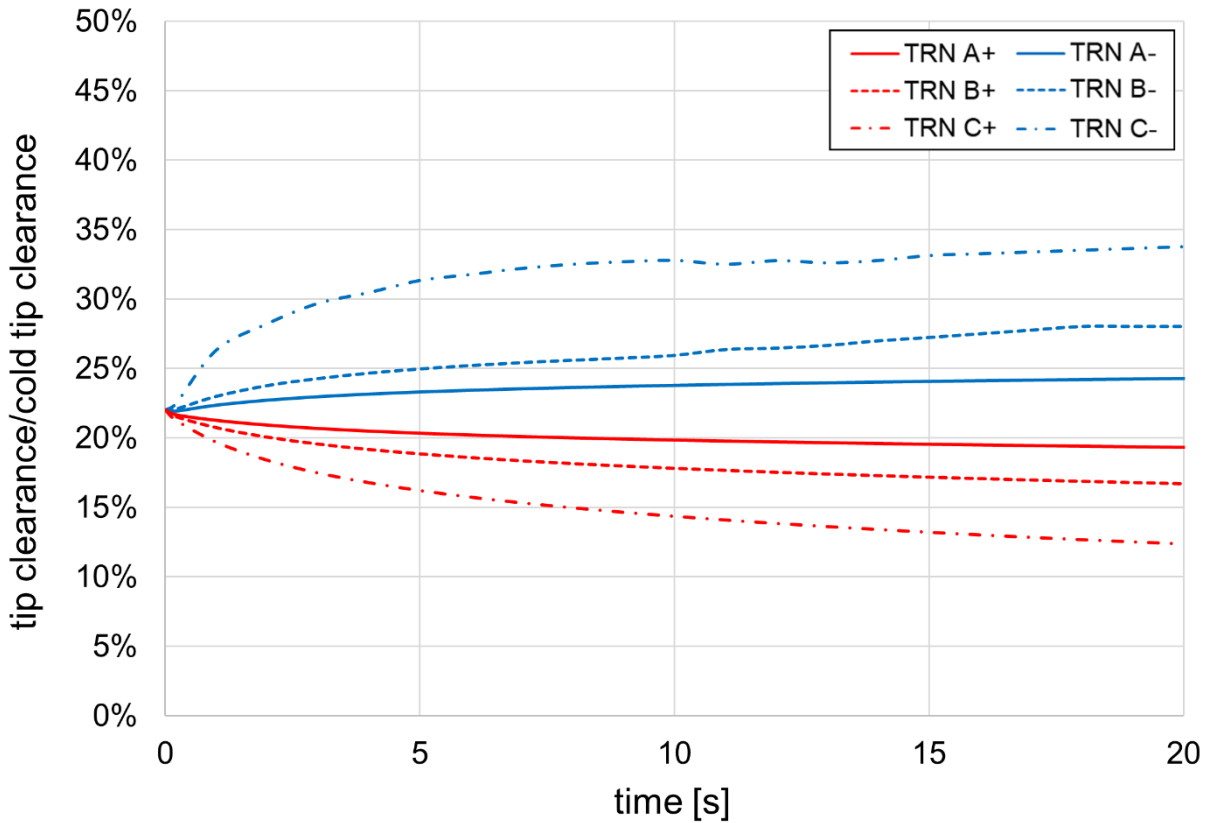
Figure 5.42   Evolution of the tip clearance height for the analyzed transient processes.

As a final remark, the calculation time (in terms of hours) of the adopted thermal transient approach, compared to the one of an unsteady CHT calculation, is shown in Table 5.7.

Approach	Steady-state CHT	Steady-state CFD	Thermal transient (CHT)	Thermal transient (solid domain)	Structural transient	Total
Transient CHT	x	x	$\sim 10^5$ h	x	0.5 h	$\sim 10^5$ h
Transient-BC-FVM	96 h	32 h	x	0.2 h	0.5 h	~ 128 h

Table 5.7   Computational time estimation of different thermal transient modelling approaches.

The evaluation of calculation time was performed based on the mesh settings and computational resources employed in the present activity. Calculation time can be reduced by employing coarser meshes and increasing the computational power, however, it is apparent that a straightforward transient CHT approach is unfeasible for this application.

6 - Aerodynamic optimization

6.1 - Case study

The engine under consideration is a 4-cylinder, 3000 cm^3 diesel unit featuring a rated power of 51 kW. The tested turbocharger unit was the one provided by the supplier for the engine under study, without any modification. Even though it is apparently not possible to declare the turbocharger model and its details, it is worth stating that the compressor wheel has a diameter of 51 mm and features 7 main and 7 splitter blades. The turbine is of single entry type: its wheel has a diameter of 43 mm and features 11 blades. Figure 6.1 shows the compressor and turbine stages of the turbocharger.

(a) **(b)**
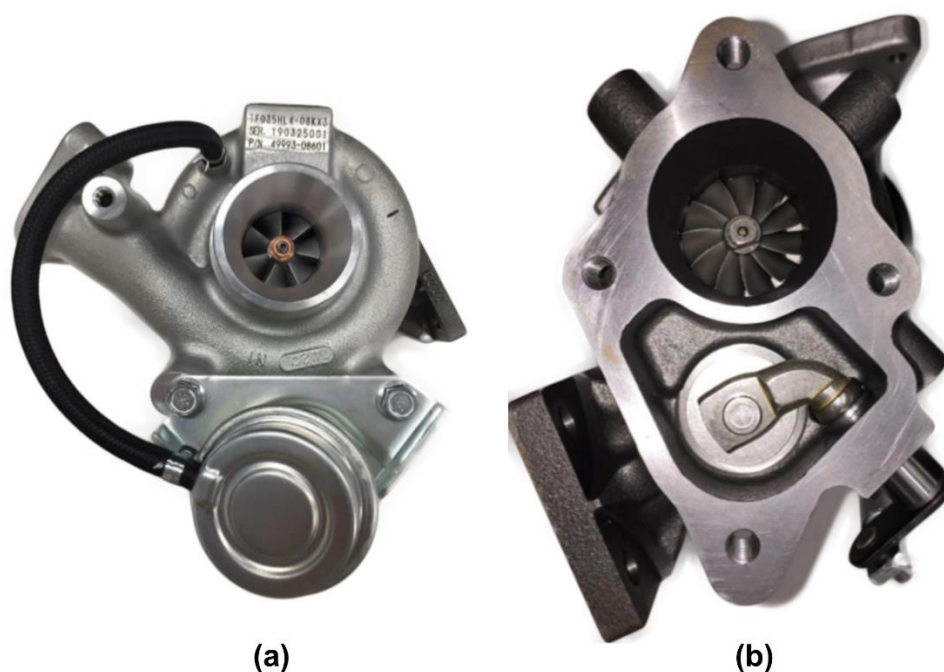
Figure 6.1   Test case (a) compressor and (b) turbine stage.

Experimental tests on the baseline turbocharger represent one of the point of strengths of the present study, allowing to thoroughly test the accuracy of the numerical approach that was adopted. Tests were commissioned by the industrial partner to a worldwide-recognized external company. The thermodynamic conditions of air declared by the testing company were ambient temperature for the compressor, while the turbine inlet temperature was maintained at 600 °C. The wastegate valve of the turbine was kept closed. Data acquisition for the performance evaluation was achieved by means of pressure and temperature sensors located inside straight pipes at 200 mm from the compressor and turbine inlets, and at 300 mm from the compressor and turbine outlets. A through-bore speed sensor was fitted inside the compressor and used to

measure the rotating speed of the turbocharger. Figure 6.2 and Figure 6.3 show the available performance maps of the compressor stage, obtained by means of experimental testing.
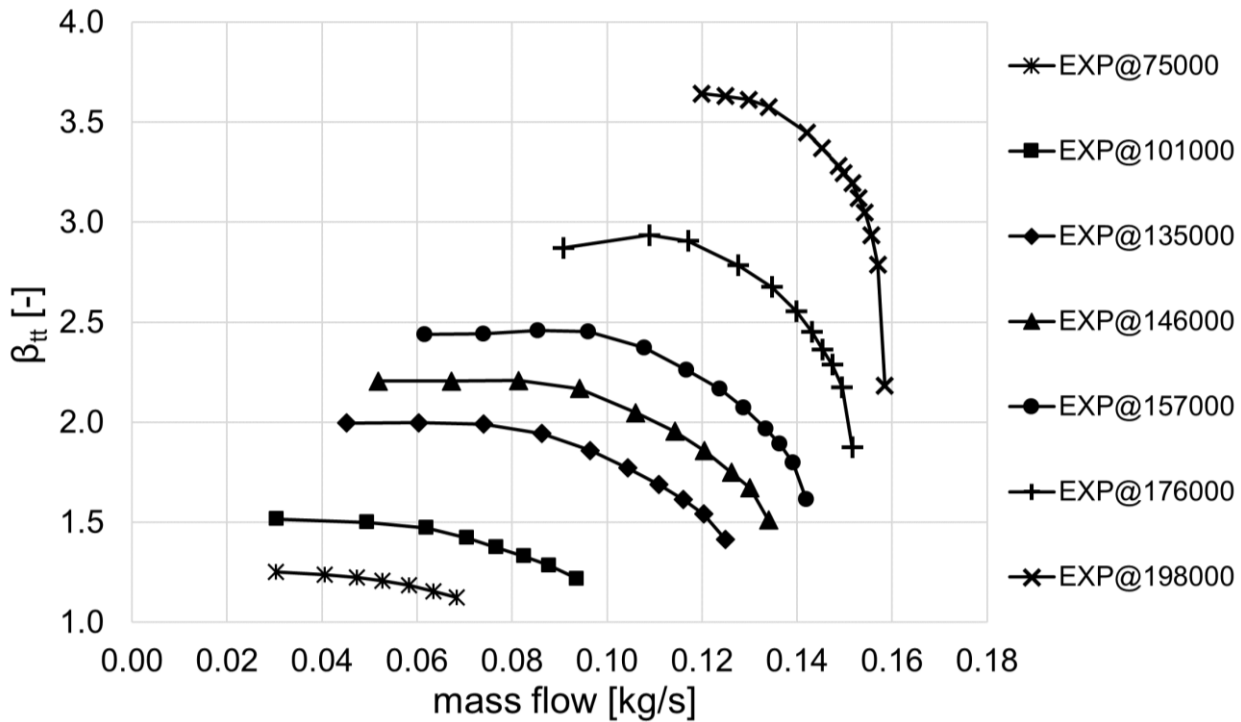
Figure 6.2   Compressor stage total pressure ratio speedlines.
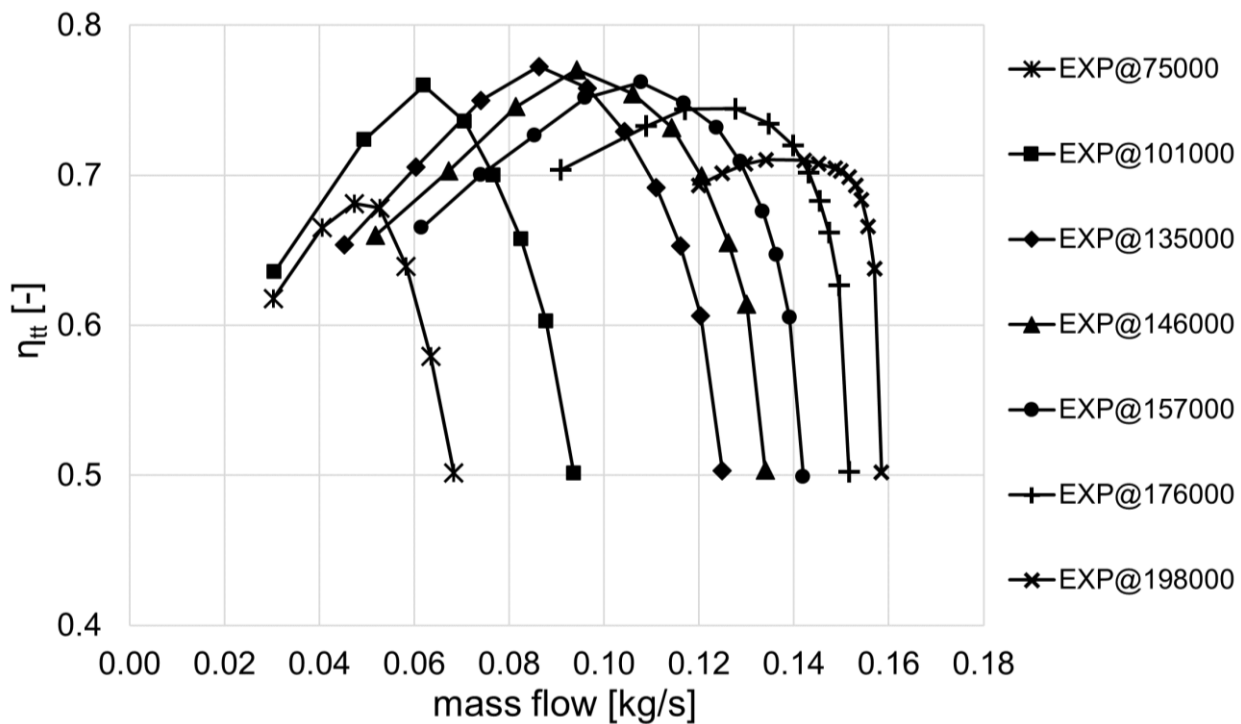
Figure 6.3   Compressor stage total-to-total efficiency speedlines.

6.2 - Methods

6.2.1 - Workflow overview

The goal of the present activity is to define an integrated procedure for optimizing the aerodynamic design of the compressor's static parts for use in a stationary engine application. Figure 6.4 schematically shows the workflow of the optimization process.
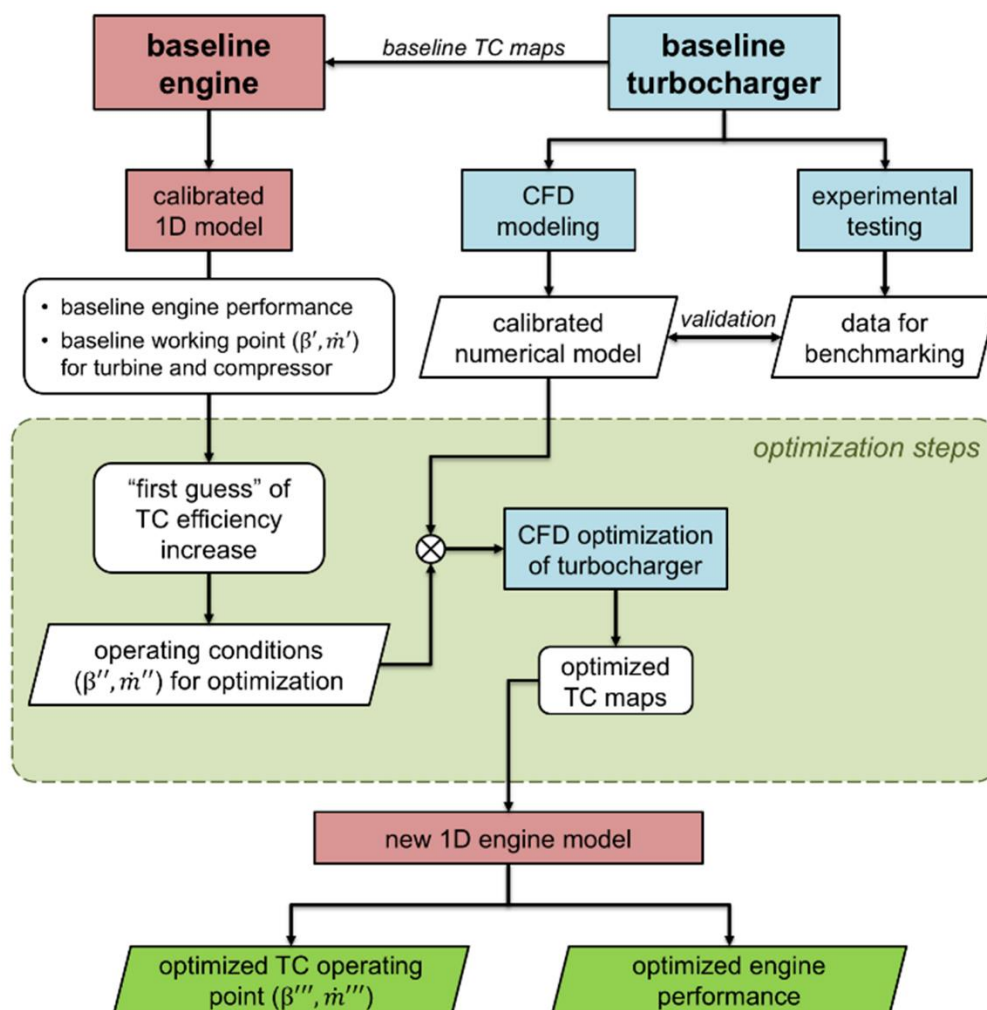
Figure 6.4   Optimization activity workflow.

As anticipated, the starting point was a commercial turbocharged engine provided by the industrial partner. This makes use of a turbocharger unit provided by an external supplier and selected with common matching criteria as the unit that best fit the application requirements. The matching was based on the turbocharger's performance maps provided by the supplier, embedded into a 1D model of the engine, developed in GT-POWER® framework, a state-of-the-art 1D tool which includes specific sub-models for combustion analysis, emissions, etc. [94]. The model was calibrated and experimentally validated by Yanmar, being therefore fully representative of the original engine. The same simulation framework was used throughout the present study in order

to allow for the fluid dynamic connection that links the reciprocating engine with the turbomachine, represented within the model by its operating maps.

For the aerodynamic optimization of the static parts of the compressor stage, a high-fidelity, three-dimensional CFD model was employed. In order ensure that the numerical model was suitable for the scope, the supplied turbocharger was tested in a dedicated test rig and the experimental measurements were used as a benchmark for the calibration of the CFD models.

Once the two main simulation frameworks were developed, a key point of the proposed approach was the development of a strategy to account for the mutual influence between the modified aerodynamic performance of the turbocharger and the engine performance, leading in turn to a change in the boundary conditions between the two. More specifically, if one optimizes the turbocharger for the inlet conditions referring to the engine working point in its baseline configuration (β',$\dot{m}'$), the new performance of the turbocharger would lead to a mismatch between the optimized system and its new working conditions.

To overcome this issue with a reasonable computational cost, a "first guess" strategy was adopted as follows:

1. an expected increase of efficiency of the compressor is reasonably hypothesized;
2. the new engine operating point under the new "first guess" maps of the turbocharger is estimated with the 1D model;
3. this new operating point allows the determination of modified boundary conditions in terms of target pressure ratio, mass flow rate and rotating speed (β'',$\dot{m}''$,n'') to be used in the optimization activity;
4. the optimized design of the turbocharger is defined;
5. once new performance is calculated, steps 2-4 can be repeated until convergence.

Focusing more specifically on the aerodynamic optimization process, the compressor stage, featured with all the static parts (i.e. scrolls, diffuser and inlet/outlet ducts) and the clearance at the impeller blades' tip, was investigated to obtain the optimized performance parameters (β''',$\dot{m}'''$) to be used as the main input of 1D the engine model.

6.2.2 - 1D engine model

The 1D model used for the study was the one realized and experimentally calibrated by the industrial partner for its baseline engine within GT-POWER® environment. Therefore, it can be considered fully predictive of the engine performance. Figure 6.5 shows an overview of the 1D engine model, featuring the engine subsystem and the compressor and turbine blocks that represent the turbocharger.
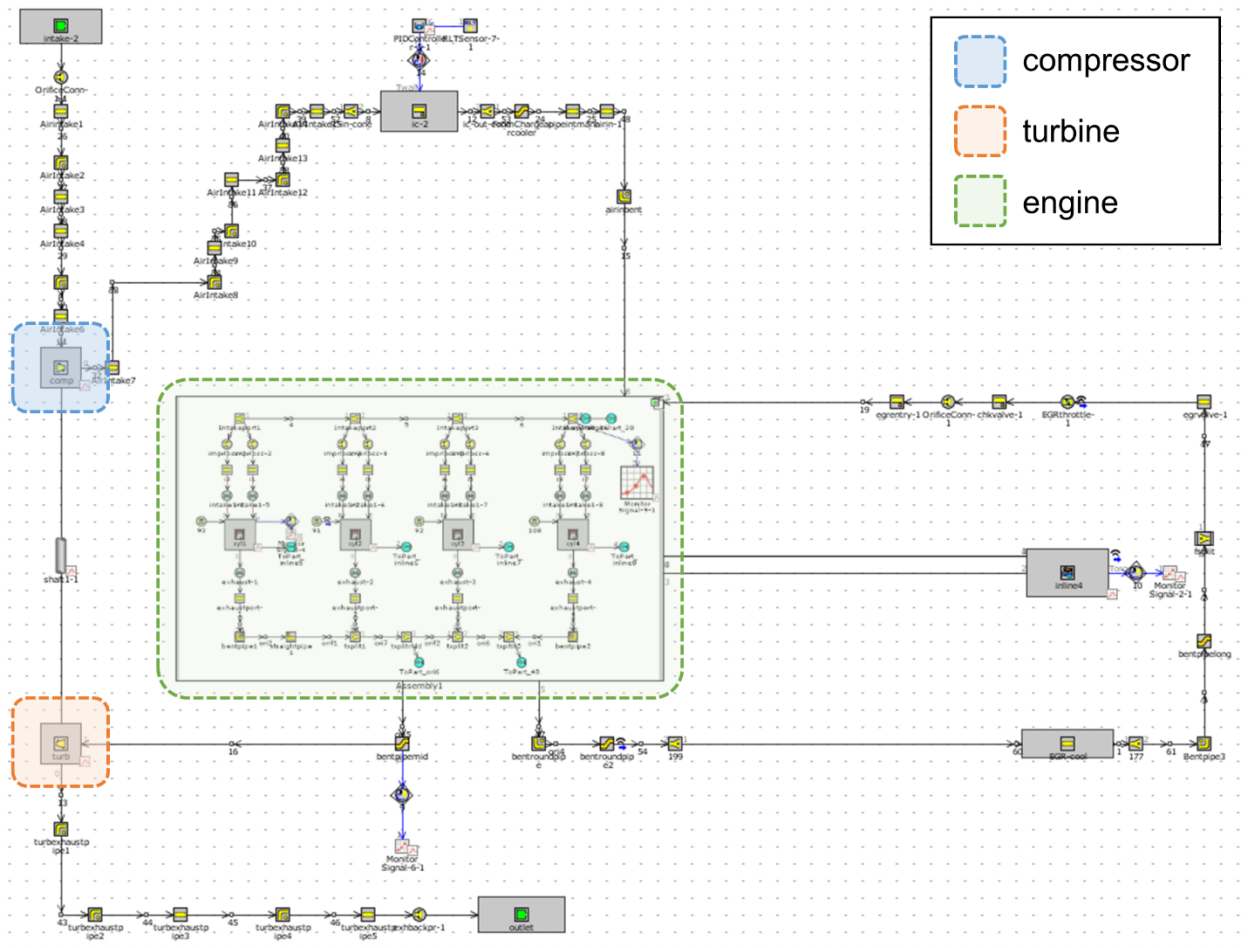
Figure 6.5   1D engine model within GT-POWER® simulation framework.

Following the common practice of the present simulation environment, turbocharger maps were implemented within the 1D model as look-up tables. By doing so, for the target design point in terms of load (i.e. torque) and speed of the stationary engine, the 1D calculation is able to return the operating conditions of the turbocharger in terms of mass flow, rotating speed, inlet and outlet temperature and pressure. Further details about the engine subsystem are not available due to non-disclosure agreement with the industrial partner. It is also worth noting that, since the test case is a large 4-cylinder engine running at a constant, low revolution speed, the fluctuation of turbine mass flow and rotating speed were roughly ±5% and ±2%, respectively. Such low variability allowed to reasonably perform a time averaging of the quantities to obtain the boundary conditions for the 3D CFD analysis.

6.2.3 - 3D CFD compressor stage model

The commercial code ANSYS® CFX® was used for the analysis of the compressor stage and for the optimization of its static parts. The selection of this software, very common for these applications, is due to the great flexibility in handling complex geometries. A steady-state RANS approach, using a pressure-based formulation of the solver, was adopted. The shear stress

transport (SST) turbulence model [44] was used, together with an automatic near-wall treatment that allows the solver to overcome mesh resolution requirements by gradually switching between wall functions treatment and low-Re formulations [92]. A high resolution, second order upwind scheme was used for the spatial discretization of the RANS and turbulence equations.

The computational domain for the stage analysis, based on the mixing plane approach, includes the volute geometry and a single blade passage of the rotor with cyclic boundaries, featuring hub fillets and tip clearance. Figure 6.6 shows the computational domain and its boundaries.
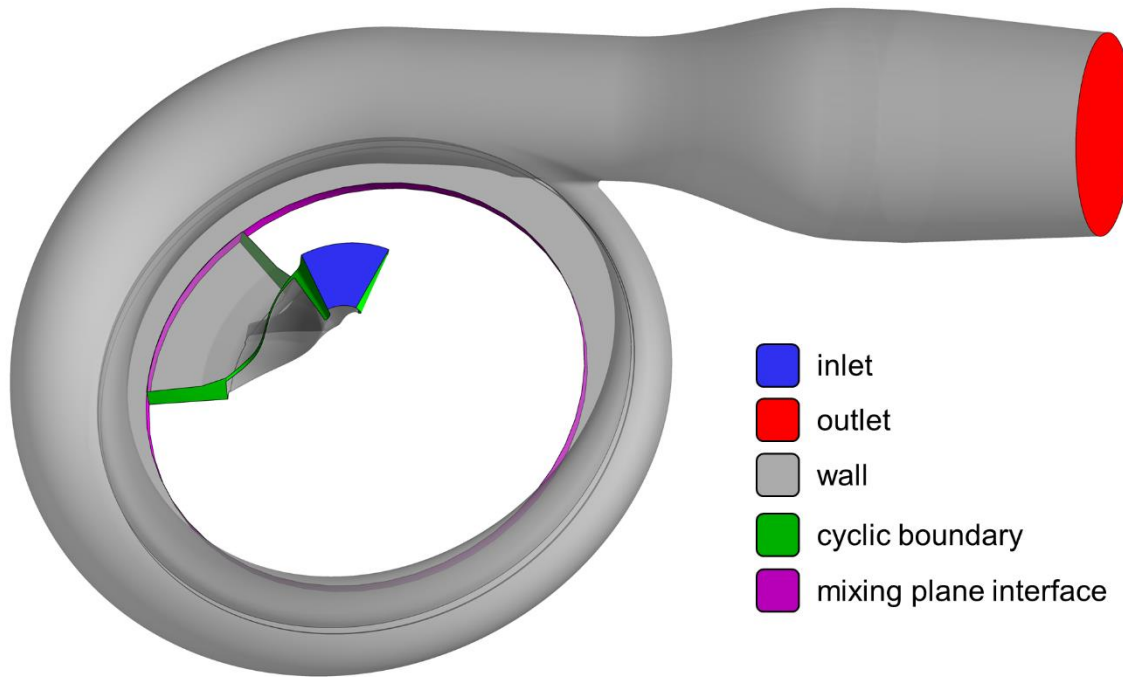
Figure 6.6   Compressor stage computational domain and its boundaries.

The flow inside the blade passage of the wheel is solved in the relative frame and a mixing plane rotor-stator interface is set between the volute and the blade passage. The exit of the compressor volute has been slightly pinched, in order to prevent flow separation at the outlet section. Mass flow rate and total temperature were imposed at the inlet boundary, while static pressure was set at the outlet boundary. These values were set according to the results of the 1D engine simulations. The walls, both stationary and rotating, were set as adiabatic. For the simulations, the fluid was set as air (ideal gas), with temperature-dependent specific heat capacity at constant pressure, as shown in Eq. (6.1). Table 6.1 shows the coefficients of Eq. (6.1).

$$c_p(T) = [A_0 + A_1 \cdot T + A_2 \cdot T^2 + A_3 \cdot T^3 + A_4 \cdot T^4] \cdot R_{gas} \qquad (6.1)$$

Coefficient	A_0	A_1	A_2	A_3	A_4	R_{gas}

Unit	-	K^{-1}	K^{-2}	K^{-3}	K^{-4}	$J\,kg^{-1}K^{-1}$
Value	3.692	$-1.675 \cdot 10^{-3}$	$4.299 \cdot 10^{-6}$	$-3.107 \cdot 10^{-9}$	$7.650 \cdot 10^{-13}$	287.05

Table 6.1   Cp correlation coefficients.

Concerning transport properties, both dynamic viscosity (μ) and thermal conductivity (k) were calculated as a function of temperature through Sutherland's law (Eq. (6.2) and Eq. (6.3)). Table 6.2 shows Sutherland's law coefficients for the fluid's transport properties.

$$\mu(T) = \mu_0 \frac{T_{ref}+S}{T+S}\left(\frac{T}{T_{ref}}\right)^n \tag{6.2}$$

$$k(T) = k_0 \frac{T_{ref}+S}{T+S}\left(\frac{T}{T_{ref}}\right)^n \tag{6.3}$$

Quantity	μ				k			
Coefficient	μ_0	T_{ref}	S	n	k_0	T_{ref}	S	n
Unit	$kg\,m^{-1}s^{-1}$	K	K	-	$W\,m^{-1}K^{-1}$	K	K	-
Value	$1.716 \cdot 10^{-5}$	273.15	110.4	1.5	$2.436 \cdot 10^{-2}$	273.15	110.4	1.5

Table 6.2   Sutherland's law coefficients for transport properties.

The computational grid, of unstructured and hybrid type, was generated with ANSYS® Meshing®. A tetrahedral-based grid was adopted in the core flow region, with the addition of prismatic elements in the boundary layer zones. The first element height was chosen to guarantee that the dimensionless wall distance at the grid nodes of the first prismatic layer from the walls did not exceed the limit of y⁺=1. In order to achieve mesh-independent results, a mesh sensitivity analysis was carried out: three meshes, differing in element sizing and, therefore, number, were considered. Their properties are summarized in Table 6.3.

Mesh	A	B	C
# elements (M)	10.0	20.5	28.0
Volute global sizing [mm]	0.70	0.50	0.35
Impeller global sizing [mm]	0.50	0.30	0.20
First layer height [mm]	$1.0 \cdot 10^{-3}$	$1.0 \cdot 10^{-3}$	$1.0 \cdot 10^{-3}$
# layers	16	16	16
Growth rate	1.15	1.15	1.15

Table 6.3   Properties of the tested meshes.

The results of the compressor grid independency analysis are shown in Figure 6.7. The values obtained with the finest refinement level were used to non-dimensionalize the pressure ratio and

efficiency, and a convergence threshold of 0.1% on both compression ratio and efficiency was set. As apparent from the figure, the medium refinement level (i.e. mesh B) was able to respect the threshold and it was therefore selected as the best tradeoff between calculation accuracy and computational effort.
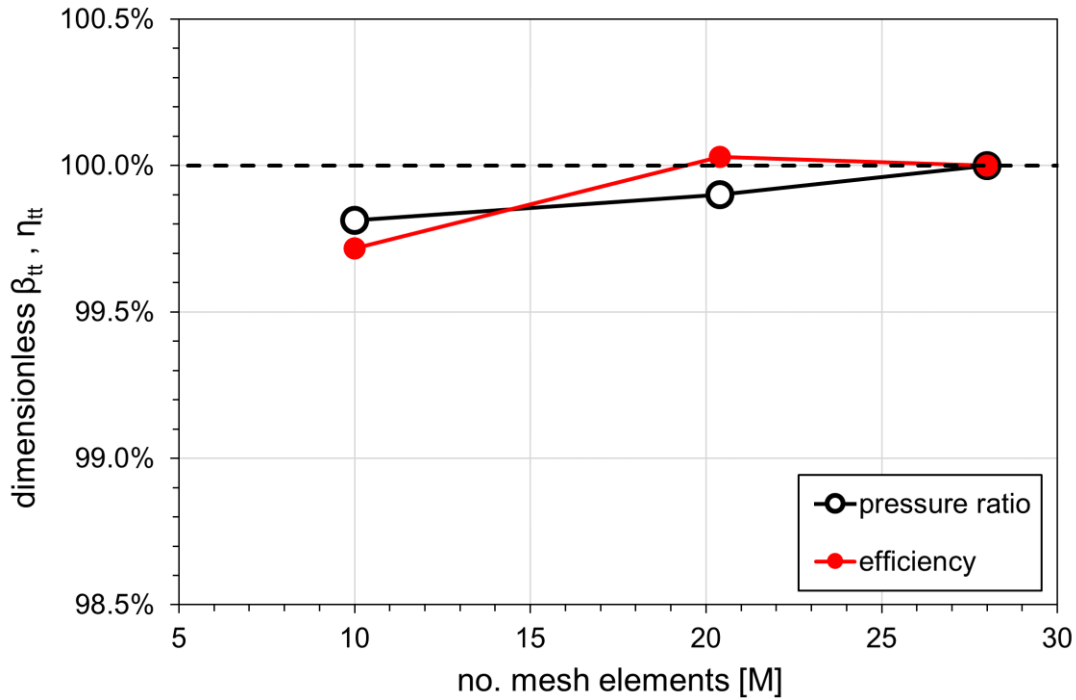
Figure 6.7   Mesh sensitivity analysis results.

Figure 6.8 and Figure 6.9 show the mesh of the volute domain and the impeller domain, respectively. Local mesh refinements were necessary at the splitter blade tip, as apparent from Figure 6.9(a).
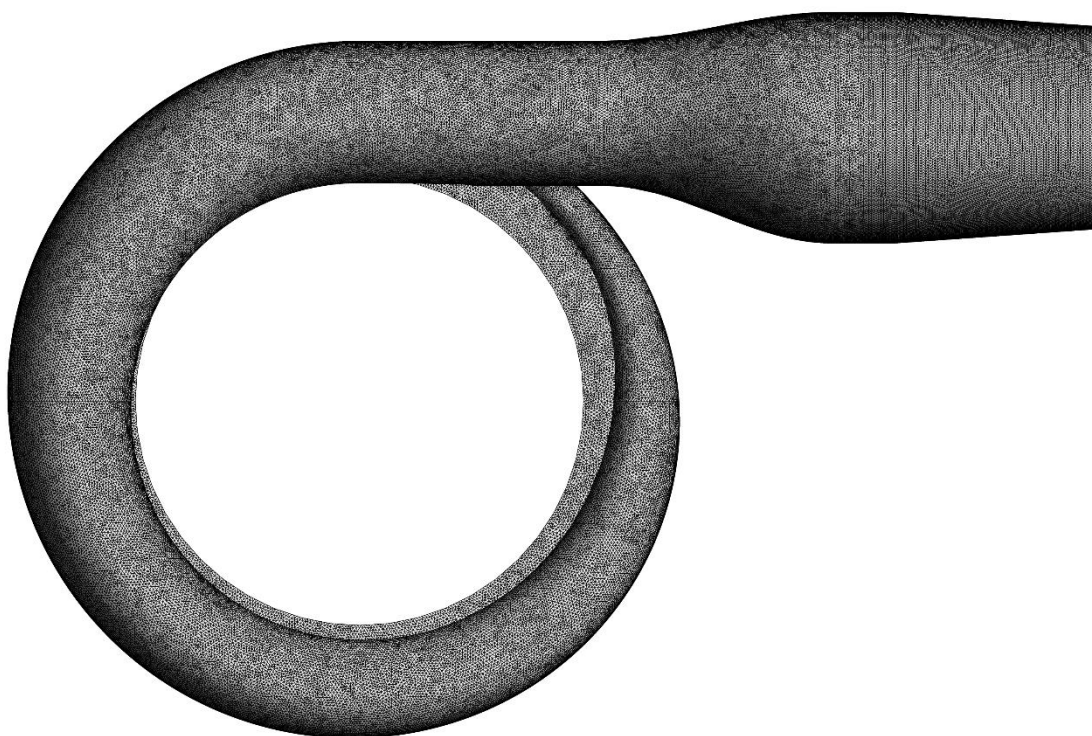
Figure 6.8   Compressor volute mesh.

(a)   **(b)**
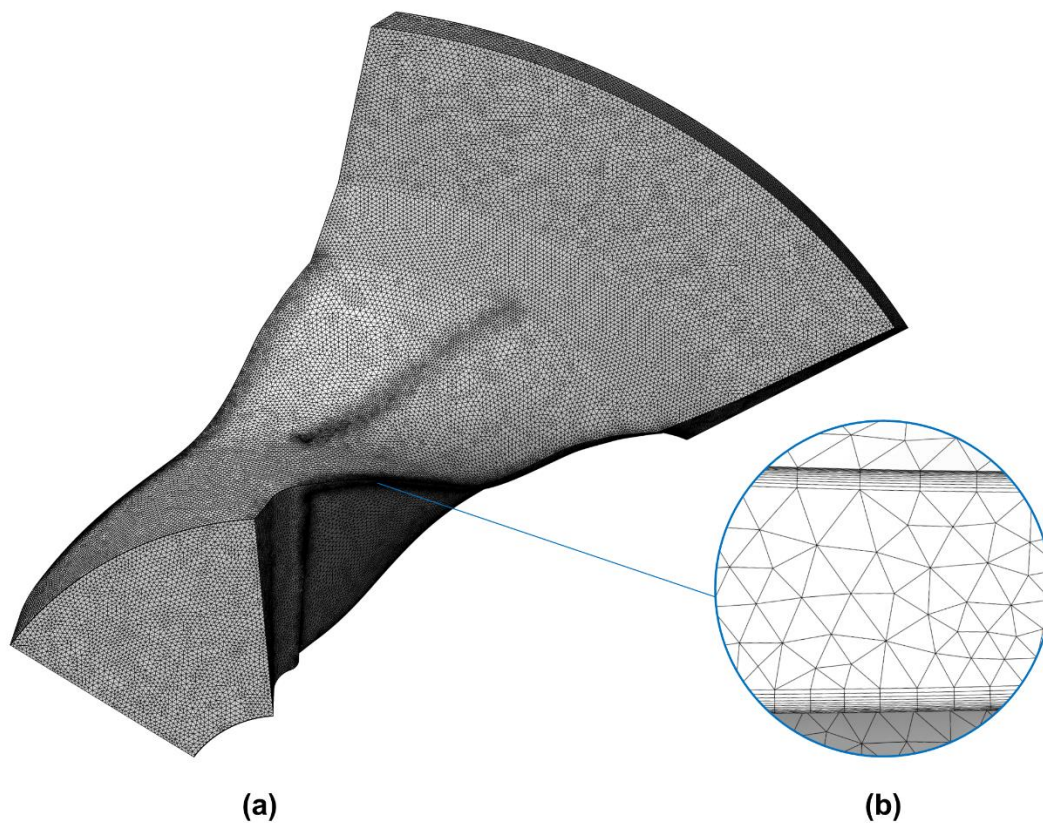
Figure 6.9   Impeller (a) single blade passage mesh and (b) detail of the tip clearance region.

The 3D CFD model of the compressor stage was validated against experimental data, for 6 speedlines, comparing both total pressure ratio and isentropic efficiency. As a convergence criterion for the solution, a tolerance of 10^{-6} was set to all residuals and the solution stability was checked in terms of fluctuation of pressure ratio and outlet mass flow rate. In particular, at medium-high flow rates the solution was showing variation in the order of 0.02-0.04% for the monitored quantities, while close to surge conditions the fluctuation was just slightly higher, in the order of 0.05-0.1%. Figure 6.10 and Figure 6.11 show that CFD results are in good agreement with experimental data.
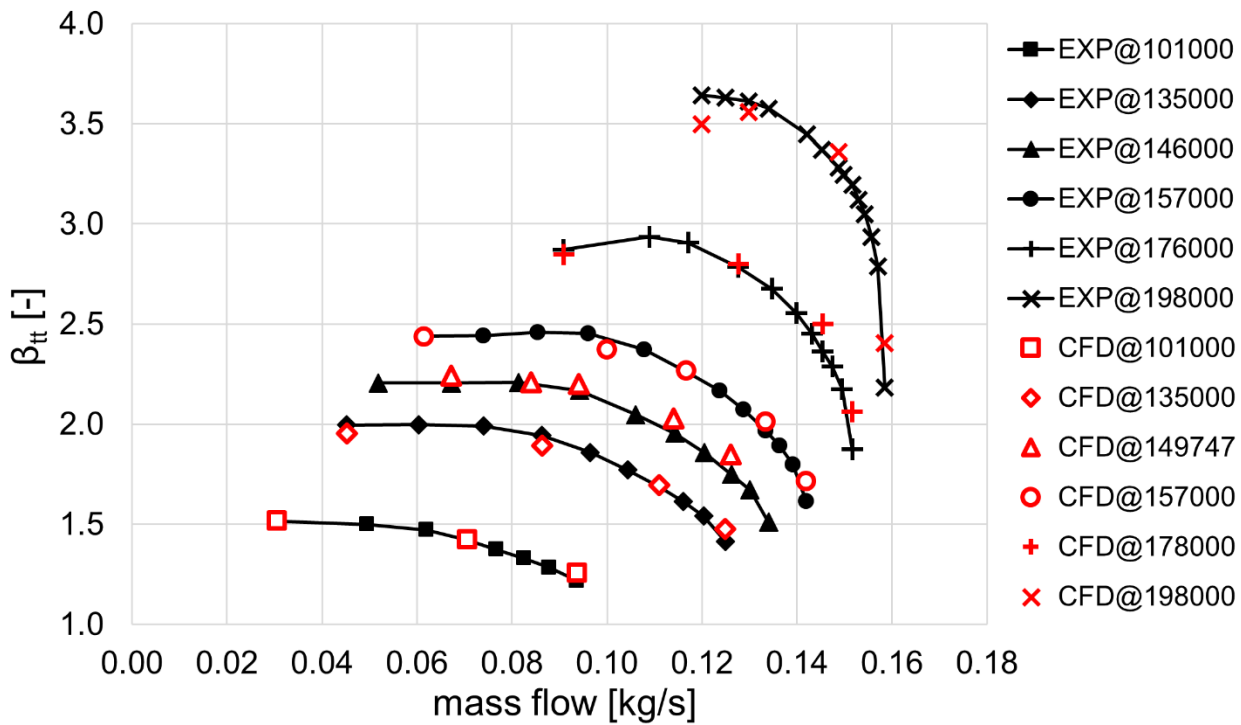
Figure 6.10   3D CFD compressor model validation: pressure ratio.
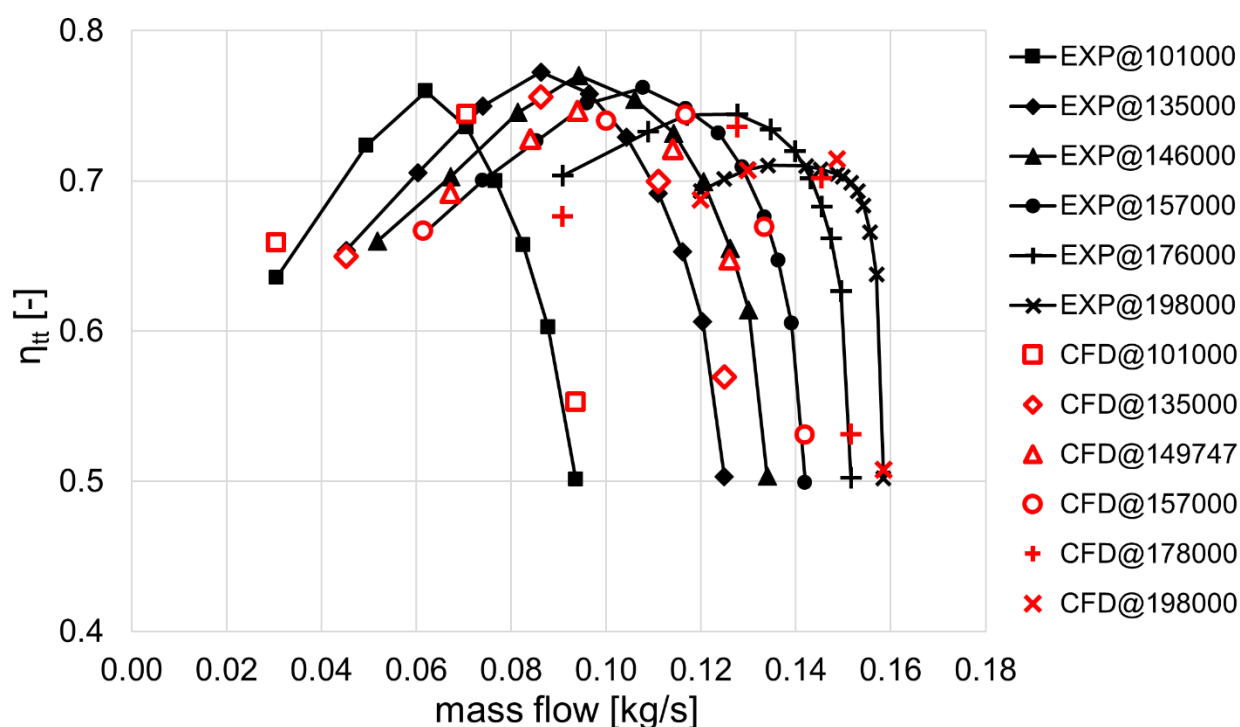
Figure 6.11   3D CFD compressor model validation: efficiency.

Regarding pressure ratio, the average relative error between CFD and experimental data is 1.73%, with a standard deviation value of 3.86%. Regarding isentropic efficiency, the average relative error between CFD and experimental data is 1.72%, with a standard deviation value of 4.32%. High values of standard deviation are attributable to relative error spikes at extreme off-design conditions. For instance, errors up to 10% in pressure ratio can be observed for the two higher velocity speedlines, at the corresponding choke conditions operating points, which are however not influent for the scopes of the present study. In fact, if the maximum efficiency points for every speedline are analyzed (i.e where the optimization analysis is thought to be performed), the average relative error is substantially lower. The average error on the pressure ratio here is 0.14%, with a standard deviation of 1.78%, while the average error on isentropic efficiency is 0.24%, with a standard deviation of 1.53%. Overall, a good agreement with experimental data was found: this suggests that, given the adiabaticity of the developed CFD model, the heat transfer effects that originate from the turbine and typically affect the compressor's efficiency maps [95,96] are not relevant in the present case study. The mitigation of such heat transfer effects may be due to the fact that the present test case mostly operates at high rotational speed and pressure ratios: this can lead to a condition where the compressed air outlet temperature is higher than the oil temperature in the bearing casing [97], reversing the typical heat flux direction (i.e. from the turbocharger's central casing to the compressor's housing). This observation is coherent with the fact that calculated (i.e. adiabatic) efficiency values are always greater than the experimental ones for the lowest speed and pressure ratio speedline. Additionally, the test-rig may operate close to quasi-adiabatic conditions by employing a water cooling circuit at the

compressor's bearing housing, allowing to minimize the temperature gradient between the central casing and the compressor [98,99]. For each speedline, the underestimation of the isentropic efficiency around the peak values may be attributable to the cooling of the compressed air due to heat transfer with the external ambient [100,101] along the compressor's discharge duct, which is not modelled by the present CFD approach. Indeed, if this was the case, the measured temperature at the compressor discharge would be lower than the corresponding CFD value, leading to an overestimation of the experimental isentropic efficiency, according to Eq. (6.4).

$$\eta_{tt} = \frac{T_{0,out,is} - T_{0,in}}{T_{0,out} - T_{0,in}} = \frac{T_{0,in}\left(\beta_{tt}^{\frac{\gamma-1}{\gamma}} - 1\right)}{T_{0,out} - T_{0,in}} \tag{6.4}$$

Conversely, isentropic efficiency was generally overestimated close to the choke conditions, mainly because of the error made in overestimating pressure ratio. Overall, notwithstanding minor discrepancies with respect to experimental measurements, the developed 3D CFD proved to be accurate and predictive of the compressor's performance.

6.2.4 - Optimization methods

As anticipated, the aerodynamic optimization of the static parts of the compressor by means of 3D CFD numerical techniques represents the core of this activity. According to paragraph 6.2.1, once the "first guess" operating conditions of the optimized compressor are estimated, they can be implemented as boundary conditions for the 3D CFD aerodynamic optimization. The compressor static parts that were considered for the optimization are the diffuser and the volute. The optimization activity that was carried out is based on Design Of Experiments (DOE) techniques: for both the diffuser and the volute, a test plan was defined considering the main known factors that affect the system's performance. While DOE input factors clearly vary between the optimization phase of the diffuser and the one of the volute, the main performance parameter (i.e. the optimization output) that was considered for both cases is the compressor isentropic efficiency, defined by Eq. (3.4). Since, as discussed in section 6.2.3, mass flow and rotating speed are set as boundary conditions, the only optimization constraint consists in achieving the target pressure ratio for the correct matching with the engine's maximum efficiency operating point. The target of the optimization, according to the adopted "first guess" strategy, is achieving the efficiency increase that was initially hypothesized.

As a first step, different diffuser configurations were considered for testing. The initial DOE involved three wedge diffuser geometries, varying for number of wedge vanes. Moreover, different configurations of the baseline vaneless diffuser, with different pinch angle (α) and pinch onset radius (R) (Figure 6.12), were tested.
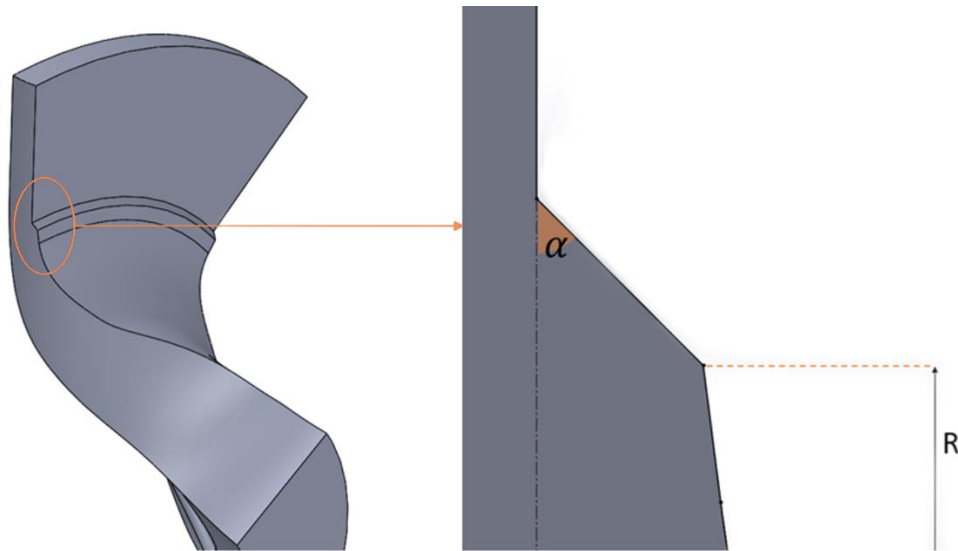
Figure 6.12 Main design parameters of the diffuser pinch region.

The DOE for the optimization of the diffuser is summarized in Table 6.4.

Nomenclature	BSL	W15	W23	W30	P1	P2	P3
# wedge vanes	vaneless	15	23	30	vaneless	vaneless	vaneless
Pinch angle [°]	7.3	7.3	7.3	7.3	45.0	45.0	26.5
Pinch onset [mm]	25.5	25.5	25.5	25.5	26.2	25.5	25.5

Table 6.4 Diffuser optimization DOE.

It is worth pointing out that the wedge geometry was designed based on the fundamental criteria from Japikse's "Centrifugal Compressor Design and Performance" [102], aiming to optimize the compressor's performance at its design operating points by testing different wedge diffuser configurations with different solidity. Besides the compressor's isentropic efficiency, additional performance parameters were employed for the diffuser analysis, specifically: the diffuser efficiency (η_d), the diffuser loss coefficient (ζ_d) and the relative variation of total pressure within the component ($\Delta P_0\%$). The definition of the above-mentioned parameters can be found in the following equations:

$$\eta_d = \frac{\left(\frac{P_{out}}{P_{in}}\right)^{\frac{\gamma-1}{\gamma}} - 1}{\left[\left(\frac{P_{0,in}}{P_{0,out}}\right)\left(\frac{P_{out}}{P_{in}}\right)\right]^{\frac{\gamma-1}{\gamma}} - 1} \tag{6.5}$$

$$\zeta_d = \frac{P_{0,in} - P_{0,out}}{P_{0,in} - P_{in}} \tag{6.6}$$

$$\Delta P_0\% = \left(\frac{P_{0,out}}{P_{0,in}} - 1\right)\% \tag{6.7}$$

It must be pointed out that every quantity that refers to a specific section of the analyzed component is mass flow-averaged over the respective section.

Regarding the compressor volute, the first design parameter that was considered in the present study is the shape of the cross-section: as highlighted by many studies [103–105], the effects of this feature on the volute performance cannot be neglected. Figure 6.13 shows the cross-section shapes selected for the activity.

(a)   (b)   (c)   (d)
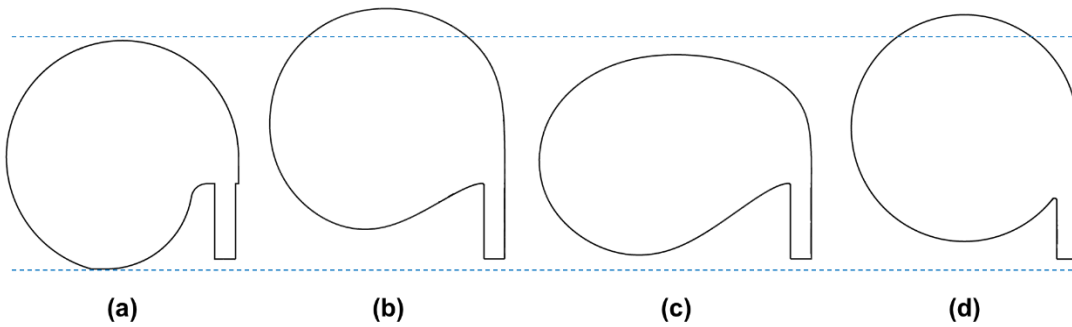
Figure 6.13   Volute cross-section shapes for the optimization phase: (a) baseline, overhung shape, (b) less overhung shape, (c) elliptical and (d) circular shape.

The less overhung configuration (Figure 6.13b) is based on the baseline configuration (Figure 6.13a): the radial dimension of the volute is unconstrained in the present application, and the selected shape tends to a more circular shape while maintaining the baseline design. The circular configuration (Figure 6.13d) is the standard for the design of compressor volutes and it has been identified by many authors [103–105] as the one providing the best average performance at all operating conditions. Nonetheless, Mojaddam et al. [105] found out in their study how an elliptical shape (Figure 6.13c) may perform even better than the circular one, in terms of efficiency, over the whole operating range of the compressor.

The second design parameter that was considered in the present study is the the shape of the circumferential area distribution characterizing the volute geometry. According to many authors [106–108], this variable has a remarkable impact on the volute performance. The area distribution law defines the growth of the cross-section area along the azimuthal direction (Figure 6.14a). In this study, two area distribution laws were tested: the baseline, linear one, and a quadratic distribution that was selected based on a previous comprehensive study by Melani et al. (2020) of the Università degli Studi di Firenze [109]. Figure 6.14b shows the area distribution laws that were selected for this study.
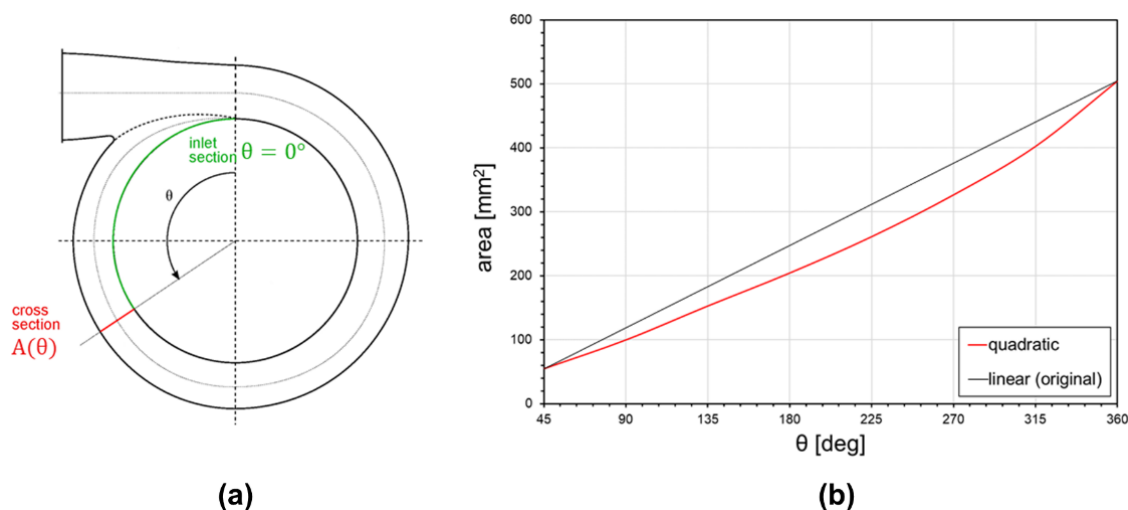
Figure 6.14   Volute (a) layout and (b) tested area distribution laws.

The DOE for the optimization of the volute is summarized in Table 6.5.

Nomenclature	BSL	V1	V2	V3	V3Q
Cross-section shape	baseline	less overhung	elliptical	circular	circular
Area distribution law	linear	linear	linear	linear	quadratic

Table 6.5   Volute optimization DOE.

As anticipated, the performance of the analyzed static parts was assessed through the isentropic efficiency of the whole compressor stage. During the volute optimization activity, the volute loss coefficient (ζ_v) was also considered for performance assessment, together with the static pressure recovery coefficient (K_P) and the azimuthal static pressure recovery coefficient (K_P^θ). These parameters are defined in the following equations.

$$\zeta_v = \frac{P_{0,in} - P_{0,out}}{P_{0,in} - P_{in}}$$

(6.8)

$$K_P = \frac{P_{out} - P_{in}}{P_{0,in} - P_{in}}$$

(6.9)

$$K_P^\theta = \frac{P(\theta) - P_{in}}{P_{0,in} - P_{in}}$$

(6.10)

Where $P(\theta)$ is the mass flow-averaged static pressure at each corresponding azimuthal section. For a deeper understanding of loss mechanisms inside the volute, local total pressure coefficient (P_0^*) contour plots were analyzed. The local total pressure coefficient is defined in Eq. (6.11):

$$P_0^* = \frac{P_0 - P_{0,out}}{P_{0,in} - P_{0,out}}$$

(6.11)

Additionally, entropy generation rate contours were analyzed. Denton [49] encourages the use of entropy generation rate contours in adiabatic turbomachines to improve the understanding of

many details of loss generation, since any irreversible flow process creates entropy, thus reducing the isentropic efficiency. The advantage in case of CFD simulations is the possibility to compute the local entropy generation in the postprocessing phase, without the need of an additional equations to be solved during runtime. Indeed, entropy generation can be expressed as a function of both the flow field and the scalar properties, such as temperature and turbulence quantities. Concerning the physics of turbochargers volutes, the main phenomena that are responsible for thermodynamic irreversibilities leading to entropy creation are heat transfer and viscous friction in boundary layers and free shear layers. To identify the entropy production sources, an entropy equation (Eq. 6.12) can be obtained [33,35,110,111] by combining the equations of conservation of momentum and energy with the second law of thermodynamics:

$$\frac{Ds}{Dt} = \frac{Q}{T} - \frac{1}{\rho T}\frac{\partial q_i}{\partial x_i} + \frac{1}{\rho T}\tau_{ij}\frac{\partial u_i}{\partial x_j} \tag{6.12}$$

where s is the entropy per unit mass and Q is the heat addition, which can be neglected in first approximation due to the assumption of adiabatic conditions. The second and third terms on the right hand side of Eq. (6.12) represent the contributions to entropy generation by heat conduction and friction, respectively. In addition, τ_{ij} is the viscous stress tensor related to velocity gradients, defined as:

$$\tau_{ij} = \mu\left[\left(\frac{\partial u_i}{\partial x_j} + \frac{\partial u_j}{\partial x_i}\right) - \frac{2}{3}\delta_{ij}\frac{\partial u_k}{\partial x_k}\right] \tag{6.13}$$

For turbulent flows solved using the Reynolds Average Navier-Stokes (RANS) approach, the entropy generation rate per unit volume ($\dot{S}_v$) can be analytically derived and expressed in terms of heat transfer due to finite temperature gradients and dissipation due to velocity gradients:

$$\dot{S}_v = \frac{\lambda}{T^2}\overline{\left(\frac{\partial T}{\partial x_i}\right)^2} + \frac{1}{T}\overline{\tau_{ij}\frac{\partial u_i}{\partial x_j}} \tag{6.14}$$

where λ is the thermal conductivity. Since the instantaneous values of T and u_i can be split into time-mean and fluctuating parts, both terms on the right hand side of Eq. (6.14) can be also split in terms of mean and fluctuating quantities. According to Herwig [110], it is possible to define the entropy generation rate due to viscous (direct) dissipation as:

$$\dot{S}_{v,\overline{D}} = \overline{\tau}_{ij}\frac{\partial \overline{u}_i}{\partial x_j} \tag{6.15}$$

and the entropy generation rate due to turbulent (indirect) dissipation as:

$$\dot{S}_{v,D'} = \frac{1}{T}\overline{\tau'_{ij}\frac{\partial u'_i}{\partial x_j}} = \rho\frac{\varepsilon}{T} \tag{6.16}$$

where ε is the dissipation rate of turbulent kinetic energy.

With the same approach, similar equations can be derived for the entropy production due to thermal diffusion. The entropy generation rate by heat conduction due to mean temperature gradients is defined as:

$$\dot{S}_{v,\bar{C}} = \frac{\lambda}{\bar{T}^2}\left(\frac{\partial \bar{T}}{\partial x_i}\right)^2 \tag{6.17}$$

and the entropy generation rate by heat conduction due to fluctuating temperature gradients is defined as:

$$\dot{S}_{v,C'} = \frac{\lambda_t}{\bar{T}^2}\left(\frac{\partial \bar{T}}{\partial x_i}\right)^2 \tag{6.18}$$

where the turbulent thermal conductivity (λ_t) is computed by Eq. (6.19) assuming a value of unity for the turbulent Prandtl number [35]:

$$\lambda_t = \frac{c_p \mu_t}{Pr_t} \tag{6.19}$$

Summarizing the four terms above, the entropy generation rate describing the irreversibility is determined as:

$$\dot{S}_v = \dot{S}_{v,\bar{D}} + \dot{S}_{v,D'} + \dot{S}_{v,\bar{C}} + \dot{S}_{v,C'} \tag{6.20}$$

Following the definition of Eq. (6.20), $\dot{S}_v$ can be used as a local quantity to evaluate the spatial distribution of sources of loss. In addition, it can be integrated in the whole computational domain to give the total entropy generation rate:

$$\dot{S} = \int_v \dot{S}_v \, dV \tag{6.21}$$

The above-presented calculations were manually implemented in the post-processing phase to evaluate entropy generation. Figure 6.15 shows, as a practical example, entropy generation rate contour plots for two compressor volute cross-sections. In this example case, based on the contour plots, greater losses are expected for the elliptical shape.
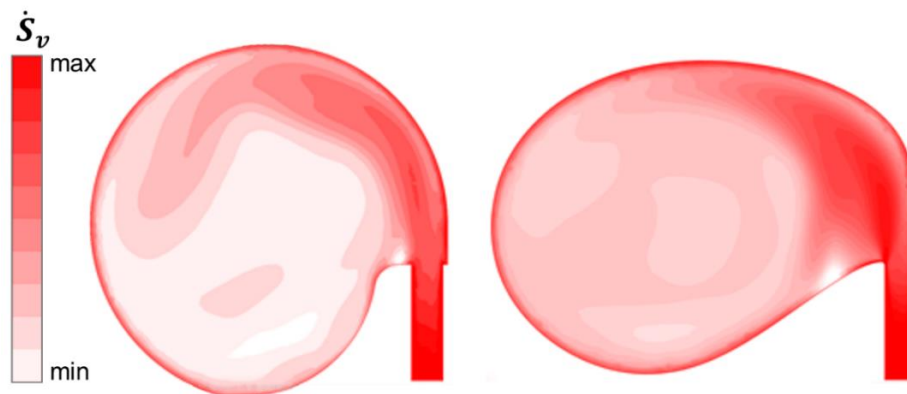
Figure 6.15 Example of entropy generation rate contour plots.

6.3 - Results

6.3.1 - Estimation of the new engine operating conditions

As discussed in section 6.2.1, the iterative optimization process started with an estimation of the new expected functioning conditions of the engine based on a "first guess" of the target efficiency improvement of the compressor.

Figure 6.16 shows the starting design point of the baseline compressor resulting from the 1D engine model working in stationary condition at the rated power output.
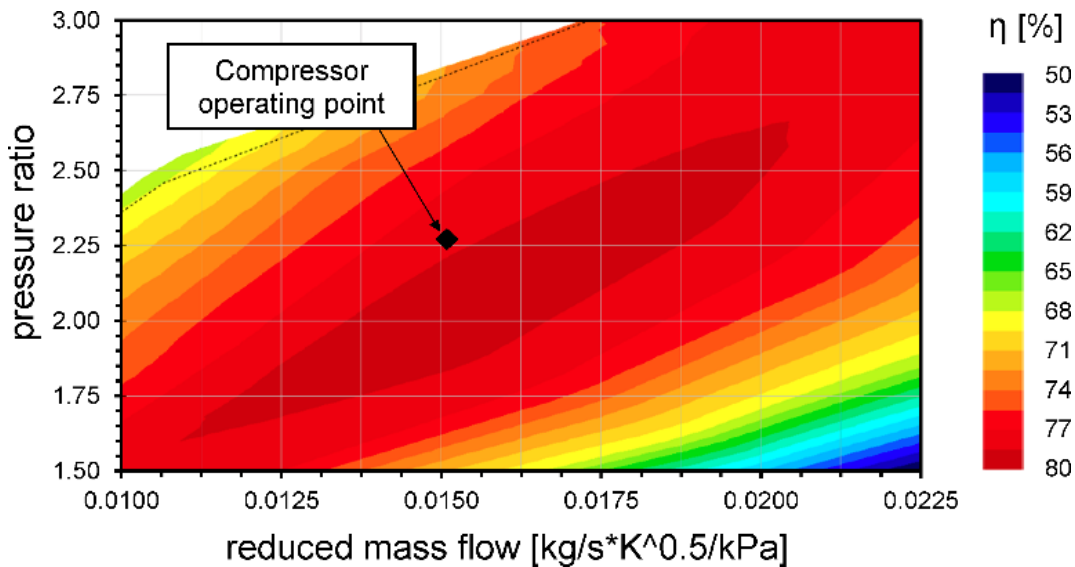
Figure 6.16 Starting design point of the compressor, resulting from 1D engine model calculations.

The optimization strategy was defined by assuming that the final optimized geometry would guarantee, on the one hand, an exact matching between the engine's and the turbocharger's maximum efficiency points and, on the other hand, a higher value of the maximum efficiency due to the forthcoming optimization of the static parts of the compressor. Overall, an increase of isentropic efficiency of 1 percentage point was hypothesized. In order to allow the evaluation of the shifting of the engine/turbocharger system towards the best efficiency point, custom-corrected turbocharger maps with constant efficiency (set at the maximum hypothesized value) were loaded into the 1D engine model. By doing so, the results of the corrected engine calculations were assumed as the "first guess" to estimate the operating conditions of the system with the optimized turbocharger. The variation of rotational speed, mass flow rate and pressure ratio of compressor and turbine stages is shown in Table 6.6.

Configuration	Rev. Speed [rpm]	Mass flow [kg/h]	Pressure ratio
BSL	149747	302.5	2.28
FIRST GUESS	157157	313.5	2.43

Table 6.6   Original (BSL) and estimated (FIRST GUESS) operating conditions of the compressor.

6.3.2 - Diffuser analysis and optimization

The optimization of the diffuser represents the first phase of the compressor stage aerodynamic optimization by means of 3D CFD analyses. The diffuser of the baseline configuration is of the vaneless type, as shown in Figure 6.17a. Typically, vaneless diffusers offer a wider operating range with respect to vaned diffusers, at the expense of lower pressure recovery and efficiency. Since the purpose of the present activity is, in brief, to enhance the compressor performance for a single operating point, a vaned diffuser might represent a promising solution.

As anticipated, 3 wedge diffuser configurations were tested, namely *W15* (Figure 6.17b), *W23* (Figure 6.17c), *W30* (Figure 6.17d). A wedge diffuser represents one of the simplest types of vaned diffuser and its main effects are twofold: firstly, pressure recovery is enhanced due to the flow diffusion inside the blade passages. Secondly, the flow exiting the impeller is guided and gains a stronger radial component: its path is therefore shorter with respect to the logarithmic spiral of a vaneless diffuser and lower friction losses can be expected.
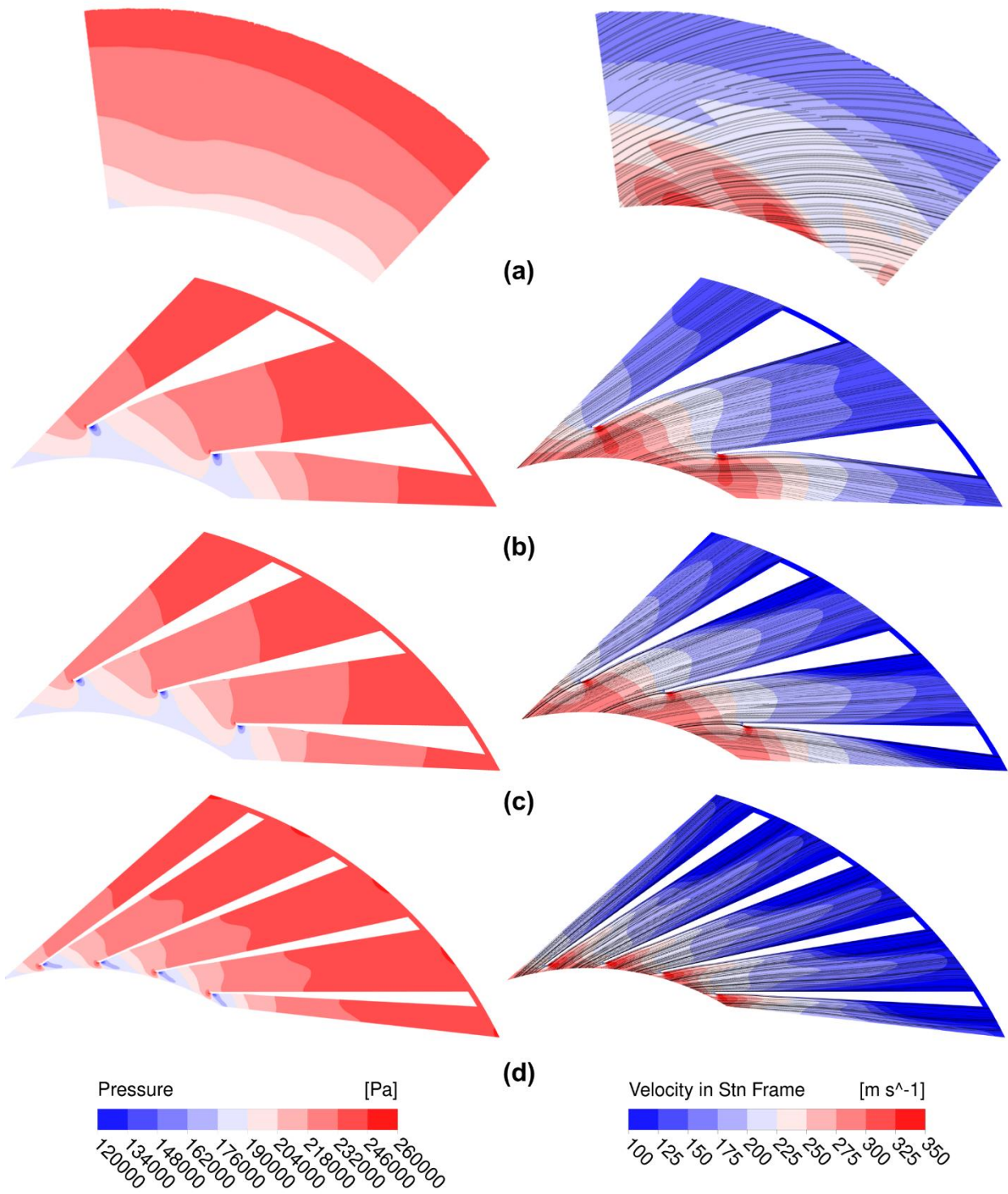
Figure 6.17 Static pressure and velocity contour plots of the (a) BSL, (b) W15, (c) W23 and (d) W30 diffuser configurations; flow streamlines overlap the velocity contour plots.

The performance of the different diffuser configurations is presented in terms of percentage points variation from the *BSL* configuation: Figure 6.18 shows the analysis results in terms of diffuser efficiency, diffuser loss coefficient and total pressure losses. The diffuser efficiency is a good indicator of the overall performance of the diffuser, since it includes the contribution of both total and static pressure ratio between the diffuser inlet and outlet. The diffuser loss coefficient, similarly to the volute loss coefficient, evaluates the total pressure losses scaled with the inlet

dynamic pressure: it is an indicator of how effectively friction losses are contained inside the diffuser. The higher the efficiency and the lower the loss coefficient and total pressure losses, the better the diffuser performance: in the following plots, solid color filling is used for beneficial variations, while dashed filling is used for variations that deteriorate performance.
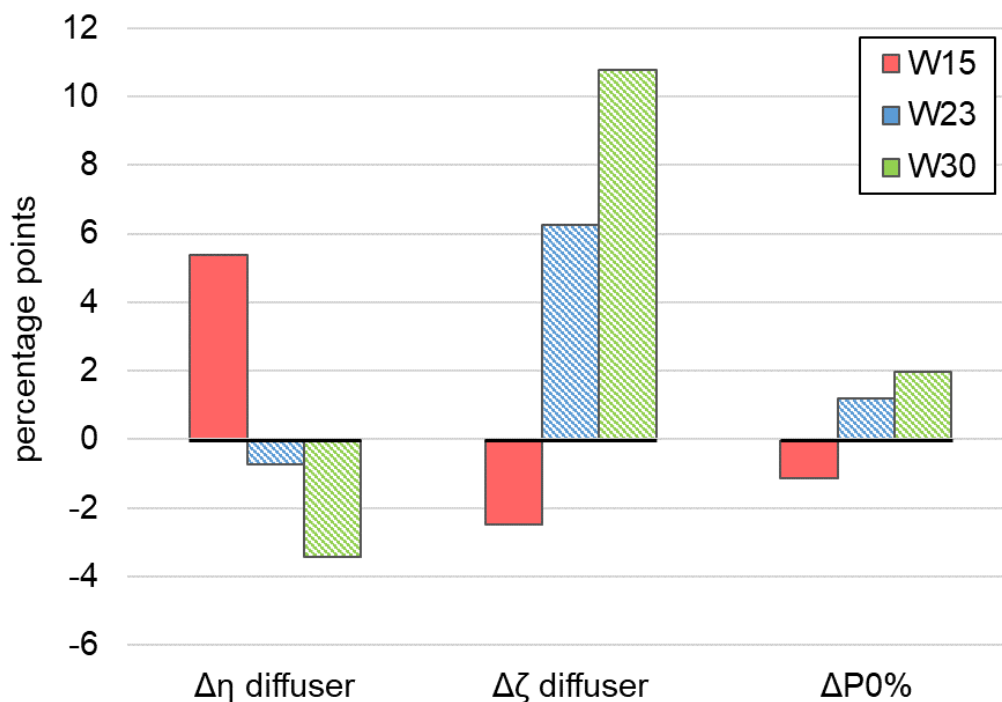
Figure 6.18   Comparison of different diffuser configurations with respect to the baseline.

It is apparent that the 15-wedge vanes diffuser (*W15*) is the only configuration with enhanced performance. Not only it performs better than the other wedge diffuser configurations, but surpasses the baseline configuration in every performance parameter that is considered. Efficiency is roughly 5 percentage points higher than the vaneless, reference diffuser, and a loss coefficient reduction of 2 percentage points can be observed.

The efficiency of the 23-wedge vanes configuration (*W23*) is similar with respect to the baseline, but the increased wet surface area generates more friction losses with respect to both the baseline and *W15* configuration: this effect is reflected by the increased total pressure losses. Furthermore, as apparent from the velocity plot contour in Figure 6.17c, flow velocity greatly reduces close to the diffuser exit: this may suggest the inception of boundary layer separation phenomena caused by the pressure recovery inside the blade passage. The performance of the 30-wedge vanes configuration (*W30*) confirms the trend due to the increased solidity that started with *W23*. As apparent from flow streamlines of Figure 6.17d, the higher number of vanes grants a well-guided flow. Indeed, the flow path is reduced with respect to the logarithmic spiral of the *BSL* configuration: this, paired with the reduced flow velocity due to diffusion, generates lower friction losses at hub and shroud. However, due to the very high solidity of this configuration, this effect is countered by the increased friction losses along the wedges' walls, reflected by the

increased diffuser loss coefficient and total pressure loss variation, which is the highest among the tested configurations.

Furthermore, it is worth pointing out that the different diffuser configurations have relevant effects downstream of the diffuser, in other words, inside the volute. Figure 6.19 shows the main performance parameters of the volute, for the tested diffuser configurations. For every configuration, the baseline volute geometry was employed.

Figure 6.19   The effects of different diffusers on volute performance.

It is apparent that the *W15* configuration grants better volute performance. The reduced volute loss coefficient suggests that the flow conditions at the diffuser exit are optimal for the volute's operation, even more than the *BSL* configuration. *W23* and *W30*, on the contrary, lead to higher loss coeffcients, but, due to the flow diffusion effects, total pressure losses are lower than *BSL*. Indeed, for every configuration, the velocity of the flow exiting the diffuser is lower with respect to the baseline configuration, leading to lower friction losses inside the volute.

Moving from this discussion, it is apparent that *W15* is the only tested configuration that enhances the performance of the diffuser. Still, the diffuser is only one of the compressor components and, as anticipated, the objective function of the present optimization is the total-to-total isentropic efficiency of the whole compressor stage. Figure 6.20 shows both the stage efficiency and the impeller efficiency variations with respect to the *BSL* configuration, for *W15*, *W23* and *W30*. Eq. (3.4) was employed to calculate these quantities: in order to assess either the stage or the impeller efficiency, different inlet and outlet sections were considered accordingly.
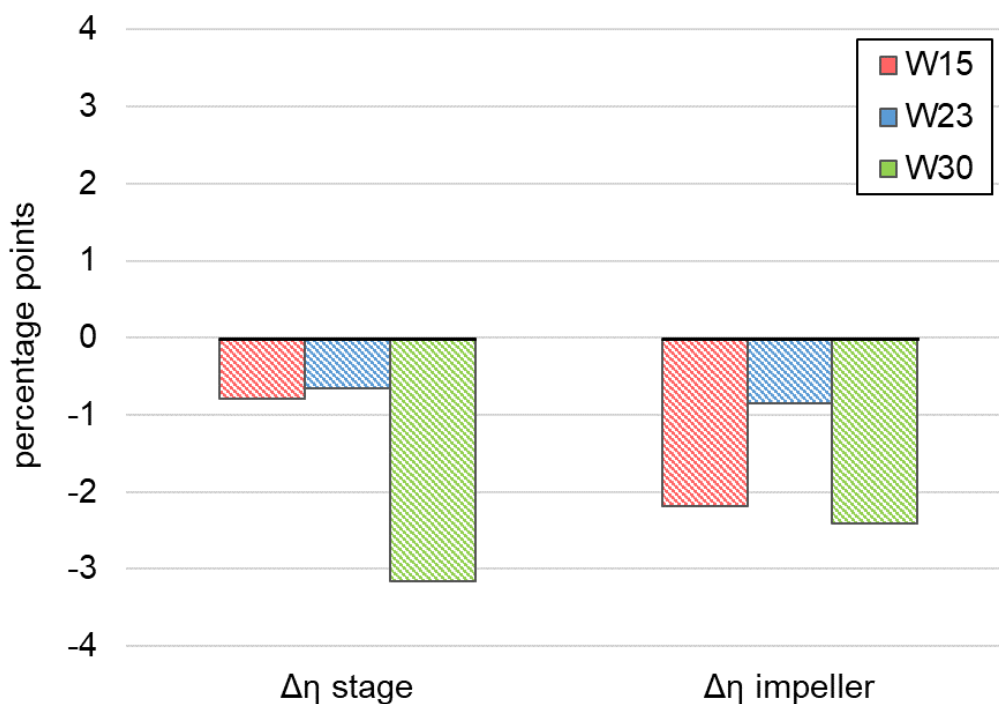
Figure 6.20   Stage and impeller efficiency variations for different diffuser configurations.

When considering the compressor stage efficiency, it is apparent that none of the wedge diffuser configurations grants improved performance with respect to the baseline, vaneless diffuser. According to the above-discussed results, this may seem counterintuitive: indeed, *W15* achieves better diffuser performance with respect to the other tested configurations. Moreover, *W15* also enhances the performance of the baseline volute. The reason for the reduced stage efficiency can be found when observing the impeller efficiency variations. Specifically, *W15* and *W30* configurations, more than *W23*, lead to lower impeller efficiency and the overall stage efficiency deteriorates: not even the superior diffuser performance of *W15* counterbalances this effect.

The reason for this behavior can be found in the flow distortion effects upstream of the diffuser. The effects of the different diffuser configurations on flow direction have already been discussed, and Figure 6.17 allows for a visualization of the flow streamlines; for a deeper understanding of the flow structure upstream of the diffuser, however, the impeller's aerodynamics must be analyzed. Figure 6.21 shows the impeller exit velocity triangle at midspan, in case of baseline, vaneless diffuser. It is worth pointing out that the velocity components were obtained by post-processing 3D CFD calculations, therefore slip factor is already taken into account.
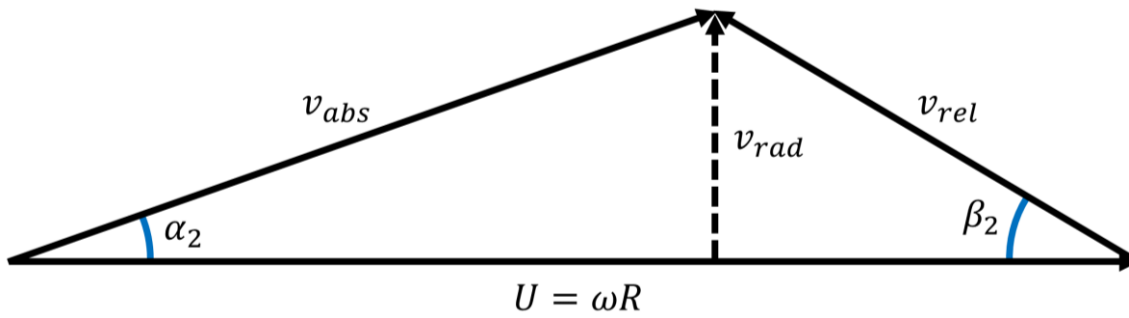
Figure 6.21   Impeller exit velocity triangle at midspan for BSL diffuser configuration.

As expected, the velocity triangle is typical of backswept centrifugal compressor blades, with the exit angle $\beta_2 < 90°$. Since velocity triangles are typically used to relate flow properties to blade design parameters, it is reasonable to consider the *BSL* velocity triangle depicted in Figure 6.21 as the one that optimizes the impeller's performance, including its efficiency. Figure 6.22 shows the comparison of different velocity triangles from the tested diffuser configurations: *W30* is represented by a dashed line due to the overlap with *W15* configuration.
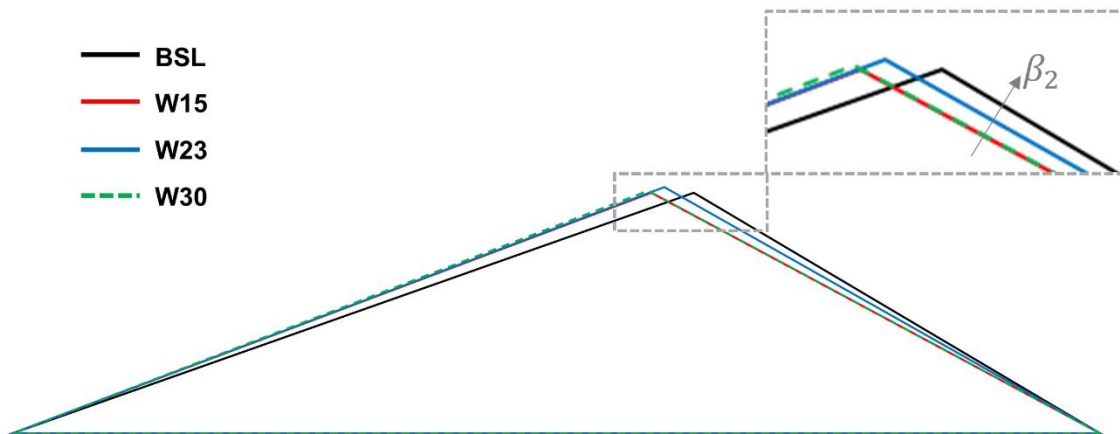
Figure 6.22   Comparison of the velocity triangles of the different diffuser configurations.

It is apparent that all three wedge diffusers increase the relative velocity component at the impeller exit, but only the *W23* configuration also grants an increase in the radial component. As a result, the exit angle β_2 of the *W23* configuration is greater with respect to *W15* and *W30*, although still lower than the *BSL* configuration. This flow behavior is reflected in the impeller efficiency trends: apparently, lower β_2 deteriorate the efficiency of the impeller, as shown in Figure 6.23.
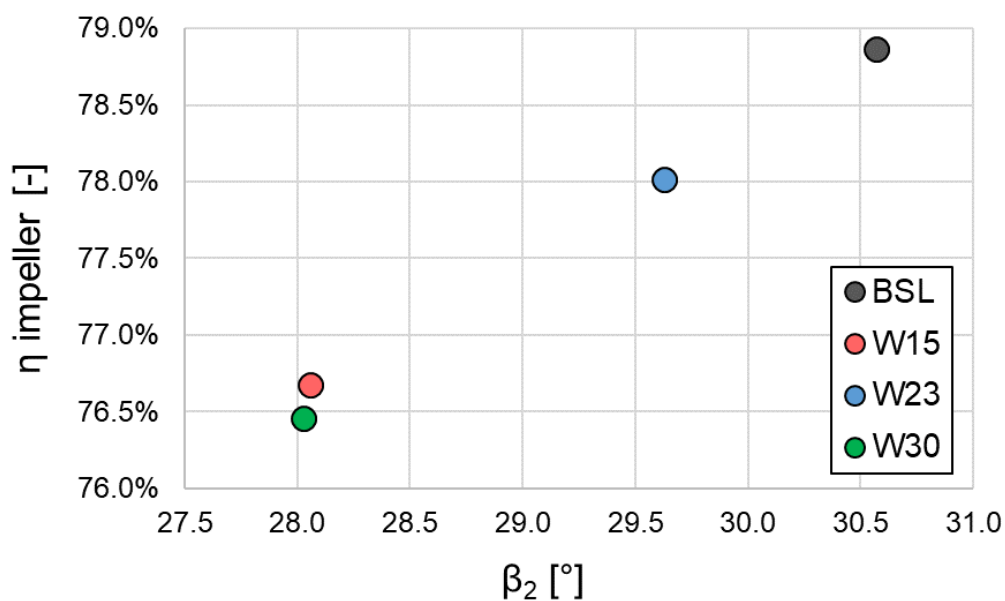
Figure 6.23   Impeller efficiency as a function of midspan β_2 exit angle.

In the end, the *W15* configuration has high diffuser efficiency and low impeller efficiency, while the *W23* configuration shows moderate reductions in both diffuser and impeller efficiency with respect to the baseline. The net effects of the *W15* behavior on stage efficiency are, eventually, even more deteriorating than the ones of *W23*. Compressor performance is overall inferior when employing the *W30* configuration.

Moving from these results, because of the above-described interactions betweene diffuser and impeller, and the impossibility of redesigning the impeller blade, the wedge diffuser architecture was deemed as not optimal for the present application and, as discussed in section 6.2.4, a fine-tuning of the baseline, vaneless diffuser was carried out. Specifically, different configurations of the pinch section at the impeller exit were tested. Pinched diffuser inlets are typically employed to stabilize the flow prior to diffusion, in order to prevent boundary layer separation phenomena along the diffuser. In the present case of a vaneless diffuser, pressure recovery is not as strong as in vaned diffusers and flow separation is not an issue to be addressed.

Indeed, the main aim of this optimization step is to minimize losses due to recirculating flow at the impeller exit, near the blade tip. In addition to the spanwise leakage flows that affect any unshrouded impeller blade tip, a backflow in the streamwise direction develops due to the adverse pressure gradient, as shown in Figure 6.24.
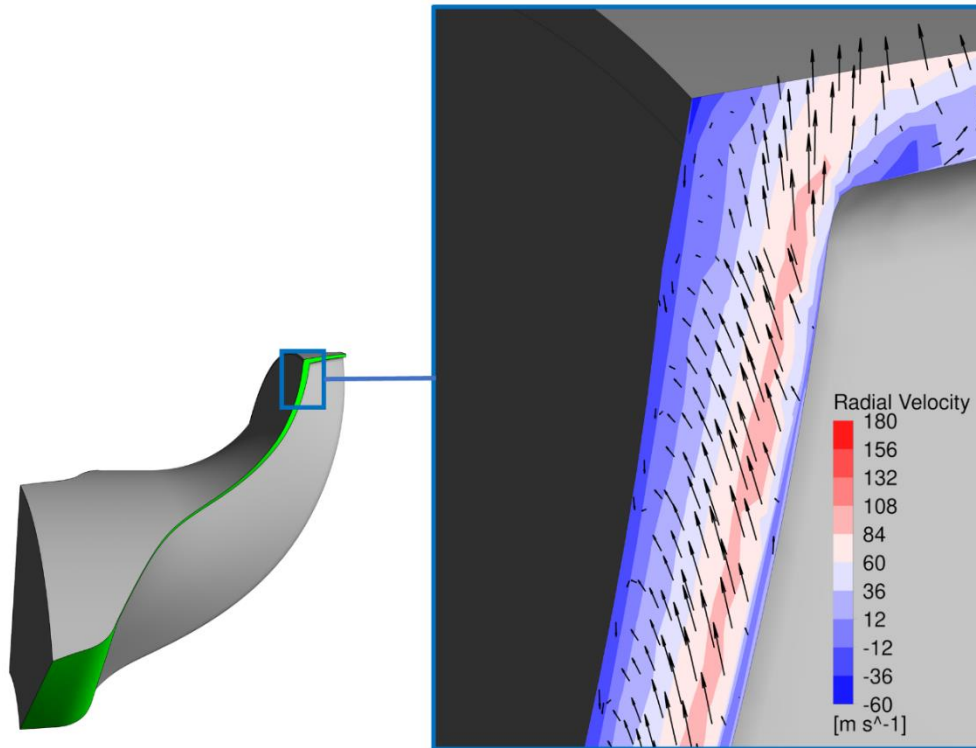
Figure 6.24   Streamwise flow recirculation at the impeller main blade tip.

The area of flow recirculation extends to the initial portion of the diffuser, as apparent from Figure 6.25, which shows the different pinch configuration that were tested with radial velocity contour plots.
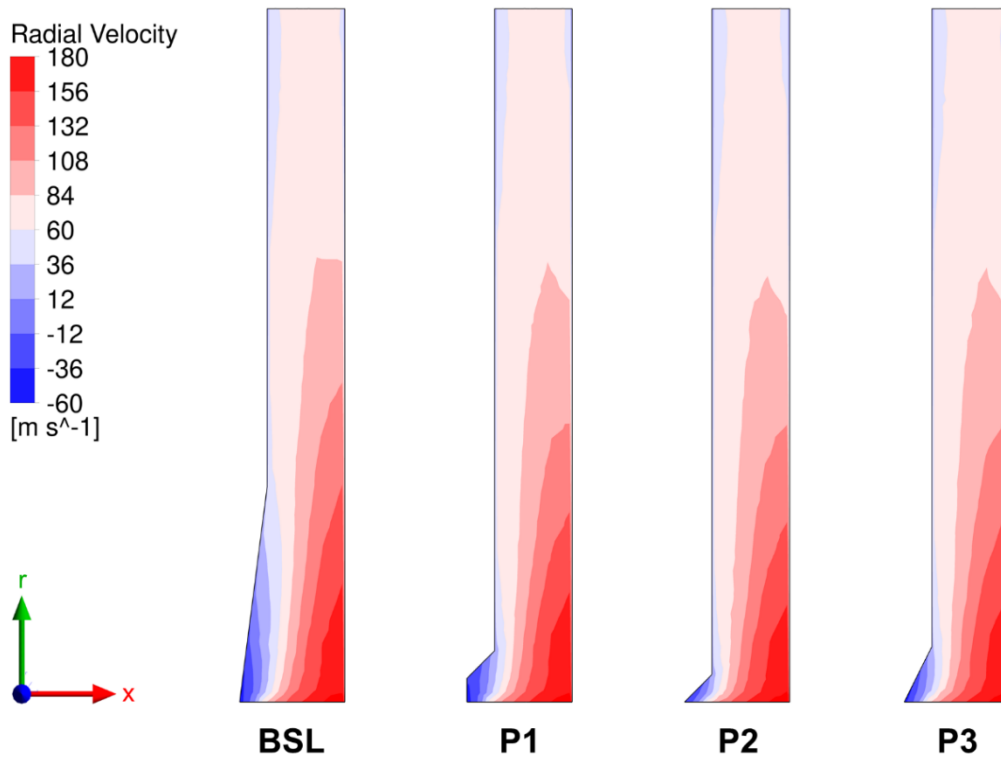
Figure 6.25   Radial velocity contour plots of the tested pinch configurations.

Indeed, recirculation can be appreciated for every configuration, but this phenomenon can be mitigated by properly tuning the pinch section of the diffuser. As apparent from Figure 6.25, the pinch angle is greater than the baseline for every configuration: indeed, it had been hypothesized that a more abrupt pinch could stabilize the flow earlier and more effectively. Furthermore, sensitivity on pinch onset radius was carried out at constant pinch angle (i.e. *P1* vs *P2*). Figure 6.26 shows a detailed view of the flow recirculating at the pinched section of the diffuser: velocity vectors allow for a better visualization of the flow direction.
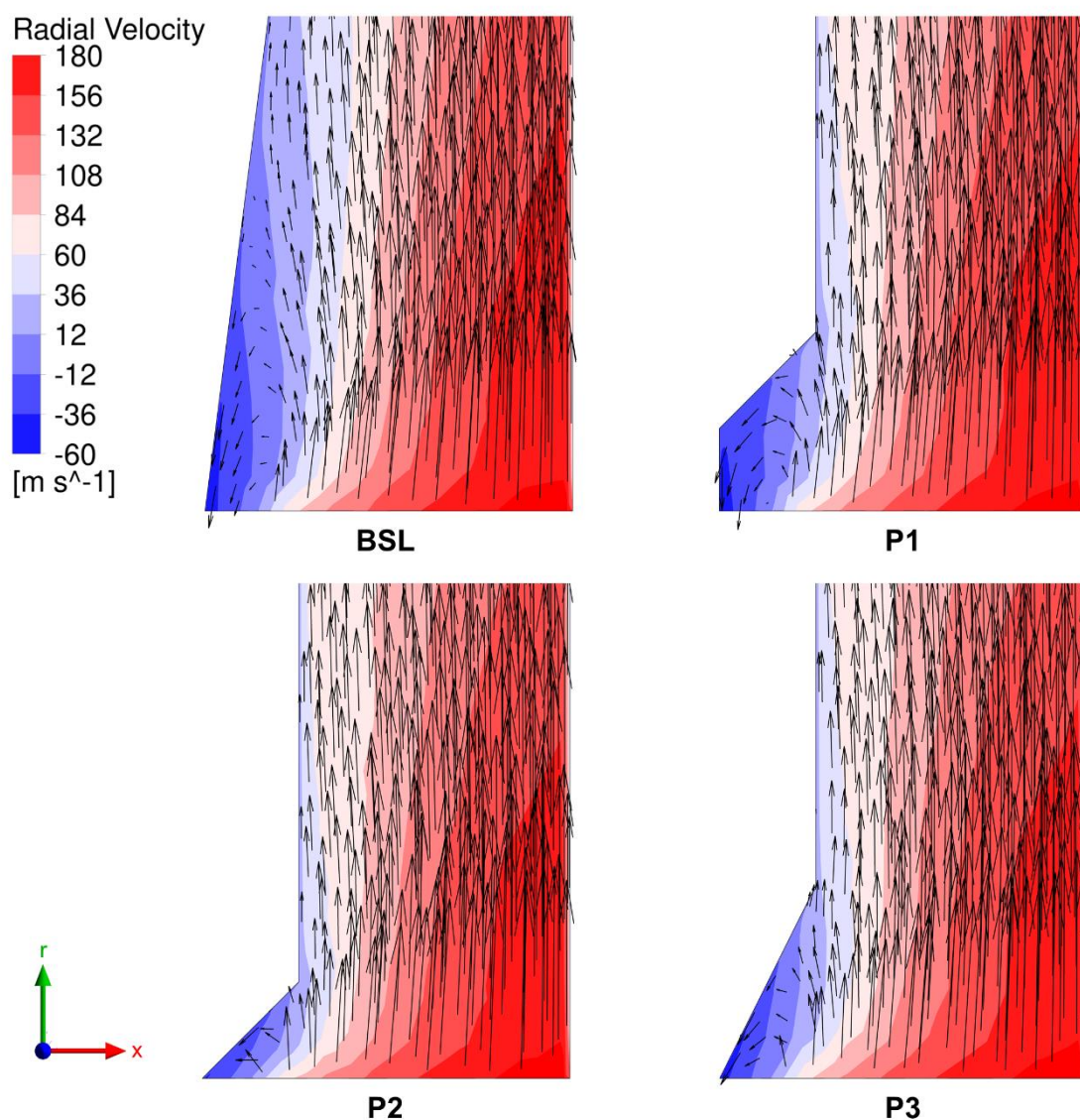
Figure 6.26   View of the flow structures at the pinched section of the diffuser.

The recirculation area of the baseline (*BSL*) diffuser is definitely larger with respect to the other configurations; velocity gradients in the recirculation zone are, however, similar with respect to the other configurations. Therefore, due to the increased recirculation area, higher losses due to shear stress can be expected. *P1* and *P2* configurations have the same pinch angle (i.e. 45°) and can be analyzed to assess the effects of the pinch onset radius. *P2* appears to be more effective in mitigating the recirculation near the shroud: indeed, the affected area is smaller and backflow

velocity is lower than *P1*. Still on *P2,* given the proximity of the pinch to the impeller exit, one may argue that its blockage can distort the flow upstream, possibly deteriorating the impeller performance: this, however, is disproven by a further analysis of the flow exiting the impeller, summarized in Figure 6.27.
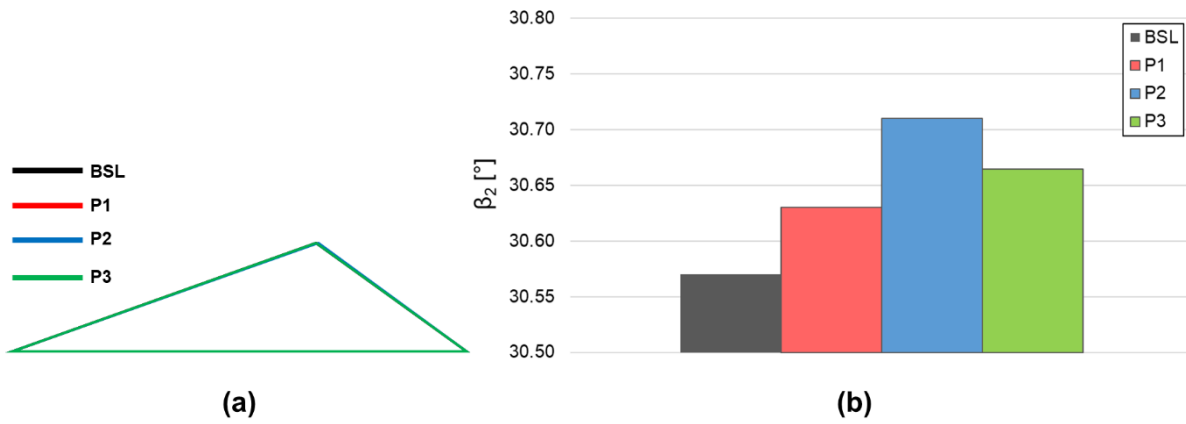
Figure 6.27   Impeller exit (a) velocity triangles and (b) β₂ exit angle.

For every tested configuration, velocity triangles overlap, and the exit angle (β_2) shows limited variations due to the flow acceleration in the different pinched sections. *P3* configuration confirms the trend determined by the analysis of *P1* and *P2*: a more pronounced pinch close to the impeller exit allows for a reduction of the recirculating area near the diffuser shroud. Results in terms efficiency and total pressure loss, shown in Figure 6.28, back up the observations that were presented so far.
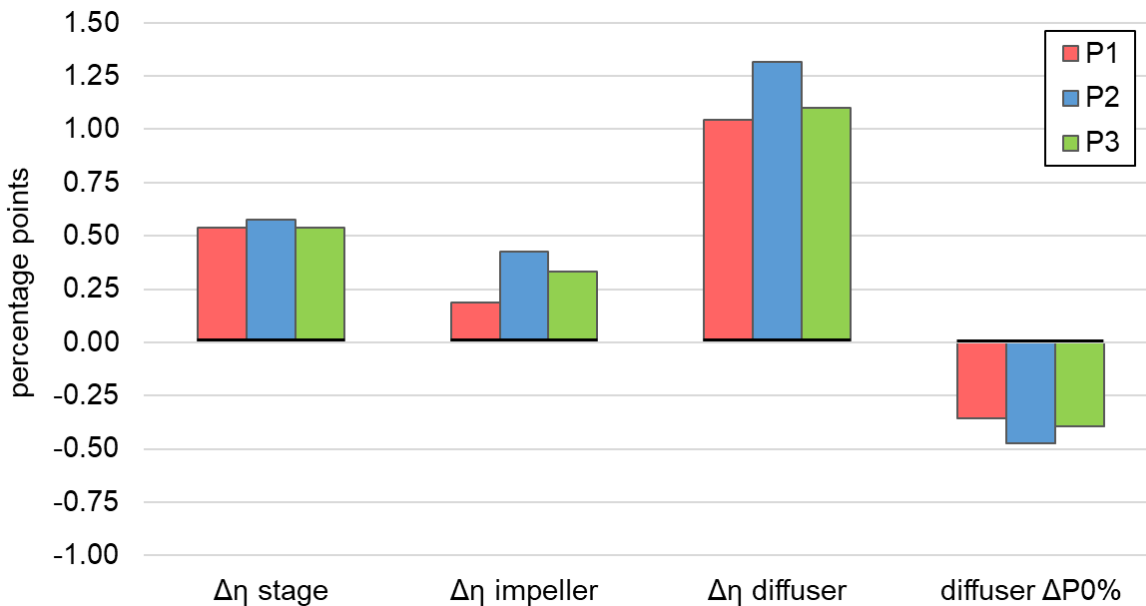
Figure 6.28   Compressor performance for the tested pinched vaneless diffuser configurations.

Overall, a more abrupt pinch is beneficial to the compressor performance. Indeed, all the tested configurations perform better than the baseline because of the greater pinch angle; in addition,

the closer the pinch to the impeller exit, the better the perfomance, as confirmed by the comparison between *P1* and *P2*. *P2* configuration, being the most extreme in terms of both pitch angle and pitch onset location, grants the highest stage efficiency and therefore subsistutes the baseline diffuser for the subsequent optimization steps.

6.3.3 - Volute analysis and optimization

Moving from the diffuser, the compressor volute represents the last stationary component to be optimized. As previously discussed, different cross-sectional shapes and two cross-sectional area circumferential distributions were analyzed in order enhance the performance of the volute in terms of stage isentropic efficiency.

As a first step, four cross-sectional shapes were analyzed: the baseline one (*BSL*), one similar to the baseline but less overhung (*V1*), an elliptical shape that is significantly extended in the axial direction (*V2*) and a circular shape (*V3*). The tested shapes are depicted in Figure 6.13. Initially, volute performance was evaluated by means of its static pressure recovery coefficient (K_p) and loss coefficient (ζ), both scaled with respect to a reference value which corresponds to the one of the *BSL* configuration. Figure 6.29 shows the effects of the cross-sectional shape on volute performance.
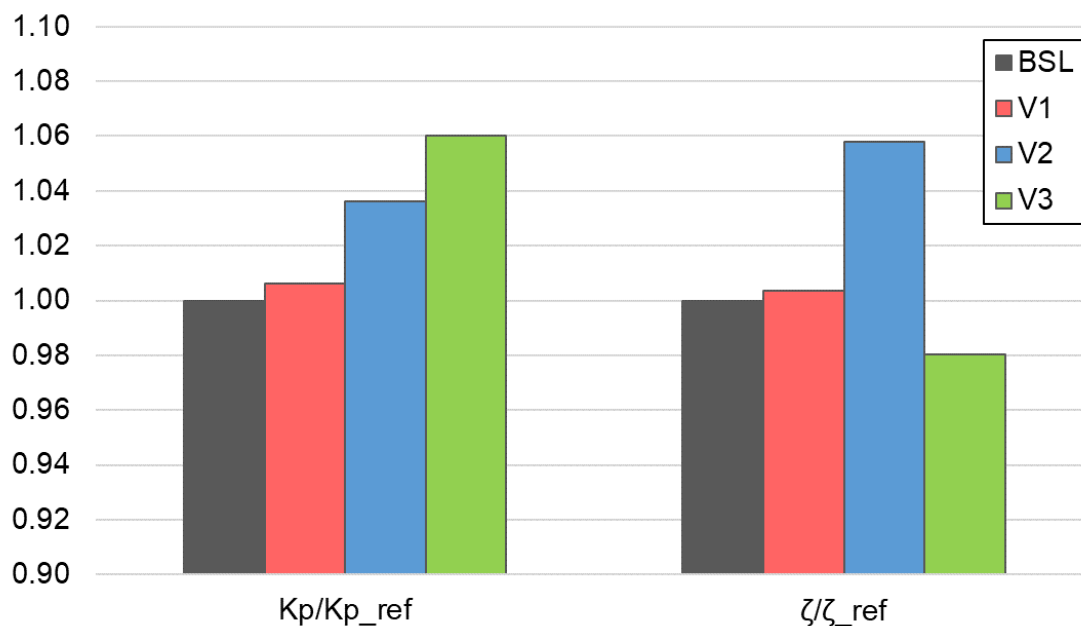
Figure 6.29   Effects of the cross-sectional shape on volute performance.

V1 represents the configuration whose performance is most similar to that of the baseline, in terms of both static pressure recovery and loss coefficients. This outcome was expected, since *V1* basically maintains the same shape and aspect ratio as the *BSL* configuration. Indeed, the main difference between the two configurations is a less pronounced overhung shape, which is allowed by the lack of space constraints in the present optimization activity. The reason for the

slightly higher loss coefficient of the *V1* configuration can be found in Figure 6.30 and Figure 6.31, which show contour plots of dimensionless total pressure and entropy generation rate, respectively, at different volute cross-sections.
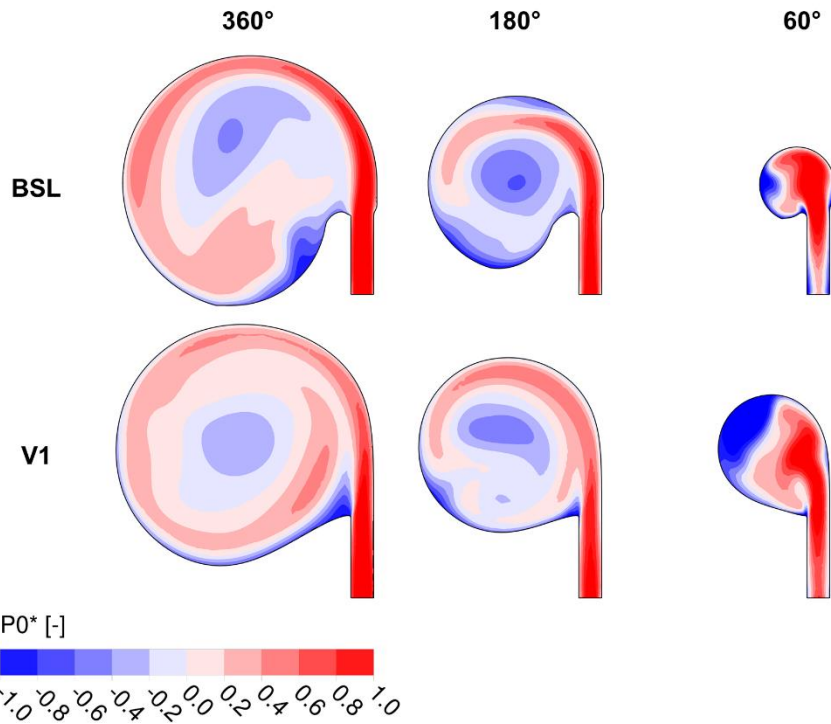
Figure 6.30   Dimensionless total pressure at different sections, for *BSL* and *V1* configurations.
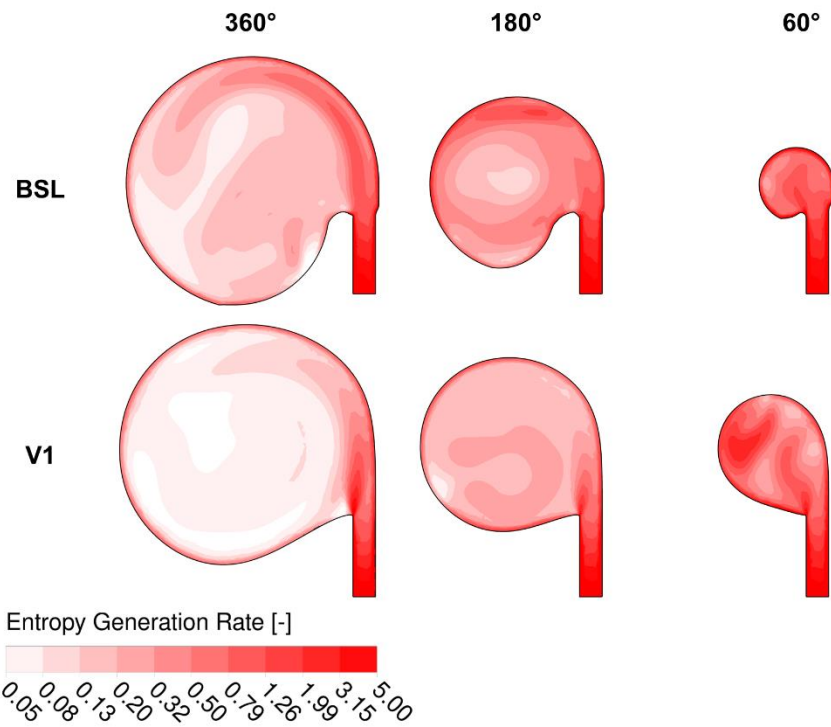
Figure 6.31   Entropy generation rate at different sections, for *BSL* and *V1* configurations.

It is apparent that, at the largest cross-section (θ=360°), *V1* performs better than BSL. Indeed, thanks to the more radially-oriented shape, flow separation at the bottom portion of the section is better contained: this results in a better guidance of the flow, which is reflected by the more regular, circular shape of the cross-section vortex. Entropy generation rate contour plots confirm that total pressure losses are mitigated at θ=360°: notwithstanding the entropy generation rate streak at the leftmost corner of the diffuser outlet of *V1*, the overall entropy generation rate of *V1* is remarkably lower with respect to *BSL*. At θ=180° the two configurations show a similar behavior, with flow separation phenomena still more intense in the bottom part of the *BSL* volute. Issues arise for the smaller cross-section close to the volute tongue (θ=60°): here, while the *BSL* configuration grants good flow guidance with a small recirculation area at the leftmost portion of the section, *V1* shows that the main flow from the diffuser is disrupted inside the volute. Indeed, a significant recirculation area can be observed at the top-left portion of the cross-section: here, the recirculating flow not only prevents optimal flow guidance, but also generates friction losses due to the local velocity gradients. The latter aspect is reflected by the entropy generation contour plot at θ=60°. The large recirculation area is probably related to the negative incidence exerted by the inlet flow on the volute's tongue, as thoroughly described by Pan et al. [103], which results in an extended flow separation on both the scroll first quadrant and the outlet duct. Evidence of such phenomenon can also be found in the section at θ=360°, where the cross-section vortex core, identified by the loss region at the section centroid [112], is distorted by the presence of a high-energy jet coming from the tongue. Eventually, notwithstanding the improved flow structure at θ=360°, the performance deterioration near the volute tongue determines the slightly higher loss coefficient of *V1* with respect to *BSL*.

V2 configuration performs significantly worse than the baseline, with a loss coefficient roughly 6% higher than the one of *BSL*. The reasons for this can be found by means of, again, an in-depth analysis of the flow structures inside the volute: Figure 6.32 and Figure 6.33 show contour plots of dimensionless total pressure and entropy generation rate, respectively, at different volute cross-sections.

360°   180°   60°

BSL

V2

P0* [-]

-1.0 -0.8 -0.6 -0.4 -0.2 0.0 0.2 0.4 0.6 0.8 1.0

Figure 6.32   Dimensionless total pressure at different sections, for *BSL* and *V2* configurations.

360°   180°   60°

BSL

V2

Entropy Generation Rate [-]

0.05 0.08 0.13 0.20 0.32 0.50 0.79 1.26 1.99 3.15 5.00

Figure 6.33   Entropy generation rate at different sections, for *BSL* and *V2* configurations.

At θ=360°, *V2*'s recirculation area at the bottom-right is larger than *BSL*'s, leading to increased losses, as confirmed by the entropy generation rate contours. This elliptical shape still grants

good flow guidance at the upper part of the shroud, but major flow separation is an issue at the bottom part due to the extreme aspect-ratio of the cross-sectional shape. This phenomenon is especially noticeable at θ=180°, where the bottom recirculation area is prominent and thicker than the one of the *BSL* confguration. Close to the volute tongue, similar observation as the ones made for *V1* can be made: a significant portion of the cross-section is affected by a recirculating flow that disrupts the main flow structure exiting the diffuser and contributes to friction losses, as confirmed by the entropy generation rate contours. Overall, *V2* configuration is definitely not the optimal one for the considered operating point: its aspect-ratio, together with its strong static pressure recovery capability make flow separation a major issue.

The circular cross-sectional shape (*V3*), on the other hand, is the only configuration that shows a lower loss coefficient than the *BSL*, while offering the highest static pressure recovery of all the tested configurations. Figure 6.34 and Figure 6.35 show contour plots of dimensionless total pressure and entropy generation rate, respectively, at different volute cross-sections.
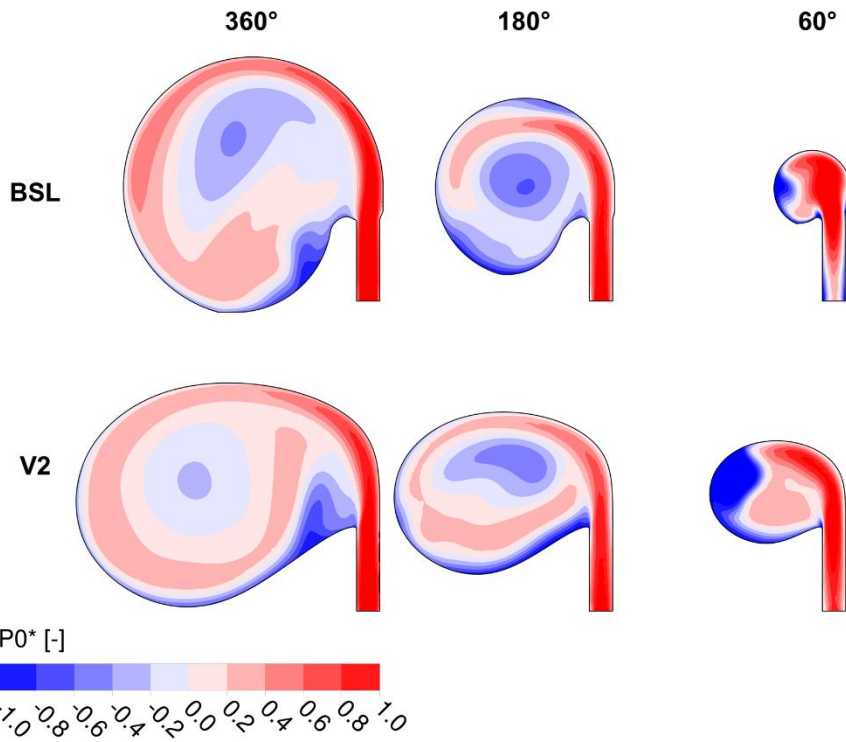

Figure 6.34   Dimensionless total pressure at different sections, for *BSL* and *V3* configurations.
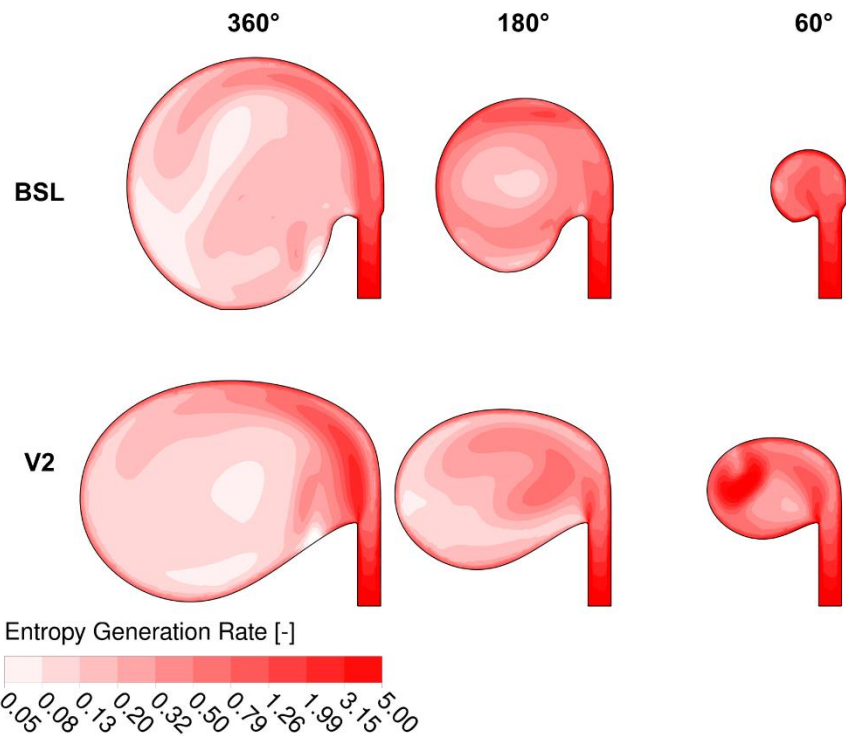
Figure 6.35   Entropy generation rate at different sections, for *BSL* and *V3* configurations.

At the largest cross-section (θ=360°), the *V3* configuration is able to almost completely suppress flow separation at the bottom portion of the section. The improved flow guidance of the circular shape is reflected in the entropy generation rate contours, which show lower values with respect to *BSL* in the lower half of the cross-section. At θ=180°, the mitigation of flow separation phenomena is less prominent, as indicated by the two recirculation zones at the top-left and bottom-left of the cross-section. However, the topmost recirculation area of the *BSL* configuration is absent in *V3*, and the one on the bottom-left is thicker with respect to the one of *V3*. Overall, total pressure is higher in the case of circular volute, thanks to the better flow guidance with respect to the baseline, overhung configuration. Still on θ=180° section, it is worth pointing out how losses at the topmost region of the section are mitigated in *V3*, compared to the ones of the *BSL* configuration. At the smaller section close to the volute tongue, (θ=60°), performance of *V3* slightly deteriorates with respect to *BSL*. Indeed, a strong recirculation due to a forced vortex can be observed near the volute inlet, where the vortex flow mixes the with the high-velocity flow exiting the diffuser. This phenomenon is related to the high radial velocity component entering the volute, which is converted into a swirling flow by the interaction with the scroll: this flow structure collects the low-momentum fluid coming from the wall boundary layer into its core, where a concentrated pressure loss can be observed [113]. However, contrary to *V1* and *V2* configurations, *V3* is not affected by a large recirculation area at the leftmost part of the cross-section, therefore losses in that area are limited, as confirmed by the entropy generation rate contour plot.

Moving from this discussion, the circular cross-sectional shape (i.e. the *V3* configuration) was selected as the optimal design of the considered operating point. As anticipated, the second design parameter that was considered in the present study is the the shape of the circumferential area distribution characterizing the volute geometry. Up to this point, every tested configuration was characterized by a linear area distribution law: with the aim of further improving the performance from the *V3* configuration, a new volute geometry (named *V3Q*) with the same circular cross-sectional shape as *V3* and a quadratic area distribution law was analyzed. Figure 6.36 shows the effects of the area distribution law on the volute's static pressure recovery coefficient and loss coefficient.
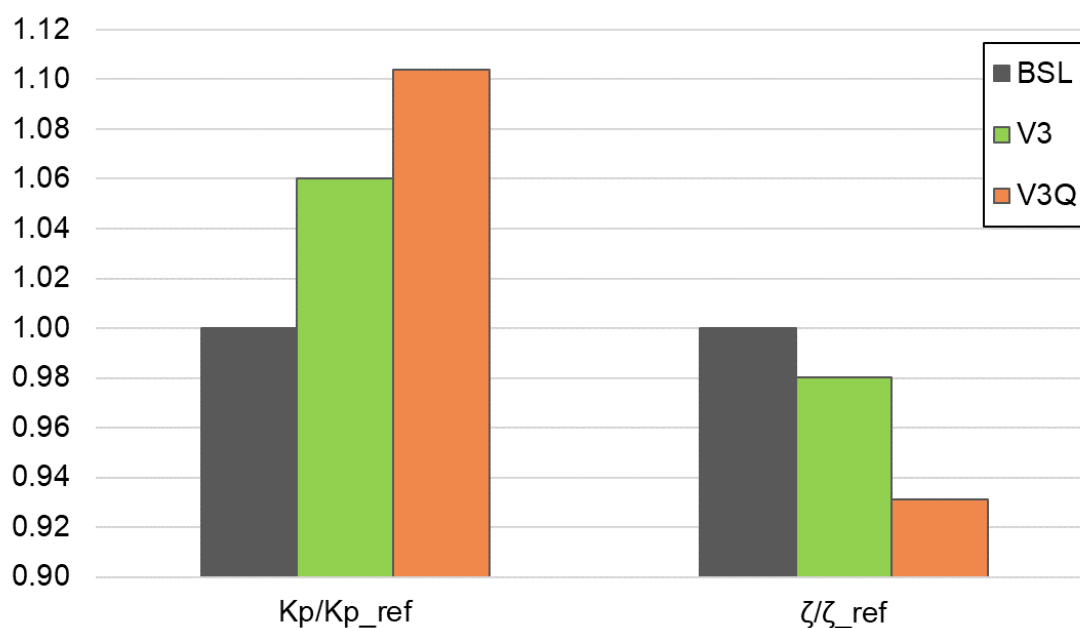
Figure 6.36   Effects of different area distribution functions on volute performance.

It is apparent that there is a relevant performance improvement in case of quadratic area distribution: the loss coefficient of *V3Q* is roughly 5% lower than the one of *V3* and therefore 7% lower than the baseline one. At the same time, pressure recovery inside *V3Q* is enhanced. Figure 6.37 and Figure 6.38 show contour plots of dimensionless total pressure and entropy generation rate, respectively, at different volute cross-sections.
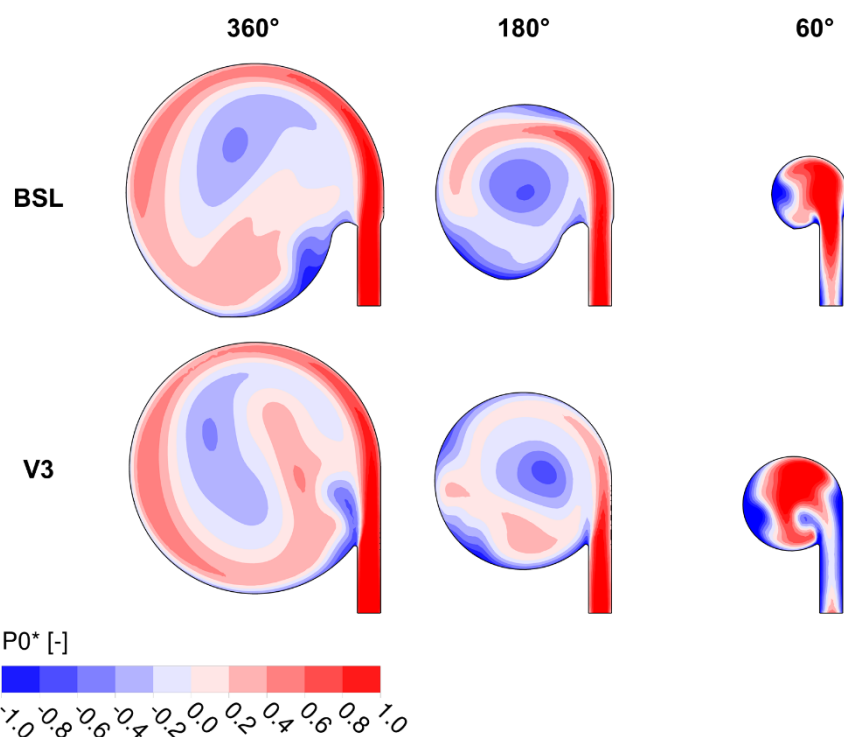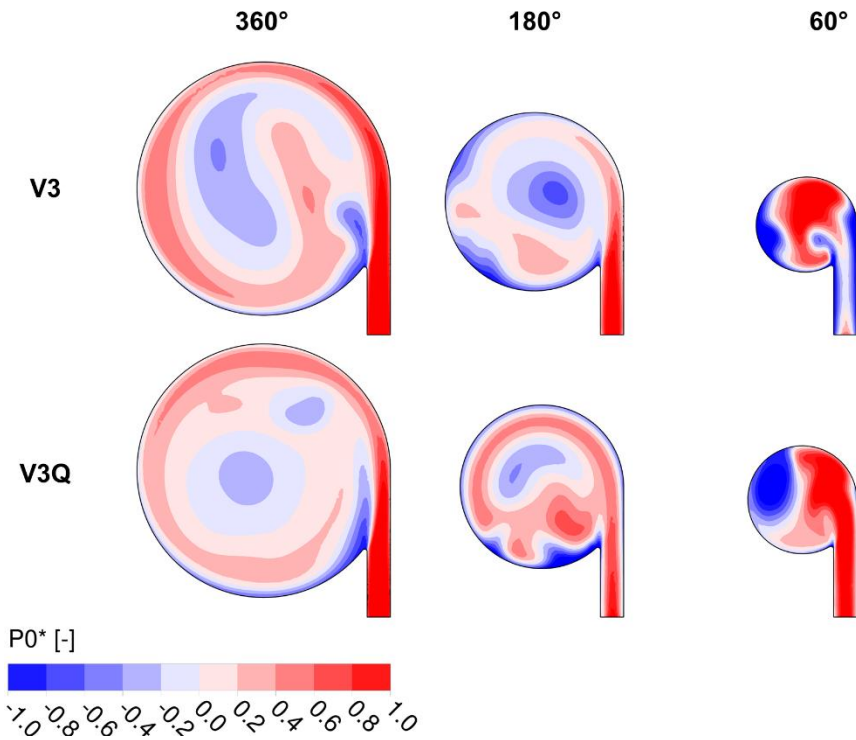
Figure 6.37   Dimensionless total pressure at different sections, for *V3* and *V3Q* configurations.
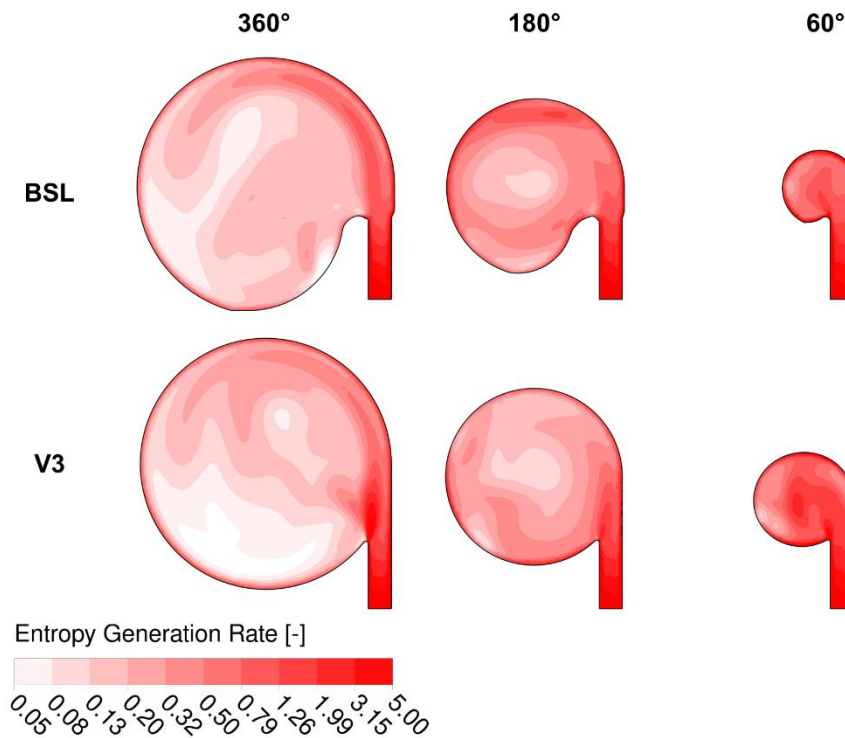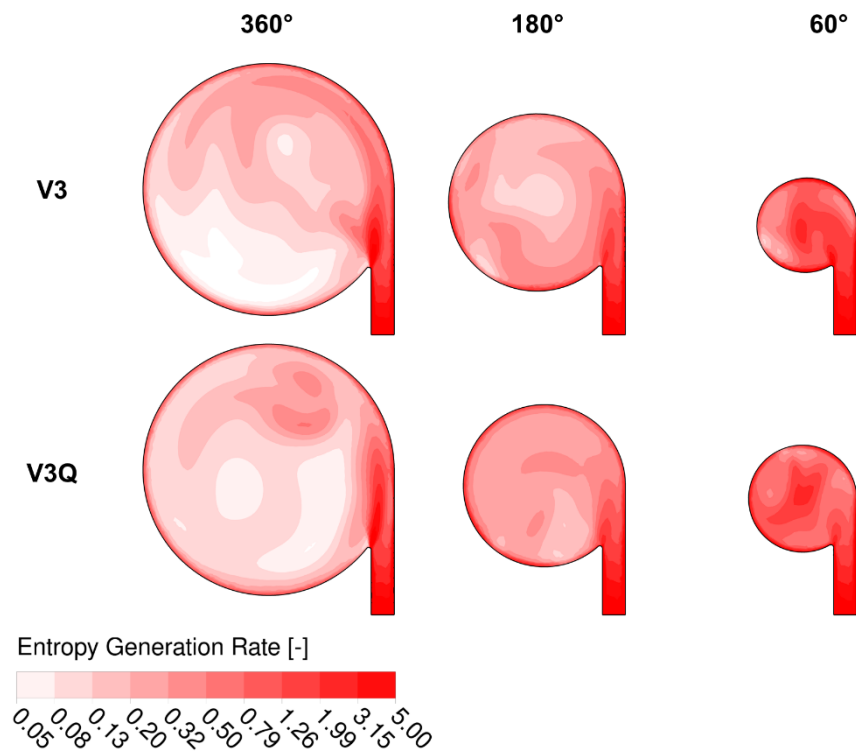

Figure 6.38   Entropy generation rate at different sections, for *V3* and *V3Q* configurations.

At θ=360°, the flow structure of *V3Q* is similar to the one of *V3*, the main difference being a slightly narrower, but more radially extended recirculation zone where the vortex mixes with the flow entering the volute. At θ=180°, two recirculation zones at the bottom portion of the scroll can be observed for the *V3Q* configuration. At the top portion, however, it is apparent that total pressure

losses are inferior with respect to the *V3* configuration, therefore, considering both effects, one may expect *V3Q* to have similar or better performance than *V3* at θ=180°. At θ=60°, near the volute's tongue, *V3Q* performance deteriorates due to the significant recirculation zone that can be observed at the top-left portion of the cross-section. Again, this is likely related to the negative incidence of the flow on the volute's tongue. Nontheless, the forced vortex at the diffuser fillet region which characterizes the same section of the *V3* configuration, although still present, is less prominent in *V3Q*. Eventually, entropy generation contour plots are similar for *V3* and *V3Q* configurations. Given the same cross-sectional shape and therefore similar flow guidance capability of the volute, the analysis of different area distribution laws requires that special attention is brought to the diffusion of the flow inside the volute. To this end, Figure 6.39 shows the evolution of the azimuthal static pressure recovery coefficient (K_p^{θ}) for the *BSL*, *V3* and *V3Q* configurations.
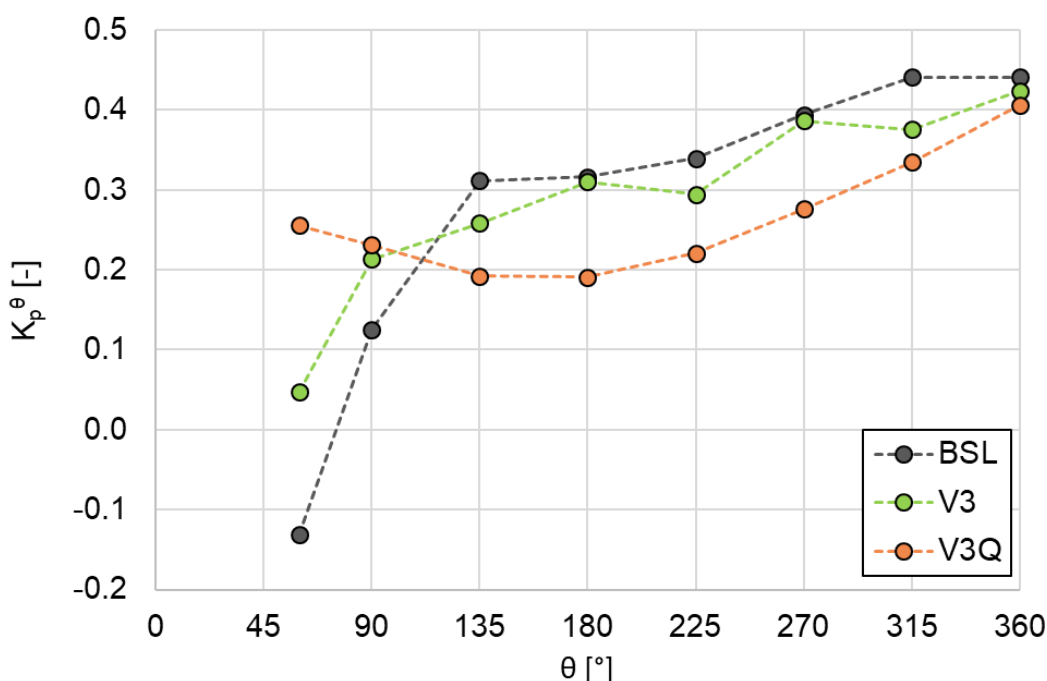
Figure 6.39   Azimuthal static pressure recovery coefficient.

It is apparent that a linear area distribution (*BSL, V3*) tends to concentrate the flow diffusion in the first portion of the scroll (θ < 135°), destabilizing the volute flow in a region where the reduced cross-section dimensions and the influence of the tongue already carry an extremely complex and dissipative flow pattern. An opposite behavior is shown by the V3Q configuration. Indeed, the volute flow is characterized by an expansion in the first half of the scroll, whilst concentrating flow diffusion in the second half. As confirmed by some studies [107,108], this is extremely beneficial for the volute performance, since it allows a stabilization of the flow near the tongue.

Moving from these results, the effects of the volute's cross-sectional shape and area distribution law on the compressor stage's efficiency were assessed.
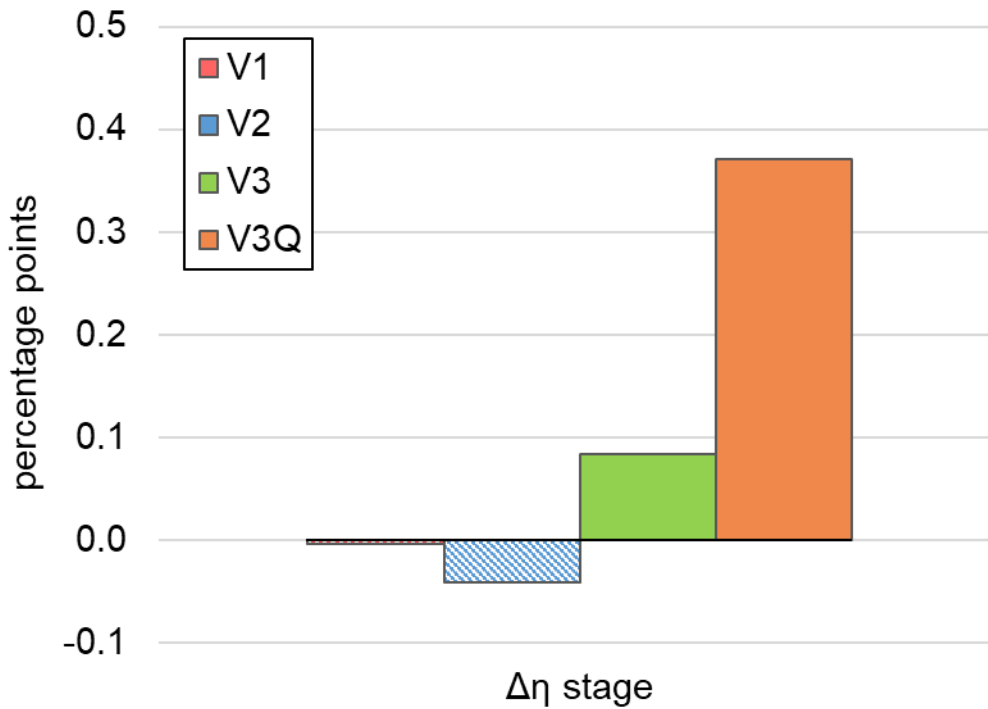
Figure 6.40   Variation of the compressor stage efficiency for the tested volute configuratons, with respect to the latest baseline configuration (*P2*).

The improved design of the volute (*V3Q*) is able to grant a stage efficiency which is roughly 0.4 percentage points higher with respect to the latest baseline configuration (*P2*). As expected, *V1* and *V2* deteriorate the compressor performance, while *V3* brings a small efficiency improvement which is not sufficient for the goals of the optimization, given the fundamental hypothesis of the adopted "first-guess" approach. Indeed, as expected from a previous study [109], a circular cross-sectional shape with a quadratic, concave area distribution law allows for better performance, which is reflected in the efficiency of the whole compressor stage.

6.3.4 - Engine performance assessment

Moving from the previous discussion, two configurations of the compressor can eventually be considered: the baseline (*BSL*) configuration, which consists in the original test case, and the optimized (*OPT*) configuration, which combines the geometrical features of the *P2* and *V3Q* configurations. Considering the isentropic efficiency enhancement firstly obtained with the *P2* vaneless diffuser and lastly with the *V3Q* volute, the stage isentropic efficiency of the *OPT* configuration is about 1 percentage point higher than the *BSL* one. Having reached the target efficiency increase that had been defined as a "first guess" at the target pressure ratio and mass flow rate, the performance maps of the optimized configuration were obtained by means of steady-state 3D CFD calculations (Figure 6.41 and Figure 6.42).
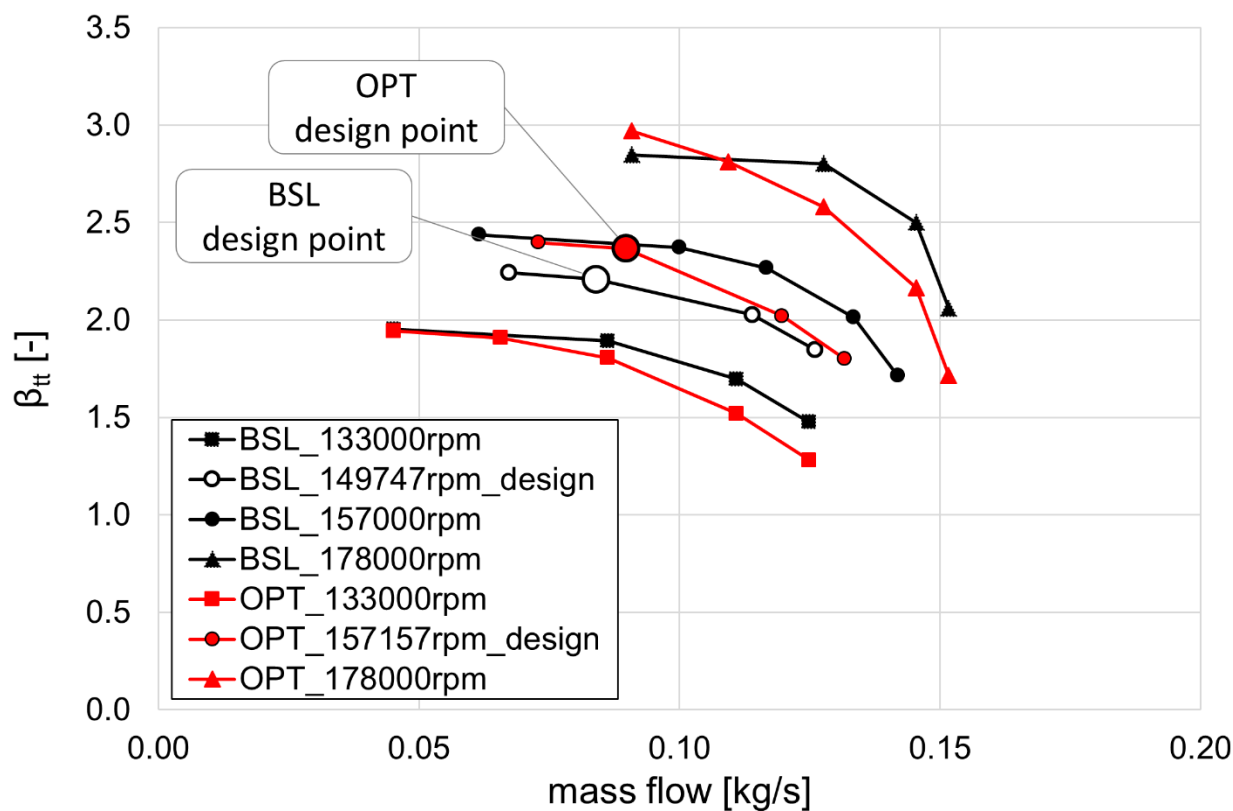
Figure 6.41   Total pressure ratio speedlines for BSL and OPT configurations.
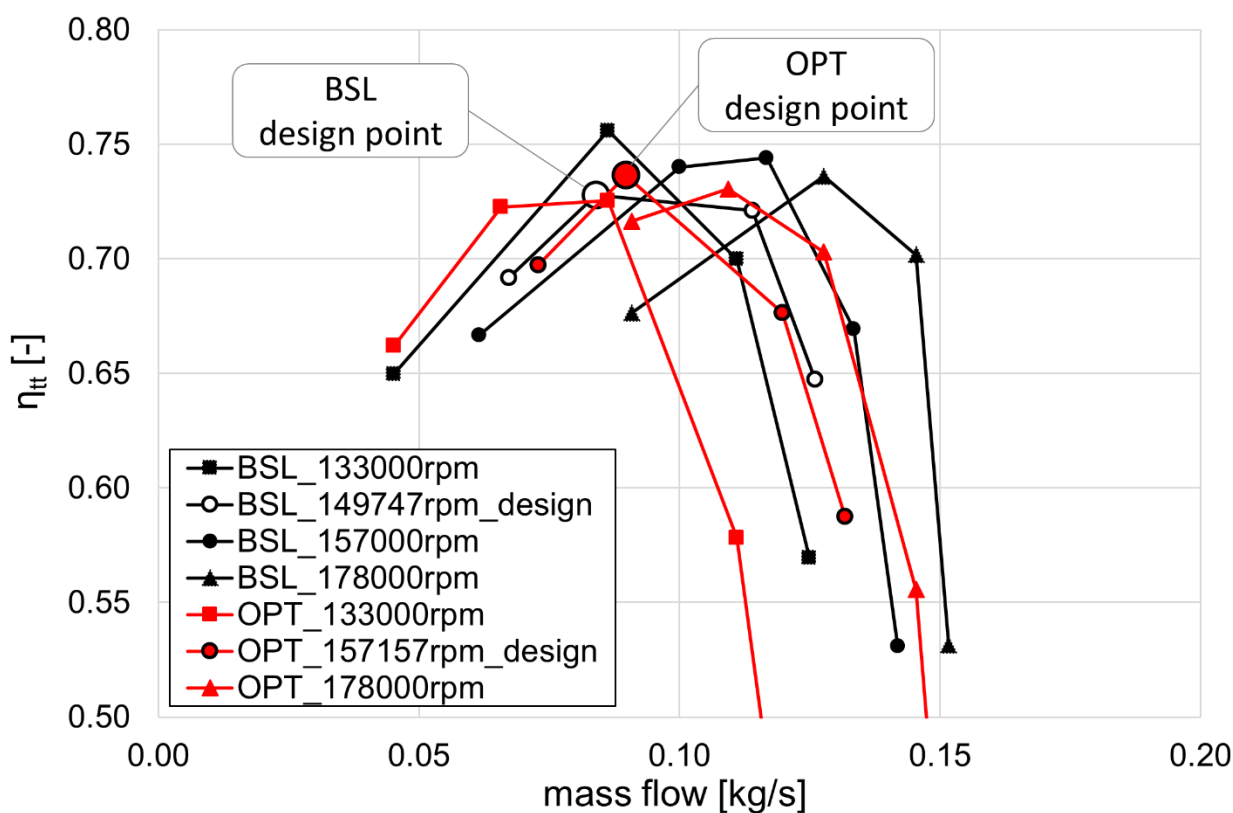
Figure 6.42   Total-to-total isentropic efficiency speedlines for BSL and OPT configurations.

For the final step of the workflow, the 1D engine model was updated with the optimized compressor maps, with the aim of assessing the actual performance of the engine working with

the optimized turbocharger. The results of the 1D analyses is reported in Table 6.7, showing that the optimized turbocharger working condition is very close to the operating condition that was initially guessed. The guessed values of mass flow rates, pressure ratios and isentropic efficiencies were, overall, just slightly overpredicted.

Component	Quantity	OPT vs BSL	FIRST GUESS vs BSL
COMPRESSOR	$\dot{m}$	+3.90 %	+3.63 %
	β_{tt}	+5.10 %	+6.58 %
	η_{tt}	+0.95 pp	+1.00 pp
ENGINE	*TC speed*	+4.98 %	+4.95 %
	$BSFC$	-0.60 %	-0.62 %
	η	+0.70 %	+0.74 %

Table 6.7 Final assessment of the engine performance: 1D engine model results.

It is apparent that the developed "first guess" optimization technique effectively led to an enhancement in engine performance: indeed, the mass of fuel necessary for guaranteeing the same engine power output is reduced for the *OPT* configuration, thus resulting in a 0.7% increase of the engine thermal efficiency. In terms of greenhouse gas emission, this translates into a 3.7 gCO_2/kWh saving, equivalent to a yearly reduction of 1510 kg of carbon dioxide emission (assuming the normal operating time of this type of engines).

Conclusions

The present work is focused on investigating multi-physics and multi-fidelity numerical techniques for the modelling of turbochargers. With the aim of developing computationally efficient methods for the analysis and optimization of both the turbine and the compressor stages, special attention was put on steady-state approaches. For this reason, the prediction capability of steady-state 3D CFD models was initially assessed by analyzing a double-entry turbine under equal and partial admission operation. Only then, more advanced simulation models were investigated on different test cases. Firstly, a thermo-structural transient analysis was carried out on a single-entry turbine for automotive application; lastly, the compressor's volute and diffuser of a turbocharged engine-generator were optimized by means of a dedicated multi-fidelity design optimization technique. The simulation techniques that were developed proved to be effective and computationally efficient: the final results are summarized in the following paragraphs.

Steady-state 3D CFD techniques for the performance characterization of turbochargers

The first part of the study focuses on assessing whether steady-state techniques represent a viable option to model a turbocharger's turbine in case of steady-state operation. Indeed, even under the engine's steady-state operation, a turbine coupled to an internal combustion engines is inherently supplied with a pulsating flow: this may hinder the prediction capabilities of a steady-state approach. The case study selected for this analysis is a double-entry turbine. This design allows the turbine to operate under partial (or "single") admission, a condition that involves the exhaust gas supply to be cut off at one of the turbine inlets and this operating condition may further enhance flow unsteadiness. The main outcomes of the study are the following:

- An introductory literature review on the modelling of pulsating flow was carried out, concluding that it is possible to quantify the turbine's flow unsteadiness by Strouhal number and pulse amplitude evaluations. If the level of unsteadiness is low, then the quasi-steady assumption is valid and steady-state approaches can be employed.

- Steady-state approaches such as the Mixing Plane (MP) and Frozen Rotor (FR) volute-rotor interface models can predict mass flow maps in both full and partial admission operation with a good level of accuracy, if mesh density is adequately high. The MP approach tends to be more accurate than the FR one, although only the FR approach can give some insight on the flow structures within the turbine: for this precise purpose, however, transient modelling is still recommended.

Literature findings on double-entry turbines are remarkably scarce and mostly consist in transient analyses that are carried out with very coarse meshes and simpler turbulence models, and understandably so. In such framework, a direct comparison against steady-state modelling might be uneven because of the low mesh density required by the transient approach. In the present

work, high density meshes and state-of-the-art RANS turbulence models were used for steady-state analyses, first, and then for a benchmark transient analysis, which was carried out with the sliding mesh approach. The prediction capability of the developed steady-state models was assessed against mass flow parameter and efficiency maps obtained from a hot gas test bench. The availability of experimental measurements for validation significantly improves the robustness of the study: among the steady-state approaches, the Mixing Plane (MP) shows the best agreement with experimental data. Another interesting outcome of the study is that the transient simulation shows similar results to the one performed with a steady-state MP approach, while all the available findings on double-entry turbines steady-state analyses take advantage of the Frozen Rotor approach: indeed, as far as the author is aware, no example applications of the Mixing Plane model are available in literature for this turbine design.

Transient thermo-structural analysis of a turbine wheel

Moving from the results of the previous analysis, effort was put in the development of a computationally efficient method for the transient thermo-structural analysis of a turbine wheel. The developed transient thermal model allows to carry out analyses that only feature the solid domain, taking advantage of adequate boundary conditions that model the effects of the fluid domain without simultaneously solving it. The main outcomes of the study are the following:

- A computationally efficient transient thermal model was developed, allowing to bypass computationally expensive or, in some cases, plainly unfeasible transient CHT analyses. Specifically, the developed model allows to perform transient thermal calculations on solid domains without concurrently solving the fluid domain like in a CHT calculation. The main advantage of this method is that the time-marching solution of the solid domain requires a timestep that is about 4 orders of magnitude larger than the one required to solve the fluid flow: therefore, calculation time is greatly reduced. The effects of the fluid flow are instead modelled through a time-dependent heat transfer coefficient (HTC) distribution that is set at the solid domain's wet boundaries. This HTC distribution can be obtained by adequately post-processing the following steady-state calculations:

  - one CHT calculation with pre-transient flow conditions;
  - one CHT calculation with the final steady-state flow conditions;
  - one CFD calculation with the final steady-state flow conditions and the solid boundaries' temperature fixed at its pre-transient values.

  The overall calculation time of the developed model is about 3 orders of magnitude lower with respect to that of a transient CHT simulation.

- Transient thermo-structural analyses deriving from different engine maneuvers were carried out. The results show that the wheel's backdisc shows the highest stress,

especially at the hub fillet and at higher radius, where strong thermal gradients combine with significant centrifugal stress.

In the development of the thermo-structural numerical setup, several modelling aspects were investigated, ranging from the effects of environmental heat transfer of the turbine's housing to the cooling effects of the oil lubricates the turbine's shaft, enhancing the robustness and scientific interest of the study.

Aerodynamic optimization of the static parts of a compressor stage

Moving from the automotive to the power generation sector, a multi-fidelity methodology for the aerodynamic optimization of a compressor's diffuser and volute was developed. Throughout the optimization activity, a 1D engine model was coupled to the developed 3D CFD model with the aim of modelling the fluid dynamic interactions between engine and turbocharger. The main outcomes of the study are the following:

- A DOE-based optimization strategy was developed and carried out by means of multi-fidelity simulation techniques.

- Several diffuser configurations were generated and tested, and flow structures were thoroughly investigated to better understand the resulting performance parameters. A vaneless diffuser with an abrupt pinch close to the impeller's exit was selected as the best performing configuration.

- Different volute cross-sectional shape and area distribution laws were analyzed. For each configuration, contour plots of total pressure and entropy generation rate were employed to investigate the flow behavior within the volute. Eventually, the volute with a circular cross-sectional shape and a quadratic area distribution law performed better than every other configuration.

- Stage isentropic efficiency increased of roughly 1 percentage points with the only optimization of the compressor's static parts. A 0.7% increase in engine efficiency was eventually assessed, equivalent to a yearly reduction of 1510 kg of carbon dioxide emission.

As a continuation for this study, the interaction between the 1D engine model and the 3D CFD model might be implemented in an automated way, extending the developed optimization technique from DOE-based to state-of-the-art automatic optimization algorithms.

List of References

[1]   Cox, P. M., Betts, R. A., Jones, C. D., Spall, S. A., and Totterdell, I. J., 2000, "Acceleration of Global Warming Due to Carbon-Cycle Feedbacks in a Coupled Climate Model," Nature, **408**(6809), pp. 184–187, 10.1038/35041539.

[2]   Cox, P. M., Pearson, D., Booth, B. B., Friedlingstein, P., Huntingford, C., Jones, C. D., and Luke, C. M., 2013, "Sensitivity of Tropical Carbon to Climate Change Constrained by Carbon Dioxide Variability," Nature, **494**(7437), pp. 341–344, 10.1038/nature11882.

[3]   ACEA, 2016, "European Automobile Manufactures Association: Consolidated Registrations - by Country."

[4]   Heywood, J. B., 1988, *Internal Combustion Engine Fundamentals*, McGraw-Hill, New York.

[5]   Fraser, N., Blaxill, H., Lumsden, G., and Bassett, M., 2009, "Challenges for Increased Efficiency through Gasoline Engine Downsizing," SAE Int. J. Engines, **2**(1), pp. 991–1008, 10.4271/2009-01-1053.

[6]   Shahed, S. M., and Bauer, K.-H., 2009, "Parametric Studies of the Impact of Turbocharging on Gasoline Engine Downsizing," SAE Int. J. Engines, **2**(1), pp. 1347–1358, 10.4271/2009-01-1472.

[7]   Hoag K., Primus R.J., 2012, "Turbocharging for Fuel Economy and Emissions, Web Seminar, SAE International."

[8]   Costall, A., 2008, "A One-Dimensional Study of Unsteady Wave Propagation in Turbocharger Turbines," PhD Thesis, Imperial College London.

[9]   García-Cuevas, L. M., 2014, "Experiments and Modelling of Automotive Turbochargers under Unsteady Conditions," PhD Thesis, Universitat Politecnica de Valencia.

[10]   Spinner, G., Dahinten, F., Dauscher, S., and Munz, S., 2018, "Electrified Boosting Systems in Today's and Future Automotive Applications," *2018 Thirteenth International Conference on Ecological Vehicles and Renewable Energies (EVER)*, IEEE, Monte-Carlo, pp. 1–5.

[11]   Mihaylov, M., Stoyanov, I., and Iliev, T., 2021, "Reduction of the Battery Capacity of Hybrid Electric Vehicle with the Help of Electrically Assisted Turbocharger," E3S Web Conf., **327**, p. 04003, 10.1051/e3sconf/202132704003.

[12]   Uchida, H., 2006, "Trend of Turbocharger Technologies," R&D Review of Toyota CRDL, **41**(3).

[13]   Marelli, S., Capobianco, M., and Zamboni, G., 2014, "Pulsating Flow Performance of a Turbocharger Compressor for Automotive Application," International Journal of Heat and Fluid Flow, **45**, pp. 158–165, 10.1016/j.ijheatfluidflow.2013.11.001.

[14]   Newton, P., Romagnoli, A., Martinez-Botas, R., Copeland, C., and Seiler, M., 2014, "A Method of Map Extrapolation for Unequal and Partial Admission in a Double Entry Turbine," Journal of Turbomachinery, **136**(6), p. 061019, 10.1115/1.4025763.

[15]   Perrot, N., Chesse, P., Dubouil, R., and Goumy, G., 2017, "Experimental Characterization for Modelling of Turbocharger Friction Losses," pp. 2017-24–0013.

[16]   Pesiridis, A., Salim, W. S.-I. W., and Martinez-Botas, R. F., 2012, "Turbocharger Matching Methodology for Improved Exhaust Energy Recovery," *10th International Conference on Turbochargers and Turbocharging,* Elsevier, pp. 203–218.

[17]   Zeng, T., and Zhu, G. G., 2018, "Control-Oriented Turbine Power Model for a Variable-Geometry Turbocharger," Proceedings of the Institution of Mechanical Engineers, Part D: Journal of Automobile Engineering, **232**(4), pp. 466–481, 10.1177/0954407017702996.

[18]   Hendricks, E., 1989, "The Analysis of Mean Value Engine Models," p. 890563.

[19]   Jensen, J.-P., Kristensen, A. F., Sorenson, S. C., Houbak, N., and Hendricks, E., 1991, "Mean Value Modeling of a Small Turbocharged Diesel Engine," p. 910070.

[20]   Wu, H., Wang, X., Winsor, R., and Baumgard, K., 2011, "Mean Value Engine Modeling for a Diesel Engine with GT-Power 1D Detail Model," pp. 2011-01–1294.

[21]   Li, R., Huang, Y., Li, G., Han, K., and Song, H., 2013, "Calibration and Validation of a Mean Value Model for Turbocharged Diesel Engine," Advances in Mechanical Engineering, **5**, p. 579503, 10.1155/2013/579503.

[22]   Marzouk Abdel-Hamid, M., 1976, "Simulation of Turbocharged Diesel Engines Under Transient Conditions," PhD Thesis, Imperial College London.

[23]   Baines, N. C., Hajilouy-Benisi, A., and Yeo, J. H., 1994, "The Pulse Flow Performance and Modelling of Radial Inflow Turbines," Turbocharging and Turbochargers, IMechE.

[24]   menacer, brahim, Department of Mechanical Engineering,University of Sciences and the Technology of Oran, Bouchetara, M., and University of Sciences and the Technology of Oran, Algeria, 2016, "Thermodynamic Analysis of a Turbocharged Diesel Engine Operating under Steady State Condition," JAFM, **9**(2), pp. 573–585, 10.18869/acadpub.jafm.68.225.24661.

[25]   Baines, N. C., "Turbocharger Turbine Pulse Flow Performance and Modelling – 25 Years On."

[26]   Ding, Z., Zhuge, W., Zhang, Y., Chen, H., Martinez-Botas, R., and Yang, M., 2017, "A One-Dimensional Unsteady Performance Model for Turbocharger Turbines," Energy, **132**, pp. 341–355, 10.1016/j.energy.2017.04.154.

[27]   Piscaglia, F., Onorati, A., Marelli, S., and Capobianco, M., 2019, "A Detailed One-Dimensional Model to Predict the Unsteady Behavior of Turbocharger Turbines for Internal Combustion Engine Applications," International Journal of Engine Research, **20**(3), pp. 327–349, 10.1177/1468087417752525.

[28] Wallace, F. J., 1958, "Theoretical Assessment of the Performance Characteristics of Inward Radial Flow Turbines," Proceedings of the Institution of Mechanical Engineers, **172**(1), pp. 931–952, 10.1243/PIME_PROC_1958_172_072_02.

[29] Montenegro, G., Tamborski, M., Marinoni, A., Torre, A. D., Onorati, A., and Marelli, S., 2019, "A Quasi 3D Approach for the Modelling of an Automotive Turbocharger's Compressor," Erode, India, p. 020113.

[30] Montenegro, G., and Onorati, A., 2009, "1D Thermo-Fluid Dynamic Modeling of Reacting Flows inside Three-Way Catalytic Converters," SAE Int. J. Engines, **2**(1), pp. 1444–1459, 10.4271/2009-01-1510.

[31] Montenegro, G., and Onorati, A., 2006, "1D Thermo-Fluid Dynamic Modelling of de-NOx SCR Systems for Diesel Engine Exhaust Gas after-Treatment," IJVD, **41**(1/2/3/4), p. 285, 10.1504/IJVD.2006.009672.

[32] Cerri, T., D'Errico, G., Montenegro, G., Onorati, A., Koltsakis, G., Samaras, Z., Michos, K., Tziolas, V., Zingopis, N., Dimopoulos Eggenschwiler, P., Papetti, V., Rojewski, J., and Soltic, P., 2019, "A Novel 1D Co-Simulation Framework for the Prediction of Tailpipe Emissions under Different IC Engine Operating Conditions," pp. 2019-24–0147.

[33] Newton, P., Copeland, C., Martinez-Botas, R., and Seiler, M., 2012, "An Audit of Aerodynamic Loss in a Double Entry Turbine under Full and Partial Admission," International Journal of Heat and Fluid Flow, **33**(1), pp. 70–80, 10.1016/j.ijheatfluidflow.2011.10.001.

[34] Galindo, J., Tiseira, A., Fajardo, P., and García-Cuevas, L. M., 2014, "Development and Validation of a Radial Variable Geometry Turbine Model for Transient Pulsating Flow Applications," Energy Conversion and Management, **85**, pp. 190–203, 10.1016/j.enconman.2014.05.072.

[35] Palenschat, T., Newton, P., Martinez-Botas, R. F., Müller, M., and Leweux, J., 2017, "3-D Computational Loss Analysis of an Asymmetric Volute Twin-Scroll Turbocharger," *Volume 8: Microturbines, Turbochargers and Small Turbomachines; Steam Turbines*, American Society of Mechanical Engineers, Charlotte, North Carolina, USA, p. V008T26A016.

[36] Galindo, J., Tiseira, A., Navarro, R., and López, M. A., 2015, "Influence of Tip Clearance on Flow Behavior and Noise Generation of Centrifugal Compressors in Near-Surge Conditions," International Journal of Heat and Fluid Flow, **52**, pp. 129–139, 10.1016/j.ijheatfluidflow.2014.12.004.

[37] Mueller, L., and Verstraete, T., 2017, "CAD Integrated Multipoint Adjoint-Based Optimization of a Turbocharger Radial Turbine," IJTPP, **2**(3), p. 14, 10.3390/ijtpp2030014.

[38] Khairuddin, U., Costall, A. W., and Martinez-Botas, R. F., 2015, "Influence of Geometrical Parameters on Aerodynamic Optimization of a Mixed-Flow Turbocharger Turbine," *Volume 2C: Turbomachinery*, American Society of Mechanical Engineers, Montreal, Quebec, Canada, p. V02CT42A002.

[39]   Montenegro, G., Onorati, A., Piscaglia, F., and D'Errico, G., 2007, "Integrated 1D-MultiD Fluid Dynamic Models for the Simulation of I.C.E. Intake and Exhaust Systems," pp. 2007-01–0495.

[40]   Versteeg, H. K., and Malalasekera, W., 2007, *An Introduction to Computational Fluid Dynamics: The Finite Volume Method*, Pearson Education Ltd, Harlow, England ; New York.

[41]   Pope, S. B., 2000, *Turbulent Flows*, Cambridge University Press.

[42]   Kundu, P. K., Cohen, I. M., Dowling, D. R., and Tryggvason, G., 2016, *Fluid Mechanics*, Elsevier/AP, Amsterdam ; Boston.

[43]   Wilcox, D. C., 2006, *Turbulence Modeling for CFD*, DCW Industries, La Cãnada, Calif.

[44]   Menter, F. R., 1994, "Two-Equation Eddy-Viscosity Turbulence Models for Engineering Applications," AIAA Journal, **32**(8), pp. 1598–1605, 10.2514/3.12149.

[45]   Łuczyński, P., Giesen, M., Gier, T.-S., and Wirsum, M., 2019, "Uncoupled CFD-FEA Methods for the Thermo-Structural Analysis of Turbochargers," IJTPP, **4**(4), p. 39, 10.3390/ijtpp4040039.

[46]   Diefenthal, M., Luczynski, P., and Wirsum, M., 2017, "Speed-Up Methods for The Modeling of Transient Temperatures With Regard to Thermal and Thermomechanical Fatigue," Stockholm, Sweden.

[47]   Diefenthal, M., Łuczyński, P., Rakut, C., Wirsum, M., and Heuer, T., 2017, "Thermomechanical Analysis of Transient Temperatures in a Radial Turbine Wheel," Journal of Turbomachinery, **139**(9), p. 091001, 10.1115/1.4036104.

[48]   Sitayoung, T., Luczynski, P., and Juntasaro, E., 2022, "Thermomechanical Analysis of a Radial Turbine in Stationary and Transient Operation," Chiang Mai, Thailand, p. 020005.

[49]   Denton, J. D., 1993, "The 1993 IGTI Scholar Lecture: Loss Mechanisms in Turbomachines," Journal of Turbomachinery, **115**(4), pp. 621–656, 10.1115/1.2929299.

[50]   Naidu, A. D., Vogel, K., and Fischer, M., 2017, "A Comparative Study of Transient Blade Row and Blade Count Scaling Approaches for Numerical Forced Response Analysis in a Transonic Turbine," Stockholm, Sweden.

[51]   Biesinger, T., Kölzer, M., Schukmann, A., Roclawski, H., Kainz, M., Godin, P., Morales, J. C., and Zori, L., 2022, "Application of the Harmonic Balance Method for Large Spread Multiple Frequency Scales," *Volume 10D: Turbomachinery — Multidisciplinary Design Approaches, Optimization, and Uncertainty Quantification; Turbomachinery General Interest; Unsteady Flows in Turbomachinery*, American Society of Mechanical Engineers, Rotterdam, Netherlands, p. V10DT37A005.

[52]   Benson, R. S., and Scrimshaw, K. H., 1965, "Paper 23: An Experimental Investigation of Non-Steady Flow in a Radial Gas Turbine," Proceedings of the Institution of Mechanical Engineers, Conference Proceedings, **180**(10), pp. 74–85, 10.1243/PIME_CONF_1965_180_283_02.

[53] Benson, R. S., 1974, "Nonsteady Flow in a Turbocharger Nozzleless Radial Gas Turbine," p. 740739.

[54] Wallace, F. J., and Blair, G. P., 1965, "The Pulsating-Flow Performance of Inward Radial-Flow Turbines," *ASME 1965 Gas Turbine Conference and Products Show*, American Society of Mechanical Engineers, Washington, DC, USA, p. V001T01A021.

[55] Wallace, F.J , Adgey, J.M and Blair, G.P., 1970, "Performance of Inward Flow Turbines under Unsteady Flow Conditions," IMechE Proc., **184**.

[56] Wallace, F. and Miles, J., 1971, "Performance of Inward Radial Flow Turbines under Unsteady Flow Conditions with Full and Partial Admission," IMechE Proc., **185**.

[57] Kosuge, H., Yamanaka, N., Ariga, I., and Watanabe, I., 1976, "Performance of Radial Flow Turbines Under Pulsating Flow Conditions," Journal of Engineering for Power, **98**(1), pp. 53–59, 10.1115/1.3446110.

[58] Capobianco, M., and Gambarotta, A., 1989, "Influence of the Pulsating Flow Operation on the Turbine Characteristics of a Small Internal Combustion Engine Turbocharger," IMechE Proc., **C372/019**.

[59] Capobianco, M., and Gambarotta, A., 1990, "Unsteady Flow Performance of Turbocharger Radial Turbines," IMechE Proc., **C405/017**.

[60] Capobianco, M., and Gambarotta, A., 1992, "Unsteady Flow Performance of Turbocharger Radial Turbines," Journal of Engineering for Gas Turbines and Power, **114**, pp. 553–560.

[61] Costall, A. W., McDavid, R. M., Martinez-Botas, R. F., and Baines, N. C., 2011, "Pulse Performance Modeling of a Twin Entry Turbocharger Turbine Under Full and Unequal Admission," Journal of Turbomachinery, **133**(2), p. 021005, 10.1115/1.4000566.

[62] Copeland, C. D., Martinez-Botas, R., and Seiler, M., 2012, "Unsteady Performance of a Double Entry Turbocharger Turbine With a Comparison to Steady Flow Conditions," Journal of Turbomachinery, **134**(2), p. 021022, 10.1115/1.4003171.

[63] Copeland, C. D., Martinez-Botas, R., and Seiler, M., 2011, "Comparison Between Steady and Unsteady Double-Entry Turbine Performance Using the Quasi-Steady Assumption," Journal of Turbomachinery, **133**(3), p. 031001, 10.1115/1.4000580.

[64] Szymko, S., 2006, "The Development of an Eddy Current Dynamometer for Evaluation of Steady and Pulsating Turbocharger Turbine Performance," PhD Thesis, Imperial College London.

[65] Costall, A., Szymko, S., Martinez-Botas, R. F., Filsinger, D., and Ninkovic, D., 2006, "Assessment of Unsteady Behavior in Turbocharger Turbines," *Volume 6: Turbomachinery, Parts A and B*, ASMEDC, Barcelona, Spain, pp. 1023–1038.

[66] ostall, A., Rajoo, S. and Martinez-Botas, R. F., 2006, "Modelling and Experimental Study of the Unsteady Effects and Their Significance for Nozzleless and Nozzled Turbine Performance."

[67]   Copeland, C. D., Newton, P., Martinez-Botas, R. F., and Seiler, M., 2012, "A Comparison of Timescales within a Pulsed Flow Turbocharger Turbine," *10th International Conference on Turbochargers and Turbocharging*, Elsevier, pp. 389–404.

[68]   Romagnoli, A., Copeland, C., Martinez-Botas, R., Rajoo, S., Seiler, M., and Costall, A., 2011, "Comparison Between the Steady Performance of Double-Entry and Twin-Entry Turbocharger Turbines."

[69]   Lee, J., Tan, C. S., Sirakov, B. T., Wilkins, C., Im, H.-S., Babak, M., and Tisserant, D., 2016, "Performance Metric for Turbine Stage Under Unsteady Pulsating Flow Environment."

[70]   Newton, P., Martinez-Botas, R., and Seiler, M., 2014, "A 3-Dimensional Computational Study of Pulsating Flow Inside a Double Entry Turbine," *Volume 2D: Turbomachinery*, American Society of Mechanical Engineers, Düsseldorf, Germany, p. V02DT42A026.

[71]   Copeland, C. D., Newton, P. J., Martinez-Botas, R., and Seiler, M., 2012, "The Effect of Unequal Admission on the Performance and Loss Generation in a Double-Entry Turbocharger Turbine," Journal of Turbomachinery, **134**(2), p. 021004, 10.1115/1.4003226.

[72]   Lückmann, D., Stadermann, M., Aymanns, R., and Pischinger, S., 2016, "Investigation of Cross Flow in Double Entry Turbocharger Turbines," *Volume 8: Microturbines, Turbochargers and Small Turbomachines; Steam Turbines*, American Society of Mechanical Engineers, Seoul, South Korea, p. V008T23A024.

[73]   Walkingshaw, J., Iosifidis, G., Scheuermann, T., Filsinger, D., and Ikeya, N., 2016, "A Comparison of a Mono-, Twin-, and Double-Scroll Turbine for Automotive Applications," Journal of Engineering for Gas Turbines and Power, **138**(5), p. 052301, 10.1115/1.4031449.

[74]   Lee, J., Tan, C. S., Sirakov, B. T., Wilkins, C., Im, H.-S., Babak, M., and Tisserant, D., 2016, "Performance Characterization of Twin Scroll Turbine Stage for Vehicular Turbocharger Under Unsteady Pulsating Flow Environment."

[75]   Heuer, T., Engels, B., Klein, A., and Heger, H., 2006, "Numerical and Experimental Analysis of the Thermo-Mechanical Load on Turbine Wheels of Turbochargers," *Volume 5: Marine; Microturbines and Small Turbomachinery; Oil and Gas Applications; Structures and Dynamics, Parts A and B*, ASMEDC, Barcelona, Spain, pp. 325–332.

[76]   Heuer, T., Engels, B., and Wollscheid, P., 2005, "Thermomechanical Analysis of a Turbocharger Based on Conjugate Heat Transfer," *Volume 1: Turbo Expo 2005*, ASMEDC, Reno, Nevada, USA, pp. 829–836.

[77]   Ahdad, F., Kannusamy, R., and Damodharan, B., 2010, "Analytical Approach of TMF Prediction for Complex Loading," *Volume 6: Structures and Dynamics, Parts A and B*, ASMEDC, Glasgow, UK, pp. 581–590.

[78] Oberste-Brandenburg, C., Shoghi, K., Gugau, M., and Kruse, F., 2012, "On the Influence of Thermal Boundary Conditions on the Thermo Mechanical Analysis of Turbine Housing of a Turbocharger," *10th International Conference on Turbochargers and Turbocharging*, Elsevier, pp. 83–95.

[79] Makarenko, I., Lehmayr, B., Bogner, M., Klaus, M., and Singer, R. F., 2012, "Thermomechanical Behaviour of Turbocharger Compressor Wheels," *Volume 4: Heat Transfer, Parts A and B*, American Society of Mechanical Engineers, Copenhagen, Denmark, pp. 1089–1098.

[80] Breeze, P., 2018, *Piston Engine-Based Power Plants*, Academic Press, an imprint of Elsevier, London, United Kingdom.

[81] Watson, N., and Janota, M. S., 1982, *Turbocharging the Internal Combustion Engine*, Macmillan Education UK, London.

[82] Van den Braembussche, R. A., 2008, "Numerical Optimization for Advanced Turbomachinery Design," *Optimization and Computational Fluid Dynamics*, D. Thévenin, and G. Janiga, eds., Springer Berlin Heidelberg, Berlin, Heidelberg, pp. 147–189.

[83] Lotz, R. D., 2017, "Aerodynamic Optimization Process for Turbocharger Compressor Impellers," *Volume 2B: Turbomachinery*, American Society of Mechanical Engineers, Charlotte, North Carolina, USA, p. V02BT41A036.

[84] Rahbar, K., Mahmoud, S., Al-Dadah, R. K., and Moazami, N., 2015, "Parametric Analysis and Optimization of a Small-Scale Radial Turbine for Organic Rankine Cycle," Energy, **83**, pp. 696–711, 10.1016/j.energy.2015.02.079.

[85] Liu, Z., and Copeland, C., 2020, "Optimization of a Radial Turbine for Pulsating Flows," Journal of Engineering for Gas Turbines and Power, **142**(5), p. 051009, 10.1115/1.4046235.

[86] Mueller, L., Alsalihi, Z., and Verstraete, T., 2013, "Multidisciplinary Optimization of a Turbocharger Radial Turbine," Journal of Turbomachinery, **135**(2), p. 021022, 10.1115/1.4007507.

[87] Zhang, F., and Baar, R., 2017, "Geometric Optimization of Turbocharger Compressor and Its Influence on Engine Performance," MATEC Web Conf., **108**, p. 08012, 10.1051/matecconf/201710808012.

[88] Baines, N. C., 2005, *Fundamentals of Turbocharging*, Concepts NREC, White River Junction, Vt.

[89] Marelli, S., Marmorato, G., Capobianco, M., and Boulanger, J.-M., 2016, "Towards the Direct Evaluation of Turbine Isentropic Efficiency in Turbocharger Testing," pp. 2016-01–1033.

[90] Marelli, S., Usai, V., Capobianco, M., Montenegro, G., Della Torre, A., and Onorati, A., 2019, "Direct Evaluation of Turbine Isentropic Efficiency in Turbochargers: CFD Assisted Design of an Innovative Measuring Technique," pp. 2019-01–0324.

[91]   Usai, V., Cordalonga, C., and Marelli, S., 2022, "Experimental Evaluation of Isentropic Efficiency in Turbocharger Twin-Entry Turbines," J. Phys.: Conf. Ser., **2385**(1), p. 012135, 10.1088/1742-6596/2385/1/012135.

[92]   ANSYS, "Automatic Near-Wall Treatment for Omega-Based Models," ANSYS CFX modeling guide, 4.2.3.

[93]   Catalani, I., Agnolucci, A., Balduzzi, F., Bianchini, A., Arnone, A., Ferrara, G., Vichi, G., Bellissima, A., Minamino, R., and Asai, G., 2021, "Aerodynamic Optimization of a Turbocharger Unit Based on the Overall Efficiency Enhancement of an Internal Combustion Engine for Stationary Power Production," *Volume 6: Ceramics and Ceramic Composites; Coal, Biomass, Hydrogen, and Alternative Fuels; Microturbines, Turbochargers, and Small Turbomachines*, American Society of Mechanical Engineers, Virtual, Online, p. V006T19A004.

[94]   Gamma Technologies, "Gamma Technologies Website" [Online]. Available: https://www.gtisoft.com/gt-suite-applications/propulsion-systems/gt-power-engine-simulation-software.

[95]   Tanda, G., Marelli, S., Marmorato, G., and Capobianco, M., 2017, "An Experimental Investigation of Internal Heat Transfer in an Automotive Turbocharger Compressor," Applied Energy, **193**, pp. 531–539, 10.1016/j.apenergy.2017.02.053.

[96]   Marelli, S., Marmorato, G., and Capobianco, M., 2016, "Evaluation of Heat Transfer Effects in Small Turbochargers by Theoretical Model and Its Experimental Validation," Energy, **112**, pp. 264–272, 10.1016/j.energy.2016.06.067.

[97]   Marelli, S., Marmorato, G., Capobianco, M., and Rinaldi, A., 2015, "Heat Transfer Effects on Performance Map of a Turbocharger Compressor for Automotive Application," pp. 2015-01–1287.

[98]   Marelli, S., Gandolfi, S., and Capobianco, M., 2017, "Heat Transfer Effect on Performance Map of a Turbocharger Turbine for Automotive Application," pp. 2017-01–1036.

[99]   Cormerais M. , Chesse P. , Hetet J., 2009, "Turbocharger Heat Transfer Modeling Under Steady and Transient Conditions," International Journal of Thermodynamics, **12**(4), pp. 193–202.

[100]   Serrano, J., Olmeda, P., Arnau, F., Reyes-Belmonte, M., and Lefebvre, A., 2013, "Importance of Heat Transfer Phenomena in Small Turbochargers for Passenger Car Applications," SAE Int. J. Engines, **6**(2), pp. 716–728, 10.4271/2013-01-0576.

[101]   Aghaali, H., Ångström, H.-E., and Serrano, J. R., 2015, "Evaluation of Different Heat Transfer Conditions on an Automotive Turbocharger," International Journal of Engine Research, **16**(2), pp. 137–151, 10.1177/1468087414524755.

[102]   Japikse, D., 1996, *Centrifugal Compressor Design and Performance*, Concepts ETI, Wilder, Vt.

[103] Pan, D., Whitfield, A., and Wilson, M., 1999, "Design Considerations for the Volutes of Centrifugal Fans and Compressors," Proceedings of the Institution of Mechanical Engineers, Part C: Journal of Mechanical Engineering Science, **213**(4), pp. 401–410, 10.1243/0954406991522356.

[104] Qiang, X., Teng, J., and Du, Z., 2010, "Influence of Various Volute Designs on Volute Overall Performance," J. Therm. Sci., **19**(6), pp. 505–513, 10.1007/s11630-010-0416-7.

[105] Mojaddam, M., Benisi, A. H., and Movahhedi, M. R., 2012, "Investigation on Effect of Centrifugal Compressor Volute Cross-Section Shape on Performance and Flow Field," *Volume 8: Turbomachinery, Parts A, B, and C*, American Society of Mechanical Engineers, Copenhagen, Denmark, pp. 871–880.

[106] Mojaddam, M., Hajilouy-Benisi, A., and Movahhedy, M. R., 2014, "Optimal Design of the Volute for a Turbocharger Radial Flow Compressor," *Volume 2D: Turbomachinery*, American Society of Mechanical Engineers, Düsseldorf, Germany, p. V02DT42A037.

[107] Yu, L., Cousins, W. T., Shen, F., Kalitzin, G., Sishtla, V., and Sharma, O., 2016, "Numerical Investigation of the Effect of Diffuser and Volute Design Parameters on the Performance of a Centrifugal Compressor Stage," *Volume 2D: Turbomachinery*, American Society of Mechanical Engineers, Seoul, South Korea, p. V02DT42A024.

[108] Chen, H., and Li, P., 2013, "Compressor Housing Design for Small Turbocharger Compressors," *Volume 6C: Turbomachinery*, American Society of Mechanical Engineers, San Antonio, Texas, USA, p. V06CT40A003.

[109] Melani, P. F., Balduzzi, F., Bianchini, A., Ferrara, G., Hoffer, P.-A., Montesino, S., and Brenner, M., 2020, "Influence of Key Design Parameters on the Aerodynamic Performance of a Centrifugal Compressor Volute for Turbocharger Applications."

[110] Herwig, H., and Kock, F., 2006, "Local Entropy Production in Turbulent Shear Flows: A Tool for Evaluating Heat Transfer Performance," J. of Therm. Sci., **15**(2), pp. 159–167, 10.1007/s11630-006-0159-7.

[111] Zhang, L., Zhuge, W., Zhang, Y., and Chen, T., 2017, "Similarity Theory Based Radial Turbine Performance and Loss Mechanism Comparison between R245fa and Air for Heavy-Duty Diesel Engine Organic Rankine Cycles," Entropy, **19**(1), p. 25, 10.3390/e19010025.

[112] Van den Braembussche, R. A., and Ha¨nde, B. M., 1990, "Experimental and Theoretical Study of the Swirling Flow in Centrifugal Compressor Volutes," Journal of Turbomachinery, **112**(1), pp. 38–43, 10.1115/1.2927418.

[113] Hagelstein, D., Hillewaert, K., Van den Braembussche, R. A., Engeda, A., Keiper, R., and Rautenberg, M., 2000, "Experimental and Numerical Investigation of the Flow in a Centrifugal Compressor Volute," Journal of Turbomachinery, **122**(1), pp. 22–31, 10.1115/1.555423.